Skoltech
Skolkovo Institute of Science and Technology

Jury Member Report – Doctor of Philosophy thesis

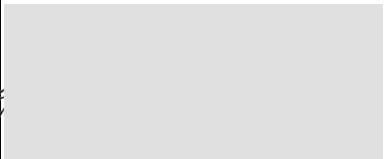**Name of Candidate:** Julijana Cvjetinovic

PhD Program: Physics

Title of Thesis: Optical and mechanical properties of diatom algae and related materials

Supervisor: Professor Dmitry Gorin
Co-supervisor: Professor Alexander Korsunsky

Name of the Reviewer:

I confirm the absence of any conflict of interest	
	Date: 20-09-2023

The purpose of this report is to obtain an independent review from the members of PhD defense Jury before the thesis defense. The members of PhD defense Jury are asked to submit signed copy of the report at least 30 days prior the thesis defense. The Reviewers are asked to bring a copy of the completed report to the thesis defense and to discuss the contents of each report with each other before the thesis defense.

If the reviewers have any queries about the thesis which they wish to raise in advance, please contact the Chair of the Jury.

Reviewer's Report

Reviewers report should contain the following items:

- Brief evaluation of the thesis quality and overall structure of the dissertation.
- The relevance of the topic of dissertation work to its actual content
- The relevance of the methods used in the dissertation
- The scientific significance of the results obtained and their compliance with the international level and current state of the art
- The relevance of the obtained results to applications (if applicable)
- The quality of publications

The summary of issues to be addressed before/during the thesis defense

This is a very interesting and, potentially, solid thesis. It details a highly interdisciplinary work, which bridges biology, solid mechanics, advanced materials and nanophotonics. The work involves the investigation of various aspects of the functionality of diatom algae on different scales: (i) colonies suspended in water, (ii) individual living cells and just frustules, and (iii) diatomite powder. The underlying efforts represent a tremendous amount of work carried out by the candidate, which has already resulted in 8 peer-reviewed publications, where the candidate is a lead author (including Scientific Reports, Photoacoustics and Physical Chemistry and Chemical Physics), another 9 co-authored papers (including Nanomaterials, ACS Photonics and ACS Applied Nano Materials), 2 book chapters and 13 oral talks given by the candidate at national and international conferences and workshops.

The candidate's research presented across Chapters 4, 6 and 8 is novel and of a high standard, as would be expected of work already published in good peer-reviewed journals. Such work is time consuming and requires the mastery of scientific principles across disciplines, which the candidate may not have been originally trained in, and the candidate should be applauded for this work. Yet, it feels that the thesis has been put together in a rush with some of its sections (and even chapters) appearing more finished than others. For instance, chapter 7, which presents a systematic study of the optical properties of diatom frustules, is overall of an average quality – most notably, it lacks proper analysis and discussion of the obtained results and the novelty of the work there has not been clearly communicated. The structure of the thesis also needs improving, as there are considerable overlaps between various sections/chapters, duplications and repetitions in the text, while division into sections (and even chapters) in some parts of the thesis does not seem to be justified.

Below I summarize minor and major issues to be addressed, while my comments and recommendations can be found in the marked up copy of the thesis attached to this report.

> Formatting

The size of pages the candidate chose for her thesis corresponds to Letter, while the current standard is A4, I believe.

> Writing style

In some places of the thesis the candidate refers to herself using royal "we" and in other places passive voice is used. While "we" is perfectly acceptable for an ordinary scientific publication (which is typically authored by more than one person), a thesis can have only one author and so the use of "we" does not seem appropriate. Hence, my recommendation for the candidate is to use passive voice throughout the thesis and refer to herself as "the author" where needed.

> Thesis structure

There are a number of shortcomings in the structure of the thesis, which need mending. In particular, there are quite a few repetitions and duplications throughout the thesis. For example, applications are discussed in the introduction in sub-section 2.4.5 and then again in sub-section 2.5.3, as well as in various other parts of section 2.5, yet the entire sub-section 2.5.5 is seemingly dedicated to applications. The fabrication of gold-coated diatomite is given in both section 8.2 and chapter 3. The detailed description of frustules appears in both sections 5.2 and 6.2.

Some sections in the thesis contain irrelevant or misplaced pieces of information or discussions. For example in MEMS intro section 2.6 the candidate talks about optical structures, photonic integrated circuits and optical properties. The thesis introductory chapter features the description of the

methodology (see, for example, section 2.3) that is later described in chapter 3. One will be surprised to find a detailed description of how chloroplasts control their position and orientation in response to changing light conditions in section 7.4.3, which is meant to discuss the distribution of electric field intensity in a frustule integrated over all incident angles and polarizations. Some methods are descried in chapters other than chapter 3 (for example, FLIM visialisation in section 5.4, or research methodology in section 6.1)

Also, I am not convinced that certain chapters are worth being included in the thesis, at least as parts of its main body. In particular, chapter 5 is descriptive in nature, providing information on the size and shape of frustules, and the distribution of chloroplasts inside the frustules. It does not really feature any novelty or intellectual contribution from the candidate (at least, that has not been conveyed) and, essentially, just describes the 'materials' that the candidate used in her studies (which should have, actually, appeared in chapter 3). Chapter 3 contains the description of various methods/techniques, many of which are fairly standard and/or well documented anyway. On the other hand, the investigative chapters also feature the description of several methods, some of which either overlap with those in chapter 3 or appear exclusive to the project. Therefore, the best course of action for the candidate, perhaps, would be to leave only the standard methods/techniques in chapter 3, and transform chapter 3 and 5 into new appendices (or add them to the existing ones). Then, the methods and setups developed and/or improved by the candidate exclusively for her projects can be described in the investigative chapters in the context of relevant studies.

> Plagiarism

Some sections/chapters (e.g., most of section of Chapter 2, Chapters 3, 4 and 5) are seemingly better composed and feature better English than others, which suggests that the text there might have been copied from published sources. While self-plagiarism (i.e., the use of text from the publications authored/co-authored by the candidate) is acceptable, the instances of plagiarism (if it does take place) must be avoided all together, for example, by paraphrasing the respective sections of text.

> Citing candidate's own papers

The candidate does not have to (and, in fact, should not) refer to her published papers in the thesis as if they represent the sources of additional information. This thesis is not a review of the candidate's own publications – it is the primary source of information for the work the candidate did in the course of her postgraduate research. The thesis is, in fact, expected to provide a much more detail account of the candidate's research than the papers she co-authored.

While it is very good that the candidate has managed to publish her work in a number of peer-reviewed journals by now, that did not have to be the case – the candidate's papers could have been still under review or not even submitted. Hence, I recommend the candidate to provide at the beginning of each chapter a list of relevant papers she co-authored (e.g., like she has done so far) but, otherwise, write her thesis as a **self-contained** piece of research pretending that the work has not been published yet. Correspondingly, rather than referencing her papers in the thesis, the candidate should refer to relevant chapters/sections instead.

Apart from investigative chapters, the candidate also explicitly refers to her own publications in introductory chapters, which looks rather odd if not confusing. The introductory chapters are meant to give an overview of the existing body of literature on the topic and serve to provide a context for the candidate's postgraduate research detailed in the following chapters. Hence, one does not expect to

find a review of the candidate's work in the introduction. If the candidate wants to introduce/mention the relevant work that she did outside/prior to her postgraduate research, then I suggest those publications should be treated on the same footing as all other papers reviewed in the introduction (i.e., without mentioning explicitly their relation to the candidate).

> Figures

I expect the candidate to use her original plots and diagrams (i.e., created by her) in the thesis, in which case she does not need to refer to her publications in figure captions.

If, instead, the candidate requires to reproduce certain images or diagrams directly from either her publications (say, because they were created by other co-authors) or papers published by other groups (e.g., Figure 3), it is my understanding that the candidate needs to obtain copyright permissions from the publishers of those works. Once permissions have been granted (it maybe just a matter of checking copyright statements of respective publishers, who often allow the re-use of figures in one's thesis), the candidate should add to figure captions the corresponding statements along with justifications/reasons for including in her thesis someone else's results/creations.

Quite often figure captions appear to have been split across two pages (or even completely moved to the next page) – this does not look professional. A figure and its figure caption are a single entity and should appear on the same page. For a particularly large figure the candidate should use a whole page. If a whole page is not enough then the figure contains too many panels and/or its figure caption is unnecessarily detailed. In such case the candidate should consider dividing the figure into several separate figures and/or trimming its figure caption. Alternatively, some of the panels/plots may well be moved into an appendix, as quite often only few panels in multi-panel figures are properly discussed/analysed in this thesis.

In some figures (and/or plots in figures) the numbers and notations are hard to see because the fonts are too small. This is because the candidate elected to squeeze too many plots in such figures. My recommendation would be as above – the candidate should divide such figures into several separate figures and/or move some plots into an appendix.

Dividing large figures will also help the candidate avoid copyright issues in those cases when the figures are taken from the candidate's publications.

> Tables

As per my comments above regarding figures, the candidate should also use her original tables, in which case no acknowledgement or reference to the candidate's publication is needed.

Some tables appear split across two pages – this should be (and can be) avoided. Also, some tables need mending, as text/numbers in those tables appear corrupted.

> Acknowledging colleague's contributions

Given the tremendous amount of material presented in the thesis, I could not help but wonder whether the candidate managed to do all the work herself. If the candidate happened to receive some help with collecting and/or preparing samples, developing of apparatus and setups, taking measurements, data processing, analysing results, simulations etc., it should be properly acknowledged in the relevant places of the text. Also, if the candidate included in the thesis rather large chunks of the work/results that were done/collected by others, she needs to explain the reason for doing so (because this thesis is about the

candidate's work and the results she obtained).

> **Data analysis and conclusions**

Many plots and tables are presented in the thesis without proper analysis or discussion. The candidate needs not to forget that experiments or simulations are conducted in order to test/verify the existing theories/hypothesis or find new dependencies/effects not covered by or contradicting the current understanding. Otherwise, one's research activity simply turns into 'stamp collecting'. I appreciate the desire of the candidate to include in her thesis all the data she collected/simulated in the course of her postgraduate research, but without interpretation and analysis such data present little scientific value, as well as invites one to question the candidates analytical skills and overall interest in the research. Therefore, I recommend that the data, the analysis of which has not been commenced or finished yet, should be moved from the main text into an appendix, and then the candidate's intention to carry out the analysis of that data in the near future should be indicated in Outlook section (which is, by the way, currently missing).

Also, it would be great to see some sort of conclusions at the end of investigative chapters. For example, at the end of MEMS chapter the candidate could have concluded that the mechanical resonance frequencies of diatom frustules that were determined in the study were in the right range for certain MEMS applications etc.

Provisional Recommendation

☐ *I recommend that the candidate should defend the thesis by means of a formal thesis defense*

☒ *I recommend that the candidate should defend the thesis by means of a formal thesis defense only after appropriate changes would be introduced in candidate's thesis according to the recommendations of the present report*

☐ *The thesis is not acceptable and I recommend that the candidate be exempt from the formal thesis defense*

Skoltech

Skolkovo Institute of Science and Technology

Skolkovo Institute of Science and Technology

OPTICAL AND MECHANICAL PROPERTIES OF DIATOM ALGAE AND
RELATED MATERIALS

Doctoral Thesis

by

JULIJANA CVJETINOVIC

DOCTORAL PROGRAM IN PHYSICS

Supervisor
Professor Dmitry Gorin
Co-advisor
Professor Alexander Korsunsky

Moscow - 2023

I hereby declare that the work presented in this thesis was carried out by myself at Skolkovo Institute of Science and Technology, Moscow, except where due acknowledgement is made, and has not been submitted for any other degree.

Candidate (Julijana Cvjetinovic)

Supervisor (Prof. Dmitry Gorin)

Co-advisor (Prof. Alexander Korsunsky)

Abstract

Nanostructured natural objects featuring advanced properties serve as an endless source of inspiration for the development of new materials and devices. A rich gallery of such objects are the skeletons of diatom algae – Nature's glass (silica) lace. The neat slender structures resemble woven lace that combines elegance with strength and durability, and provoke the effort to explore the organization and properties of the objects created and refined by nature over millions of years of evolution.

In recent years, climate change due to global warming from greenhouse gas emissions, particularly carbon dioxide (CO_2), has become an increasingly pressing issue. Diatoms have shown impressive performance in removing CO_2 from the atmosphere through photosynthesis. To maximize the amount of CO_2 that can be extracted using diatoms and their biomass production, it is vital to properly monitor them and identify any issues that may be limiting their growth. Novel optical methods proposed here, such as fluorescence and photoacoustic (optoacoustic) visualization, can be readily used for monitoring algae growth, not only in laboratory conditions but also in their natural environment.

Interrogating the structure and properties of diatoms down to nanometer scale leads to breakthrough advances reported here in the mechanical and optical characterization of silica frustules, as well as of air-dried and wet cells with organic content. Static and dynamic mode Atomic Force Microscopy (AFM) and *in situ* nanoindentation in the scanning electron microscope column revealed the peculiarities of diatom response with separate contributions from material nanoscale behavior and membrane deformation of the

3

entire valve. The optical properties of diatoms that stem from their periodic photonic crystal structure are of interest in the development of new devices for photonic applications. By studying the optical and mechanical properties of diatoms in tandem, a holistic view of their interdependent structure-property relationships can provide insights into materials design. Through the functionalization, diatom properties and the range of applications can be further upgraded and expanded. The modification of the diatomite with gold nanoparticles presented in this work has the potential to create a versatile material with enhanced properties that can be used as surface enhanced Raman scattering (SERS) platform and for sensing applications.

This dissertation examines the potential for using novel optical methods to monitor diatom colonies and the combination of optical and mechanical properties of diatoms as well as novel techniques to alter silica surface for future development of advanced technologies with the potential to create new materials and devices.

Keywords: diatoms, carbon dioxide, hierarchical structure, monitoring, growth, optical properties, mechanical properties, modification, diatomite

Thesis related publications

1. **Cvjetinovic J**, Luchkin S, Statnik E, Davidovich N, Somov P, Salimon A, Korsunsky A, Gorin D. Revealing the static and dynamic nanomechanical properties of diatom frustules—Nature's glass lace. *Scientific Reports*. 2023; 13, 5518: 1-12.

(The main and corresponding author, IF 4.996, Q1)

2. **Cvjetinovic J**, Salimon I, Novoselova M, Sapozhnikov Ph, Shirshin E, Yashchenok A, Kalinina O, Korsunsky A, Gorin D. Photoacoustic and fluorescence lifetime imaging of diatoms. *Photoacoustics.* 2020; 18; 100171.

(The main and corresponding author, IF 9.656, Q1)

3. **Cvjetinovic J**, Merdalimova A, Kirsanova M, Somov P, Salimon A, Korsunsky A, Gorin D. SERS Platform Based on Diatomite Modified by Gold Nanoparticles Using a Combination of Layer-by-Layer Assembly and Freezing-Induced Loading Method. *Physical Chemistry Chemical Physics*. 2022; 24: 8901-8912.

(The main and corresponding author, IF 3.945, Q1)

4. **Cvjetinovic J**, Perkov S, Kurochkin M, Sergeev I, German S, Bedoshvili Ye, Davidovich N, Korsunsky A, Gorin D. Concentration dependence of optical transmission and extinction of different diatom cultures. *Journal of Biomedical Photonics and Engineering*. 2023; 9(1):1-9.

(The main and corresponding author, IF 1.4, Q2)

5. **Cvjetinovic J**, Bedoshvili Ye, Nozdriukhin D, Salimon A, Korsunsky A, Gorin D. Photonic tools for evaluating the growth of diatom colonies during long-term batch cultivation. *Journal of Physics: Conference Series*. 2022; 2172; 012011.

(The main and corresponding author)

6. **Cvjetinovic J**, Nozdriukhin D, Bedoshvili Ye, Salimon A, Korsunsky A, Gorin A. Assessment of diatom growth using fluorescence imaging. *Journal of Physics: Conference Series*. 2021; 1984; 012017.

(The main and corresponding author)

7. **Cvjetinovic J**, Bedoshvili Ye, Nozdriukhin D, Efimova O, Salimon A, Volokitina N, Korsunsky A, Gorin D. In situ fluorescence/photoacoustic monitoring of diatom algae. *SPIE Proceedings* Dynamics and Fluctuations in Biomedical Photonics XVIII; 2021; 11641; 116410G.

(The main and corresponding author)

8. Aggrey P, Nartey M, Kan Y, **Cvjetinovic J**, Andrews A, Salimon A, Dragnevski K, Korsunsky A. On the diatomite-based nanostructure-preserving material synthesis for energy applications. *RSC Advances*, 2021; 11; 31884-31922.

(Wrote several sections of the review article, IF 4.036, Q1)

9. Korsunsky A, Bedoshvili Ye, **Cvjetinovic J**, Aggrey P, Dragnevski K, Gorin D, Salimon A, Likhoshway Ye. Siliceous diatom frustules - a smart nanotechnology platform. *Materials today: Proceedings*. 2020; 33(4):2032-2040.

(Wrote several sections of the review article, IF 1.46, Q2)

10. **Cvjetinovic J**, Salimon A, Novoselova M, Sapozhnikov Ph, Kalinina O, Korsunsky A, Gorin D. Photoacoustic visualization of diatom algae. *Limnology and Freshwater Biology*. 2020; 4.

(The main and corresponding author)

11. Salimon A, Sapozhnikov Ph, Everaerts J, Kalinina O, Besnard C, Papadaki C, **Cvjetinovic J**, Statnik E, Kan Y, Aggrey P, Kalyaev V, Lukashova M, Somov P,

Korsunsky A. A Mini-Atlas of diatom frustule electron microscopy images at different magnifications. *Materials Today: Proceedings*. 2020; 33(4):1924-1933.

(Participated in collecting SEM images, IF 1.46, Q2)

12. Sapozhnikov Ph, Salimon A, Korsunsky A, Kalinina O, Senatov F, Statnik E, **Cvjetinovic J**. Features of formation of colonial settlements of marine benthic diatoms on the surface of synthetic polymer. *Marine Biological Journal*. 2020; 5(2):88-104.

(Participated in writing of the manuscript)

13. Salimon A, **Cvjetinovic J**, Kan Y, Statnik E, Aggrey A, Somov P, Salimon I, Everaerts J, Bedoshvili Ye, Gorin D, Likhoshway Ye, Sapozhnikov Ph, Davidovich N, Kalinina O, Dragnevski K, Korsunsky M. On the Mathematical Description of Diatom Algae: From Siliceous Exoskeleton Structure and Properties to Colony Growth Kinetics, and Prospective Nanoengineering Applications, in the book The Mathematical Biology of Diatoms, ed. Janice L. Pappas, Scrivener Publishing LLC, 2023; 63-102.

(Performed experiments related to the colony growth kinetics, wrote several sections, performed final editing)

14. **Cvjetinovic J**, Nozdriukhin D, Mokrousov M, Novikov A, Novoselova M, Tuchin V, Gorin D. Enhancement of contrast in photoacoustic – fluorescence tomography and cytometry using optical clearing and contrast agents, in the book Handbook of Tissue Optical Clearing, ed. Valery Tuchin, Dan Zhu, Elina Genina, Taylor and Francis Group, CRC Press, 2022

(The main and corresponding author)

Other publications

1. M. R. Chetyrkina, **J. Cvjetinovic**, F. S. Fedorov, S. V. Perevoschikov, E. S. Prikhozhdenko, B. F. Mikladal, Y. G. Gladush, A. G. Nasibulin, D. A. Gorin. ACS Photonics 2022, 9, 10, 3429–3439 (Q1, IF 7.077)

2. T. O. Abakumova, O. I. Gusliakova, **J. Cvjetinovic**, O. I. Efimova, E. V. Konovalova, A. A. Schulga, T. S. Zatsepin, D. A. Gorin, A. M. Yashchenok, and S. M. Deyev. *ACS Applied Nano Materials*. 2022, 5, 8, 10744–10754 (Q1, IF 6.14)

3. Kan Y, Bondareva JV, Statnik ES, **Cvjetinovic J**, Lipovskikh S, Abdurashitov AS, Kirsanova MA, Sukhorukhov GB, Evlashin SA, Salimon AI, Korsunsky AM. *Nanomaterials*. 2022; 12(6):998. (Q1, IF 5.719)

4. Kaydanov, N, Perevoschikov, S, German, S, Romanov, S, Ermatov, T, Kozyrev, A, **Cvjetinovic, J**, Machnev, A, Noskov, R, Kosolobov, S, Skibina, J, Nasibulin, A, Zakian, C, Lagoudakis, P, Gorin, D. *ACS Photonics*, 2021, 8(11), 3346-3356 (Q1, IF 7.077)

5. Y. Kan, **J. Cvjetinovic**, E. S. Statnik, S. V. Ryazantsev, N. Yu. Anisimova, M. V. Kiselevskiy, A. I. Salimon, A. V. Maksimkin, A. M. Korsunsky. *Materials Today Communications* 24 (2020) 101052 (Q2, IF 3.662)

Conferences

1. **Cvjetinovic, Julijana**; Salimon, Alexey; Novoselova, Marina; Sapozhnikov, Philipp; Kalinina, Olga; Korsunsky, Alexander; Gorin, Dmitry. Photoacoustic and fluorescence lifetime imaging of diatoms. The VIIth Vereschagin Baikal Conference. 2020, Irkutsk, Russia (oral talk)

2. **Cvjetinovic, Julijana**; Salimon, Alexey; Korsunsky, Alexander; Novoselova, Marina; Sapozhnikov, Philipp; Kalinina, Olga; Bedoshvili, Yekaterina; Gayer, Alexey; Efimova, Olga; Yaschenok, Alexey; Gorin, Dmitry. Diatoms: where photoacoustics meets fluorescence. The XXIV Annual Conference Saratov Fall Meeting. 2020, Saratov, Russia (oral talk)

3. **Cvjetinovic, Julijana**; Bedoshvili, Yekaterina; Nozdriukhin, Daniil; Efimova, Olga; Salimon, Alexey; Volokitina, Nadezhda; Korsunsky, Alexander; Gorin, Dmitry. In situ fluorescence/photo acoustic monitoring of diatom algae. SPIE Photonics West Digital forum. 2021, San Francisco, USA (oral talk)

4. **Cvjetinovic, Julijana**; Nozdriukhin, Daniil; Bedoshvili, Yekaterina; Efimova, Olga; Salimon, Alexey; Somov, Pavel; Korsunsky, Alexander; Gorin, Dmitry. Monitoring of diatom algae growth using fluorescence and photoacoustic imaging techniques. SPb Photonic, Optoelectronic, & Electronic Materials (SPb POEM). 2021, Saint Petersburg, Russia (oral talk)

5. **Cvjetinovic, Julijana**; Gorin, Dmitry. Photoacoustic contrast agents for in vitro/in vivo visualization. II Международная научно-практическая конференция

«Фундаментальная наука для практической медицины-2021» (Basic science for practical medicine-2021). 2021, Elbrus, Russia (oral talk)

6. **Cvjetinovic, Julijana**; Bedoshvili, Yekaterina; Davidovich, Nickolai; Salimon, Alexey; Korsunsky, Alexander; Gorin, Dmitry. Photonic tools for studying freshwater and marine diatoms during long-term cultivation. The XXV Saratov Fall Meeting. 2021, Saratov, Russia (oral talk)

7. **Cvjetinovic, Julijana**; Nozdriukhin, Daniil; Kirsanova, Maria; Somov, Pavel; Salimon, Alexey; Korsunsky, Alexander; Gorin, Dmitry. Hybrid materials based on diatomite modified by gold nanoparticles: fabrication and photoacoustic characterization. SNAIA (Smart NanoMaterials: Advances, Innovation and Applications). 2021, Paris, France (oral talk)

8. **Cvjetinovic, Julijana**; Nozdriukhin, Daniil; Bedoshvili, Yekaterina; Davidovich, Olga; Efimova, Olga; Davidovich, Nickolai; Somov, Pavel; Salimon, Alexey; Korsunsky, Alexander; Gorin, Dmitry. Photonic methods for studying diatom algae. UK-Russia conference – Advanced materials to combat cancer. 2021, Lancaster, United Kingdom (oral talk)

9. **Cvjetinovic, Julijana**; Bedoshvili, Yekaterina; Davidovich, Nickolai; Luchkin, Sergey; Salimon, Alexey; Korsunsky, Alexander; Gorin, Dmitry. Optical properties of diatom algae: research methods and potential applications. The 6th International Conference on the Physics of Optical Materials and Devices AND The 5th International Workshop of Persistent and Photostimulable Phosphors (IWPPP-5). 2022, Belgrade, Serbia (oral talk)

10. **Cvjetinovic, Julijana**; Merdalimova, Anastasiia; Kirsanova, Maria; Somov, Pavel; Nozdriukhin, Daniil; Salimon, Alexey; Korsunsky, Alexander; Gorin, Dmitry. Nanostructured biosilica exoskeletons functionalized by gold nanoparticles as SERS-active materials. The XXVI Saratov Fall Meeting. 2022, Saratov, Russia (oral talk)

11. **Cvjetinovic, Julijana**; Luchkin, Sergey; Statnik, Eugene; Davidovich, Nickolai; Bedoshvili, Yekaterina; Somov, Pavel; Salimon, Alexey; Korsunsky, Alexander; Gorin, Dmitry. The nanomechanics of diatom silica exoskeletons. The 13th International Conference on Key Engineering Materials (ICKEM 2023). 2023, Istanbul, Turkey (oral talk)

12. **Cvjetinovic, Julijana**; Dyakov, Sergey; Maksimov, Eugene; Davidovich, Nickolai; Salimon, Alexey; Lagoudakis, Pavlos; Korsunsky, Alexander; Gippius, Nikolay; Gorin, Dmitry. Diatom optics: unlocking the potential of biogenic photonic crystals. BRICS Workshop on biophotonics II. 2023, Saratov, Russia (oral talk)

13. **Cvjetinovic, Julijana**; Perkov, Sergei; Kurochkin, Maxim; Sergeev, Igor; German, Sergey; Bedoshvili, Yekaterina, Davidovich, Nickolai; Korsunsky, Alexander; Gorin, Dmitry. Optical characteristics of diatoms: relationship between concentration and transmission/extinction. Workshop on current trends in biophotonics. 2023, Nizhny Novgorod, Russia (oral talk)

Acknowledgements

First and foremost, I would like to express my sincere gratitude to my advisor, Prof. Dmitry Gorin for his guidance and tutoring. I could not have achieved the accomplishments inside or outside this thesis work without his constant encouragement, resourcefulness and diligence which have set the high standard for my PhD research. I would also like to express my deep appreciation for the help and guidance from my co-advisor, Prof. Alexander Korsunsky, a tutor of great knowledge, vision and wisdom. Their faith and insights in the potential of diatom study have been the source of my inspiration, and the key driving forces for me to pursue the wonderful researches presented in this work. I would like to thank Dr. Alexey Salimon for introducing me to the world of diatoms, for his support, ideas and guidance throughout my PhD studies. I would also like to extend my gratitude towards Dr. Yekaterina Bedoshvili and Prof. Nickolai Davidovich for providing me with the diatom cultures and being the best collaborators. Their help in the study of diatom structure, feedbacks and discussions have been of great value for my thesis work.

I would also like to thank Dr. Sergey Luchkin, Eugene Statnik and Pavel Somov for their help with the study of mechanical properties, Prof. Sergey Dyakov and Prof. Nikolay Gippius for the numerical calculations of optical properties, Prof. Vladimir Drachev and Prof. Pavlos Lagoudakis for patiently listening to my talks and providing useful advice. Whenever I was confused and lost in the wonderland of new methods and approaches, they all provided priceless insights and helping hands regardless of the differences in our research directions.

My special thanks also go to Dr. Sergei German for help with monitoring diatom division in a microfluidic cell, Dr. Maxim Kurochkin and Sergei Perkov for development of optical setup to measure changes in diatom concentrations, Daniil Nozdriukhin for fabrication of the first version of bioreactor, Stanislav Perevoschikov for calculations of diatom resonant frequencies, Anastasiia Merdalimova for performing Raman measurements of gold-coated diatomite. I have been inspired by their approaches in solving many complicated scientific problems. I am beyond grateful to my dear colleagues and friends Dr. Yuliya Kan, Margarita Chetyrkina and Maksim Mokrousov for their company, advice, support, pleasant memories and many fruitful discussions that we usually had over a cup of tea. I have also had the great pleasures working with all the wonderful colleagues from Biophotonics Lab.

I would also like to acknowledge the Center for Photonic Science and Engineering, "Bioimaging and Spectroscopy" Core Facility as well as Advanced Imaging Core Facility at Skoltech and Russian Science Foundation for support through grant No. 22-14-00209.

Last but not least, I would like to express my sincere gratitude to my family members for their endless love and support throughout my academic journey. My parents, sister, niece and my grandparents have been my source of inspiration, constantly encouraging me to pursue my dreams and reminding me of the importance of hard work and discipline. At the very last, I would like to thank my husband Andrey for everything he did for me and for our small family. I could not have made so far without his company, unwavering support, patience and love. Thank you for being there for me every step of the way.

Table of contents

List of Symbols, Abbreviations

AFM – atomic force microscopy

AMFM – amplitude modulation- frequency modulation

BANSAM – Bio-Assisted Nanometer Size Additive Manufacturing

BF-TEM – Bright-field transmission electron microscopy

DI – deionized

DMT – Derjaguin-Muller-Toropov

FIL – freezing-induced loading

FLIM – fluorescence lifetime imaging microscopy

FMM – Fourier modal method

HAADF – high angle annular darkfield

EDX – energy dispersive X-ray

LbL – Layer-by-layer

MEMS – microelectromechanical systems

NEMS – nanoelectromechanical system

PAH – polyallylamine hydrochloride

RSOM – Raster scanning optoacoustic mesoscopy

SEM – scanning electron microscopy

SERS – Surface enhanced Raman spectroscopy

STEM – scanning transmission electron microscopy

TCSPS – time-correlated single-photon-counting

TEM – transmission electron microscopy

List of Figures

List of Tables

Chapter 1. Introduction

Diatoms are single cell microalgae enclosed in silica exoskeletons called frustules that provide inspiration for advanced hybrid nanostructure designs mimicking multi-scale porosity to achieve outstanding mechanical and optical properties.[1] They are of planetary ecological importance, making a huge contribution to biomineralization and carbon dioxide capture by accounting for approximately 20% of oxygen production via photosynthesis[2–4].

The global concentration of CO_2 in the atmosphere has reached levels that are higher than those in the past several hundred thousand years.[5] This poses significant threats to our ecosystems, natural resources and modern civilization. Thus, measures to reduce the amount of CO_2 released into the atmosphere and technologies to efficiently extract CO_2 from the atmosphere are urgently needed. Extracting CO_2 from the atmosphere is a challenging problem because it is a very dilute gas in air, and the extraction and storage process is energy-intensive and expensive. Meanwhile, the current energy-intensive methods of extracting and purifying CO_2 require time-consuming processes, high temperatures and pressures, and large capital investment. Therefore, alternative technologies and innovative strategies are needed to address the problem of CO_2 extraction and storage while minimizing energy consumption and cost.
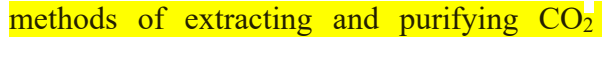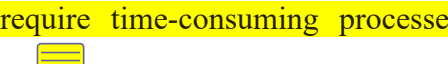
In order to use diatom algae for carbon dioxide extraction, we need to be able to grow them in large quantities. Monitoring the growth of diatom algae is important because it allows us to optimize their growth conditions, such as nutrient availability and light intensity, and ensure that they are healthy and productive. By carefully monitoring their

growth, we can identify and take steps to address any issues that may be limiting their growth. This will ultimately help us to maximize the amount of carbon dioxide that can be extracted from the atmosphere using diatom algae and their biomass production for biotechnological applications. The need to monitor the growth of diatom algae using novel optical methods arises from the limitations of traditional methods. Traditional methods of monitoring diatom growth involve manual counting of cells, which is time-consuming and labor-intensive. Additionally, these methods are prone to errors and may not provide accurate measurements of growth rates. Novel optical methods, such as fluorescence and photoacoustic visualization, offer several advantages over traditional methods as they provide non-invasive and real-time information about the physiological state of the algae, which can help to optimize growth conditions for biotechnology applications or to assess the impact of environmental changes on diatom populations.

However, diatoms garner attention not solely for their ecological significance but also for the distinctive characteristics of their highly porous silica cell wall. A unique micro- and nano-scale architecture of diatom silica exoskeletons provides high-performance optical and mechanical properties with the potential for advanced materials. Studying the optical and mechanical properties of diatoms is essential for developing new technologies and materials inspired by natural systems.[1] In order to design effective technologies and materials, a deep understanding of the fundamental properties and structure of natural materials is needed. The optical properties of diatoms, such as their light scattering and absorption properties, are of interest in the development of new sensors and devices for environmental monitoring, as well as for photonic and biomedical

applications. Similarly, the mechanical properties of diatoms, such as their strength, stiffness, and fracture toughness, are of great interest for applications such as biomimetic materials development, the production of microelectronic and nanophotonic devices, and biodegradable implants.

Another important aspect for future application of diatom frustules is the modification of the surface to further improve their properties. For example, modifying the surface of diatomite with gold nanoparticles has the potential to create a composite material for sensing applications. Gold nanoparticles on the surface of diatomite can act as a catalyst for chemical reactions, while the porous structure of diatomite can provide a large surface area for adsorption of pollutants or other molecules. Additionally, the combination of gold nanoparticles and diatomite can be used in biomedical applications, where the unique properties of both materials can be leveraged to create new and innovative solutions.

Hence, this thesis undertakes a comprehensive investigation of diatoms on three levels, encompassing the study of colonies in suspension, individual living diatoms, as well as purified frustules and diatomite powder, as schematically shown in Figure 1.
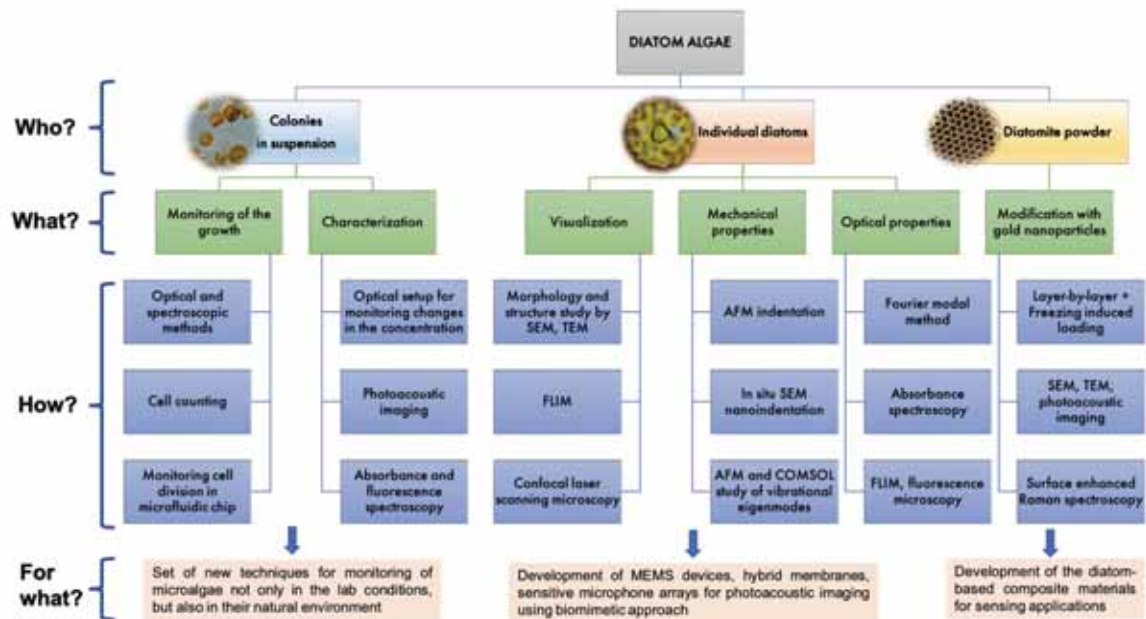
Figure 1. Research design and methodology

The main tasks in this dissertation are based on the monitoring of diatom growth by novel optical methods, study of optical and mechanical properties of diatoms, and modification of their surface which is of great importance for advancing our understanding of fundamental physics, developing new materials, and addressing pressing environmental and technological challenges. After a thorough study of the literature, no report was found on a fundamental and systematic study of the relationship between the structural and topographic features of diatom frustules, as well as wet and air-dry cells containing organic material, and their mechanical characteristics under static and dynamic loading. Therefore, one of the key objectives of my research is to fill this gap and understand the mechanical behavior of diatom frustules and living cells under different conditions. Given the fact that the diatom frustule itself can be considered as a nanostructured membrane, the

determination of the mechanical properties of both membranes and cells with all organic components present seems extremely important and necessary both from the point of view of fundamental research and from the point of view of the use of these systems as functional materials for new devices. By characterizing the mechanical properties of diatom frustules, we can gain insights into their ability to withstand external forces and protect the cell from damage. Leveraging a biomimetic approach, it becomes feasible to fabricate micro-electro-mechanical systems (MEMS) devices based on diatoms, hybrid membranes, and sensitive optoacoustic microphone arrays for minimally invasive endoscopic procedures.

Another important aspect of my research is to investigate the role of the hierarchical structure in determining the optical properties of diatom frustules. By using advanced imaging techniques such as electron microscopy and fluorescence lifetime imaging microscopy as well as numerical simulations, the goal is to study the interaction of light with the highly porous hierarchical frustule, taking into account the chloroplast distribution within, and how they contribute to the overall optical performance of the nature-based photonic crystal.

By revealing the underlying relationship in the diatom structure-properties-function chain, this dissertation aims to contribute to our understanding of these fascinating organisms and the development of new approaches and practices to address the problem of efficient diatom monitoring, while also providing insight and inspiration for future research. By combining physics, biology, and materials science, we can unlock new insights into the natural world and develop new technologies that benefit society.

Chapter 2. Literature review

2.1 Introduction to the world of diatoms

Phytoplankton is a diverse group of photosynthetic microorganisms that includes diatoms, dinoflagellates, cyanobacteria, coccolithophores and other types of algae. It is estimated that these single-celled primary producers account for about half of the global fixation of carbon, and are responsible for the export of fixed carbon to the deep ocean through the biological carbon pump[6]. The main functional groups of marine phytoplankton include nitrogen fixers (cyanobacteria), silicifiers (diatoms), and calcifiers (coccolithophores). Phylogenetic diversity of these eukaryotes is illustrated in Figure 2.
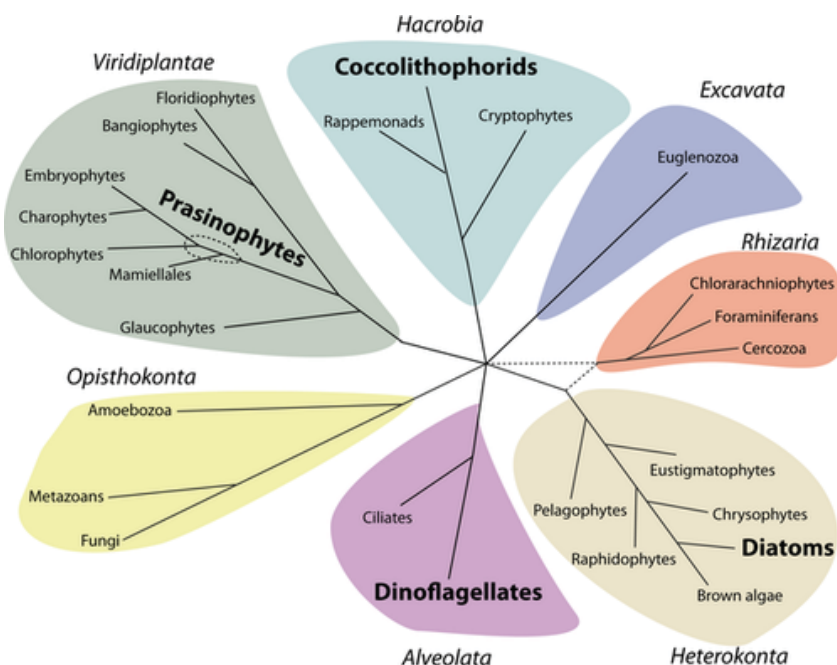
Figure 2. Phylogenetic diversity of eukaryotes showing the four major lineages of phytoplankton highlighted in bold typeface (prasinophytes, coccolithophorids, diatoms and dinoflagellates)[6].

At present, diatoms are considered to be an extensive taxonomic group of unicellular microorganisms at the type or division level (Biota: Chromista, Kingdom: Harosa, Subkingdom: Heterokonta, Infrakingdom: Bacillariophyta, Phylum). Despite the fact that many species of diatoms are capable of forming colonies of considerable size, at the individual level they remain unicellular. Figures on the origination period of diatoms as an evolutionary group of marine organisms differ depending on the method of study. There are several specific assumptions about the lifetime of diatoms depending on the various studies on their age. Thus, according to the estimation using the molecular clock method, they may be as old as 240 million years[7,8]. However, paleontological approaches—revolving around an age analysis of ancient microfossils—indicate that diatoms were separated as a group in the world ocean about 145 million years ago[9]. The paleontological approach with respect to the diatoms should now be considered as more reliable.

According to the taxonomy used by Algaebase.org[10], the diatoms include the centric species with multiradial and bipolar symmetry (classes *Coscinodiscophyceae* and *Mediophyceae*), and pennate species with bilateral symmetry (class Bacillariophyceae)[11]. The latter includes the subclasses *Fragilariophycidae* and *Urneidophycidae* (without raphe on the valve) and *Bacillariophycidae* (with raphe)[11]. They appear as individual cells or colonies in different shapes (filaments, chains, ribbons, fans, zigzags, or stellate), either as free-floating (planktonic) or attached to the substrate (benthic or periphytic)[12]. The frustule consists of two intersecting halves: the upper, called the epitheca, and the lower, the hypotheca[13], which fit into each other, resembling a Petri dish, with sizes varying from 2

µm up to several mm. Figure 3 shows basic diatom terminology, division and structural elements[14].
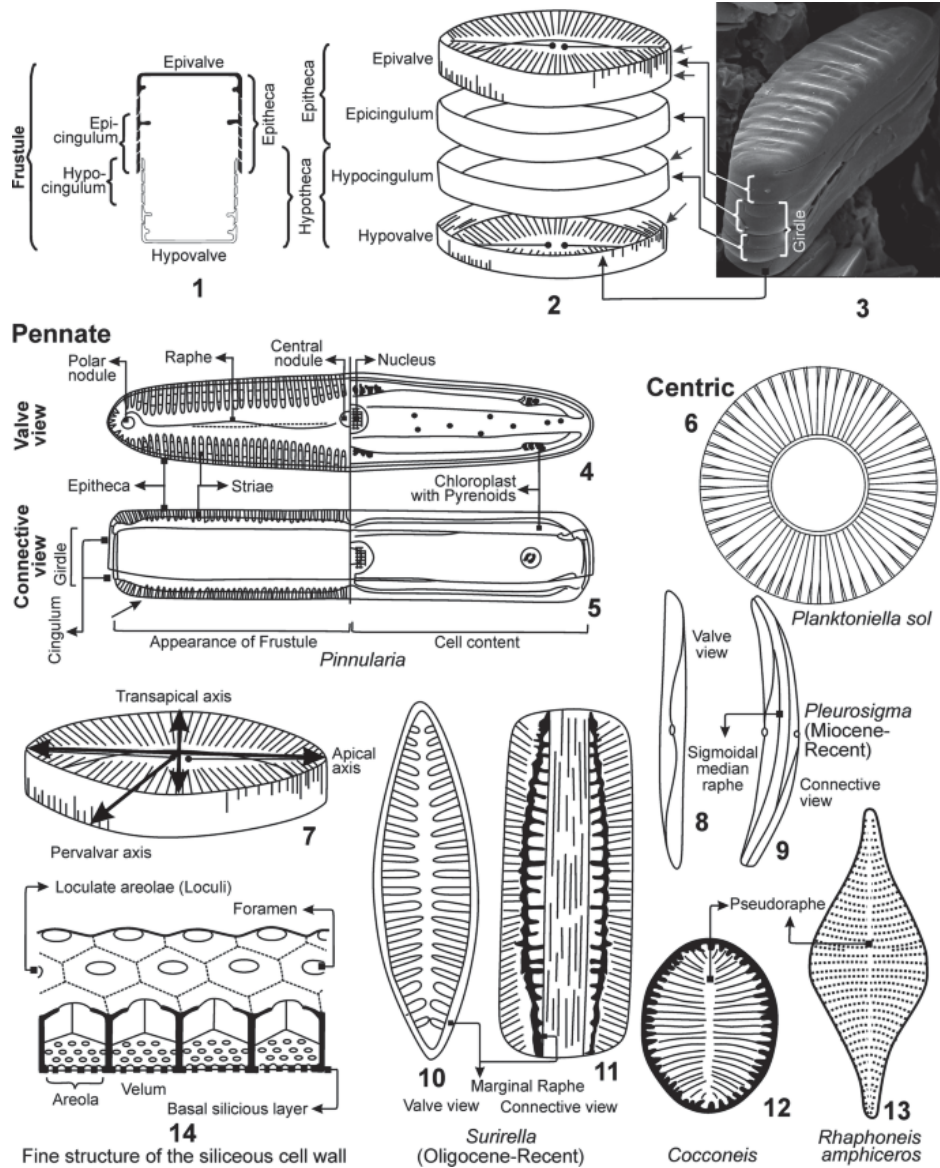
Figure 3. Diatom terminology. 1–3: Frustule terminology; 4–6: Examples of two major orders of diatom based on frustule shape—elliptical (pennate) (4 and 5) or circular (centric) (6) in valve view; these make up the two orders of diatoms (Pennales and Centrales, respectively). 4 and 5: Pennate diatom; 4: Valve view; 5: Connective view. 6: Centric

46

diatom. 7: Symmetry axes. 8–11: Diatom species showing Raphe. 12 and 13: Diatom species showing pseudoraphe. 14: Structural details of the cell wall.[14]

Figure 4 shows the general cell features and the main terms associated with diatoms using as an example *Karayevia amoena* (*K. amoena*)[15]. The valve surfaces are ornamented with radiate and parallel striae, represented by a row of pores called areolae. Striae are formed between nonornamented, thickened ribs called costae.
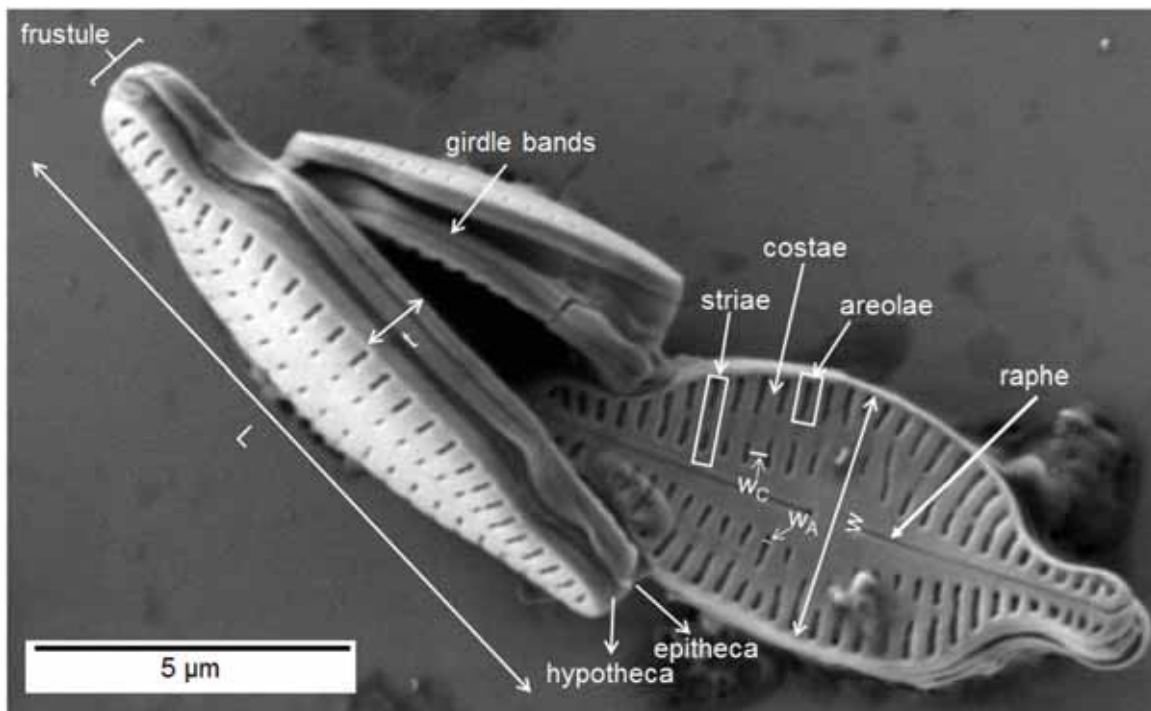
Figure 4. SEM image of *K. amoena* showing basic cell structure and frustule dimensions: length L, width w, areola width w_A, costa width w_C, girdle band thickness t[15].

Humans have been fascinated by the intricate structure of diatom frustules for well over a century. Figure 5 contains reproduction of plates from Ernst Haeckel's

"Kunstformen der Natur"[16] published in 1899–1904. Haeckel made hand drawings as the basis for fabricating engraving plates, in a manner similar to that used by Hooke in preparation of his Micrographia treatise[17]. Their beauty fascinated even Charles Darwin, who mentioned them in his work "On the origin of species by means of natural selection, or the preservation of favoured races in the struggle for life": "Few objects are more beautiful than the minute siliceous cases of diatoms, were they only created to be admired under the microscope?"[18]
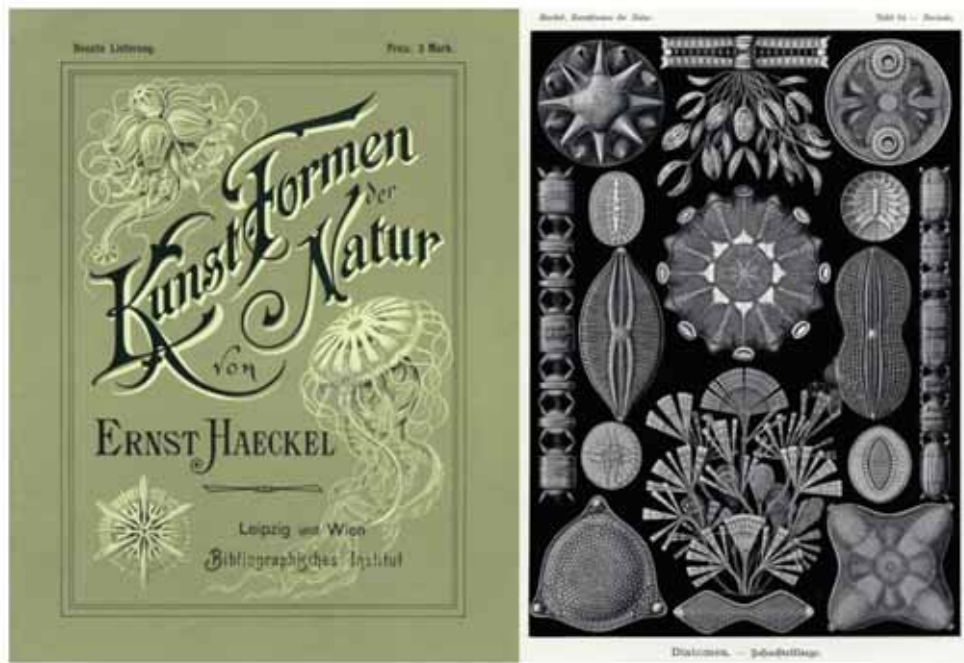
Figure 5. Left – Cover page of Ernst Haeckel's Kunstformen der Natur. Right – Plate 84 devoted to diatomea.[17]

These organisms formed in vast lagoons with variable salinity. The earliest diatoms lived in conditions where the rains filled the lagoons with water, and then the sun dried them up again. They formed dense silicon shells around them, through which they

interacted with the habitat, where temperature and mineralization often changed. Since then, gradually evolving and assimilating new ecological niches, diatoms have spread across the world. They populated a variety of aquatic and semi-aquatic biotopes: seas, rivers, lakes, streams, wet rocks and wet salt crusts, swamps, moss clumps, tree bark and soil. There are several types of diatoms that live on the surface of rocks, at an altitude of over 3 km, while others have found stable ecological niches on the skin of whales[19]. In the areas of water bodies, diatoms live both in the water column (in plankton) and at the bottom (as part of benthos, to depths of several hundred meters), as well as on macroalgae, on the covers of invertebrates and fish, and on floating objects (as part of communities of periphyton). In recent decades, when different types of plastic ended up in the water bodies of the planet as garbage, some species of diatoms have successfully adapted to life and on artificial polymers. They even formed very special communities on them, capable of surviving in a rather aggressive environment. Planktonic diatoms are most often endowed with a radial symmetry of the shell, benthic and periphyton (feathery), or, in various forms, bilateral, although representatives of some genera look like a loaf of bread (Figure 6)[7]. In terms of the number of species, pennate (bilaterally symmetric) diatoms clearly predominate over the centric diatoms accounting for only 19% of the nearly 17,000 diatom species within the accepted taxonomic description[1]. However, planktonic species, mainly centric ones, are responsible for the bulk of diatom population by numbers and volume, especially in nutrient-rich and well illuminated marine waters[20]. According to some estimates, diatoms are the largest group of eukaryotic algae, numbering over 100,000 known species[21,22].
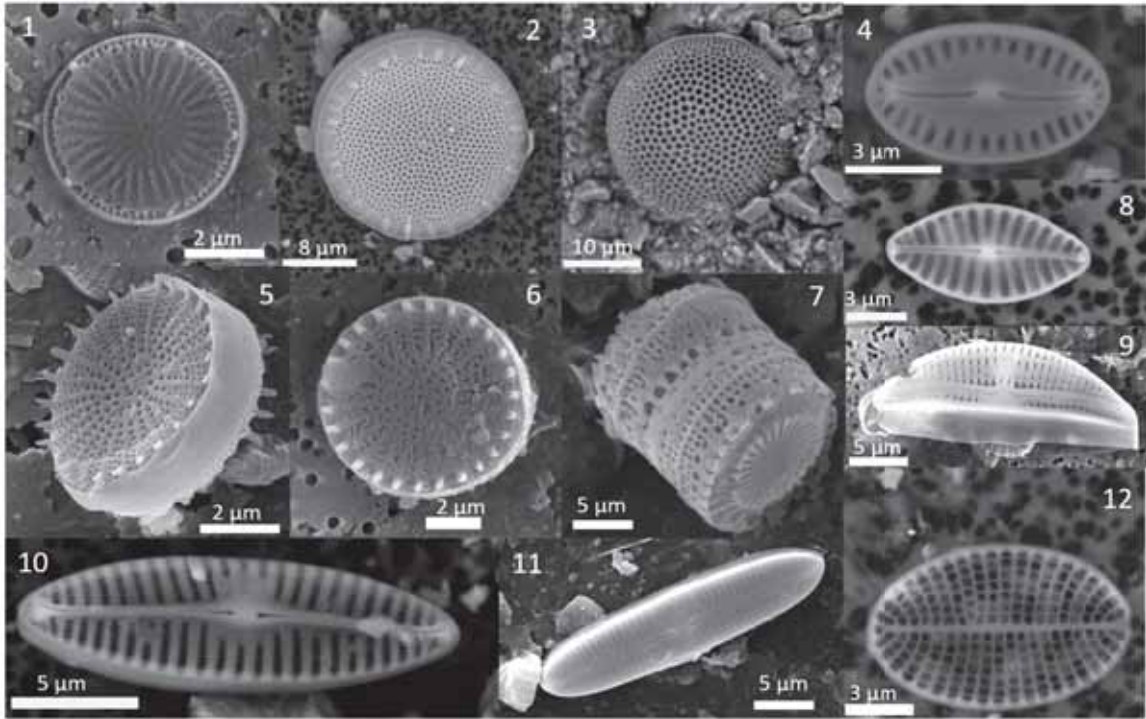
Figure 6. Centric diatoms (a–c, e–g); pennate diatoms (d, h–l)[7].

According to Zhang et al.[23], the diatom frustules may be classified into three categories: rod shaped, flake shaped and generic 3D shape, as illustrated in Figure 7. The plane of the valve surface is defined as x, y plane. The major axis of the valve is X, while the minor axis of the valve is Y (for pennate diatoms only; for centric diatoms: X=Y). The valve-through axis is z-axis, and the length of the line connecting the centers of epivalve and hypovalve is Z.
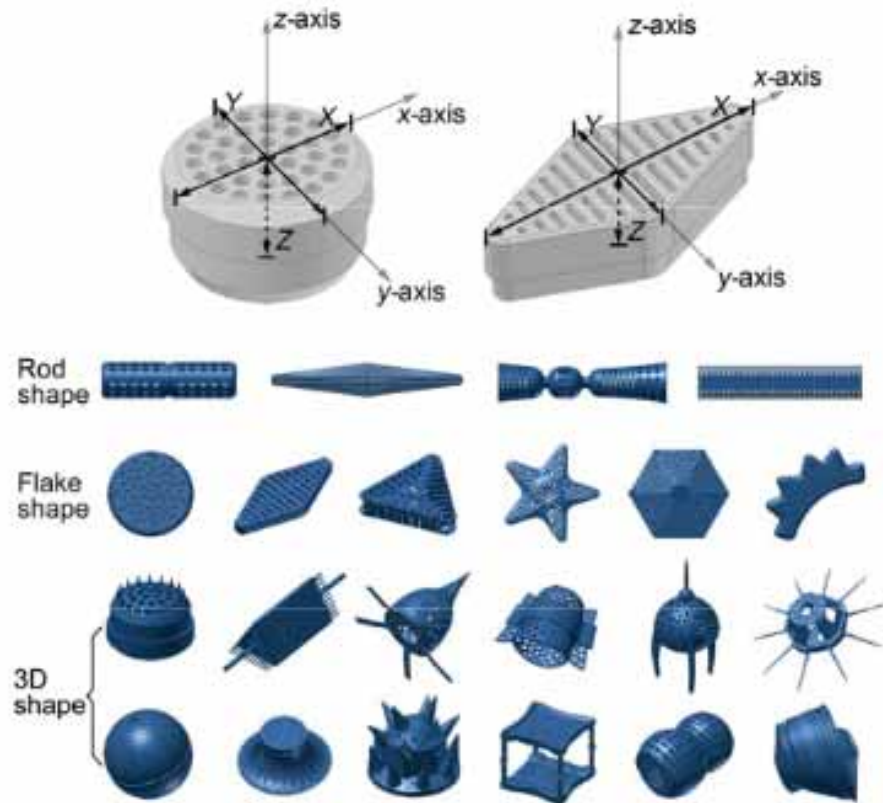
Figure 7. Shape classification of diatom frustules[23]

The diatom's complex adaptations allow it to survive, carry out metabolic functions, and reproduce successfully in any biotope. Many of them are reflected in the form of their shells, in the way the pores are arranged, the configuration of the pore apparatus itself, sutures, outgrowths, in the size of the cells and the thickness of the shell. Diatom shells reflect the evolutionary path and adaptive response of the species to the varying environmental conditions in which it has evolved. Mobile diatoms (class *Bacillariophyceae*)[24] capable of sliding at different speeds among thickets or sediment particles have a bilateral shell shape and are endowed with special devices for locomotion – variously organized raphes[7]. The forms with radial symmetry of the frustule are grouped

into the *Coscinodiscophyceae* class. These diatoms have characteristic adaptations that allow them to float in the water column: singly or in colonies. For example, thalassiosiroids have cells in the form of tablets, forming chains during division using exopolymers[25,26]. They excrete exopolymers through special pore structures (fultoportula and rimoportula), which also increases the ability of the colony to float in water. The coscinodiscoids shown in Figure 8 hover due to the large size of single cells, have thin-walled shells and contain large vacuoles in the cells, which balance their density with the surrounding water[7].
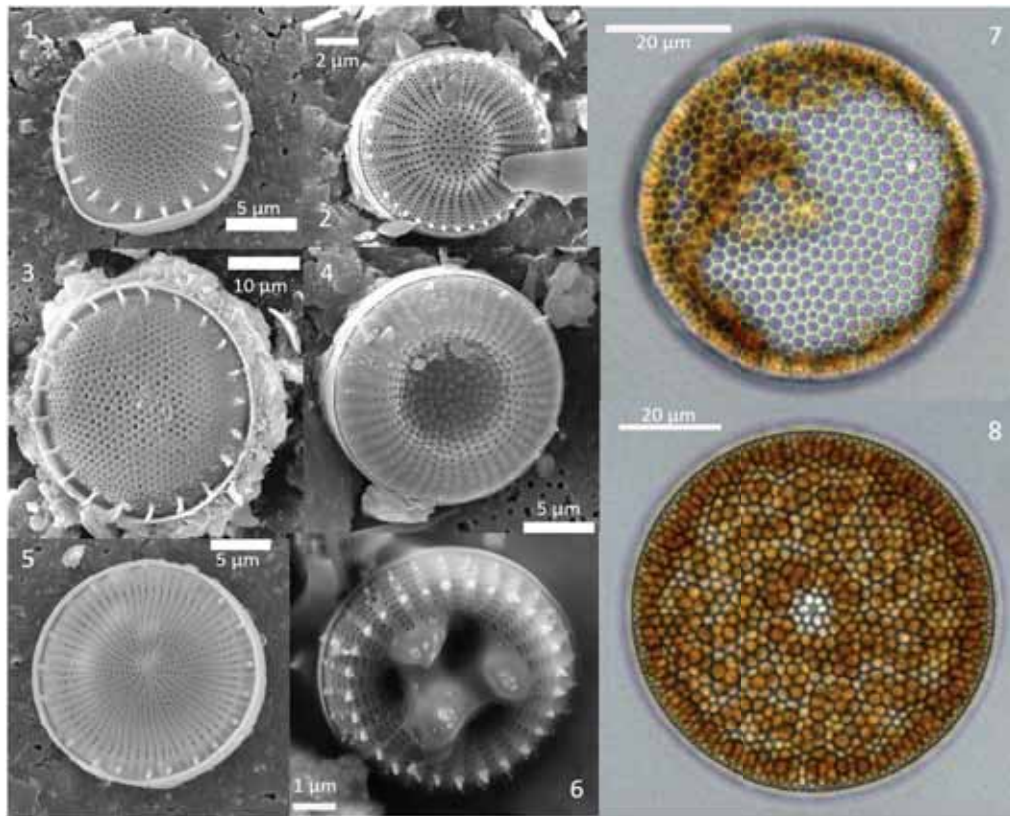
Figure 8. Different representatives of thalassiosiroids (1–6) and coscinodiscoids *Coscinodiscus radiatus* (7, 8).[7]

The presence of a silica exoskeleton called frustule ensures the performance of many vital functions of the unicellular micro-organisms – the interaction and exchange

52

between diatom cells and the surrounding environment, protection from external mechanical influences, attachment to substrates, filtration, regulation of metabolism processes, control of light absorption during photosynthesis and the protection of DNA from UV radiation[22,27–29].

Due to the large number of pores of various sizes, cells have a high specific surface area, high adsorption and porosity, the ability to change the structure using genetic manipulation or chemical reactions, high mechanical stability, biocompatibility, low cost and toxicity[30]. To proliferate in the shallow well-illuminated waters in the presence of predators, diatoms must protect themselves from various mechanical influences using a stable and lightweight structure.

2.2 Hierarchical structuring of diatom algae

Essentially, hierarchical structure refers to the thoughtful and purposeful organization of material building blocks at each dimensional level in order to create multifunctional structures and mechanisms[7]. Nature provides numerous examples of successful hierarchical structuring in soft and hard tissues to satisfy the diverse and frequently contradictory requirements posed by the varying environments of living organisms[31]. Generally speaking, the fundamental reason for hierarchical structuring, i.e., scale specific arrangement of parts and components, lies in the alteration of the predominant physical interaction mechanisms with the significant change of the dimensional scale of consideration that entails the dominance of certain physical forces acting at the characteristic lengths comparable with the size of material entities.

The hierarchical structuring of diatom algae is a fascinating area of study that has attracted the attention of researchers for many years. At the macroscopic level, diatoms exhibit a wide range of shapes and sizes, which are determined by the intricate patterning of their frustules. These patterns are highly complex and can vary greatly between different species, making them an important tool for taxonomic classification. At the microscopic level, the frustule is composed of a series of layers that are arranged in a hierarchical manner[1,32]. The outermost layer is typically composed of large, irregularly shaped pores that allow for the exchange of nutrients and gases with the surrounding environment. Beneath this layer, there is a series of smaller pores that are arranged in a regular pattern. These pores are thought to play a role in the control of water flow around the diatom cell, which is important for nutrient uptake and waste removal. The innermost layer of the frustule is composed of a dense, highly ordered lattice structure that is responsible for the overall strength and rigidity of the cell wall. This lattice structure is made up of silica nanoparticles that are arranged in a hierarchical manner, with smaller particles forming the building blocks for larger structures. Such hierarchical structure is well demonstrated in Figure 9a[23]. Figure 9b shows regular array of large pores – foramen; a circular or hexagonal chamber – areola, under the foramen; second-level pores with a diameter of 200 nm, located at the bottom of the areolae. Sieve pores with diameter 40 nm are distributed inside second-level pores (Figure 9c). The mantle and girdle band also contain numerous pores, as shown in Figure 9d. It is also believed that the formation of these patterns is the result of a self-organized phase separation process[33].
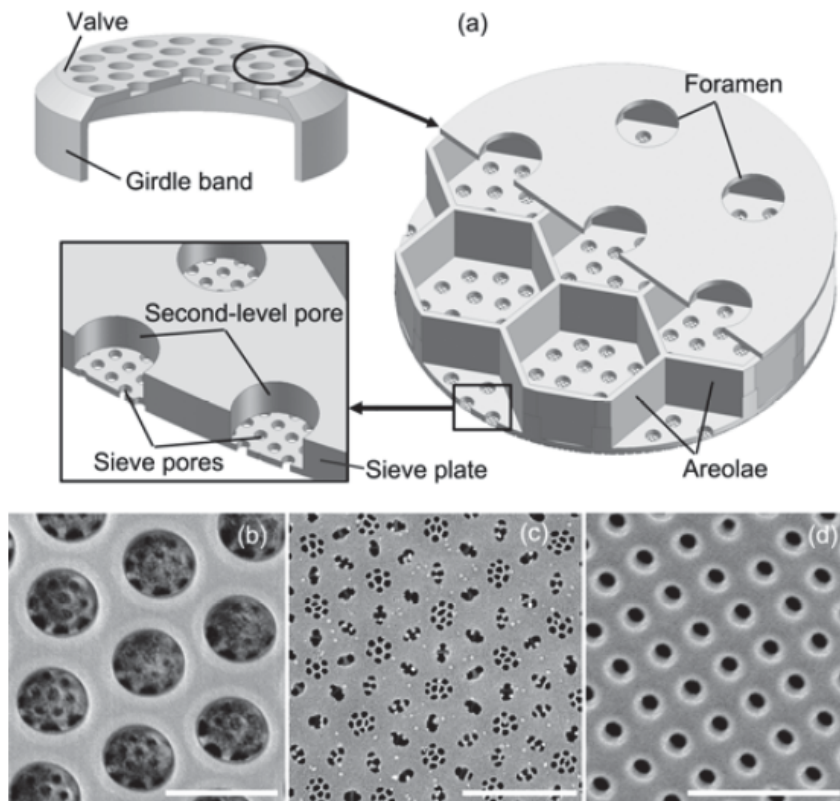
Figure 9. Typical structure of multilevel pores (Coscinodiscus sp.). a) 3D model; b) arrays of foramen and second-level pores, scale bar 1 µm; c) array of sieve pores, scale bar 2 µm; d) array of nanopores on girdle band, scale bar 1 µm.[23]

In our book chapter[7], we discussed the structural design of diatom shells in pursuit of the idea that the variety of appearance of diatoms and the key structural features of the shells are closely related to their specific living conditions, which require different mechanical and optical properties for optimal shell performance. Recent advances in imaging techniques have allowed researchers to study the hierarchical structuring of diatom algae in unprecedented detail[22]. For example, electron microscopy has been used to

visualize the intricate patterning of the frustule at the nanoscale level[34], while X-ray tomography[35] has been used to study the internal structure of diatoms.

Certain hierarchical multifunctional architecture of a diatom frustule is DNA-coded and biologically driven. For example, the biosilicification process in diatoms is demonstrated on *Thalassiosira pseudonana* (Figure 10)[36].
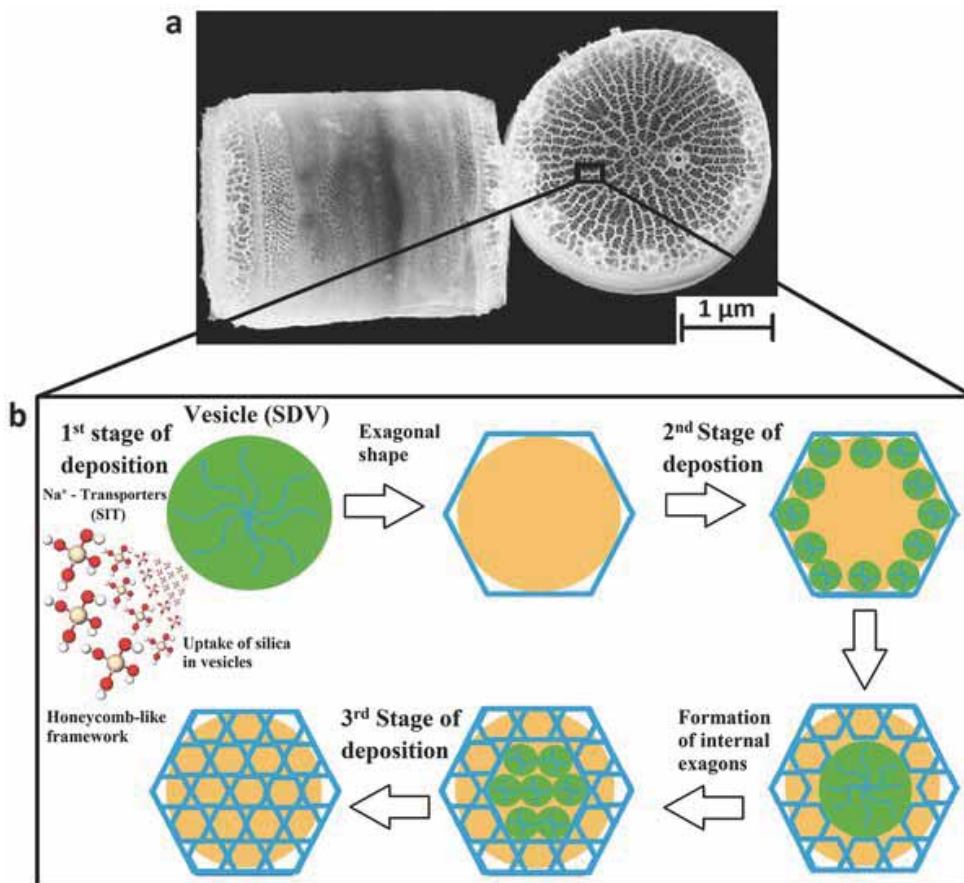
Figure 10. Biosilicification in diatoms. a) *Thalassiosira pseudonana* diatom (credit to University of Washington). b) Biosilicification mechanisms in the formation of hierarchical silica-based honeycomb-like structure of diatom skeleton. [36]

Diatom frustules formation is a complex process that involves the synthesis and assembly of a silica shell, which serves as a protective layer and structural support for diatoms. The process requires water-soluble silicic acid $Si(OH)_4$, which is transported by silica transport vesicles (STV) to the silica deposition vesicles (SDV) where the valves are formed[23] as shown in Figure 11a. The silanol groups of $Si(OH)_4$ are hydrolyzed in SDV and form Si-O-Si bonds. Silaffins proteins and long chain polyamines (LCPA) in SDV catalyze the hydrolysis reaction and influence the valve structure[37]. Firstly, the framework structure is produced, followed with thickening of the valve and development of microstructure. Once the silica layer formation is complete, the diatom cell separates into two; each half inherits one valve and undergoes an identical frustule formation process. This process results in two new cells with symmetrically placed valves, but with different sizes labelled as 1 and 2; the newly formed "half-thecas" in SDV are slightly smaller (labeled as 2 and 3) (Figure 11b). After the first division, the two daughter cells have frustules composed of 1–2 and 2–3 separately. After the second division, four daughter cells are produced, and so on. Every act of division reduces the size of frustule by dozens of nanometers, but without the change in the pore size. When the size of a cell reduces to below two-thirds of the biggest cell, the cells undergo a unique form of cell division called the auxospore formation, which allows them to restore their size and morphology.
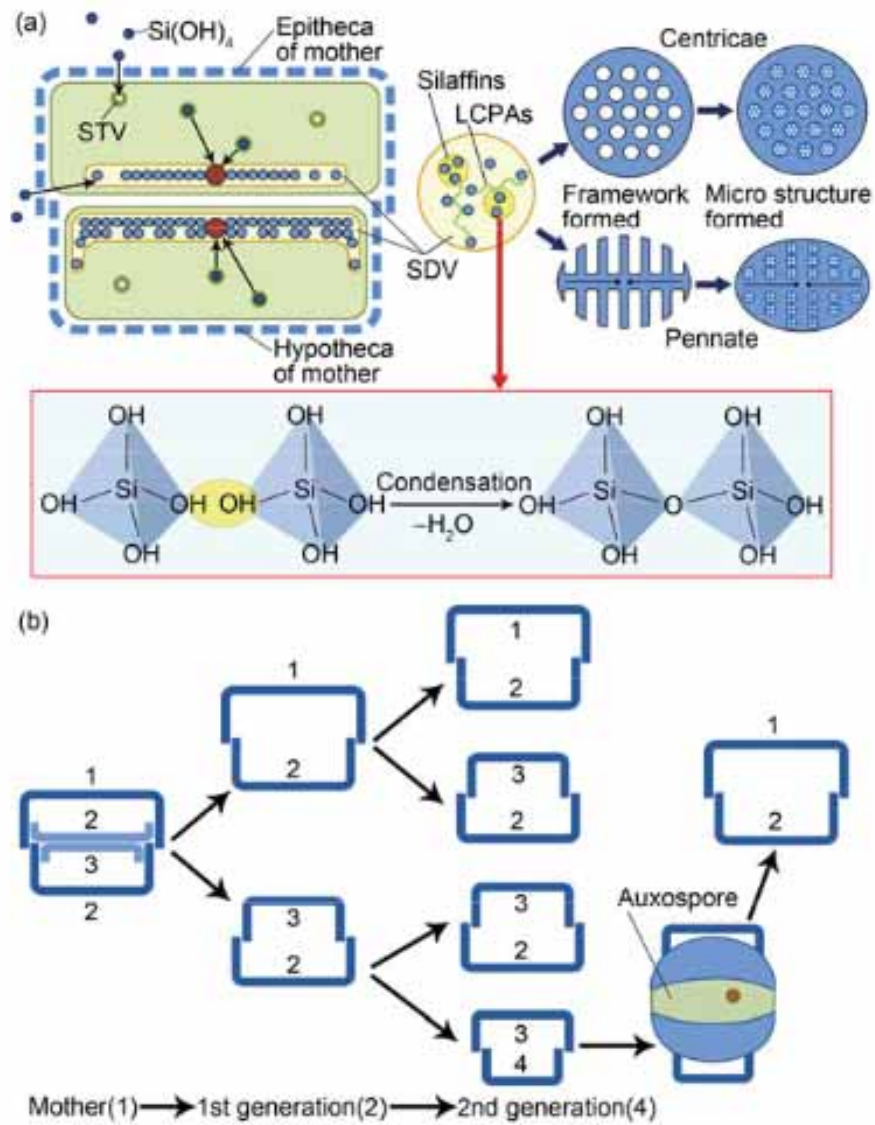
Figure 11. Schematic illustrations of: a) formation, b) reproduction of diatom frustules.[23]

Nevertheless, the fine local mechanisms of phase separation in silica deposition vesicles at the nanometer scale still needs to be systematically studied to be understood. This would open the pathways for these processes to be directed and customized, and

potentially used to implement the paradigm of Bio-Assisted Nanometer Size Additive Manufacturing (BANSAM)[7]. BANSAM assumes the transition to nature-like fabrication technologies of the 21st century that are simultaneously green, sustainable, non-carbon, and possess nanometer tolerance.

2.3 The mechanical properties of diatoms

The material, shape and thickness of the frustules, as well as the spatial order of the pores and the topology of the channels connecting them determine such engineering properties as stiffness, strength and natural oscillation frequency. However, the fine structure of the frustule porosity and the nanomechanical properties associated with it present challenges for the experimental study involving the application and detection of forces at scales relevant to the diatom cell. The elastic modulus, hardness, and tensile strength of various diatom species were studied using various experimental methods such as nanoindentation[38], AFM probing[39–41], and bending with glass microneedles[42]. In the most significant pioneering work of C.E. Hamm et al.[42] the mechanical performance of the diatom frustule was assessed by performing loading tests with calibrated glass microneedles which led to the conclusion that the frustules evolved to provide necessary mechanical protection for the cells against predators, as shown in Figure 12.
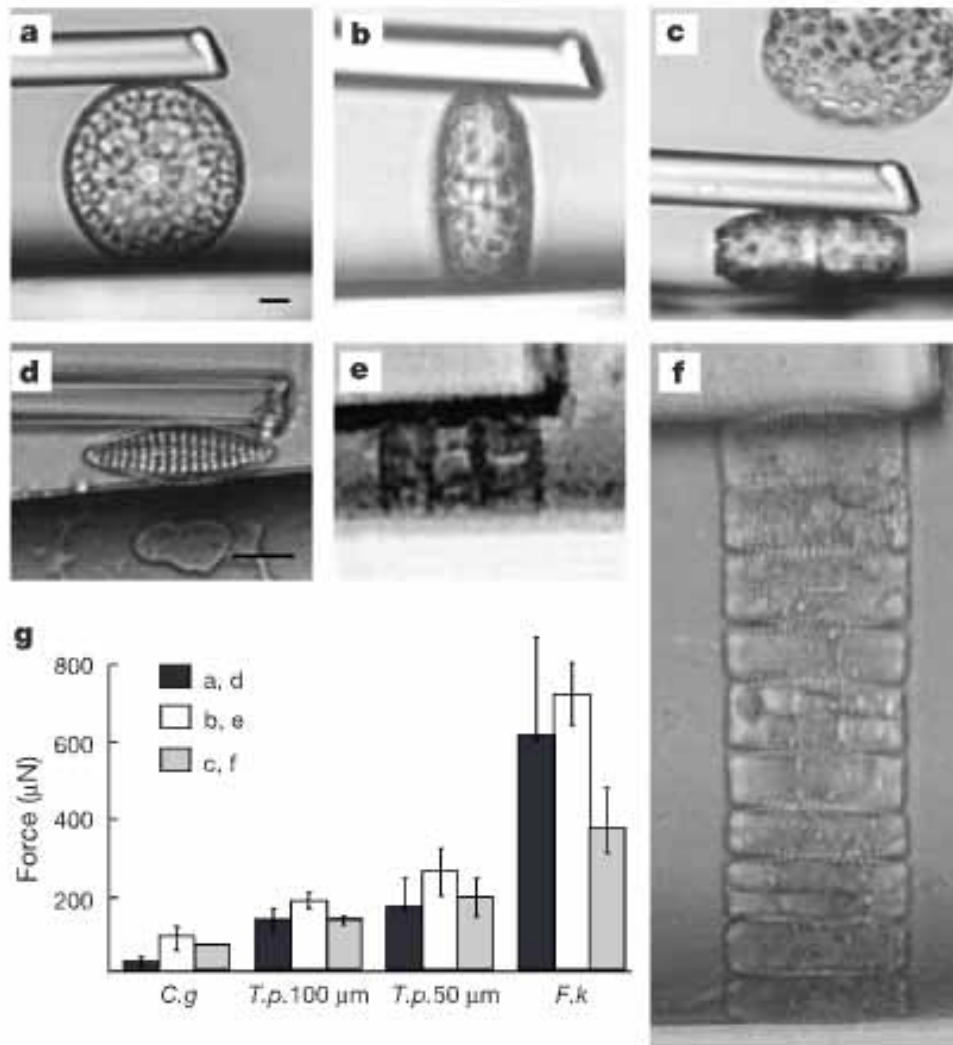
Figure 12. Glass needle tests: Live single cells of *T. punctigera* (a–c) and *F. kerguelensis* (d–f), in chains (e,f). Pressures applied along the girdle bands, (a,d), across the girdle bands (b,e), and across the centre of the valves (c,f). g) Forces necessary to break frustules. Scale bars, 10 μm.[42]

The first AFM studies related to the mechanical behavior of diatom silica nanostructure were done in 2001 on dried diatoms by Almqvist et al.[41] They measured

elasticity and hardness of the diatom *Navicula pelliculosa* semi-quantitatively with a resolution down to approximately 10 nm and found that Young's modulus varied from seven GPa to hundreds of GPa, depending on the location. At the same time, hardness values ranged from 1 GPa to 12 GPa. The elastic modulus was calculated from the AFM force curves using indentation and deflection methods. Even though both methods revealed the same overall elastic pattern, differences in absolute elastic modulus observed on the hardest part of the frustules could be explained by the calibration of the AFM cantilever. Besides, it was assumed that the elastic response is due to the deformation of the shell material, which is valid only at the central nodule (CN) and central rib (CR) where the modulus is high, but not on the transapical rib (TR), where the shell gets elastically deformed. On the other hand, hardness, which is directly related to the material's structure, was also higher on the CN and at the curved-end side of the raphe fissure (RF).

These results confirmed that micromechanical characteristics are not restricted only to the biosilica itself, but they are also influenced by the hierarchical three-dimensional morphology of the porous structures of the exoskeleton on scales from nanometers to micrometers. Also, the change in mechanical properties can potentially be explained by differences in silica content and phase of development of a frustule. This study firstly confirmed that the micromechanical properties could be studied using AFM method. However, the authors suggested that in order to increase knowledge of silica biomineralization, the instrumentation should be improved along with the comparison of the properties of several species under physiological conditions and the study of the mucilaginous organic coating.

61

Later, Losic et al.[39] mapped the nanoscale mechanical properties of *Coscinodiscus* sp. at different locations along the frustule using an AFM nanoindenter and calculated the hardness and elastic modulus from force penetration curves. AFM nanoindentation tests confirmed significant variations of the elastic modulus E (1.7-15.6 GPa) and hardness H (0.076-0.53 GPa) depending on frustule morphological features as pore size, porosity, and distance between pores. The lowest values were obtained on the cribellum and the girdle band. The location of the indentation, different biomineralization processes, and the quality of the nutrition can also influence the micromechanical properties of diatom frustules. Figure 13 shows AFM images of the internal plate with a series of indentations performed at various positions from the central region to the periphery and a typical force penetration curve.
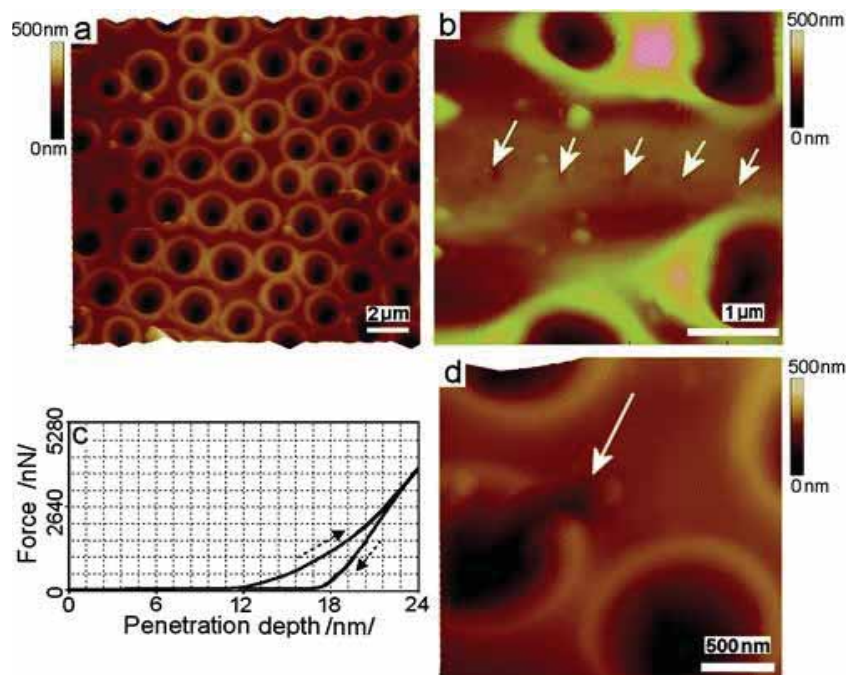
Figure 13. a) Low-resolution AFM image of the internal plate after nanoindentation. b) Series of indentation points (solid arrows) obtained using a force of 1.5-

3 μN. c) Typical force penetration curve showing loading and unloading parts (dashed arrows). d) AFM image showing nanoindentation performed on an areola rib at higher applied load (12 μN). White scale bar is 10 μm.[39]

Overall, the studies performed by AFM and nanoindentation demonstrated significant variations of the elastic modulus depending on the location[38,39,41] which may be due to the porous structure, nonuniform distribution of pores having different sizes and shapes, orientation of the frustule, location of the indent, etc. As the authors suggested[41], improved instrumentation and the study of several species under physiological conditions are needed to gain more knowledge about the native mechanical properties and their link to morphogenesis, i.e., the process of silica biomineralization.

Coscinodiscus sp. were also tested in situ by three-point bending. Aitken et al.[11] analyzed the bending of the beam with a square cross section and obtained a brittle fracture of the diatom frustule at the average stress of 1.1 GPa and strain 3.0% with the elastic modulus of 36.4 ± 8.3 GPa. Moreover, they estimated the relative frustule density near 30% and got the highest strength-to-density ratio, approximately 1700 N·m/kg among all known biologic materials, as provided by Ashby plot[43] in Figure 14.
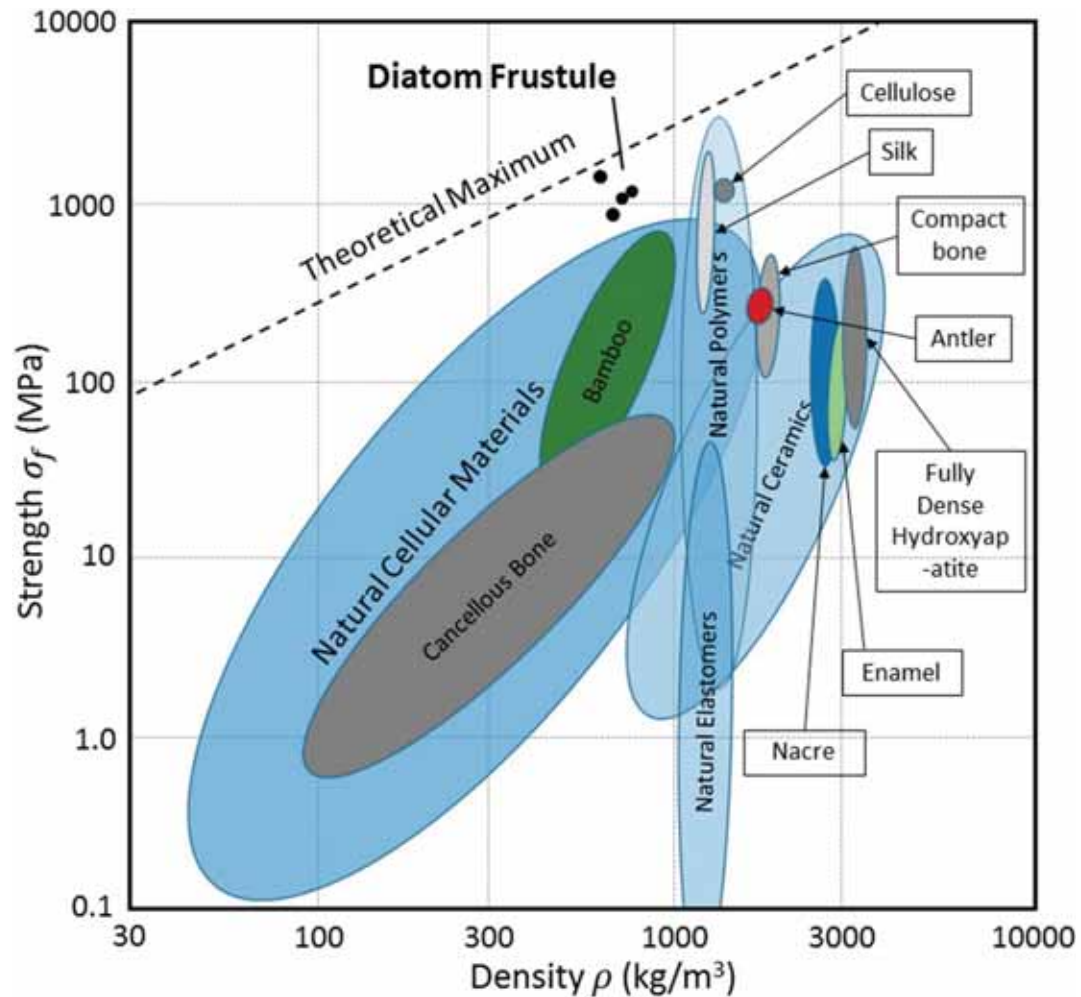
Figure 14. Ashby plot of strength vs. density for naturally occurring biological materials, including diatoms.[11,43]

The authors proved the given results via nanoindentation of the girdle band of the frustule with modulus from 21.0 ± 7.7 GPa at 28 nm to 39.7 ± 8.3 GPa at 217 nm, which corresponds with the mechanics of the bending test. These results clearly showed how nature could build live organisms with hierarchical architecture simultaneously with the record lightweight and strength.

Xing et al.[44] reconstructed a complex three-dimensional structure and built a numerical model of the radially symmetric frustule in a diatom from the genus *Coscinodiscus* after tomography using ion etching in a scanning microscope column. De Tomassi et al.[27] summarized the data on the selective properties and effects observed in the interaction of light and the hierarchical nanoporous structure of diatom shells with central symmetry: optical tunnelling, selective transmission, and photoluminescence.

As already mentioned, an array of purposes can be served by frustules, from blocking virus entry to protecting against predator jaws and preventing them from being digested, among other things. As a result, diatoms are especially useful when it comes to the design of armor and other protective items. Perhaps, the reduction (by means of magnesiothermic reaction[45]) of silica to ultimately obtain silicon frustule would allow to eliminate the natural variability of hydrosilica material and through this to exclude the contribution of this factor in mechanical response interpretation. In our study we examined mechanical behaviour of living diatoms as well as cleaned frustules in the static and dynamic mode, revealing differences in nanomechanical properties of layers, depending on silica hydration and support from internal organic content, and providing insights for the design of new nanodevices[1]. The summary of nanoindentation and bending experiments of diatom algae is shown in Table 1.

Table 1. The summary of various experiments of diatom algae by nanoindentation and bending tests.[7]

Genus	Test Type	Specimen Location	Stress or Load, mN	Strain or Penetration Depth, nm	Young's Modulus, GPa	Hardness, GPa	Reference
Coscinodiscus	A*	girdle	1.1 ± 0.3 GPa	3.5 ± 0.7 %	36.4 ± 8.3	–	
	B**		–	28	21.0 ± 7.7	–	11
			–	217	39.7 ± 8.3	–	
Coscinodiscus	B	center	0.01–0.03	60–100	1.1–10.6	0.10–1.03	46
Synedra	B	center	0.01	20	13.7–18.6	0.85–1.41	
Coscinodiscus	A	–	2.81 ± 0.15	2000	36.4 ± 8.3	–	47
Coscinodiscus	B	center	0.02–0.07	300–500	0.591–2.768	0.033–0.116	38
	B	edge	0.02–0.07	300–500	0.347–2.446	0.076–0.120	
Didymosphenia	B	–	0.1–1.4	1000–6000	31.8	–	48
Coscinodiscus	B	center	0.12	200	1.562	–	49
Navicula pelliculosa	B	transapical rib	0.01–0.05	4 – 8	7 – 25	–	41
		central rib		2.5 – 5	15 – 30		
		central nodule		1.5 – 4	30 – hundreds of GPa	– –	

*A = three-point bending
**B = nanoindentation

2.4 The optical properties of diatoms

For both phototrophic organisms as well as autotrophic organisms, light plays an important role in their growth, behavior, and development. Over the course of evolution, several species of animals and plants have developed highly efficient photonic structures [50,51]. A good example of the so-called biomimetic process is how micro-opto-electromechanical systems (MOEMS) are fabricated by replicating these natural photonic

structures. While bio-inspired technology is often hampered by present engineering techniques and the infeasibility of large-scale production, there are still some promising applications for it. Therefore, it becomes increasingly apparent that a bottom-up fabrication approach would be ideally suited to utilizing the ability of living organisms themselves to manufacture micro- and nano-optical devices [52].

The properties of nanoscaled well-organized silica materials enable them to be used for optical studies due to their low refractive index and extremely low absorption coefficient [53]. The species-specific patterns of pores, ridges, and indentations on the silica cell walls endow diatoms with unique appearances under high magnification. These microscale structures have profound implications for the interaction between light and diatoms, as the porous silica induces diffraction and interference based on the dimensions, forms, and configurations of the pores and ridges. Diatoms showcase an exceptional array of natural phenomena, spanning from their biodiversity and ecological roles to the optical effects and nanofabrication capabilities conferred by the silica frustules. They exemplify the capacity for microscale life to exert substantial impacts on ecosystems and global climate, as well as the potential for nanoscale structures in nature to generate remarkable optical effects and inspire novel technologies.

In recent years, considerable attention has been devoted to investigating the optical properties of diatom algae, particularly with regard to their scattering and absorption of light. Diatoms are known to efficiently absorb light in the blue, green, and ultraviolet wavelengths, and to scatter light across a broad range of angles [54,55]. This proficiency in capturing light energy renders them crucial constituents in aquatic food webs.

Optical studies of diatom frustules have the potential to yield insights into the structure and function of these microorganisms, as well as applications in nanotechnology, optics, and materials science. Researchers have investigated the optical properties of diatom frustules for use in photonic devices, such as biosensors and photovoltaic cells. Additionally, the study of diatom frustules has implications for understanding the ecological and environmental roles of diatoms. For instance, diatom frustules are responsible for a significant portion of the carbon fixation in the ocean, and knowledge of their optical properties can help to better understand the impact of climate change on marine ecosystems. Overall, optical studies of diatom frustules offer a fascinating area of research with broad-ranging applications and potential impacts.

2.4.1 Light propagation in diatoms

When light enters water, it is absorbed more strongly than in air and becomes partially polarized. Blue light penetrates much deeper depending on the concentration of dissolved matter and particles, whereas red, orange, and yellow light are quickly absorbed by water. A couple of meters below the surface, almost half of the light intensity is in the UV region (below 400 nm), compared to about 3% at the surface level, which means that diatoms live in a light environment dominated by UV and blue light, and supports the idea that the frustule may play a role in UV light protection.

However, most studies of the optical properties of diatoms are carried out on cleaned frustules without taking into account the organic material. In addition, most of these studies are conducted or simulated in the air, which is contrary to the aquatic natural

habitat of diatoms. In this sense, the calculated effects of these experiments and simulations cannot provide complete biological answers to how living diatoms benefit from the interaction between frustule and light. These differences between measurements on cleaned frustules and diatoms in their natural habitat are shown in Figure 15.
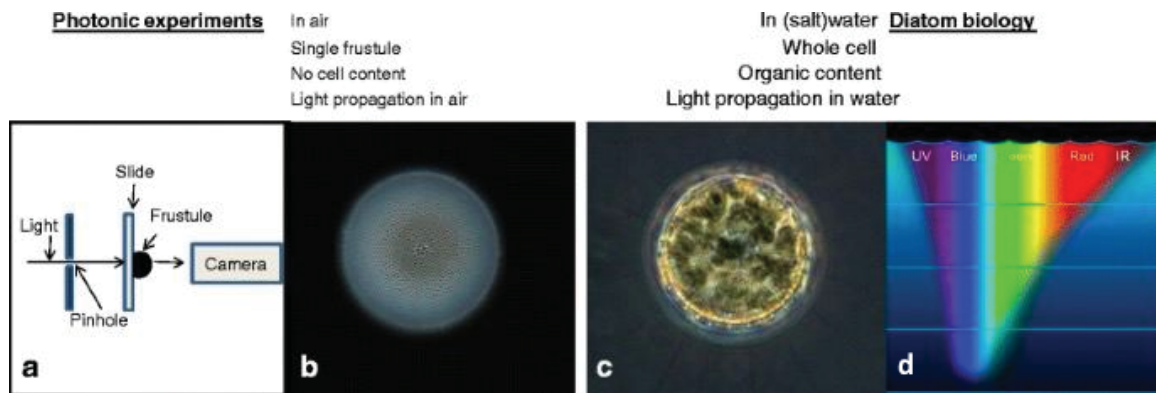
Figure 15. Overview of relevant features that differ between the diatom in its natural habitat and rinsed diatom valve in a typical photonic setup (a). b) A diatom valve rinsed of organic material, c) A living diatom in water, d) A scheme of spectral changes in light through water column.[56]

Moreover, the orientation of the frustule also affects the optical properties of diatoms when measuring the relationship between the frustule nano-and micropattern and incident light. In the natural environment, light usually falls on diatoms from the outer (convex) side, but it is quite possible that it can also be affected by the inner (concave) side when passing through the cell.

The diffraction of light by diatom frustules occurs due to the interaction of light waves with the complex surface structure of the frustule. The pores and ridges on the frustule's surface act as diffraction gratings, which split the incident light into a spectrum of colors and produce interference patterns[57]. This phenomenon has been observed in many different species of diatoms and has been studied extensively for its potential applications in optics and photonics. The diffraction patterns produced by diatom frustules can be used to create high-resolution optical devices, such as lenses, filters, and diffraction gratings, that are much smaller and more efficient than those currently available. By understanding the principles behind this phenomenon, scientists can develop new technologies that are more efficient, smaller, and more precise than those currently available. The interaction of light with the complex internal structure of diatom frustules can be described mathematically using the theory of wave propagation in periodic structures. This theory predicts that the propagation of light in diatom frustules is an interference of scattered, diffracted, and reflected waves.

2.4.2 Light focusing and concentration

Light focusing works by the diatoms harvesting photons from light, which are then scattered and refracted by their cell walls and directed into a single point. This allows the diatoms to concentrate the light into a specific area which can be used for photosynthesis or other metabolic processes. The process of light focusing in diatoms is important for the survival of the species, as it allows them to absorb more light for photosynthesis and therefore create more energy for the organism. Furthermore, the diatoms can use this

focused light to detect potential predators or food sources, allowing them to quickly react and avoid danger.

The focusing of light in diatoms has been studied extensively in the past, with some researchers suggesting that the diatom cell walls may even be able to focus light more efficiently than some optical lenses. In the study by De Stefano et al.[58], the light concentration and focusing ability of *Coscinodiscus wailesii* (*C. wailesii*) were studied using a red laser beam with a diameter 100 μm, which showed that the beam diameter was reduced by about 12 times at a distance of 104 μm from the valve position, acting like a lens, as demonstrated in Figure 16.
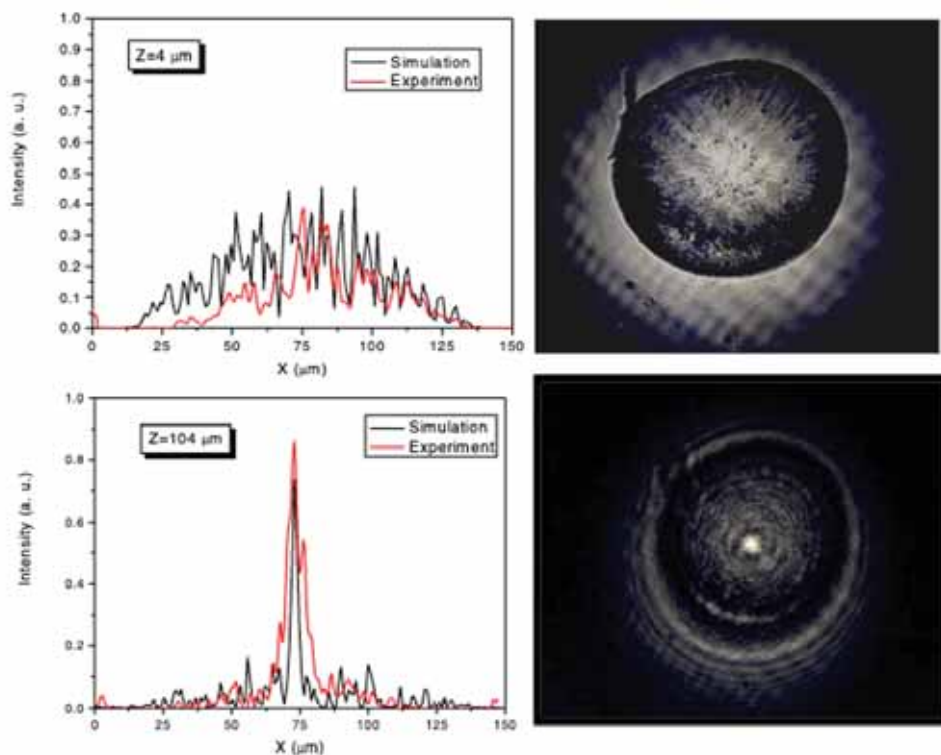
Figure 16. Left: The intensity distribution of the transmitted light at the distance (z) of 4 μm (top) and 104 μm (bottom): the red line is the experimental recorded one, the black

line is the numerically estimated. Right: The corresponding images of the diatom surface recorded by a CCD at the two distances considered.[58]

The focusing of light to a smaller diameter at a certain distance from the valve was due to the way the light waves passed through the valve's areolae. While the authors of the study attributed such behaviour to the coherent superposition of the transmitted unfocused wave through quasi-regular areolae, De Tomassi et al. explained it by the regular pore pattern and the superposition of the diffracted wave fronts.[59]

The focusing distance of the laser beam was found to be wavelength dependent, with different wavelengths (532, 557, 582, and 633 nm) resulting in different focused distances (130, 115, 110, and 105 μm), as shown in studies on *C. wailesii* (Figure 17)[59] and *Arachnoidiscus* sp., where a 633 nm laser beam was confined at a distance 163 μm.[60]
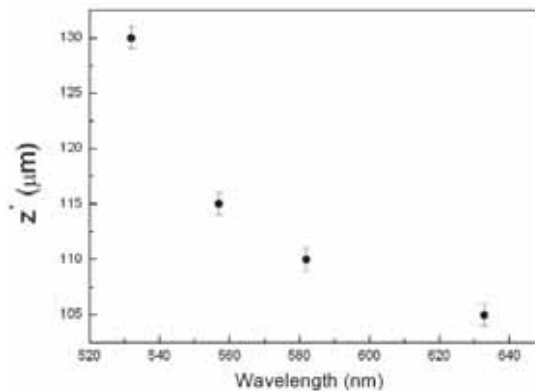
Figure 17. Distance z* of maximum intensity of the transmitted spot as a function of the wavelength of the incoming light beam. [59]

In that way, the spatial distribution of the pores in the periodic structure of the valve affects light propagation, so the valve can be considered as multifocal lens. Romann et al.[29] investigated waveguide ability and multifocal lens properties of *Coscinodiscus centralis* and *C. wailesii* using confocal hyper-spectral imaging and found that multiple light cones were transmitted through the centric valve at several wavelengths, including 485, 535, 625, and 675 nm. Additionally, they showed that the intensity of transmitted light depends on the orientation of the valve, with light intensity decreasing when the incident light illuminates the internal side of the valve and increasing when it illuminates the external side.[29] The experiment also found that tilting the incident light at an angle of 10 degrees did not change the concentration behavior of the frustule. This suggests that the material is able to maintain its optical properties even when the angle of incident light is changed, which is important because it suggests that silica-based biomaterials may have potential applications in industries that require stable and consistent optical properties, such as in the production of optical fibers or lenses. However, it is important to note that this experiment was conducted on a limited number of species and further research is needed to fully understand the optical properties of silica-based biomaterials in different environments and with different species.

The light trapping ability of *Coscinodiscus* sp. in photovoltaic application was demonstrated in the study by Chen et al. The first band diagram simulations for valve and girdle bands of *Coscinodiscus granii* (*C. granii*) showed that the generated crystal photonics modes depend on the periodicity of the structure, slab thickness, and incident wavelength.[61] However, some authors suggested that to exhibit a complete 2-D photonic

crystal band-gaps, a refractive index contrast in the material of about 2 is needed.[62] Overall, light focusing in diatoms is a fascinating example of nature's ability to create efficient and effective optical solutions.

In the experiment conducted by Kieu et al.[63] *C. wailesii* diatom valve was fixed on top of an optical fiber and irradiated with a coherent supercontinuum broadband laser with a range of 400-1700 nm in a small region of about 20 micrometers in order to study the diffracted and transmitted light through the valve as a function of the lattice constant in the periodic structure. When the valve was irradiated with different wavelengths at different angles, it generated colorful transmitted patterns in a hexagonal pattern (Figure 18), as a result of the interaction with the periodic structure of the diatom valve.
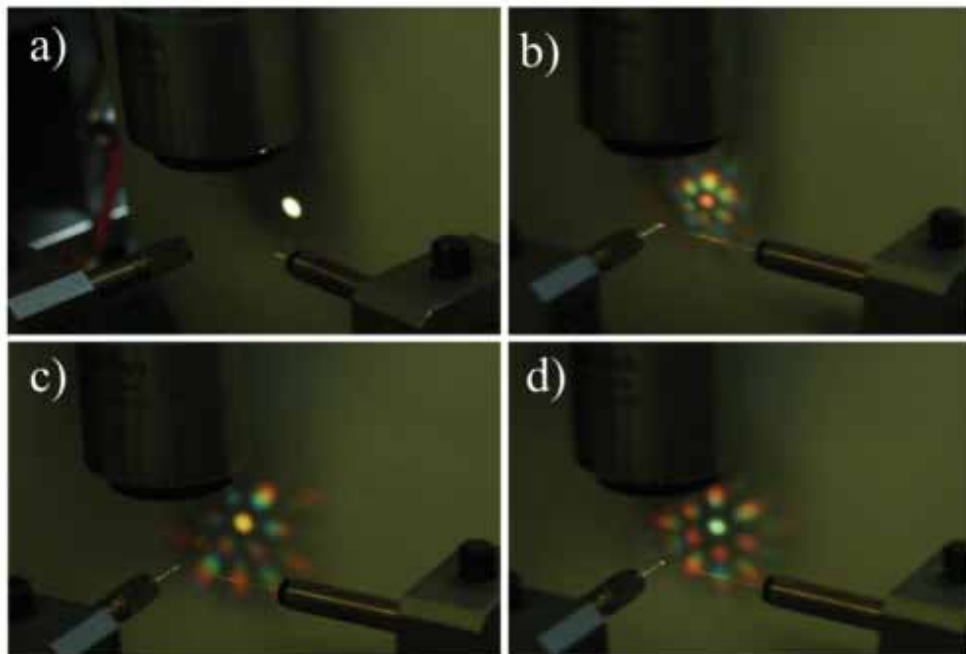
Figure 18. Optical images of the diffraction patterns obtained from the different regions of C. wailesii valve. a) No diatom was present in the beam path. b-d) The frustule

valve was present in the beam path. The color of the central spot changed according to the location of the partial photonic band gap. [63]

A study performed using a microfiber spectroscopic method found that the cylindrical frustule of the diatom *Melosira variance* (*M. variance*) has photonic crystalline characteristics that assist light absorption depending on the orientation, with a transmittance valley observed between 400 and 500 nm when irradiated through its internal side, but not when it was irradiated perpendicular to the silica side wall, as shown in Figure 19[64]. The periodicity of the refractive index in the structure was found to be related to the observed transmitted spectra.
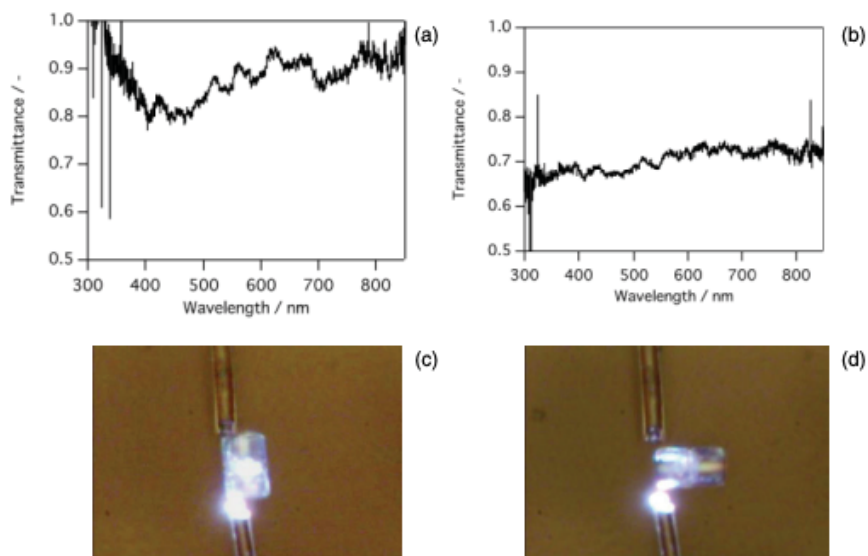
Figure 19. Transmittance spectra of a frustule using the following alignment: a) Incident light passing through the side wall of the frustule, b) Incident light passing through the frustule perpendicular to the side wall. Optical microscopy images of: c) parallel, d) perpendicular alignments. [64]

2.4.3 *Light filtration*

Light filtration is an important process in the life cycle of diatoms. To produce energy and food in the process of photosynthesis, they need to be able to access light in the water. However, light levels can vary, so the diatoms must have to filter the light in order to get the most out of their photosynthesis. Diatoms use their cell walls to absorb some of the light that enters their environment. The cell walls are made of a transparent silica, which allows most of the light to pass through. However, some of the light is filtered out as it passes through the diatoms' cell walls which helps them better regulate and take advantage of the light that is available. In addition to filtering out some of the light, the diatoms' frustules also act as a physical barrier to protect them from predators. Many of the microscopic predators in their environment cannot penetrate the frustules, so they are able to stay safe and conserve energy.

In several studies, the ability of diatoms to act as light filters has been researched, both for their fundamental properties and possible technological applications. Despite the fact that diatoms use blue and red wavelengths of sunlight for photosynthesis, an excessive supply of blue light can cause living cells to generate active oxygen molecules. Ellegaard et al.[56] investigated the protective properties of frustules and found that the frustules of certain diatom species were effective at protecting cells from harmful radiation. The samples were more transparent to the light in the visible range of the spectrum, than in the UV range, as shown in Figure 20. However, for UV-mediating effects, it is necessary to consider the periodicity of the large holes, the refractive index contrast between the frustule

and the medium, the orientation of the valves, the degree of the coverage of a layer of frustules.
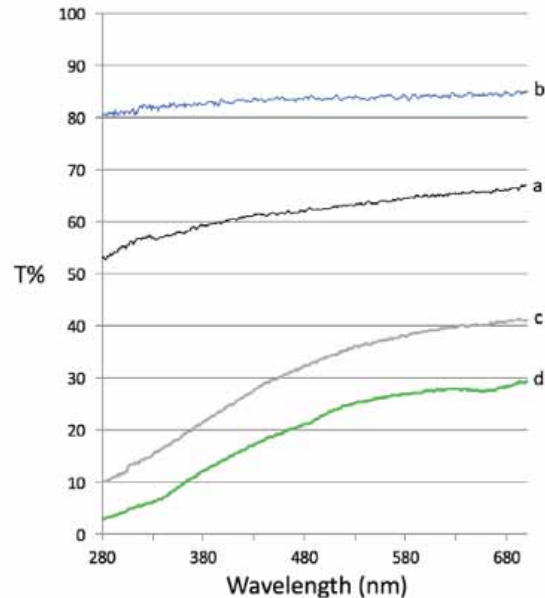
Figure 20. Transmittance spectra for: a) *Coscinodiscus concinnus* (*C. coscinodiscus*), cleaned frustules. b) *C. granii* cleaned frustules. c) *C. concinnus*, dried cells with cell content. d) *C. granii*, dried cells with cell content. The reference spectrum is the UV-transparent quartz silica microscope glass plate with nothing on top of it. [56]

M. varians frustules exhibit wavelength-dependent filtering behavior, with enhanced transmission of red light and absorption in the blue range[65]. On the other hand, Ferrara et al. showed that circular valve of *Arachnoidiscus* sp. absorb more green and red wavelengths[60]. UVB light is weakly transmitted and far away from the valve, which was in agreement with simulations. Table 2 summarizes the studies on optical properties of diatoms.

Table 2. Summary of studies on optical properties of diatoms

Species	Method	Main results	References
C. wailesii	Spectroscopy	The beam diameter was reduced by about 12 times at a distance of 104 μm from the valve position	58
C. wailesii	Spectroscopy	Focus distance depends strongly on the wavelength.	59
Arachnoidiscus sp.	Spectroscopy, digital holography	A 633 nm laser beam was confined at a distance 163 μm.	60
M. variance	Microfiber spectroscopic method	Light absorption depending on the orientation, with a transmittance valley observed between 400 and 500 nm when irradiated through its internal side	64
C. granii & concinnus	Spectroscopy	Valves more transparent in the visible region than in UV region of the spectrum	56
C. wailesii & C. centralis	Confocal hyperspectral imaging	Light trapping depends on wavelength and the valve orientation, but not on the incident angle	29
C. granii	Spectroscopy	The generated crystal photonics modes depend on the periodicity of the structure, slab thickness, and incident wavelength	62
M. variance	Spectroscopy	Enhanced transmission of red light and absorption in the blue range	65

2.4.4 Photoluminescence

Diatom shells contain various pigments, including chlorophylls and carotenoids, which absorb light and transfer the energy to other molecules, resulting in the emission of light, or luminescence. The photoluminescence (PL) properties of diatom algae have been extensively studied in recent years due to their potential use in bioluminescence applications. According to studies[66,67], upon illumination of the porous silicon (Si) and porous silica (SiO_2) by UV wavelengths, they emitted PL peaks in the visible spectral region.

The PL properties of diatom algae have been studied using spectroscopy, fluorimetry, and imaging techniques. De Tomassi et al.[68] showed that the intrinsic photoluminescence from frustules is strongly influenced by the surrounding atmosphere, since during the exposure to gases, the induced luminescence changes in the optical intensity and position of peaks. Photoluminescence responses of *Thalassiosira rotula* valves when exposed to different gases and volatile substances were demonstrated in the study by De Stefano et al.[69] The frustules were irradiated by a He-Cd laser (325 nm), which resulted in a multiband PL between 450 and 690 nm. Such result was attributed to oxidized silicon nanocrystals (533 nm), porous silicon (609 nm), and hydrogenated amorphous silicon (661 nm).

The PL properties of the frustules were then tested with different gases. The valves' PL was quenched with electrophilic gases, which are attracted to electrons, while it was enhanced for nucleophilic ones, which are attracted to positively charged ions. For example, the PL was quenched when exposed to $NO_{2(g)}$ flux, showing high sensitivity in

the order of sub-ppm level, as shown in Figure 21. This sensitivity was strongly dependent on the structure, porosity, and gas nature.[70]
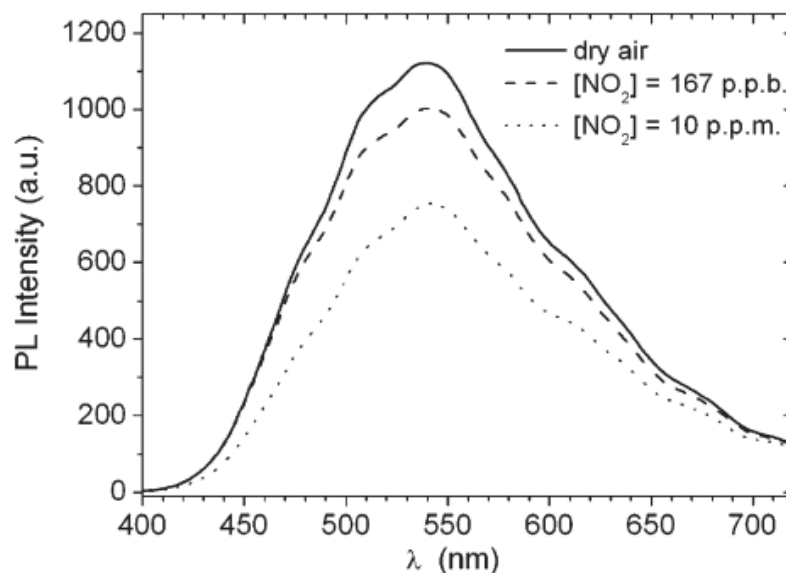
Figure 21. *Thalassiosira* photoluminescence spectrum in dry air (continuous line), in 167 ppb of NO_2 in dry air (dashed line) and in 10 ppm of NO_2 in dry air (dotted line). [70]

Some studies demonstrated the photoluminescence of chemically modified diatoms. For example, the results obtained by Townley et al. showed that intact frustules exhibited a broad PL peak in the range of 500-650 nm upon irradiation with 442 nm laser[71]. However, frustules that were grown with nickel sulfate showed a quenched PL, meaning that their PL properties were suppressed. This suggests that the chemical modification of frustules can affect their PL properties. De Stefano et al.[72] found that green PL of diatoms peaked between 520 and 560 nm, can be attributed to the Si–H groups, but also to the presence of nanostructures which enhance by quantum confinement the light emission.

Antibody doped frustules showed high sensitivity (1.2 ± 0.2 nm·µM^{-1}) and detection limit (100 nM^{-1}) when irradiated by 325 nm laser[72], while frustules from *Psammodictyon panduriforme* exhibited emission peaks at 417 nm and 534 nm due to oxygen-vacancy defects[73]. Under pulse laser excitation, the results showed a single narrow emission peak near 475 nm, which may be explained as a consequence of a putative quantum confinement effect due to the mesoporous silica and the quasi-regular pores in the frustules' structure. The PL spectra obtained in the study are shown in Figure 22[73].
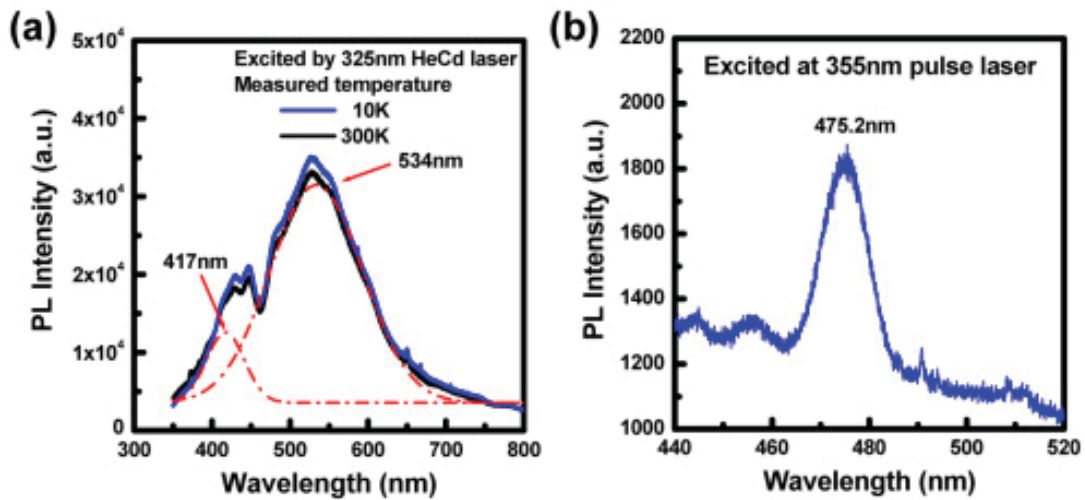
Figure 22. The micro-photoluminescence spectra of diatom frustule were measured by: a) 325 CW laser and b) 355nm pulse laser acted the excitation laser sources.[73]

Arteaga-Larios et al.[74] studied the UV-excited photoluminescence emitted by the diatoms and compared it between both species of diatoms, of different ages, and with the PL of synthetic porous SiO$_2$. They also conducted morphometric analysis of the size and arrangement of pores to observe any correlation with the PL of two diatom species of

different ages. The UV-excited PL displayed four clearly defined peaks within the blue-region spectrum, on top of the broad PL characteristic of synthetic porous silicon dioxide. The observed PL shifts are correlated with a substantial increment of Si-OH groups adsorbed on the frustule surface, as revealed by Fourier transform infrared spectroscopy.

As suggested in the study[75], the different defect states in the material cause different levels of electron excitation, which in turn causes the emission of light in the blue and green regions. The oxygen defect centers, specifically, allow for the emission of light in the blue region, while the neutral oxygen vacancy and self-trapped excitons are responsible for the emission of light in the green region.

All above mentioned studies have provided valuable insight into the photoluminescence properties of diatom algae and their potential applications. For example, they could be used to detect the presence of pollutants in aquatic environments or to illuminate underwater structures. In addition, diatom algae can be used to create novel materials for optical displays and sensing applications. However, further research is needed to fully understand how these properties arise and what factors influence their intensity and spectral characteristics.

2.4.5 Potential applications based on the optical properties

In addition to their visual appeal, the optical properties of diatoms have practical applications and have inspired new technologies. Their sensitivity to changes in the environment around them means that diatoms can be used as biosensors to detect chemicals or other factors. The nanoscale structures of diatom cell walls have also inspired new

approaches to nanofabrication, such as using diatoms as templates to create replicas of their pores and ridges in materials like metals, plastics, and ceramics. Diatoms demonstrate how intricately patterned microscale structures can be engineered to produce remarkable optical effects and nanoscale phenomena.

Figure 23 summarizes optical properties and some of the potential applications of diatom biosilica.
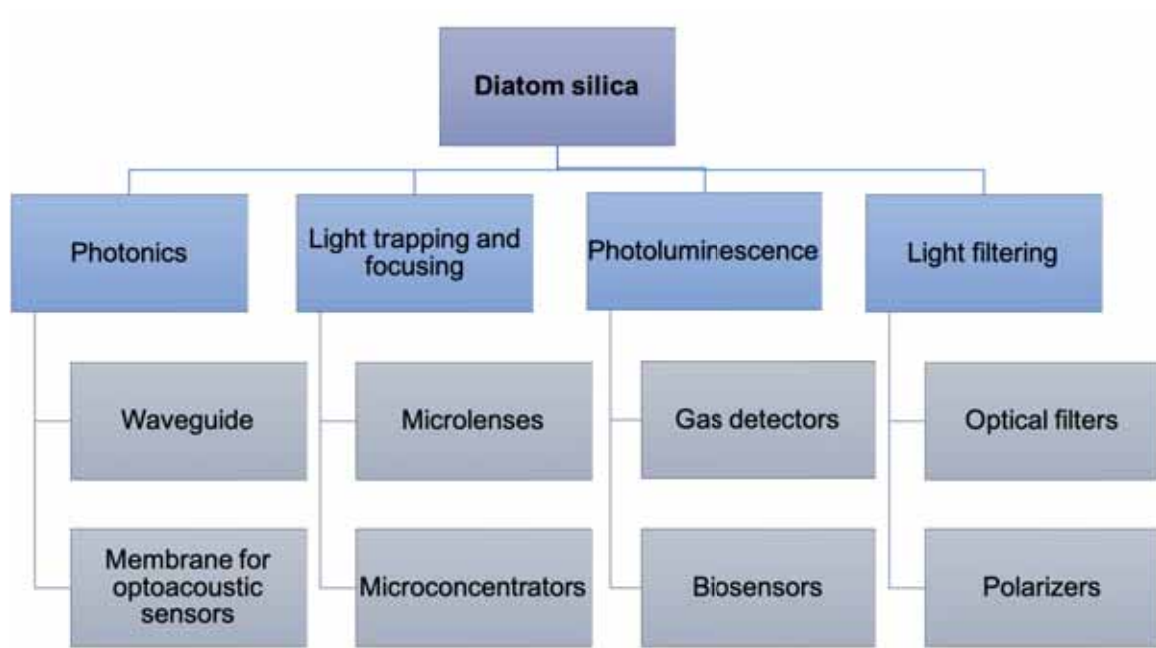
Figure 23. Diatom biosilica optical properties and their potential applications

Aulacoseira and *Thalassiosira* frustules have been employed for detecting trace amounts of pure gases such as NO(g), H_2(g), and NO_2(g)[70,76]. Diatoms have the ability to trap light, which can enhance the amount of light harvested by solar cells[62]. In addition, frustules from diatoms can be modified with TiO2 to improve the efficiency of Dye Sensitized Solar Cells (DSSC) technology[77].

Diatoms can be modified with molecules that can endow them with an ability to attract specific target molecules or pathogens. Researchers have experimented with the immobilization of proteins, antibodies, DNA and other biomolecules on the surface of diatom shells that can interact with a specific analyte, leading to detectable optical changes. Photoluminescence modulation in antibody functionalized diatom frustules of *Amphora sp.* was used by Viji et al.[78] to detect BSA protein at mM level, whereas Selvaraj et al.[79] used the same species to detect Salmonella typhi at detection limit of 10 pg. The review of diatom-based biosensors is provided in the article[75].

Biosilica has potential for photonics applications due to the nanoscale 3D structures of frustules, which can be modified with luminescent dyes for bio-hybrid luminescent materials and used as nano-plasmonic sensors for label-free chemical and biological sensing.[80,81]

2.5 The modification and applications of diatoms

There are different ways of modification of diatom algae that can transform them into a custom-designed micro/nanomaterial with desirable properties for various applications.[82]

2.5.1   Surface modification

One of the most common methods of diatom modification is surface modification, which aims to enhance the surface properties of the diatom algae, such as hydrophilicity, surface charge, and increase the surface area for higher catalytic activities. Surface modification can be achieved by changing the chemical composition of the surface using

various techniques such as chemical treatment, plasma treatment, or thermal treatment. Some of the most widely used functionalization approaches include noncovalent and covalent functionalization and chemical conversion of diatomite[83]. The surface of siliceous diatom frustules containing reactive silanol (Si-OH) groups can be readily modified with different functional groups, such as –SH, –NH2, –COOH, −CHO for the immobilization of different biomolecular probes (DNA, proteins, antibodies)[84] and drug loading[85–89]. Schematic representation of different functionalization techniques for pharmaceutical applications are shown in Figure 24.[90]

Figure 24. Schematic representation of the surface modification techniques used in pharmaceutical applications. NP: nanoparticles. Small interfering RNA (siRNA); Vitamin B 12 (B_{12}); Iron oxide nanoparticles (Iron ox. NPs); Fluorescent dye (Fluo. dye); Photoluminescent compound (PL); Carbon monoxide-releasing molecules (CORMs); Nitric oxide releasing molecules (NORMs); Scavengers of reactive oxygen species (ROS scav.). [90]

2.5.2 Genetic or metabolic modification

Diatoms' genes can be modified or transferred to enhance their properties. Genetic modification can be achieved using various techniques such as gene cloning, transfection, or CRISPR-Cas9 gene editing[91–93]. Genetic modification can alter the structure and composition of the diatom cell walls, enhancing their desirable properties, such as efficient CO_2 fixation, higher lipid production, and increased tolerance to environmental challenges.[93] Moreover, diatoms can be bioengineered by modifying their metabolism pathways through genetic or metabolic engineering. This method aims to optimize the metabolic pathways of diatoms for the production of desired products such as biofuels, high-value chemicals, and proteins. Bioengineering of diatoms can be achieved by overexpressing the genes involved in the desired metabolic pathways, or by deleting the genes involved in the non-desired metabolic pathways.

2.5.3 Incorporation of nanoparticles

The incorporation of nanoparticles into the diatom frustules can enhance the structural, optical, and electrical properties of diatoms. Nanoparticles can be incorporated into diatoms via electrostatic or bio-mineralization processes, enhancing their properties such as increased catalytic activity, improved mechanical strength, and higher optical absorption.

The possibility to insert semiconducting or metallic elements, such as germanium[55,94,95], nickel[71], titanium[96–98], aluminium[99], europium[100], tin[101], zirconium[101,102], in diatom frustules for applications in sensing, optoelectronics, solar energy harvesting, catalysis, and biomedicine is thoroughly explained in the review[103]. Losic and co-workers

demonstrated the functionalization of diatomaceous earth with dopamine-modified iron-oxide nanoparticles and proved their capability to be used as magnetically guided micro-carriers for non-invasive and targeted drug delivery.[87] Silver nanoparticles/diatomite nanocomposites exhibited antibacterial effect against infectious pathogens.[104,105]

Jantschke et al. used two approaches—covalent linking and layer-by-layer assembly (LbL)—to decorate diatom frustules with noble metal (Ag, Pt, Au) and semiconductor (CdTe) nanoparticles for surface-enhanced Raman spectroscopy (SERS) of components, for catalysis, and to obtain enhanced image quality in scanning electron microscopy.[106] Fischer and co-workers used a covalent-coupling method to prepare gold nanoparticle-decorated diatom biosilica and successfully applied the obtained catalysts for the oxidation of D-glucose to D-gluconic acid.[107] Pannico et al. used a method based on electroless deposition of gold to cover diatom frustules and showed that such composites could be used as a support for SERS.[108] According to the study by Kong et al., plasmonic nanoparticles decorated diatomite served as a lab-on-a-chip device for on-chip chromatography and label-free biosensing of small molecules from complex biological samples.[109]

Moreover, an ultrasensitive SERS immunoassay based on diatom biosilica with integrated gold nanoparticles has been developed for the detection of interleukin 8 (IL-8) in blood plasma.[110] The results confirmed that diatom frustules increase the sensitivity of the immunosensor when compared with a conventional flat glass-based sensor. It was also demonstrated that diatom shells functionalized with gold nanoparticles via a photo-deposition process could be used for the harvesting and detection of biological analytes,

such as bovine serum albumin (BSA), and chemical pollutants (mineral oil) in low dilutions down to 10^{-16} M for BSA and 50 ppm for mineral oil leading to applications in biotechnology, medicine, safety, monitoring and control of environmental hazards.[111,112] Polyethylene glycol (PEG)-modified diatomite decorated with gold nanoparticles by one-pot liquid-phase synthesis demonstrated the potential for usage as advanced nanodevices adding imaging features to the nanocomplexes.[113] Recently, Braceño et al. showed that diatom biosilica modified with gold nanoparticles by In-situ and Ex-situ methods represents a promising candidate for controlled release of the gentamicin in simulated body fluid.[114] The experimental findings showed that while In-situ method resulted in a slower release, the Ex-situ method showed a faster release of gentamicin by using gold/cetyl-trimethylammonium bromide (CTAB) nanoparticles.

2.5.4 Physical modification

Physical modification methods, such as mechanical milling or sonication, can be used to change the size and morphology of diatoms, enhancing their properties such as increased surface area, porosity, and size distribution. This method can also be used to reduce the size of the diatoms, making them more suitable for applications such as drug delivery and tissue engineering.[82]

2.5.5 Different applications of diatoms

The abundance and versatility of diatoms opens up wide opportunities for choosing the optimal types of structures with desirable characteristics. Nanostructured silica exoskeletons of diatoms are readily available both through cultivation by aquaculture methods and through the extraction of diatomite, widespread sedimentary rock, which is

widely used for the production of refractory and heat-insulating materials, as feed in animal husbandry, for filtration and sorption of various substances, including oil spills[115]. These applications exploit the standard features of diatom frustules – the chemical composition, the developed multilayered structure and the presence of an internal cavity as a thermal barrier. At the same time, such features of the specific structure of diatom exoskeletons as a diverse morphology and complex topology of nanosized pores, which determine the spectrum of natural vibration frequencies, as well as structural characteristics (stiffness and strength under quasi-static loading), have not yet been used in engineering devices.

The particular spatial organization of nano- and micropores of the diatom frustules offers promising prototypes of functional systems and elements for targeted drug delivery[116,117], electrochemical energy storage[118,119], photovoltaics[120], metamaterials[121], catalysis[122,123], filtration[124], metal modification and removal[103,125] and many others[126–128]. Some potential applications of diatoms are schematically represented in Figure 25.
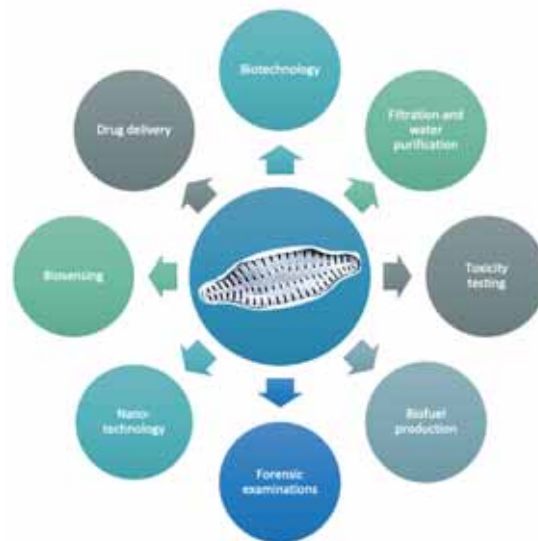
Figure 25. Different applications of diatoms.

2.6 On the MEMS perspective

The requirements of small size, specific optical properties, low density and high strength are important for numerous applications, especially in silicon photonics [129,130] and for MEMS[131,132] as well as nanoelectromechanical systems (NEMS). The interest in diatom frustules as prototypical photonic crystals for microelectronic technology arose relatively recently and has already been reflected in a number of high-profile publications[77,83,125,133–136]. Dimensional and structural correspondence between diatom exoskeletons and devices such as photonic integrated circuits (PICs) and MEMS for high-sensitivity microphones serve as a starting point for seeking further opportunities to create nanotechnology components using biomimetics and biotechnology[137]. To underpin the development of theoretical concepts in this area, comprehensive studies are required to include structural and mechanical characterization which remain small in number and limited to specific diatom species. Consequently, studies devoted to the possible use of diatom frustules as a basis for MEMS elements[138,139] rely on unproven hypotheses or numerical simulation results[140] that need validation.

Successful fabrication of nanostructured silicon structures reduced from diatomaceous silica earth and firmly integrated into silicon wafers shows that neat nanostructured objects obtained in the framework of the BANSAM paradigm[7,45,126] can be readily applied as elements in smart electronic chip technologies. Since diatoms are able to colonize silicon monocrystalline wafers[32], a simple technique of guided, highly precise deposition of single diatom cells might be developed for mass production of NEMS and

MEMS containing diatom frustules as an integral part of a sensor, such as a microphone, or an energy harvesting element.

The description of vibration behavior for a single openwork architected element is a relatively simple task for modern computational math. Numerous finite element analysis (FEA) or finite element modelling (FEM) software packages are available on the market such as Ansys, COMSOL and many others. These software tools are capable of predicting main modes of vibrations and eigenfrequency spectra processing 3D-meshed geometrical models of diatom frustules fixed to the infinitely thick substrates in a manner (boundary conditions). Figure 26 exemplifies typical results of FEM analysis of diatom frustule vibrational patterns[137].
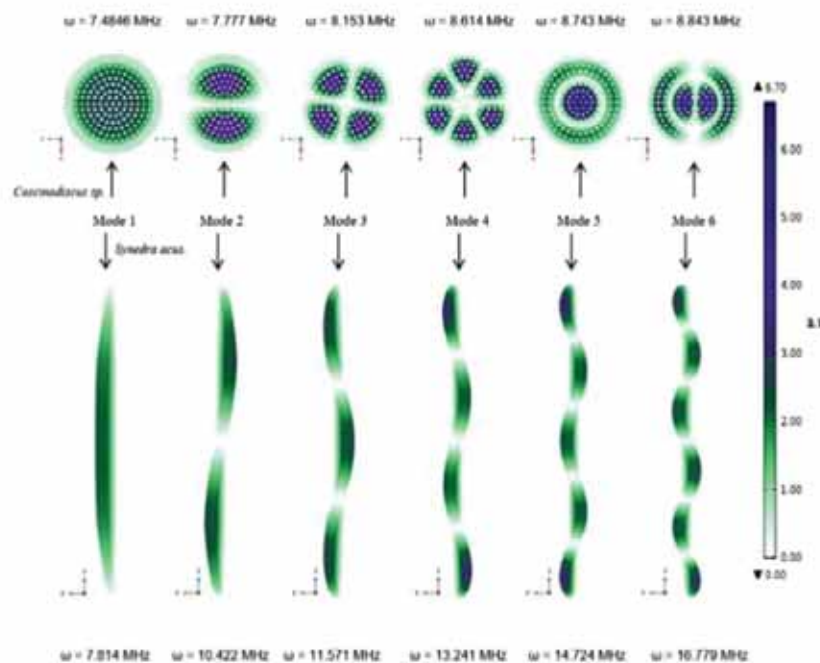
Figure 26. Mode shapes and natural frequencies of *Coscinodiscus* sp. (centric) and *Ulnaria acus* (pennate) observed in the simulation using COMSOL Multiphysics. [137]

Calculated values of eigenfrequencies of *Ulnaria acus* and *Coscinodiscus* sp. are as high as 7-17 MHz, which is undoubtedly very attractive for NEMS and MEMS elements and microelectronics in general. It is important to note that elastic modulus of amorphous hydrated silica (22.4 GPa) was input for calculations. One can suggest that the reduction of silica to silicon will increase eigenfrequencies a few times due to the dimensional thinning and material stiffening (Young's modulus of silicon is 140-180 GPa). The values of calculated eigenfrequencies for the geometrical models of diatoms are in good agreement with the data of photoacoustic measurements, which we recently conducted for several species of live diatoms[15,141,142]. Live diatoms, as believed, absorb the energy of laser pulses in chlorophyll molecules and convert some part of absorbed energy to a wide spectrum of vibrations resonating with frustules' vibrations at eigenfrequencies.

The drawback of this computational Math applied to this aspect of diatom science is quite obvious – simple 3D geometrical models of frustules capture the rough details of frustules neat architecture only. Two approaches can be put forward to deal with difficulty:

- Parametrization of a simplified analytical solution adopted from continuum mechanics of thin shells as we demonstrated at the paper by Abdusatorov et al.[137]

- the development of destructive (through FIB-SEM milling – Figure 27) or non-destructive tomography (e.g., using ptychography with help of synchrotron coherent beam – Figure 28).
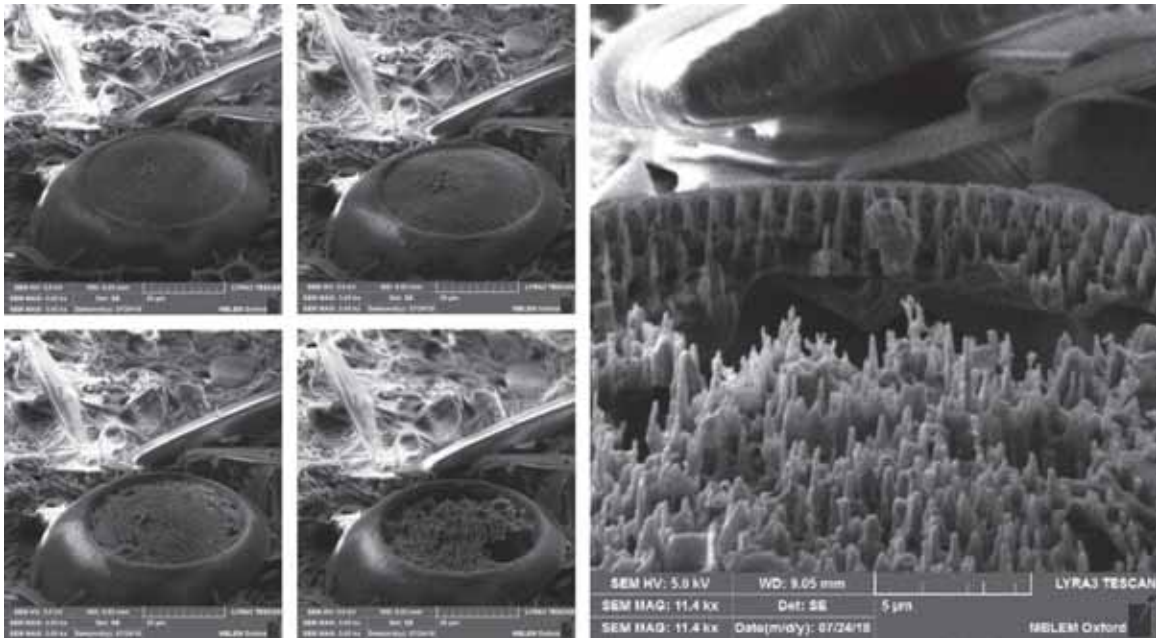
Figure 27. The example of FIB-SEM milling of diatom species (destructive method).[7]
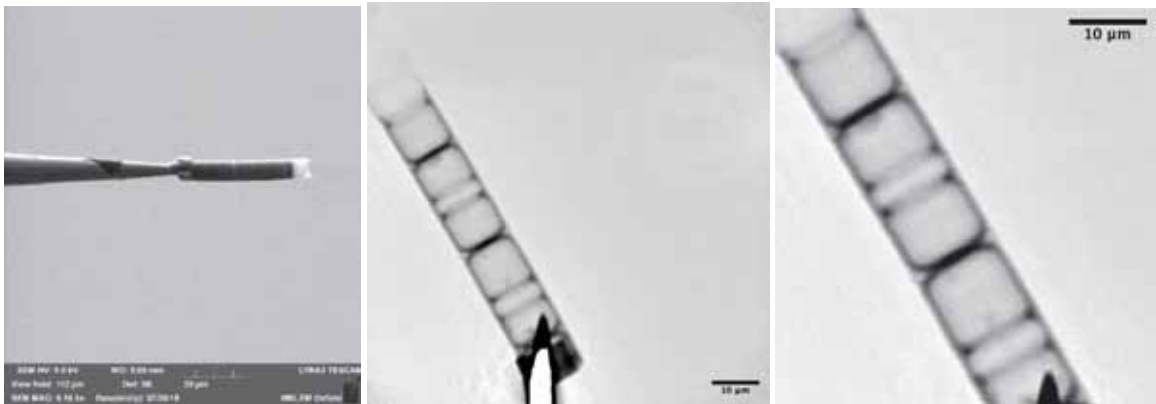
Figure 28. Ptychography of *Aulacoseira* diatom cells (courtesy of T.E.J. Moxham, University of Oxford / Diamond Light Source, U.K.).[7]

Parameterization techniques are relatively simple since they require to calibration and fitting of few parameters for the series of vibration modes, the i-th eigenfrequency of which obeys to formula[7,137]:

$$\omega_i \propto \sqrt{\frac{E}{\rho}\frac{1}{D}\left[a_i\frac{t}{D} + b_i\right] P_i\left(\frac{d}{D}\right)}$$ (1)

where E, ρ, D, d and t are Young modulus, density, diatom principal size (outer diameter for centric and longest size for pennate diatoms), pore diameter and frustule thickness, respectively.

Parameters a_i and b_i as well as morphology factor P_i are to be fitted and experimental measurements are vital in this case in order to retrieve the values of parameters from the correlation analysis.

3D-reconstruction of frustule architecture is much more complex approach that promises a valuable outcome – a robust 3D model of frustule for the computations of many particular properties – mechanical (static and vibrational for MEMS), optical (light confinement, focusing and diffraction) and hydraulic (fine filtering).

3.1 Diatom algae cultivation

3.1.1   Sampling diatoms from natural populations. Isolation and introduction into clonal cultures of certain species of diatoms. Cultivation of various types of freshwater and marine diatom algae

Marine diatoms were isolated from planktonic and benthic samples. Clones of radial centric diatoms *Coscinodiscus oculus-iridis (Ehrenberg) Ehrenberg* and *Coscinodiscus* sp., were subsequently isolated from the plankton samples at the surface water layer (depth of about 1–2 m) in the Tsushima Strait to the north of Okinashima Island and from the pier of the Karadag Scientific Station (Crimea), respectively. A benthic sample was taken in the form of a scraping of fouling from the surface of stones at a depth of about half a meter in a small bay near the settlement of Caleta de Caballo (Lanzarote Island, Canary Islands archipelago) and the polar centric diatom *Biddulphiopsis titiana (Grunow) von Stosch & R. Simonsen* was isolated from it. The samples were placed in plastic containers and delivered to the laboratory of algae and microbiota of the Karadag scientific station[143]. All diatom samples were isolated by micropipetting single cells of diatom species of interest, which gave rise to clonal cultures[144]. According to the Medlin and Kaczmarska system[145], *C. oculus-iridis* and *Coscinodiscus* sp. belong to the class *Coscinodiscophyceae*, while *B. titiana* belongs to the class *Mediophyceae*. Clonal marine diatom cultures were kept in 100 ml Erlenmeyer glass flasks filled with 40–50 ml medium. A modified ESAW medium was used as a culture medium[146]. ESAW medium is an

artificial sea water with a composition similar to natural sea water. To maintain the exponential growth phase, the cultures were reseeded once every 7–10 days. The culture flasks were placed in a room kept at $20 \pm 2°C$ near a window oriented to the north to prevent direct sunlight.

Benthic diatom species *K. amoena* were collected from the tidal zone of Gdansk Bay, Baltic Sea in the area of Zelenogradsk, in early June 2016[15]. The salinity of the interstitial water across the collection sites, as well as the water salinity of the tide pools, was 5 ppt. Samples were collected in the mid-littoral zone during the low tide in the form of strips of sand with a width of 1.5 cm, length up to 15 cm and a depth of 0.7 0.9 cm, by using a 0.5-l polyethylene terephthalate (PET) bottle. Then, the sample container was filled with water from a nearby tide pool. The specimen was not fixed, but it was preserved alive and subsequently delivered to Moscow. The material in the bottle was placed on the windowsill of the laboratory to ensure natural diffuse lighting and an alternating day/ night regime. The temperature ranged from 17 to 26 °C, and the material was kept in the same plastic bottle for 3 years. The cap of the bottle was slightly loose so as not to hamper the gas exchange between the internal space of the container and the external environment and accommodate room temperature variation. The water capacity of the sample (water + sand at the bottom of the bottle) was 400 ml. The amount of water evaporated from the sample container was recovered by trickling distilled water down the inner wall of the bottle, once the evaporation achieved more than 5 mm from the initial level. This was done to avoid the fouling diatoms inhabiting the PET bottle close to the water surface being osmotically stressed. During the growth period of the accumulation culture, no minerals were fed. At

the end of June 2016, we observed microscopic colonies of *K. amoena* on the surface of sand grains in the ground sample. Permanent preparations were used to identify the species. The frustules were purified from organic components with concentrated sulfuric acid and were embedded in rosin. The macroscopic monocultural colonies of *K. amoena*, appearing as brown spots with ramified edges (diameter, 2–3 mm), were observed on the inner surface of the PET bottle in October 2017. By mid-July 2019, a complete brown coating had already been formed by the colonies on the inner wall of the bottle. As part of this coating, *K. amoena* cells were arranged in a dense one-layer pattern and formed a complex ornamented mosaic.

Freshwater diatom strains *Amphipleura* sp. (strain № Ov 466), *Asterionella formosa* (BZ 33), *Hannaea baicalensis* (BK 479), *Nitzschia graciliformis* (BK 611, 2.5BK 576), *Ulnaria acus* (15K 595), *Achnanthidium sibiricum* (256) and *Encyonema silesiacum* (459) were isolated from the natural populations of the lake Baikal and river Yenisei. Cell isolation into monoclonal cultures was carried out according to the previously described protocol in the Limnological Institute, Siberian Branch, Russian Academy of Sciences (Irkutsk, Russia)[147]. Freshwater diatom cultures were grown on DM medium[148] in flasks at around 8 °C and illumination of 16 µM m^{-2}s^{-1} using a 12/12 hour artificial light/dark cycle.

All cultures were successfully delivered to Moscow and grown at the Skolkovo Institute of Science and Technology in T-25 culture flasks (Eppendorf, Germany) in a volume of 40 ml. Freshwater diatoms were grown in refrigerators equipped with a phytolamp to provide optimal illumination at a temperature of 10 ± 1 °C, while marine

cultures were grown in natural diffused light, on the laboratory windowsill, with alternating day and night, in the temperature range from +19 to + 22 ˚C.

3.1.2   Cultivation of diatoms in the incubator

Some part of the freshwater diatoms (*A. sibiricum*, *U. acus*, *E. silesiacum*) has been grown in a specially designed incubator in cell culture flasks "T-25" (Eppendorf, Germany), with sterile filter caps, which provide the gas exchange between the internal space of the flask and the external environment. Each flask contained approx. 30 mL of DM medium. The cultivation temperature was maintained at about 12 ± 1 °C, while the blue and red light-emitting diodes (LEDs) with a 12:12 day-night cycle promoted the growth of the strains.

The Algae reactor[141,142,149] consists of two parts: the control unit, maintaining suitable conditions for diatom algae well-being, and the growth chamber. The entire reactor is powered by a 220V AC, transformed into 12V by two independent power supply units (50W for light controlling and 150W for water cooling system). The control unit consists of two independent circuits: the first to control the day-night regime and light brightness, the second one for thermal regulation placed in the PC case. A dry-contact time relay (220V supply, 12V regulation) provides the day-night cycle with the ability to set on and off by a day of the week and time of day. In the same circuit, a smooth PWM light power controller with an operating frequency of 10 kHz (which prevents flickering of the lighting) is integrated. [141,142,149]

In the thermal regulation circuit, the purified water from the growth chamber is sucked by an impeller pump into a water block located on the 80W Peltier element's cold

side. The hot side of the Peltier element is cooled by a maintenance-free liquid cooling system with a peak dissipated power of 250 W. Feedback of the Peltier element and the pump is carried out through continuous temperature monitoring by a thermostatic controller with two sensors at the point where water is sucked into the system and water is released back into the core chamber. This way, the temperature inside the growth chamber could be maintained down to 10°C with high precision. The control unit is combined with the growth chamber with quick-release connectors on the rear panel: a 3.5 mm jacks for temperature sensors and a 12V DC-DC connector for power supply and control of the lighting system. Two silicone hoses connect the water circuit to the pump and the chilled water block. The growth chamber is a vessel, the walls of which are insulated with layers of foamed polyethylene to maintain the temperature. Inside the growth chamber, a rack is located, in which the temperature sensors and the inlet and outlet hoses are mounted. Inside this frame, another frame on which the cultural flasks with diatoms are rest. On the top cover of the growth chamber, made of 8 mm acrylic (thermal barrier), a lighting system is mounted: two LED strips with LEDs that correspond to the bands of maximum light absorption by chlorophyll (phyto light). The strips are stacked to the aluminum profile, which is both a supporting structure and a radiator, and are directed to the cultural flasks at the bottom. The scheme of the incubator is shown in Figure 29.
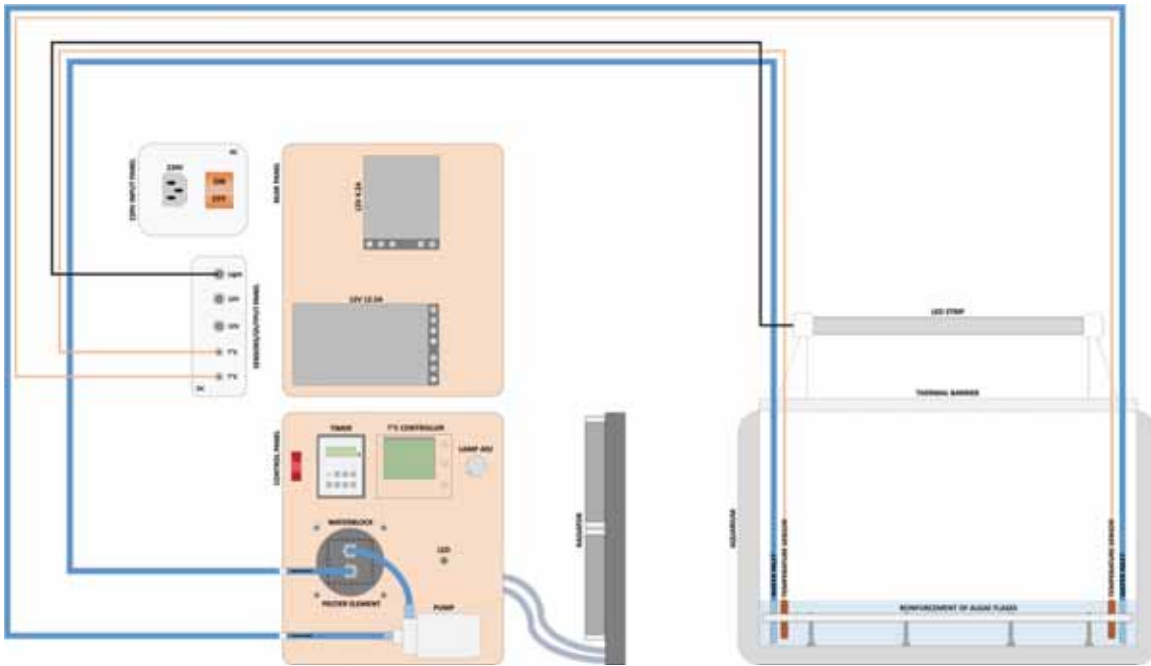
Figure 29. A scheme of the diatom algae incubator[142]

3.2 Monitoring of the growth of diatoms

3.2.1 IVIS SpectrumCT In vivo Imaging system

The IVIS SpectrumCT In Vivo Imaging System (Xenogen Corp., California, USA) was used to monitor the growth of diatoms during long-term cultivation. Different diatom cultures *(A. sibiricum, Coscinodiscus* sp., *Biddulphiopsis titiana* and *Ulnaria acus)* were monitored over a long period of time up to 100 days. Visualization of samples cultivated in 40 ml cell culture flasks was carried out without preliminary sample preparation. The frame with flasks containing diatom cultures cultivated in the incubator was transferred directly from the incubator to the chamber of the setup for monitoring. The fluorescence signal was excited by optical radiation at a wavelength of 465 nm and recorded at 680 nm. The images were acquired and analyzed with Living Image 4.7.3.[141,142,149]

Besides, suspensions of diatoms in a 96-well plate and diatoms mixed with agarose gel were also visualized. To prepare diatom-agarose phantoms, in one case, 3 µL of a diatom suspension was mixed with 7 µL of 1 % agarose gel (A9045-5G, Sigma Aldrich, Germany) and pipetted into a petri dish. In another case, 15 µL of diatoms were mixed with 35 µL of melted agarose. Agarose drop served as a reference sample. [142]

3.2.2 Spectroscopy measurements

To verify the results, fluorescence spectra were obtained using an Infinite M Nano+ spectrophotometer (Tecan Trading AG, Switzerland). The fluorescence excitation wavelength was 465 nm, and the emission was recorded in the region of 620–750 nm.[15,141,142,149,150] The absorbance spectra were also collected in the wavelength range 400–700 nm on the specific days during cultivation. [141,142,149]

3.2.3 RSOM monitoring

To monitor the growth of diatoms using RSOM Explorer P50, cultures of *A. sibiricum* (strain 256), *C. oculus-iridis* (strain 0.1211-OD), *Coscinodiscus* sp. (strain 21.0407-OA), *B. titiana* (strain 0.0212-OH), and *U. acus* (strain 15k 595) were mixed with agarose gel and measured on the certain days during cultivation. For this purpose, a mixture of 3 µl of diatom suspension with 7 µl of 1% melted agarose was prepared. Drops of diatoms immersed in agarose gel were pipetted onto the bottom of a Petri dish and, after solidification, filled with deionized water to ensure coupling between the ultrasonic sensor and samples. Diatom-agarose drops were scanned with a scanning step of 20 µm and the field of view up to 12 × 12 × 3 mm. The images were processed using the ImageJ software. The average pixel intensity in the region of interest was found from the MIP RGB images

by analyzing color image histograms that show the average pixel intensity for the red (11-33 MHz) and green (33-99 MHz) channels. [141,142]

3.2.4 *Monitoring of the growth of diatoms using microfluidic cell*

For in situ monitoring of the process of growth and division of diatoms, a microfluidic cell was developed with the ability to adjust the temperature (from 10 to 40 °C), medium flow rate (1-6000 µl/min) and CO_2 content (0.01-5 vol.). The schematic diagram of the monitoring device is shown in Figure 30.

The flow cell is made in the form of a microfluidic chip. The cell body was cast from Sylgard 184 polydimethylsiloxane elastomer (Dow Corning, USA). The casting mold was made by photopolymer 3D printing using SLA technology. A spacer was used to prevent inhibition of polymerization of the elastomer. The flow cell has a central working channel 1 mm wide, which in the middle has an expansion of up to 5 mm. This makes it possible to reduce the flow rate in the region of observation of the growth of diatoms. The entrance and exit from the channel are carried out using fluoroplastic tubes with an outer diameter of 1 mm. To reduce the number of air bubbles in the tubes, a peristaltic pump (Figure 30 (pump 1)) is installed at the outlet of the cell, and the cell inlet tube is immersed directly into the nutrient medium receiver. A cavity is formed around the main channel in the chip, forming a pressure suction cup. This cavity is connected through a PTFE tube to a compact membrane vacuum pump. When creating a vacuum, the suction cup securely presses the flow cell against the glass slide and provides a tight connection between the main channel and the glass. Such a scheme of the device allows you to quickly disassemble and assemble the flow cell for washing, it is very compact and easy to use. In terms of size,

such a cell practically does not differ from a non-separable one and is installed on a standard microscope slide with a standard preparation driver.
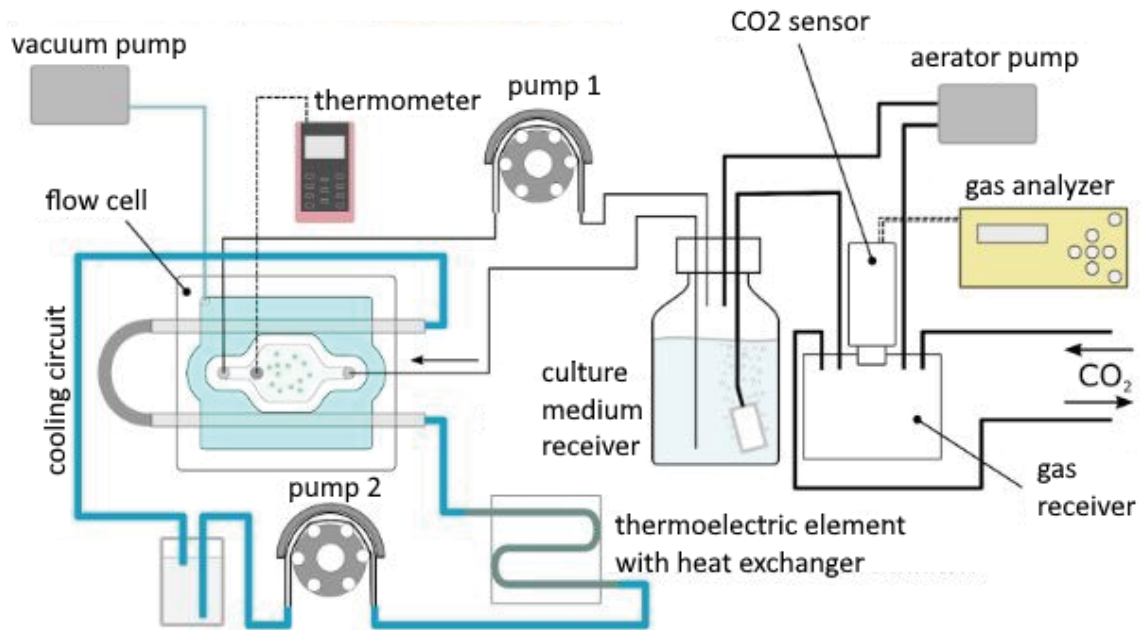
Figure 30. Scheme of a setup with a microfluidic cell for monitoring the growth of diatoms using optical microscopy

The cooling system of the flow cell is liquid. Two stainless steel tubes with a diameter of 1.2 mm are installed in the cell body. The tubes are connected in series to the cooling circuit. The presence of metal tubes built into the cell body allows it to be cooled more evenly. As a cooler in the cooling circuit, a thermoelectric element (TV-71-1.0-1.3, Kryotherm, Russia) with a copper heat exchanger is used, to which a coil made of a 2 mm stainless steel tube is soldered, which is included in the cell cooling circuit. The reverse side of the Peltier element is cooled by a copper-aluminum radiator, which is blown by a fan. The Shenchen Lab V-1 peristaltic pump (Shenchen, China) is used as a pump in the

cooling system circuit (Figure 30 (pump 2). The flow rate in the cooling system is 2 ml/min. A 40% aqueous ethanol solution is used as the coolant in the cooling circuit, since pure water freezes in the heat exchanger when the flow cell is strongly cooled. A k-type thermocouple is installed in the main channel to control the temperature. The temperature is measured using a UNI-T UT325 thermometer (Uni Trend Group, China) connected to a PC.

An aerator is installed in the nutrient medium receiver to accelerate the exchange of gases between the nutrient medium and the gas receiver. The aerator pump constantly pumps gas through the gas receiver and delivers it to the aerator atomizer. To control the CO_2 content in the gas receiver, a sensor is installed, connected to the Hobbit-T-CO2 gas analyzer (Informanalitika Group, Russia). CO_2 is supplied to the gas receiver from a cylinder through a reducer and a throttle, which allow accurate dosing of gas in small quantities. The division of diatoms was monitored by installing a flow cell in an inverted fluorescent microscope NIB-FL (LOMO-Microsystems, St. Petersburg, Russia).

3.2.5   Monitoring of diatom concentration changes using photoacoustic imaging

Before measurements, *K. amoena* stock suspension was removed from the bottom of the plastic bottle and was diluted 1:2 seven times. A 0.1-g portion of agarose (Low type 1-B, A-0576, Sigma-Aldrich, Germany) was mixed with 10 ml of distilled water at 120 °C to obtain agarose gel. The concentration was determined with a hemocytometer (Goryaev's chamber). Different *K. amoena* concentrations (1080, 540, 270, 135, 67.5, 33.8 16.9, and 8.4 cells/µl) were mixed with agarose (3 µl of the suspension plus 7 µl of 1 % melted agarose). *K. amoena*-free agarose and *K. amoena*–agarose mixtures (in descending order

of dilutions) were pipetted into a petri dish that was subsequently filled with water and placed in the imaging chamber of an RSOM Explorer P50 setup (iThera Medical GmbH, Germany). The photoacoustic signal of the agarose-gel-embedded *K. amoena* was excited by a Wedge HB frequency-doubled flashlamp-pumped Nd:YAG laser (Bright Solutions, Pavia, Italy) at an excitation wavelength of 532 nm (repetition rate, 1–2 kHz; pulse energy, 200 μJ; pulse length, 2.5 ns). The agarose–diatom samples were scanned over an 11 × 11 × 2.5 mm field of view with a raster step size of 20 μm. The axial and lateral resolution capabilities of the RSOM system were 10 μm and 40 μm, respectively. Induced photoacoustic signals were detected with a custom-made spherically focused $LiNbO_3$ detector (center frequency, 50 MHz; bandwidth, 11–99 MHz; focal diameter, 3 mm; focal distance, 3 mm).[15,151]

3.2.6 *Setup for optical monitoring of diatom concentration changes*

An optical setup developed to monitor changes in algae concentrations is shown in Figure 31a-c.[150] A light emitting diode (LED) with a central wavelength of 505 nm was used as a light source. This wavelength was chosen to match the absorption maximum of carotenoids[152] presented in diatoms, such as fucoxanthin and beta-carotene[54]. The emission spectrum of LED is shown in Figure 31d. Emitted light was coupled in a multimode optical fiber with 105 μm core for spatial filtering then collimated by f=7.5 mm aspheric lens, passed through plastic cuvette with analyzed volume of algae suspended in nutrient medium and measured by a linear photodiode (PD) with preamplifier (OPT101P, Texas Instruments, USA). The data transfer between the optical system and the personal computer was performed using a microcontroller Arduino Nano. The LED and the photodiode were

powered by a 5V voltage source. The diameter of the probe light beam was 1.5 mm. The PD square shaped photosensitive area size was 1.7x1.7 mm. Discretization frequency for Arduino analog-to-digital converter (ADC) was set to 100 Hz. A python code was used to read the data from Arduino, and calculate mean value and standard deviation over 12000 measurements during 2 minutes. To avoid external illumination influence, the optical setup was covered with a non-transparent enclosure.
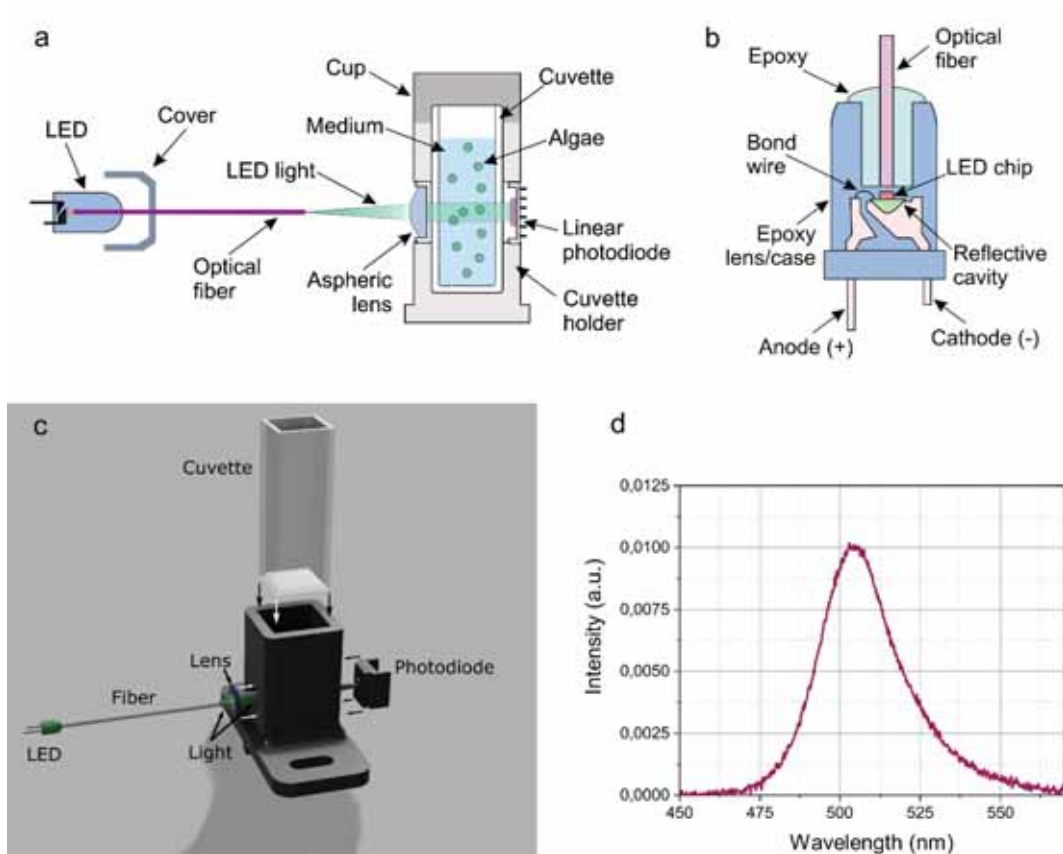
Figure 31. Experimental setup for monitoring changes in the diatom algae concentration. (a) Direct LED light coupling in multimode optical fiber. (b) Artistic representation of an optical system for measuring the transmission of algae in a nutrient medium depending on their fractional dilution. (c) Schematic representation of the

experimental setup key components for transmission measurements. (d) Emission spectrum of LED. [150]

LED illumination was coupled into an optical fiber by placing the end of the optical fiber to the LED light-emitting crystal at a distance of 200 µm. For this purpose, a 350 µm diameter hole was drilled in the LED transparent body under the optical control of a stereomicroscope ADF S645. An optical fiber was placed in the LED drilled hole and fixed using epoxy resin as shown on Figure 31b. The resulting output power of the LED light output of the collimating aspheric lens was 8.5 µW. Mounting elements of the optical system were produced by photopolymer printing approach.

To verify cell counting ability of the experimental setup, 7 diatom strains were examined.[150] For optical measurements, 1.5 mL of each strain were put into a plastic cuvette in the experimental setup. A custom python script was used to record light intensity values for 2 minutes, and, subsequently, average them over measurement time and calculate standard deviation. Then, for each strain the sample was diluted x1.154 times. This new sample was placed into the experimental setup, and new light intensity values were recorded. This procedure of dilution and measurement was repeated 11 times for each strain. The well-plate with the same 12 dilutions for each of 7 diatoms strains was placed into a spectrophotometer Tecan Infinite M Nano+ (Tecan Trading AG, Männedorf, Switzerland). For all the initial diatoms concentrations extinction and fluorescence spectra (the excitation wavelength was set to 430 nm) were measured. Then for each sample extinction value and fluorescence intensity were measured. Extinction was measured at the

wavelength of 505 nm. The fluorescence intensity was registered at 680 nm, when the excitation wavelength was set to 430 nm.

3.3 Cleaning of diatom cells from organic components

Purification of diatoms from organic material by chemical (acid) treatment consists of several stages. In the case of a marine culture in the initial medium, it is replaced with distilled water for 3 days, after which the cells are washed several times with distilled water to remove the remaining salts with centrifugation in a 5340 centrifuge (Eppendorf, Germany) (500 × g, 5 min). To remove a thick polysaccharide layer between the shell and the cell of freshwater diatom species, they were first washed 3 times in 6% sodium dodecyl sulfate (SDS) for 30 min at 95°C and successively washed with distilled water. The next step is boiling in concentrated nitric acid for 1-2 hours at 95°C. The boiling process can be repeated the next day by adding fresh nitric acid. After centrifugation (500×g, 5 min) and washing with distilled water at least 8 times, concentrated hydrochloric acid (36%) was added and left for 24 hours, followed by washing. Cleaned shells were stored in 50% ethanol to avoid bacterial growth and other possible contamination.

3.4 Characterization of the morphology and structure of diatoms

3.4.1 Scanning electron microscopy

A variety of scanning electron microscopes were used to image diatom samples over the course of 4 years, depending on the purpose and the need for high resolution images. To study diatom cultures before purification, as well as after acid treatment, a

scanning electron microscope TESCAN VEGA 3 (TESCAN ORSAY HOLDING, Brno, Czech Republic) was used. Samples were mounted on an aluminum holder using double-sided carbon tape and visualized without sputtering at 10 kV.

SEM images of *Coscinodiscus oculus-iridis* were acquired using a TESCAN CLARA (Brno, Czech Republic) electron microscope. Samples were mounted on a standard aluminum stub using carbon adhesive tape and visualized without sputter coating in a high vacuum at 1 keV landing energy and 30 pA beam current. The cross-sections of cleaned diatom samples were obtained by focused ion beam (FIB) under high vacuum in a TESCAN SOLARIS S9000 (TESCAN ORSAY HOLDING, Brno, Czech Republic) electron microscope.[1]

Scanning electron microscope (Quattro S, Thermo Fisher Scientific, USA) was used to investigate the appearance, morphology, and dimensions of *K. amoena* diatoms. Before SEM analysis, 20 μl of a stock suspension of *K. amoena* was deposited on a precleaned crystalline silicon substrate and three-stage drying in a vacuum oven (50 °C for 5 h, 80 °C for 3 h, and 100 °C for 1 h) was carried out to eliminate any organic components. Samples were analyzed without sputter coating at an accelerating voltage of 2.5–5 kV. [15] Such microscope was also used to examine the morphology of precleaned frustules of A. sibiricum at an accelerating voltage of 3 kV.[149]

FIB-SEM TESCAN SOLARIS S9000 (Tescan, Czech Republic) electron microscope was used to study the surface of *A. sibiricum* frustules at the energy of 1 keV with a Mid-Angle BSE detector.

3.4.2   Transmission electron microscopy

To describe the ultrastructure, the cells of several strains were fixed for transmission electron microscopy (TEM) with a mixture of 2.5% glutaraldehyde (Sigma-Aldrich, Germany) and 1% paraformaldehyde (Sigma-Aldrich, Germany) in the medium for 1 hour, then in solution 2.5% glutaraldehyde and 2% paraformaldehyde in phosphate buffer (0.1 M, pH 7.4) with the addition of tannic acid (Sigma-Aldrich, Germany) for 2.5 h. After that, the cells were washed with the same phosphate buffer and post-fixed in 1% osmium oxide solution (Sigma-Aldrich, Germany). The further procedure of dehydration and inclusion in the embedding medium was done as described previously[153]. Sections were obtained using a Diatome diamond knife (Germany) and stained with uranyl acetate and lead citrate. Sections were examined with a transmission electron microscope at an accelerating voltage of 80 kV. The micrographs were taken with a Mega View II Zeiss digital camera.

3.5 Visualization of living diatom cells

3.5.1   Optical microscopy

Diatoms were visualized and counted under the inverted luminescent microscope NIB-FL (LOMO-MA, Russia) using PH10x and PH40x objectives. Images were taken with an UltraHD-4k (35k/s) camera.

3.5.2   Confocal laser scanning microscopy

A. sibiricum diatoms were studied by confocal microscopy using Zeiss Axio Observer.Z1 inverted microscope with PlanApochromat 40×/1.3 Oil DIC (UV) VIS-IR M27 objective and confocal unit LSM 800 (Carl Zeiss Microscopy GmbH, Germany).[142]

The microscope is equipped with four solid-state lasers for illumination of the samples at 405, 488, 561, and 647 nm, three GaAsP PMT detectors, and one T-PMT detector for transmission light detection. Diatoms were imaged using Airyscan detector for higher resolution confocal scanning with appropriate filters. Before measurements, diatoms were stained with DAPI (4′,6 diamidino-2-phenylindole, Sigma Aldrich) to visualize nucle. Briefly, the diatom cells were fixed with 4 % formaldehyde for one hour and washed with 0.1 M phosphate buffer (pH 7.4) twice. The cells were collected by centrifugation at 2000 × g for 10 min, followed by DAPI (final concentration, 10 µg/mL) staining. Subsequently, the cells were rinsed twice with the phosphate buffer and mounted using Fluoromount Aqueous Mounting Medium (Sigma Aldrich). DAPI fluorescence was excited with a 405 nm laser, and the emission was registered in the 420-470 nm region. The images were obtained and processed with ZEN 2.3 imaging software.[142]

Laser scanning microscopy (LSM) was used to observe the DNA material of diatom cells and newly formed valves during division. To accomplish this task, *U. acus*, *N. graciliformis*, *Amphipleura* sp., *A. Formosa*, *C. oculus-iridis* were exposed to the vital dye PDMPO (Thermo Fisher Scientific, USA) or LysoTracker Yellow (Thermo Fisher Scientific, USA) at a concentration of 5 µg/ml for 1 day, after which they were fixed with a 4% solution of paraformaldehyde in phosphate buffer (0 .1 M, pH 7.4) for 1 hour, washed with phosphate buffer three times and, in the case of LysoTracker Yellow staining, additionally stained with DAPI (10 µg/ml, for 10 min). The cells were then embedded in Mowiol® 40-88 (Sigma-Aldrich, Germany) and examined using an LSM 710 laser scanning microscope (Zeiss, Germany). Chlorophyll autofluorescence was excited by a

laser with a wavelength of 561 nm and its radiation was recorded in the range of 650–723 nm. Fluorescence of Lysotracker Yellow H-123 was excited by a laser with a wavelength of 488 nm; its radiation was recorded in the range of 496-647 nm. DAPI fluorescence was excited by a laser with a wavelength of 405 nm; its emission was registered in the ranges of 410-492 nm. Fluorescence of PDMPO was excited by a laser with a wavelength of 405 nm, the radiation was recorded in the range of 441–587 nm. 3D reconstruction obtained from 100 optical sections (thickness along the z axis 14.3-50 μm).

3.5.3 Operetta High Content Imaging System

For fluorescent visualization, 100 μl of each diatom strain (*Asterionella formosa* – strain BZ 33, *Amphipleura* sp. – strain Ov 466, *Hannaea baicalensis* – strain BK 479, *Ulnaria acus* – strain 15k 595, *Biddulphiopsis titiana* - strain 0.0212-OH, *Coscinodiscus oculus-iridis* - strain 0.1211-OD, *Coscinodiscus* sp. - strain 21.0407-OA) was placed in the individual well of 96-well plate (CellCarrier Ultra, PerkinElmer, USA) and imaged with a x20 and x60 magnification objectives using the Operetta High Content Imaging System (Perkin Elmer, USA) in the fluorescence mode. The chlorophyll autofluorescence was excited at 410-430 nm, while the emission was registered at 650-700 nm. The obtained images were processed using Harmony 4.1 software (Perkin Elmer, USA).[150]

3.5.4 Fluorescence lifetime imaging microscopy (FLIM)

Fluorescence lifetime imaging microscopy (FLIM) measurements of diatoms and image processing were done using a MicroTime 200 STED microscope (PicoQuant GmBH, Germany), a 402- and 638-nm laser as the excitation source, and a 690-nm bandpass filter. Measurements were carried out at a pulse rate of 40 MHz, a pulse duration

of 40 ps, and a maximum power of 50 µW. Fluorescence lifetime images were acquired in the time domain. The laser beam was focused on diatom cells with a 100 × 1.4 NA oil immersion objective (UplanSApo, Olympus, Japan). According to the dwell time of 0.2 ms with a pixel size of 0.200 µm/px, the total image acquisition time was 40 s for an image size of 400 × 400 pixels—i.e. 80 × 80 µm.[15]

3.6 Study of mechanical properties of diatoms

3.6.1 Preparation of samples for SEM nanoindentation and AFM

Cleaned diatom frustules and air-dried living cells were prepared for AFM and in situ SEM nanoindentation measurements.[1] Purification of diatoms from organic material consists of several stages. For the purpose of bacterial destruction of organic matter, the medium was first filled with distilled water and left for 3 days. After that it was washed with DI water several times to remove the remaining salts by centrifugation using the Centrifuge 5340 (Eppendorf, Germany) (500 × g, 5 min). After removing salt, the cell suspension was boiled in concentrated nitric acid for 2-3 hours. The boiling process was repeated the next day adding fresh nitric acid. The suspension was subsequently centrifuged (500 × g, 5 min) and rinsed with DI water at least 8 times. The cleaned frustule suspension was pipetted onto a silicon wafer and air-dried for further measurements. Air-dried living diatom cells containing cellular material were also placed on a silicon wafer and used for in situ SEM nanoindentation. A vial with live diatoms in water was transferred into the AFM glovebox. A drop of water with diatoms was placed on a silicon substrate. After water evaporation the live diatom cells were measured using the AFM. The diatom

samples were imaged with intact and separated frustules or the so-called valves. Separated frustules settled on the substrate exposing their interior concave surface and exterior convex surface.

3.6.2   AFM measurements

AFM measurements were performed using Cypher ES microscope (Asylum Research, Oxford Instruments) installed inside an Ar filled glove box (MBraun). Topography was measured in a tapping mode using a single crystal diamond probe with 147 kHz first resonance frequency and 3.5 N/m spring constant. Nanomechanical properties were measured in the AM-FM viscoelastic mapping mode and by force-distance curve acquisition using stiff (DRP_IN purchased from TipsNano, Estonia, k=400 N/m, Fres=750 kHz) and soft (HA_NC/FD purchased from TipsNano, Estonia, k=3.5 N/m, Fres=147 kHz) single crystal diamond probes. Nanoindentation was performed on the concave surface of a separated frustule using the stiff (k=400 N/m) diamond probe. All AFM probes were calibrated on a TGT1 test grating in order to measure radius of curvature of the tip apex and on a fused silica reference sample in order to test models for fitting experimental data. The stiff probe was additionally calibrated on a diamond coated silicon wafer in order to get accurate values of the displacement and spring constant. The DMT model was implemented for data fitting and analysis. Force-distance curves on the inner surface of the cleaned frustule and on the wet diatom cell were acquired by the stiff diamond probe (k=400 N/m) under the maximum force load of 8 µN. Force-distance curves on the outer surface of the cleaned frustule were obtained by the soft diamond probe (k=3.5 N/m) under the maximum force load of 100 nN because the cleaned cribrum is brittle and

often breaks when measured by the stiff probe. Besides, the outer surface bends as a membrane under the stiff probe. Image processing and analysis was performed using Gwyddion software.[1]

3.6.3   In situ SEM nanoindentation

The Alemnis Standard Assembly (ASA) indentation platform (Alemnis, Gwatt, Switzerland) was used to perform in situ nanoindentation testing of cleaned frustules and air-dried living diatom cells placed on silicon wafer inside the chamber of a TESCAN SOLARIS S9000 SEM (TESCAN ORSAY HOLDING, Brno, Czech Republic). In the current work, the ASA tester was equipped with a flatpunch conductive diamond indenter with the diameter of 2.5 μm on the cutting edge and 60° cone angle. The experiment implied synchronization of two parallel processes like SEM images acquisition and indentation test. In order to achieve the best SEM resolution considering design limitations of the devices, ASA platform was tilted on 20° and moved to the working distance of ~7 mm. The SEM images were recorded under the following conditions: high voltage of 5 kV, beam current of 1 nA, spot size of 15 nm, pixel size of 40 nm and recording speed of 0.5 fps. The nanoindentation testing was done in both static and dynamic modes. The static mode was done under the regime of the linear depth control where the test consisted of three stages as indenter approach, holding and indenter retraction. The dynamic mode included a sinusoidal signal instead of a holding stage. The penetration depth was estimated for each diatom cell height before the test.[1]

3.7 Study of resonant frequencies of diatoms

3.7.1   Numerical simulation using COMSOL Multiphysics

In silico calculations were done with COMSOL Multiphysics by the finite-element method. The geometrical dimensions of the computational model were taken from the corresponding SEM images of the diatom. For evaluation of vibrational eigenfrequencies, the COMSOL Multiphysics Structural Mechanics module was used. The density and Poisson ratio of the silica were described previously[137]. The Young's modulus value was obtained in our study on the mechanical properties[1]. All these values are shown in Table 6. Fixed boundary conditions were applied to the lower part of the diatom.

3.7.2   AFM measurements

Before AFM measurements, cleaned diatom frustules were prepared according to the procedure described in the section 3.3. After that, a drop of a cleaned frustule suspension was applied to a precleaned silicon wafer. The transfer of diatom frustule from a silicon substrate to an AFM chip was carried out using a nanomanipulator inside the chamber of a TESCAN Solaris microscope. Individual frustules were subsequently welded to the chip using FIB to ensure that they would not come off the surface during measurements and gold-sputtered using magnetron sputtering machine Quorum Q150R ES (Quorum, England) at sputter current 25 mA. AFM measurements were performed using Cypher ES microscope (Asylum Research, Oxford Instruments) installed inside an Ar filled glove box (MBraun). Measurements were performed by collecting thermal spectra with the subsequent FFT analysis and by mechanical excitation followed by detection via a lock-in amplifier. The thermal spectra measurements (without piezodriver swing) are

used to search for natural frequencies and calibrate the stiffness and amplitude of the AFM probes to avoid spurious frequencies. Image processing and analysis was performed using Gwyddion software.

3.8 Study of optical properties of diatoms

3.8.1 Numerical simulations using Fourier modal method

In numerical simulations, the shell is approximated by a periodic structure constituting a multidimensional array of pores in a silica matrix. To calculate the near-field field distribution of the transmitted wave, a Fourier modal method (FMM) in the scattering matrix form was used[154]. The formalism of the FMM includes splitting the periodic structure into elementary planar layers, homogeneous in Z direction. The solutions to Maxwell's equations for each layer are found by expansion of the electric and magnetic fields into Floquet-Fourier harmonics. In these numerical simulations the Fourier series is truncated on 97 harmonics.

3.8.2 Absorbance spectroscopy of individual diatoms

To measure UV-VIS steady-state absorption spectra of individual living diatom cells and cleaned frustules and kinetics of transitions induced by actinic light, a combined system consisting of a stabilized deuterium UV light source SLS204 and a stabilized tungsten-halogen lamp SLS201L/M (Thorlabs, USA) coupled to CCD detectors Flame and Maya2000Pro (Ocean Insight, USA) was used.

3.8.3 Chloroplast distribution study using FLIM

Fluorescence lifetime imaging was also performed in the time-correlated single-photon-counting (TCSPC) mode using the confocal system DCS-120 (Becker&Hickl,

Berlin, Germany) installed on the Eclipse Ti2 (Nikon, Tokyo, Japan) microscope. Excitation was performed with a 473 nm picosecond laser BDS-SM-473-LS-101 (Becker&Hickl, Berlin, Germany) with a 30 ps duration impulse driven at 50 MHz repetition rate synchronized with hybrid detector HMP-100-40 (Becker&Hickl, Berlin, Germany) via board SPC-150 (Becker&Hickl, Berlin, Germany).

3.9 Modification of diatomite with gold nanoparticles

3.9.1 Gold nanoparticle synthesis

Gold nanoparticles were synthesized by standard citrate synthesis. 88 μL of 1 M HAuCl$_4$ aqueous solution was diluted to 50 mL by deionized water and heated up to boiling. While boiling, 8.9 mL of 1% sodium citrate tribasic dihydrate was added. The resulting solution (concentration, 2×10^{12} particles/mL) was stirred at boiling temperature for 1 h, then slowly cooled, and stored in the fridge at +4 °C. Gold nanoparticle size and zeta potential were characterized by ZetaSizer Nano ZS analyzer (Malvern Panalytical, Malvern, UK), extinction spectrum was collected by Infinite M Nano+ (Tecan Trading AG, Switzerland).[83]

3.9.2 Fabrication of gold-coated diatomite

Before modification, diatomite powder was washed with DI water two times. A standard LbL procedure consists of depositing alternating layers of oppositely charged materials with washing steps in between. Firstly, 20 mg of negatively charged diatomite were suspended in positively charged polyallylamine hydrochloride (PAH) solution (2 mL; 0.1% PAH in 0.15 M sodium chloride), followed by agitation in a vortex for 15 min. After

this standard adsorption procedure, the samples were washed three times with DI by centrifugation using the Centrifuge 5340 (Eppendorf, Germany) (664 × g, 3 min). Gold nanoparticles were subsequently deposited onto the PAH-coated diatomite using FIL approach. Namely, 2 mL of gold nanoparticle solution (10^{12} particles/mL) were added, and the mixture was placed in a freezer (−20°C) in a continuously rotating flask for 2 h. After the water was completely frozen, the samples were thawed at room temperature, centrifuged at 664 × g for 3 min, and washed at least three times with DI water, resulting in the formation of a bilayer consisting of a polyelectrolyte/nanoparticle composite. Depending on the sample, the cycle was repeated up to five times to obtain a multilayered composite structure. The resulting composites were stored in water. [83]

3.9.3   Zeta potential measurements

Zeta-potential measurements of gold-coated diatomite[83] were performed upon deposition of each layer using ZetaSizer Nano ZS analyzer (Malvern Panalytical, Malvern, UK). All samples were diluted in DI water and placed in the U-cuvette. Measurements were carried out at 25 °C and repeated three times.

3.9.4   SEM study of prepared samples

Diatomite modified by gold nanoparticles was imaged with FIB-SEM TESCAN SOLARIS S9000 (Tescan, Czech Republic) under a high vacuum at 5 keV landing energy, 300 pA beam current and with registration of the signal using a backscattered electron detector. Samples were analyzed without applying a conductive coating.[83]

3.9.5 TEM and EDX measurements

Bright field TEM (BF-TEM) images, high angle annular darkfield scanning transmission electron microscopy (HAADF-STEM) images, and energy-dispersive X-ray (EDX) spectra and compositional maps were acquired in STEM-mode on an aberration corrected FEI Titan Themis Z (ThermoFisherScientific, Breda, Netherlands) transmission electron microscope equipped with a Super-X detection system and operated at 120 kV. Specimens were prepared by depositing a drop of gold-coated diatomite solution onto a holey copper grid with a carbon/lacey supporting layer and letting them dry in the air followed by transferring into TEM columns.[83]

3.9.6 Photoacoustic visualization of gold-coated diatomite

The photoacoustic signals from the gold-coated diatomite composites were obtained using RSOM setup Explorer P50 (iTheraMedical GmbH, Germany) as described in the section 3.2.5. For the purpose of imaging, we performed a 2-fold serial dilution of stock suspensions of gold-coated diatomite 5 times. 3 µl of these suspensions were mixed with melted agarose gel (7 µl), which was previously obtained by dissolving 0.1-g portion of agarose in 10 ml of distilled water at 90°C. 4-µl droplets containing different concentrations of these mixtures were pipetted into a petri dish that was filled with DI water after solidification and placed in the imaging chamber. The photoacoustic signal was collected upon illumination with 532-nm laser.[83]

3.9.7 SERS measurements of gold-coated diatomite

For SERS measurements[83], diluted suspensions of gold-coated diatomite consisting of one (Diatomite-$(PAH/Au)_1$), three (Diatomite-$(PAH/Au)_3$), and five (Diatomite-

(PAH/Au)$_5$) bilayers were mixed with 0.2 mM Rhodamine 6G in an equal volume and left overnight. The Raman spectra from liquid droplets pipetted onto the quartz glass were collected by a confocal Raman spectrometer upon excitation with 633 nm He-Ne laser. A grating with 600 grooves/mm was used throughout. Spectra were registered in the Raman-shift range 600–1700 cm^{-1} at laser power 6.1 mW with 20 s acquisition time and averaged on 10 accumulations. Baseline correction was provided by instrument-embedded software (LabSpec6, HORIBA France SAS, France) after the signal acquisition.

Chapter 4. Monitoring and characterization of diatom colonies

This chapter introduces novel methods for monitoring and characterization of diverse diatom cultures throughout their extended cultivation within controlled laboratory environments. The most of the results presented here are part of the following published articles: **Cvjetinovic J**, et al [15]. *Photoacoustics*, 2020, 18; 10017; **Cvjetinovic J**, et al.[150] *Journal of Biomedical Photonics and Engineering*, 2023, 9(1):1-9; **Cvjetinovic J**, et al.[141] *Journal of Physics: Conference Series*, 2022, 2172; 012011; **Cvjetinovic J**, et al.[149] *Journal of Physics: Conference Series*. 2021, 1984; 012017; **Cvjetinovic J**, et al.[142] *SPIE Proceedings*, 2021, 11641; 116410G.

4.1 Background

Monitoring the growth of diatoms during cultivation is crucial for optimizing their growth conditions and achieving high biomass production. Several techniques can be used to monitor the growth of diatoms during cultivation, such as optical density, dry weight, chlorophyll concentration, and cell counting.

1. Optical density measurements: Optical density (OD) measurement is a rapid and non-destructive method of measuring the biomass concentration of diatoms.[155] This method measures the amount of light scattered or absorbed by the cells in a culture using a spectrophotometer which can be related directly to cell mass or cell number. As the cell concentration increases, the OD increases proportionally, allowing for real-time

monitoring of the culture growth. However, this method does not provide information about the cell size and morphology of the diatoms.

2. Dry weight measurement: Dry weight measurement is a destructive method that estimates the biomass concentration of diatoms by weighing the dried cell pellets. This method is accurate and provides information about the cell size and morphology of the diatoms, but it requires the destruction of the entire cell culture and is time-consuming.[156]

3. Chlorophyll concentration measurement: Chlorophyll concentration measurement is a reliable method for monitoring the growth of photosynthetic diatoms, as it reflects the photosynthetic activity of the cells. This method involves the extraction of chlorophyll from the cells using organic solvents and subsequent measurement of the chlorophyll concentration using a spectrophotometer. However, this method does not provide information about the cell count or cell size of the diatoms.[157]

4. Cell counting: Cell counting is a direct and accurate method of measuring the concentration of diatoms in a culture. This method involves the use of a microscope and a hemocytometer to count the number of cells in a given volume of the culture. Cell counting provides information about the cell size, morphology, and viability of the diatoms. However, it is a time-consuming and labor-intensive method.[158,159]

Each of the above-mentioned methods has its advantages and limitations. Since microalgal cells are usually dispersed in the medium, estimating their biomass remains difficult. It is therefore impossible to perform direct gravimetric measurements due to the concentration of cells required. OD (turbidity) and chlorophyll fluorescence indirectly estimate microalgal biomass, but are susceptible to faulty measurements caused by light-

cell interference. Depending on the application and the specific requirements, one or more of these methods can be used to optimize the growth conditions of diatoms and achieve high biomass production.[157–159]

We suggested another approach to monitoring of the growth using optical methods and commercially available setup. Optical methods can be used for monitoring the growth of diatoms, and two notable techniques are photoacoustic (optoacoustic) imaging and fluorescence-based methods.[141,142]

1. Photoacoustic imaging: Photoacoustic visualization is non-invasive, high-resolution imaging technique that utilizes laser light to produce acoustic waves within the sample, which can be detected by ultrasound transducers[160]. It is readily used to collect meaningful acoustic signals from complex biological objects with unprecedented spatial accuracy of detection of their components containing light-absorbing molecules. The excitation of hierarchically finer scale objects—light-absorbing chromophore molecules (melanin, hemoglobin, water, lipid, etc.)—ultimately converts to the vibrations of much bigger, hierarchically larger-scale objects such as cell organelles (e.g., melanosomes) or whole cells (erythrocytes)[161,162]. The flow of energy across hierarchical levels of organization is associated with the changes in the underlying physical phenomena according to size and scale effects[163]. The frequencies of these vibrations, recorded owing to the optically driven acoustic signal, range from 1 MHz to 100 MHz, which is of the same order of magnitude as the eigenfrequencies of capsular mechanical objects having sub- and micrometer sizes[164]. Very limited data[165,166] are available on the photoacoustic studies of single-cell organisms—both prokaryotes (e.g., cyanobacteria) and eukaryotes (e.g.,

diatoms)—which contain light-absorbing chromophores such as chlorophyll or carotenoids. The photoacoustic visualization of such living objects may have a number of ecological, biotechnological, and biomedical applications, such as the remote and rapid control over microbial cultures and media, cell studies, sanitary control, and aquaculture. The photoacoustic technique is very interesting from the standpoint of observations on diatoms in their natural environments and also during culturing. It is potentially possible to install photoacoustic tools in vessels or in harbor constructions that are used to monitor diatoms in aquatic environments. Owing to laser irradiation and subsequent absorption of light by the diatom chromophores, the photoacoustic method is promising for studying the activity of these objects in their natural environments, as well as for monitoring their growth in bioreactors or aquaculture installations by means of the imaging of colonies.

2. Fluorescence-based methods: Fluorescence imaging and spectroscopy are highly sensitive techniques that have been widely used to monitor phytoplankton. Two types of light-harvesting pigments of diatoms are well documented[54,167,168]: chlorophylls and carotenoids. The predominant form of chlorophyll observed in diatoms is chlorophyll a, which absorbs energy in the violet-blue and orange-red regions[54,167,169]. Unlike many other types of algae, diatoms also contain chlorophyll c, which absorbs mostly blue and red light[54]. The main carotenoid identified in diatoms is fucoxanthin, which absorbs light in the blue-to-green region of the spectrum[54,167,168]. Therefore, fluorescence-based methods can be used to monitor the chlorophyll content and the growth of diatoms.[158] For example, by measuring the fluorescence intensity emitted by the chlorophyll in a culture using a fluorometer, the chlorophyll concentration and the growth rate of the diatoms can be

estimated. Fluorescence-based methods are non-destructive, fast, and sensitive, and can be used to monitor the growth of diatoms in real-time.

However, it is noteworthy that the accuracy of both methods can be affected by the density and size of the diatom population, as well as by experimental factors such as temperature and light intensity. The results on optical monitoring of diatom growth are presented separately based on the division of the cultures by natural environment and form: freshwater pennate and marine centric diatoms.

4.2 Monitoring of freshwater pennate diatoms

A. sibiricum diatoms isolated from the Baikal Lake were cultivated over 70 days in the incubator (Figure 32) and monitored using raster scanning optoacoustic mesoscopy (RSOM) approach and IVIS SpectrumCT In vivo Imaging system. To gain a better understanding of the state of diatoms during cultivation and their growth phase, we also carried out absorbance and fluorescence spectroscopy measurements in parallel with photoacoustic and fluorescence imaging. This set of monitoring techniques, as believed, will be further widely used elsewhere in aquaculture and incubator practice to facilitate the harvesting of diatom algae and diatom-derived bioactive substances for pharmaceutical and biomedical purposes.
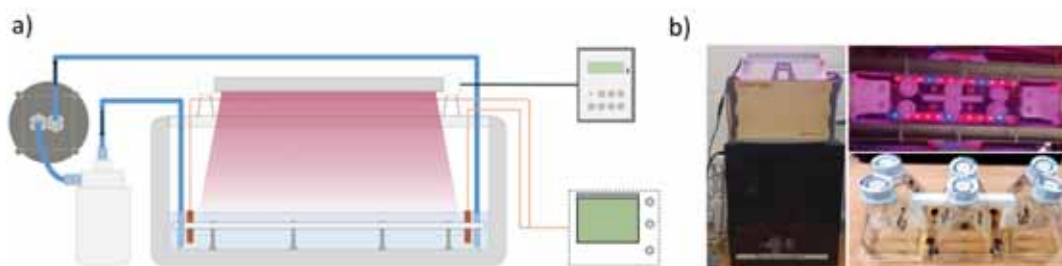
Figure 32. a) A scheme of incubator, b) photo of incubator and cell culture flasks with diatoms.[149]

A. sibiricum are monoraphid pennate diatoms with bilateral symmetry, whose raphe is present only on one valve of the frustule, as shown in Figure 33a. Valves are dorsiventral, with rounded apices. Their length ranges from 9.8 to 18.7 μm, while the width is 4.5–6.0 μm. Distal raphe ends are curved toward the ventral margin.
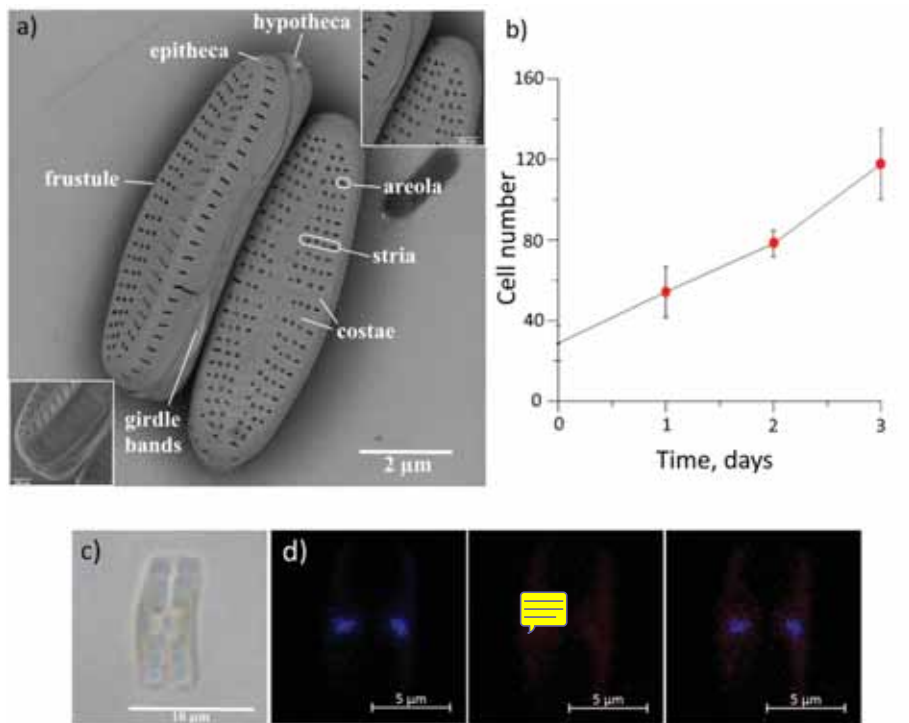
Figure 33. A. sibiricum: a) SEM image, b) culture growth during three days after inoculation, c) light image, d) confocal images of: cells fixed formaldexyde and stained with DAPI (blue, nucleus; red, chlorophyll).[142]

The growth kinetics of a periodic culture of diatoms is very similar to the growth kinetics of prokaryotic organisms[170]. In this case, the lag phase and the onset of the

exponential growth of the culture were observed by cultivating diatoms in microvolumes. Cell counting during the first four days of cultivation showed a steady growth of the culture (Figure 33b). After four days of culture, counting was difficult due to the formation of cell clusters. Light microscopy image of *A. sibiricum* is shown in Figure 33c. During the first days of culturing, we employed confocal laser microscopy to observe the DNA material of DAPI-labeled cells (Figure 33d). Nuclei, located in the center of the cells, had an oval shape (Figure 33d). The red fluorescence of the chloroplasts was excited with 647 nm wavelength. Chloroplasts occupy most of the cells, which is also confirmed by light images. The state of chloroplasts and cell division indicate the viability of the culture.

Further growth was more accurately controlled by other proposed methods—fluorescence visualization using IVIS imaging system and photoacoustic measurements with RSOM setup. Since the studied species are benthic (that is, they live on substrates [171]), and capable of secreting a lot of mucus and forming cell clusters[172], the main difficulty in counting cells in microvolume in a well-plate is the impossibility of selecting adequate aliquots and plotting growth curves with sufficiently large technical errors. The proposed methods for assessing chlorophyll, which do not require the extraction of cells from the medium, increase the accuracy of experiments.

The results of fluorescence visualization of *A. sibiricum* in cell culture flasks during 100 days of cultivation using IVIS SpectrumCT imaging system are shown in Figure 34a, b.
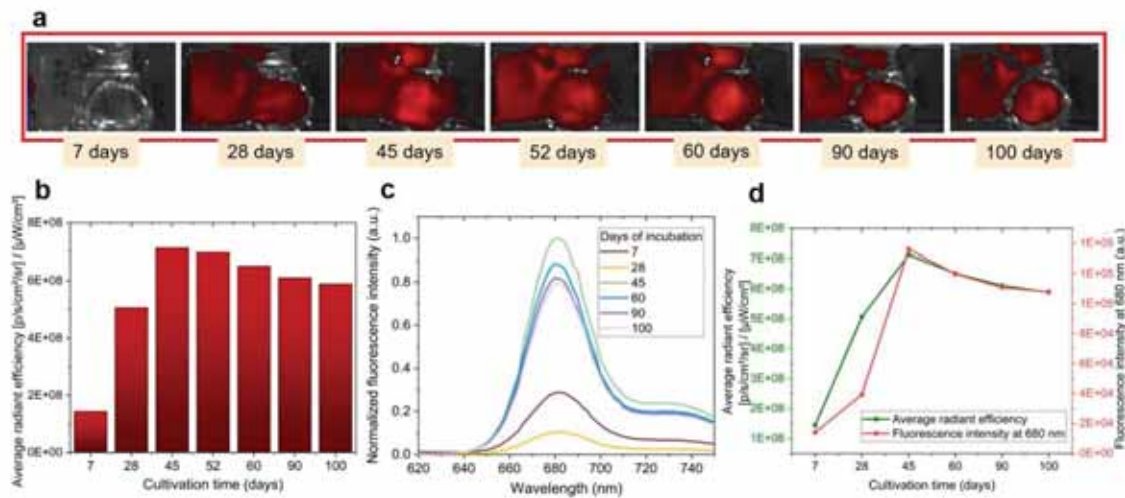
Figure 34. (a) Images of cell culture flasks containing diatoms obtained using the IVIS platform (top view), (b) The average radiant efficiency of diatoms during the cultivation period, (c) Normalized fluorescence spectra of *A. sibiricum* cells, (d) Comparison of fluorescence intensity at 680 nm and average radiant efficiency depending on the cultivation time. [141]

The average radiant efficiency increases with increasing incubation time up to 45 days, followed by a steady decrease. The result indicates that the cell division is slowed down after 45 days, probably due to the lack of necessary nutrients, since batch cultivation implies that nutrients are provided only at the beginning without further addition. However, during 100 days of monitoring, we couldn't observe the final death phase. The fluorescence spectra collected during the cultivation demonstrate an emission band, which is attributable to chlorophyll a (Figure 34c). We also compared the fluorescence intensity at 680 nm and IVIS imaging results. According to Figure 34d, the maximum values were obtained after 45 days of incubation, which corresponds well with the results obtained with the IVIS. By

using this technique, the growth of diatoms can be evaluated very quickly, without preliminary sample preparation, which would affect the integrity of the cells and sterility flask with culture.

Diatoms exhibit strong photoacoustic signals owing to the presence of chlorophylls and carotenoids that absorb very well the 532 nm wavelength upon illumination[15]. Figure 35a shows the images of diatom-agarose droplets obtained after 7, 28, 45, 60, 90, and 100 days of cultivation using the RSOM system. The dependence of the mean pixel intensity signal on the incubation time is illustrated in Figure 35b, where red color corresponds to a low-frequency signal emitted by larger samples. In contrast, a high- frequency signal, shown with green bars, is emitted by smaller structures. The highest intensity of the photoacoustic response was achieved after 45 days of cultivation. Before mixing with agarose, cells in DM medium have to be properly shaken. However, we can observe that this diatom species tends to aggregate due to secreted mucilage, which explains why the red signal at 11-33 MHz is higher. The absorbance spectra shown in Figure 35c demonstrate peaks attributable to chlorophyll a and c and the carotenoid fucoxanthin. By comparing the absorbance and photoacoustic signals in two frequency ranges (Figure 35d), we can conclude that they are in good agreement. Thus, the spectroscopic characterization confirmed the results obtained using the IVIS and RSOM imaging systems and proved their capabilities in assessing the growth of diatoms.
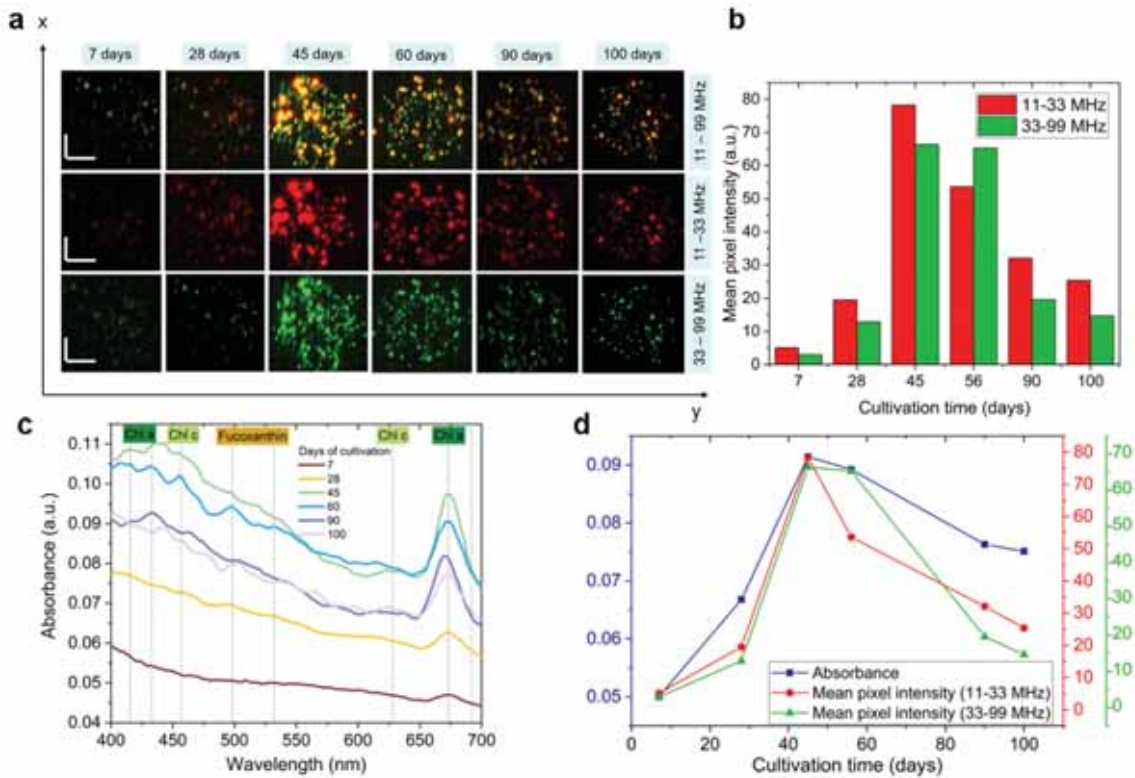
Figure 35. (a) RSOM images of *A. sibiricum* diatoms mixed with agarose gel at 11-99 MHz, 11-33 MHz (red), 33-99 MHz (green) after 7, 28, 45, 60, 90, and 100 days of cultivation. Scale bar: x, y-axis – 0.5 mm. (b) The dependence of mean pixel intensity on the cultivation time, (c) Absorbance spectra collected at different periods of cultivation, (d) Comparison of absorbance at 523 nm and mean pixel intensities at 11-33 MHz and 33-99 MHz depending on the cultivation time. [141]

4.3 Monitoring of the growth of marine centric diatoms

The same techniques were employed for monitoring of the growth of marine centric diatoms, which were cultivated on the windowsill, as described in Materials and methods

section: *Coscinodiscus* sp. (strain 21.0407-OA) and *B. titiana* (strain 0.0212-OH) (Figure 36a,b, respectively). IVIS results are shown in Figure 36c, d.
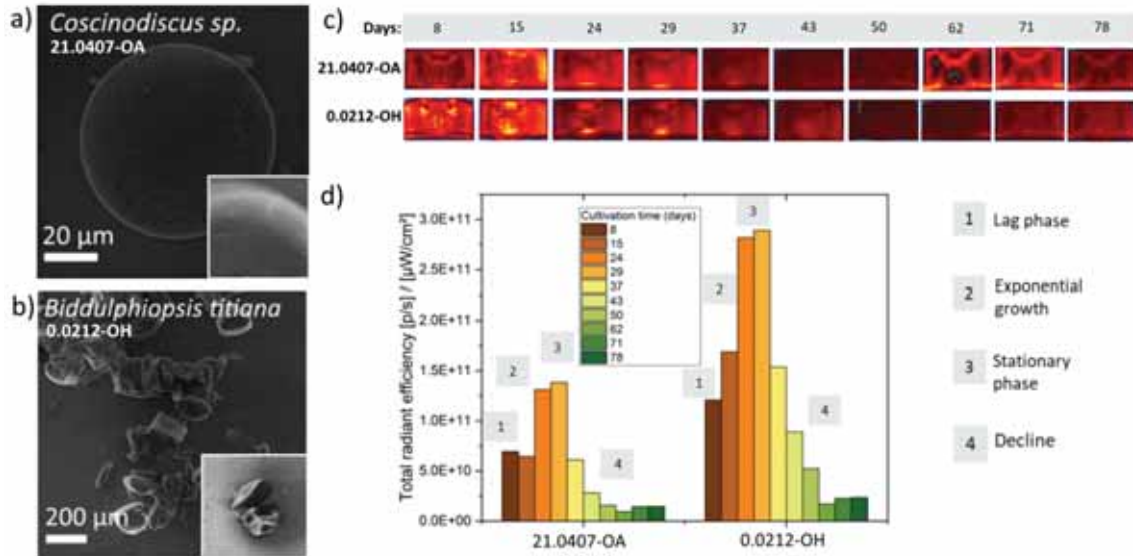
Figure 36. SEM images of: a) *Coscinodiscus* sp. (21.0407-OA), b) *B. titiana* (0.0212-OH). c) Images obtained using IVIS imaging system, d) Total radiant efficiency depending on the cultivation time of both strains.

The total radiant efficiency in both cases increases with increasing cultivation time up to 30 days, followed by a decrease in intensity (Figure 36b, c). The result indicates that the cells, after slow division, begin to die. One of the reasons for inhibition of cell growth and death is the lack of essential nutrients, as nutrients are provided only at the beginning. In addition, the passing of the mitotic cell cycle is inhibited by the products of cell metabolism that accumulate in the "old" culture.

The fluorescence spectra obtained during cultivation show an emission band that is attributed to chlorophyll *a* (Figure 37a, c). A comparison was also made between the fluorescence intensity at 680 nm and IVIS imaging results (Figure 37b, d). According to Figure 37b, d the maximum values were obtained after 30 days of incubation, which is in good agreement with the results obtained using the IVIS system.
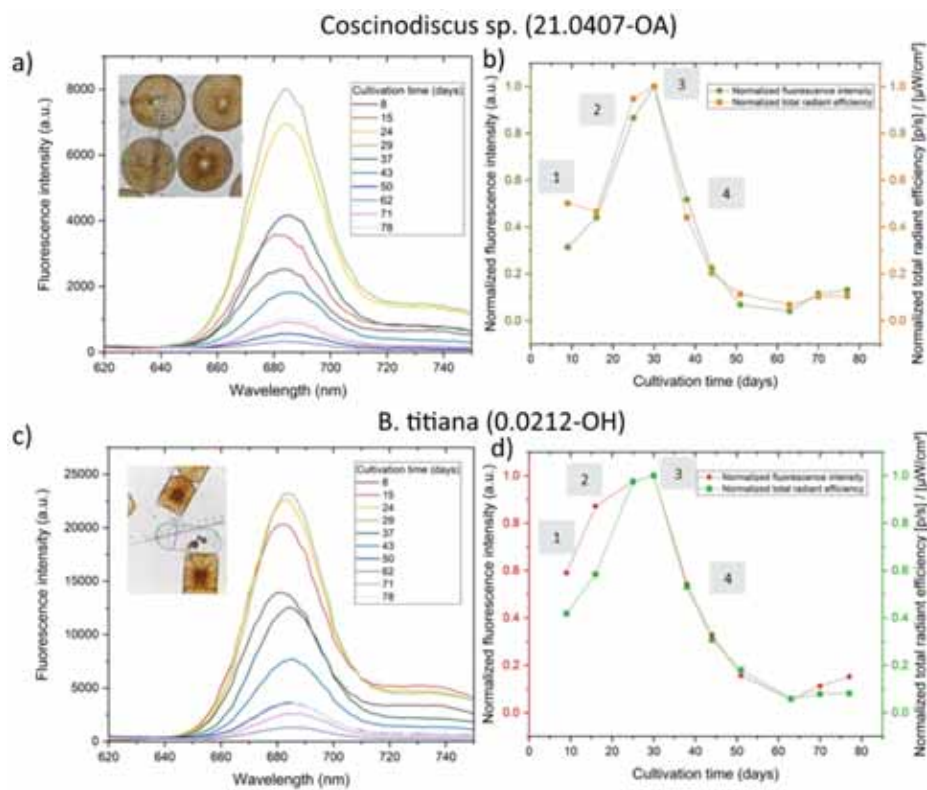
Figure 37. Fluorescence spectra of: a) *Coscinodiscus* sp., c) *B. titiana*. Comparison of normalized fluorescence intensity at 680 nm and normalized total radiant efficiency depending on the cultivation time of: b) *Coscinodiscus* sp., d) *B. titiana*. 1-lag phase, 2-exponential growth, 3-stationary phase, 4-decline.

To monitor the growth of diatoms using RSOM, cultures of *C. oculus-iridis* (strain 0.1211-OD), *Coscinodiscus* sp. (strain 21.0407-OA), *B. titiana* (strain 0.0212-OH) and *U. acus* (strain 15k 595) were mixed with agarose gel and measured on days 7, 15, 25 and 32 of cultivation, as described in the Materials and Methods section. The resulting images are shown in Figure 38.

Using the RSOM system, an optoacoustic signal from diatoms was successfully obtained (Figure 38a), excited by a laser with a wavelength of 532 nm. The dependence of the average pixel intensity signal on the cultivation time is shown in Figure 36b for each species. The red color in the figures indicates a low frequency signal obtained from the reconstruction in the frequency range 11-33 MHz and corresponds to larger samples. On the other hand, the high frequency signal in the 33-99 MHz frequency range, shown in green, comes from smaller samples. The signal intensity increases with cultivation time, reaching a maximum value after 32 days of cultivation for all cases except for strain 21.0407-OA, where the maximum is reached after 25 days. Typically, the signal in the 11-33 MHz frequency range, which occurs from larger samples, is more intense, which may also indicate possible cell aggregation and insufficient mixing of the suspension. Insufficient agitation could also result in a stronger signal in the 33-99 MHz frequency range for strain 21.0407-OA after 25 days of cultivation. The most intense signal comes from the largest species, *B. titiana*. In this case, the resolution of the microscope is large enough to receive a signal from one cell.
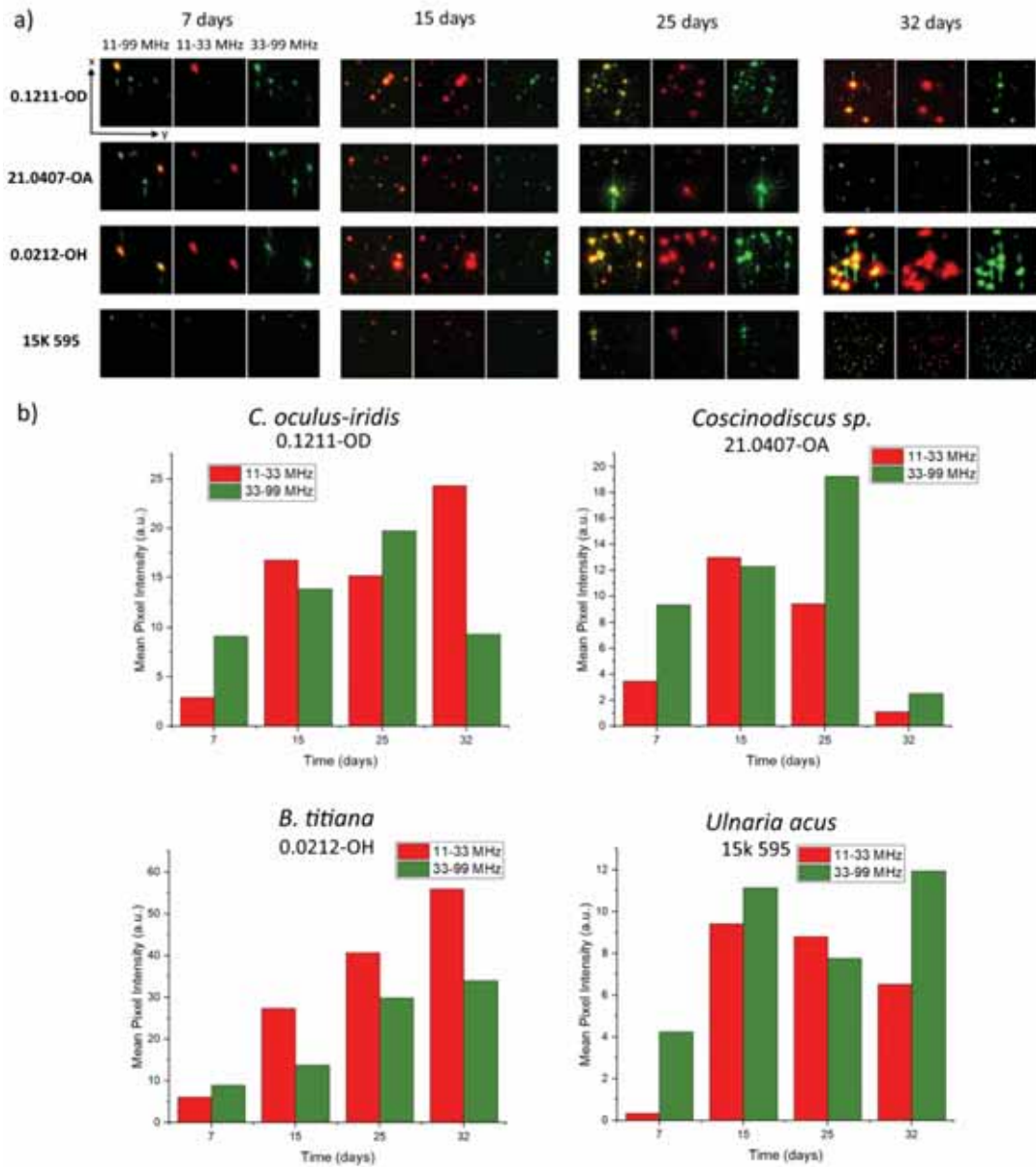
Figure 38. a) RSOM images of 4 different cultures obtained during 32 days of cultivation, b) Mean pixel intensity vs. cultivation time for all strains.

Monitoring of the growth of three different diatom species (*Coscinodiscus* sp., strain 21.0407-OA; *B. titiana*, strain 0.0212-OH, *U. acus*, strain 15k 595) was also carried

out using the spectrophotometric method. The absorption spectra obtained during long-term cultivation of diatoms are shown in Figure 39a-c. In addition, graphs of the time-dependence of the absorption of the main pigments (chlorophyll *a*, fucoxanthin, chlorophyll *c*), normalized to the maximum, were plotted (Figure 39d-f).
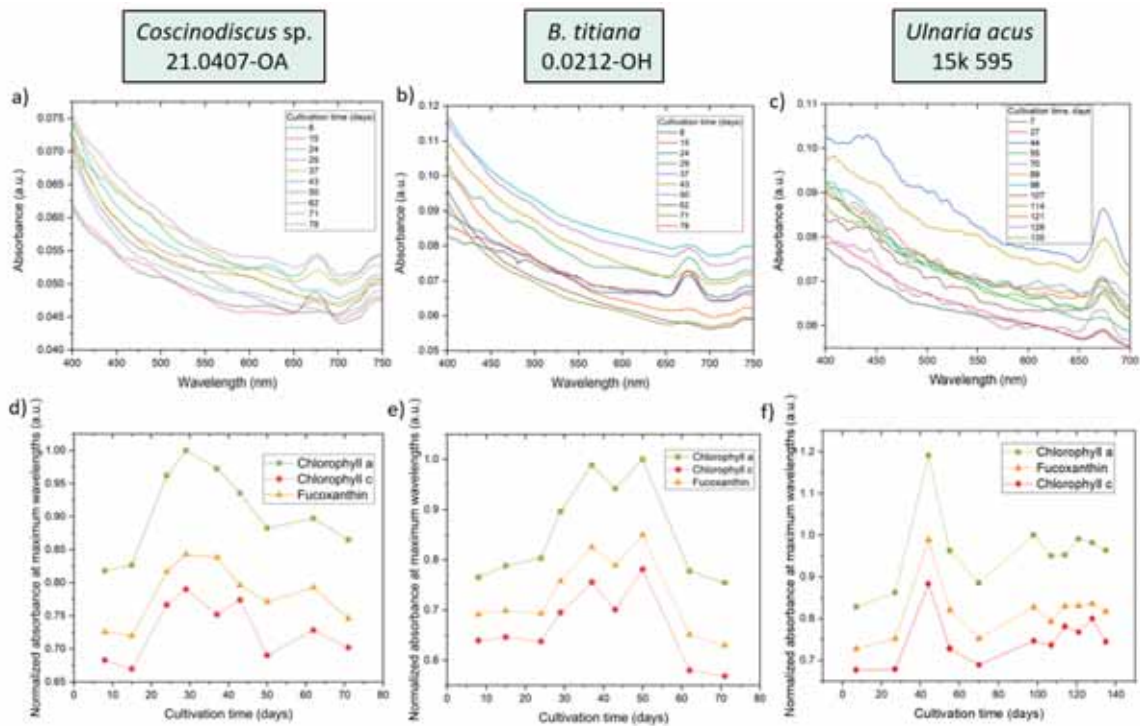
Figure 39. Absorbance spectra of: a) *Coscinodiscus* sp., b) *B. titiana*, c) *Ulnaria acus*. Normalized absorbance at maximum wavelengths of: d) *Coscinodiscus* sp., e) *B. titiana*, f) *Ulnaria acus*.

The obtained spectra correlate well with the optoacoustic measurements carried out during 32 days of cultivation. Maximum values are observed after 30 days in the case of marine species *Coscinodiscus* sp. and *B. titiana* (Figure 39d, e) and 44 days for *U. acus*

136

(Figure 39f), after which a drop is observed. One possible reason for the deviation is insufficient mixing prior to measurement. In addition, with continuous long-term cultivation, artifacts are possible due to a lack of nutrients or contamination by other algae and bacteria. Also, decomposing pigments outside a living cell are not very stable compounds and can potentially affect the change in the spectra. The data obtained by IVIS, RSOM, spectrophotometry and fluorescence spectroscopy are in good agreement in the case of marine cultures.

It should be noted that for all spectroscopic measurements, we extracted the culture, which introduces certain errors that necessarily appear when such a factor as the intensity of shaking the medium when taking an aliquot interferes. At the beginning of the cultivation, we performed the cell counting the first four days of cultivation and observed the lag phase and the onset of the exponential growth of the culture. However, small species of diatoms begin to form clusters a few days after seeding, which makes the counting almost impossible with more prolonged cultivation.[141,149] For long-term batch culturing, growth can be monitored using the proposed photonic approaches based on chlorophyll absorbance and fluorescence, which expands the possibilities of cultivation not only in laboratory conditions but also in aquaculture and bioreactor practice. [141]

4.4 Monitoring changes in diatom concentrations

4.4.1 Photoacoustic imaging

The first successful photoacoustic visualization of diatom algae is reported in our study[15]. Figure 40a-c shows clearly that the photoacoustic signal from *K. amoena* was successfully obtained. The dependence of the photoacoustic signal (represented as the

volume of 3D objects, Figure 40d) on the diatom concentration shows that the volume of the 3D objects emitting the acoustic signal and the mean pixel intensity increased with the diatom concentration. As shown in Figure 40e, a low-frequency signal (shown with red bars) is emitted by a greater number of 3D objects than a high-frequency signal (shown with green bars), whereas a high-frequency signal (33–99 MHz) shows a higher mean pixel intensity than a low-frequency signal within the whole concentration range (Figure 40f).
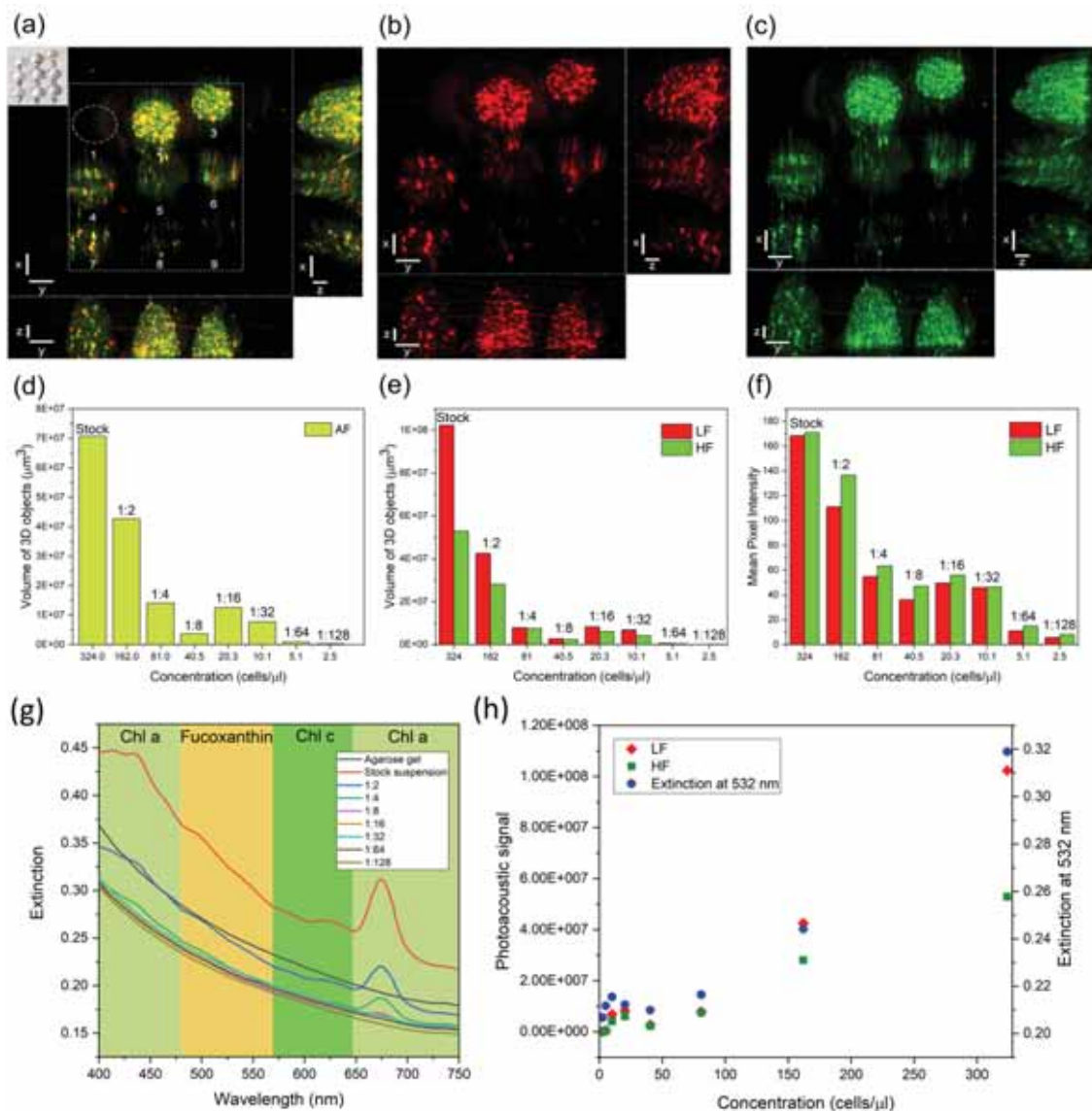
Figure 40. (a) RSOM image of different concentrations of *K. amoena* embedded in agarose gel at frequencies of 11–99 MHz. Inset: Photograph of different dilutions of *K. amoena* in agarose gel drops, where 1 – Agarose gel; 2 – Stock suspension; Diluted suspensions: 3 - 1:2; 4 – 1:4; 5 – 1:8; 6 – 1:16; 7 – 1:32; 8 – 1:64; 9 – 1:128. (b) RSOM image of *K. amoena* at low frequencies (11–33 MHz). (c) RSOM image of *K. amoena* at high frequencies (33–99 MHz). Scale bar (a,b,c): x-axis – 1 mm, y-axis – 1 mm, z-axis – 0.2 mm. (d) Volume of 3D objects vs. the concentration of diatoms mixed with agarose gel. AF – all frequencies. (e) Volume of 3D objects vs. the concentration of diatoms mixed with agarose gel. LF – low frequencies, HF – high frequencies. (f) Mean pixel intensity vs. the concentration of diatoms mixed with agarose gel. (g) Absorbance spectra of different concentrations of *K. amoena* embedded in agarose gel. Chl a – chlorophyll a, Chl c – chlorophyll c. (h) Dependence of photoacoustic signal and absorbance at 532 nm on concentration of diatoms mixed with agarose gel. [15]

The interrelation between the volume of diatoms in gel and the volume of 3D objects emitting a photoacoustic signal remains an important issue for discussion in view of the development of fidelity techniques for the quantitative analysis of diatom colonies. The volume of diatoms in an agarose gel drop, V_d, is calculated from the volume of one diatom cell, the concentration of diatom cells cd, and the volume of agarose gel drop V_{gel} by using equation:

$$V_d = \left(\frac{4}{3}\right) \pi abc \cdot c_d \cdot V_{gel} \qquad (2)$$

The diatom cell is approximated as an ellipsoid, where a, b, c are the length, width, and height, respectively. The volume of agarose gel drop V_{gel} is 10 µl. As one can see from the data in Table 3, there is a wide span of the "volume of 3D objects to the volume of diatoms" ratio for different dilutions of the diatoms in gel.

Table 3 Comparison of the volume of 3D objects obtained by using the ImageJ program with the calculated volume of diatom cells in an agarose gel drop[15]

Dilutions	Volume of 3D objects (ImageJ) / Volume of diatoms in gel (Calculated)
Stock suspension	31
1:2	38
1:4	25
1:8	13
1:16	89
1:32	109
1:64	24
1:128	13

First of all, the volume of 3D objects is one to two orders of magnitude larger than that of the diatoms. Second, this ratio seems independent of dilution, which hints that the volume of 3D objects is not related to the volume of separate diatom cells but to the volume of cell assemblies containing a number of cells. The resolution of the PA microscope is not high enough to resolve separate diatoms, and the volume of the gel surrounding separate cells is detected as the volume apparently emitting a photoacoustic signal. Another important issue is the nature of the structural element that emits the signal. The chloroplast grains are the obvious candidates; therefore, the distribution and absorption efficiency of

the chloroplast grains inside the frustules may contribute to the intensity of the photoacoustic signal.

On the other hand, we believe that the frequencies of acoustic signals emitted by diatoms may correspond to the eigenfrequencies of the natural oscillations of vibrating silica frustules, which can be described as capsular mechanical objects (membrane-shaped shells) having sub- and micrometer sizes[137,164]. Low frequency modes require less energy for excitation; therefore, even diatoms located deeper in the gel or those partly shadowed receive sufficient energy to excite these low frequencies, ultimately giving rise to 3D objects emitting an acoustic signal. High-frequency vibrations require a higher excitation energy and emit a more intense signal, which varies proportionally to the square of the frequency.

Because the extinction value for *K. amoena* (Figure 40g) at 532 nm is in agreement with the photoacoustic signal (Figure 40h), we consider chlorophyll *a* and *c* and fucoxanthin as the principal light absorbers responsible for the photoacoustic effect in diatoms, since the 532 nm laser light is absorbed by all of them. A more exact contribution of each chromophore to the detected acoustic signal remains an open question, because it should be examined with two factors in mind:

- The molar absorption coefficient of every chromophore at the wavelength of the laser causing the photoacoustic signal;

- The volume fraction and spatial distribution of the chromophores within the frustule.

141

It is worth noting that both hemoglobin and chlorophyll, whose photoacoustic behavior is well studied, are complex metal–organic molecules with a central metal atom (Fe and Mg) surrounded by pyrrole rings[173]. Fucoxanthin does not contain pyrrole rings, which supports the suggestion that chlorophyll has a leading role in the formation of a photoacoustic signal.

The application of photoacoustics to bacteria, algae, and other nonhuman natural objects is a relatively undeveloped area that leaves lacunae of knowledge and unexplored opportunities in biotechnology. Separate small diatom cells are not resolved because of the instrumental limitations, whereas diatom clusters and colonies are clearly visualized, which is of utmost importance for aquaculture monitoring. This successful demonstration of the working principle of photoacoustics for the visualization of diatom colonies promises further developments toward the photoacoustic imaging of individual cells. The fundamental cell studies related to the careful continuous characterization of algal colonies could be substantially improved, facilitated, automated, and simplified if supported by large 3D probes.

Considering the significant role of diatoms in Earth's biosphere, we suppose that our findings may pave the way to a number of applications mainly related to the rapid probing of sea, fresh, and waste water, in which the diatom concentration reflects the ecological well-being and the productivity of biomass. Recent advances in diatom biofuel[174], aquaculture[175], and the management of plastic waste in the world ocean[176] suggest that the use of rapid and remote monitoring systems based on the photoacoustic effect may find interesting applications.

4.4.2 Monitoring of diatom concentration changes using a developed optical setup

A simple device consisting of LED illumination with a central wavelength of 505 nm that allows to monitor changes in diatom concentrations was described in the Materials and methods section 3.2.6. Marine centric and freshwater pennate diatoms with different morphologies, sizes and volumes were measured to prove the ability of the developed setup to track changes in their concentrations. Sample probes were taken for measurements during the stationary phase of growth. All studied cultures are shown and described in Table 4 and Figure 41.

Table 4. The size and morphology of the studied diatom cultures[150]

No.	Diatom culture (strain number)	Type	Shape	Diameter, μm	Length (height), μm	Volume, μm^3
1	*Biddulphiopsis titiana* (0.0212-OH)	marine centric	rectangular with round corners	132	255	$3.5 \cdot 10^6$
2	*Coscinodiscus oculus-iridis* (0.1211-OD)	marine centric	disc-shaped	31	10	$7.5 \cdot 10^3$
3	*Coscinodiscus* sp. (21.0407-OA)	marine centric	cylindrical	27	36	$2.1 \cdot 10^4$
4	*Amphipleura sp.* (Ov 466)	freshwater pennate	elliptical	7	57	$2.2 \cdot 10^3$

5	*Hannaea baicalensis* (BK 479)	freshwater pennate	banana-shaped	7	65	$2.5 \cdot 10^3$
6	*Asterionella formosa* (BZ 33)	freshwater pennate	single: elongated, star-shaped colonies	5	85	$1.7 \cdot 10^3$
7	*Ulnaria acus* (15k 595)	freshwater pennate	needle-shaped	5	175	$3.4 \cdot 10^3$

Brightfield images of centric (Figure 41a-d) and pennate diatom cells (Figure 41i-l) show how the chloroplast color changes from yellow to golden brown depending on the strain. Fluorescence images demonstrate distribution of chlorophyll throughout the cells (Figure 41e-h, m-p). In the case of *Biddulphiopsis titiana* (0.0212-OH), whose size is around 250 μm, chloroplasts partly fill the volume from both sides (Figure 41e). On the other hand, chloroplasts in *Coscinodiscus* species (0.1211-OD, 21.0407-OA) are more densely packed and have oval shape (Figure 41f-h). Figures 41c, g show a side view of *Coscinodiscus oculus-iridis* in the process of division. Chloroplasts in the case of freshwater cultures *Amphipleura* sp. (Ov 466) and *Ulnaria acus* (15k 595) occupy most of the cells (Figure 41m, p), while in *Hannaea baicalensis* (BK 479) and *Asterionella formosa* (BZ 33) they are distributed in the form of grains (Figure 41n, o).
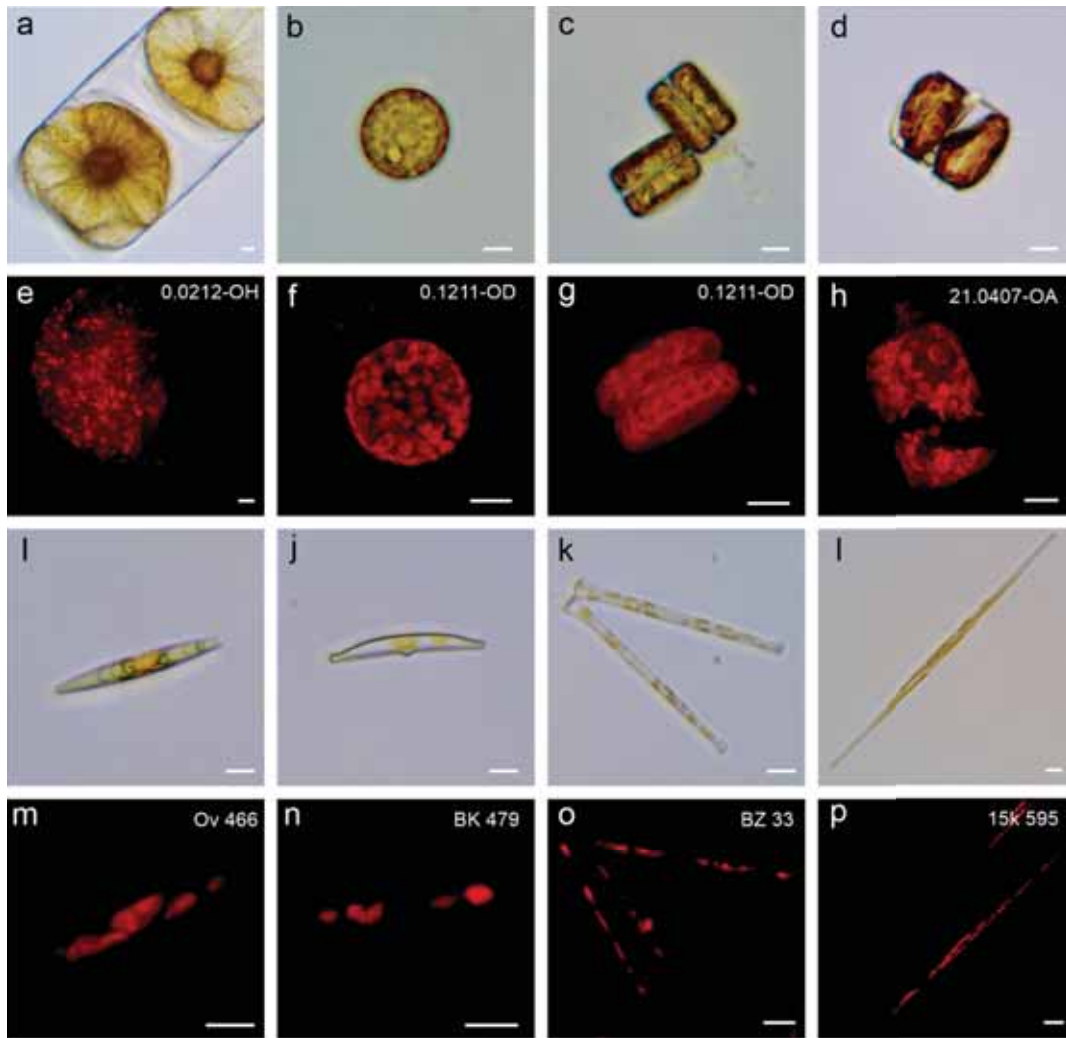
Figure 41. Brightfield microscopy images of marine centric diatoms: (a) *Biddulphiopsis titiana* (0.0212-OH), *Coscinodiscus oculus-iridis* (0.1211-OD): (b) top view, (c) side view, (d) *Coscinodiscus* sp. (21.0407-OA). Fluorescence images of marine centric diatoms: (e) *Biddulphiopsis titiana* (0.0212-OH), *Coscinodiscus oculus-iridis* (0.1211-OD): (f) top view, (g) side view, (h) *Coscinodiscus* sp. (21.0407-OA). Brightfield microscopy images of freshwater pennate diatoms: (i) *Amphipleura* sp. (Ov 466), (j) *Hannaea baicalensis* (BK 479), (k) *Asterionella formosa* (BZ 33), (l) *Ulnaria acus* (15k 595). Fluorescence images of freshwater pennate diatoms: (m) *Amphipleura* sp. (Ov 466), (n)

Hannaea baicalensis (BK 479), (o) *Asterionella formosa* (BZ 33), (p) *Ulnaria acus* (15k 595). [150]

The results of measurements obtained using experimental setup described in Figure 31 are demonstrated in Figure 42. For each diatom strain measured light intensity values were normalized by the nutrient medium light intensity values, and the concentration values were multiplied by the number of cells in mL, calculated on the microscope for each diatom strain. Standard deviation, that was calculated from 12000 measurements for each sample, cannot be seen on graph because error bars do not exceed the size of a dot. The observed dependence of the measured light intensity on the relative concentration of diatoms was approximated by the linear fit for each diatoms strain. It can be seen that all values have high correlation with the linear fit, and are in a good agreement with Bouguer-Lambert-Beer law, which states that sample's optical density has linear dependence on light absorber's concentration: $A = \varepsilon l C$, where A - absorbance, ε - molar extinction coefficient, l - optical path, C - concentration.
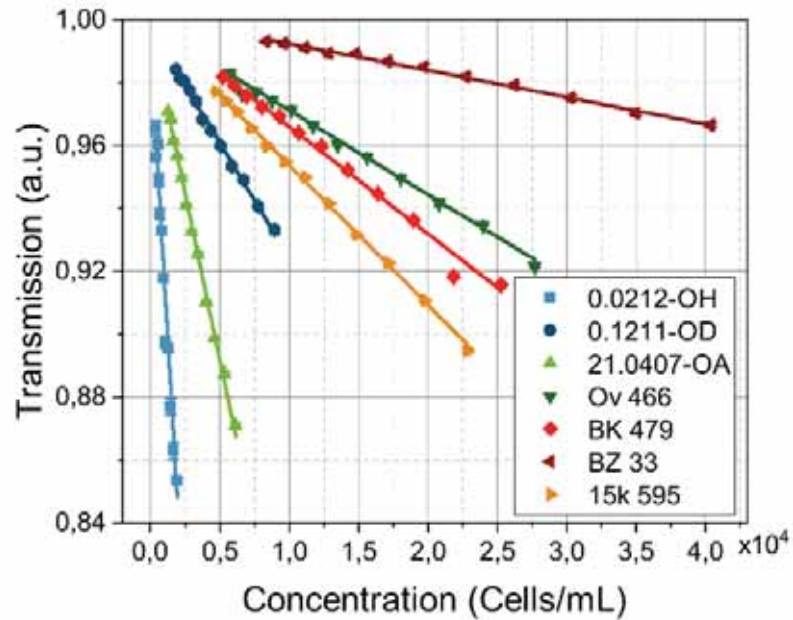
Figure 42. Optical measurements of diatom cultures. Dependence of light intensity on the relative diatom cell concentrations. Light intensity was normalized on the measurements of nutrient medium. Scatter plot represents measured values, solid lines represent linear fit. [150]

To demonstrate the advantages of our system over conventional spectrophotometric approach and investigate opportunities for future development of the device, the extinction and fluorescence intensity measurements were made. Figure 43a demonstrates extinction spectra for initial concentrations of 7 diatom strains. The dependence of diatoms extinction on the concentration is demonstrated in Figure 43b. For all strains measured values were approximated by the linear fit.

Figure 43c demonstrates fluorescence intensity spectra for initial concentrations of 7 diatom strains (excitation wavelength: 430 nm). It can be seen that all strains exhibit fluorescence except for nutrient medium and BK 479 strain. This observation correlates with the absence of extinction peak of chlorophyll c in BK 479, that should be located near 680 nm. Brightfield microscopic images and the growth curve allow to assume, that this strain was in the transition between stationary growth phase and the last (death) phase during measurements. The composition and quantity of pigments is not constant and depends on the intensity of light, its quality, the content of nutritional elements in water, as well as on the growth phase and the characteristics of diatom vital activity[54,177]. The amount of chlorophyll rather decreases at the end of the stationary phase of growth without renewal of the medium. Thus, fluorescence and extinction measurements of diatoms at the wavelength of 680 nm might be a potential marker of the diatom growth phase.

Also, Figure 43d shows the dependence of fluorescence intensity on the concentration for 7 diatom strains (excitation wavelength: 430 nm, emission wavelength: 680 nm). One can observe, that marine centric diatom cultures (strain No. 0.0212-OH, 0.1211-OD and 21.0407-OA) exhibit stronger fluorescence dependence on concentration than pennate diatom cultures (strain No. 15k 595, Ov 466, BK 479, BZ 33).
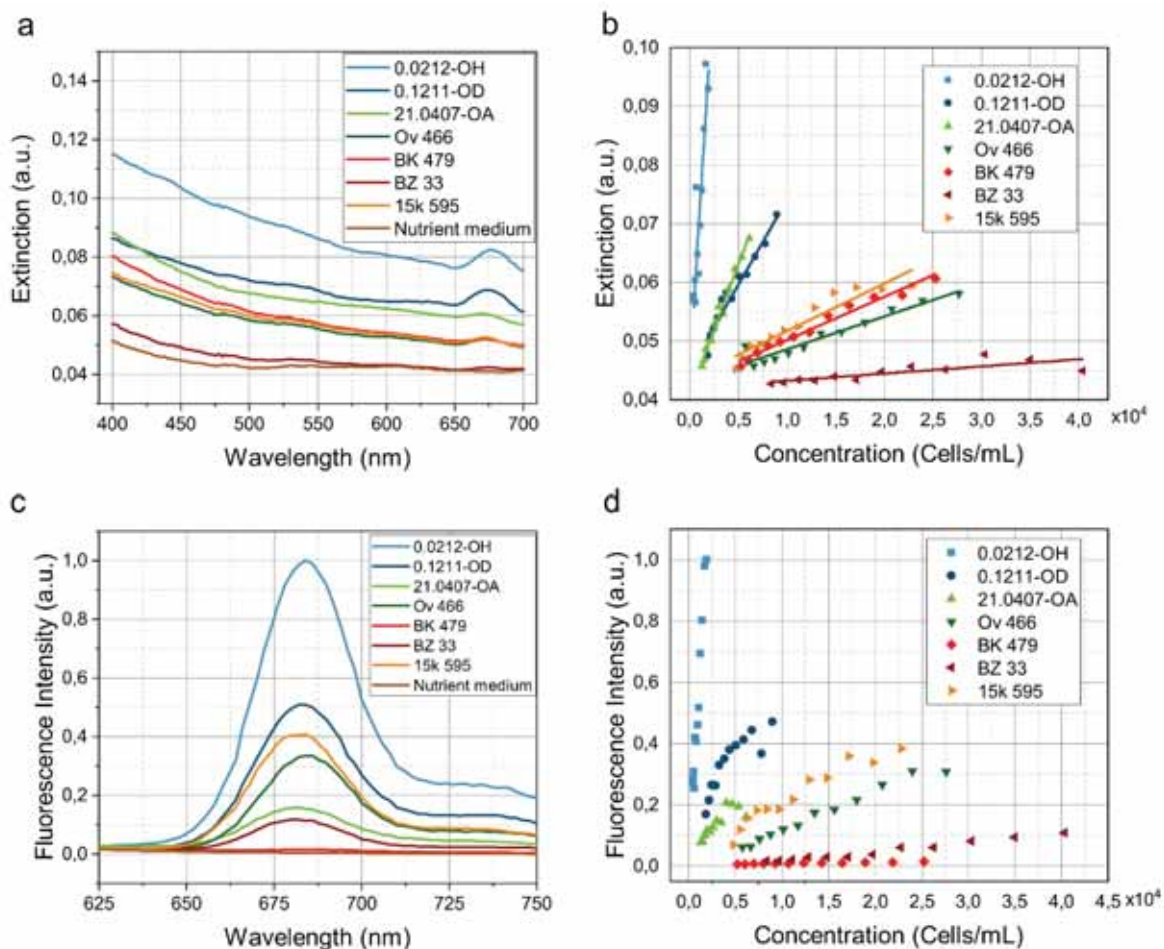
Figure 43. Spectrophotometric and fluorescence measurements of diatoms. (a) Extinction spectra. (b) Dependence of extinction ($\lambda = 505$ nm) on the diatom concentration. Scatter plot represents extinction values normalized on the nutrient medium extinction. Solid lines represent linear fit. (c) Fluorescence intensity spectra. Excitation wavelength: 430 nm. (d) Dependence of fluorescence intensity ($\lambda_{ex} = 430$ nm, $\lambda_{em} = 680$ nm) on the diatom concentration. Scatter plot represents fluorescence intensity values normalized on the nutrient medium values. [150]

The coefficients of determination (COD) for all linear fits are shown in Table 5. It can be seen, that for all strains spectrophotometric measurements demonstrate lower COD values, than optical measurements on the custom setup, which indicates higher accuracy of the last. This can be explained by the difference in the sensing volume. According to the manufacturer, the spot size of the absorbance light beam is 0.7 mm in diameter. The optical path for 200 µL sample is 6.25 mm, thus the sensing volume is $V = 2.405$ mm^3. In contrast to that, our setup has a spot size of light beam scaled to 1.5 mm in diameter, and the optical path is 10 mm. Therefore, the sensing volume in our setup is $V = 17.67$ mm^3, which is 7 times greater than in spectrophotometer. This allows our setup to average values more accurately even for small diatom cell concentrations.

Table 5. Comparison of the coefficient of determination (COD) for spectrophotometric measurements with optical measurements on the custom device. [150]

Diatom strain	Spectrophotometer, COD	Custom device, COD
0.0212-OH	0.840	0.981
0.1211-OD	0.954	0.997
21.0407-OA	0.983	0.998
Ov 466	0.929	0.996
BK 479	0.975	0.993
BZ 33	0.638	0.995
15k 595	0.901	0.999

It can be noted from Figures 42, 43, that slopes of linear fits differ between diatom strains. To be more precise, slope of linear fit is connected to geometrical parameters of a strain, and this dependence is demonstrated in Figure 44. One can clearly see the monotonic dependence of the slope on the volume of diatom cells, that was extracted from the Table 4. The relation between slopes of linear fits and diatom volume is similar in both extinction and transmission measurements and mostly determined by the extinction coefficient, that combines absorption and scattering properties of diatoms. This knowledge could be used for more accurate tuning of the photodetector sensitivity for monitoring of each diatom strain and for characterization of diatom biomass.
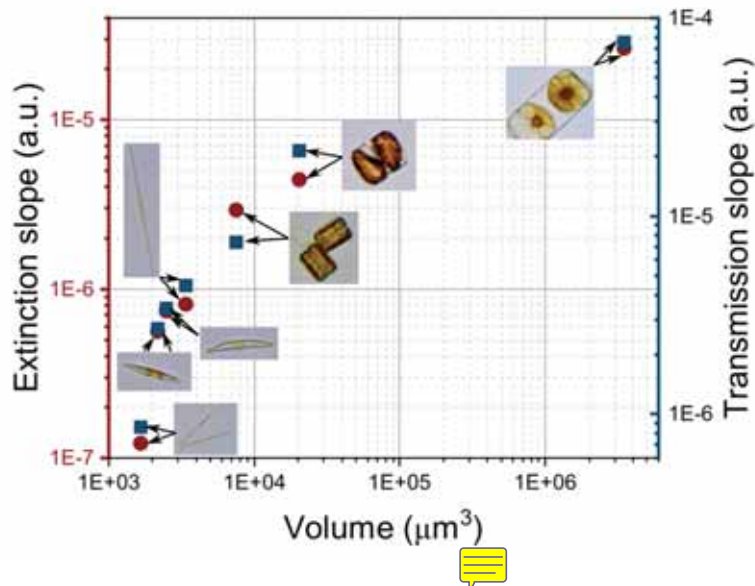
Figure 44. The dependence of linear fit slopes on the diameter of diatom cells. The red circles represent slopes of linear fit in extinction measurements. The blue squares represent absolute values of slopes of linear fit in transmission measurements on the custom-made setup described in Figure 31. [150]

151

4.5 Monitoring of the division of diatoms in a microfluidic cell

The division of diatoms was monitored by installing a microfluidic cell (Figure 30) in an inverted fluorescent microscope NIB-FL (LOMO-Microsystems, St. Petersburg, Russia), as presented in Figure 45.

Figure 45. a) Photography of the whole experiment setup, b) Photography of microfluidic cell.

Figure 46 shows the division of *Coscinodiscus oculus-iridis* in a flow cell at a temperature of 21°C, a CO_2 concentration in the gas receiver of 0.05 vol.% and a nutrient medium flow rate of 10 µl/min.
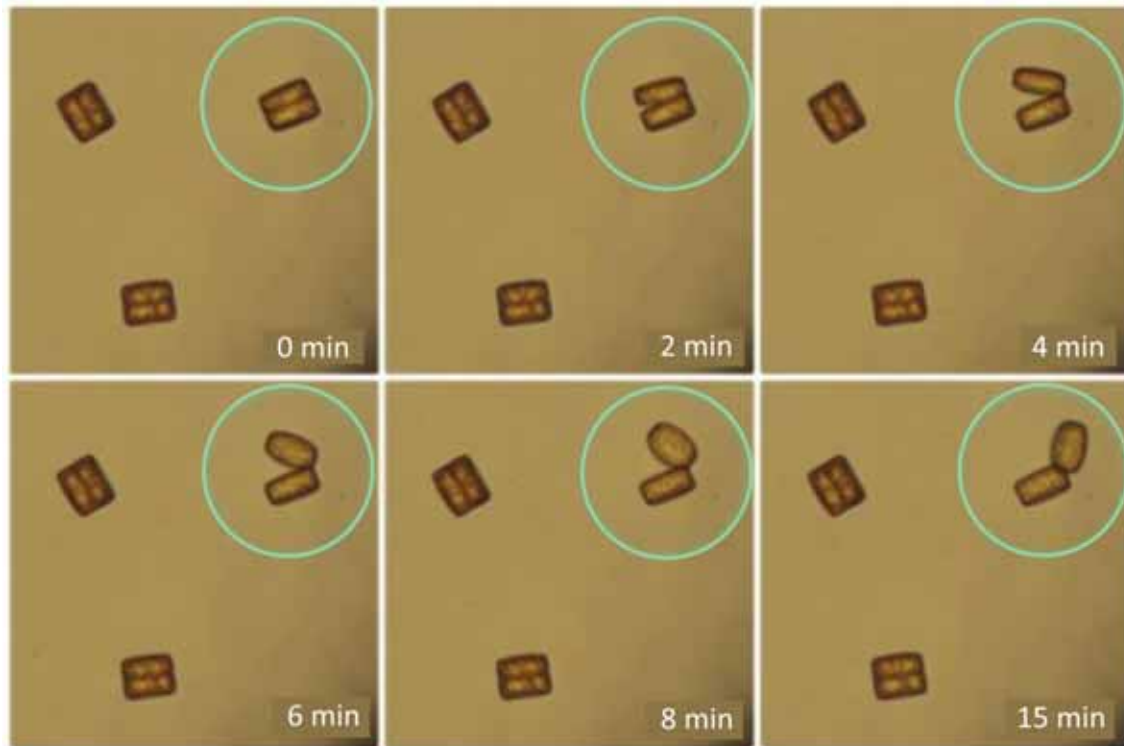
Figure 46. Division of C. oculus-iridis in the microfluidic cell

Figure 47 shows an example of a microfluidic cell temperature profile and images taken at different times while monitoring the division of the diatom Coscinodiscus oculus-iridis. Monitoring was performed at a nutrient medium flow rate of 10 μl/min and a CO_2 concentration in the gas receiver of 0.05 vol.%. Lowering the temperature to 10°C slows down the division of Coscinodiscus oculus-iridis. When the temperature rises to 23°C for 3 hours, cell division is observed. The images show that part of the algae is carried away by the flow of the nutrient medium during the observation. Therefore, further optimization of the channel configuration is required in order to reduce the flow rate directly in the field of visual observation. Thus, the device allows for several days to carry out in situ

153

monitoring of the process of division of individual cells with the possibility of varying the concentration of CO_2, temperature and flow rate of the nutrient medium.
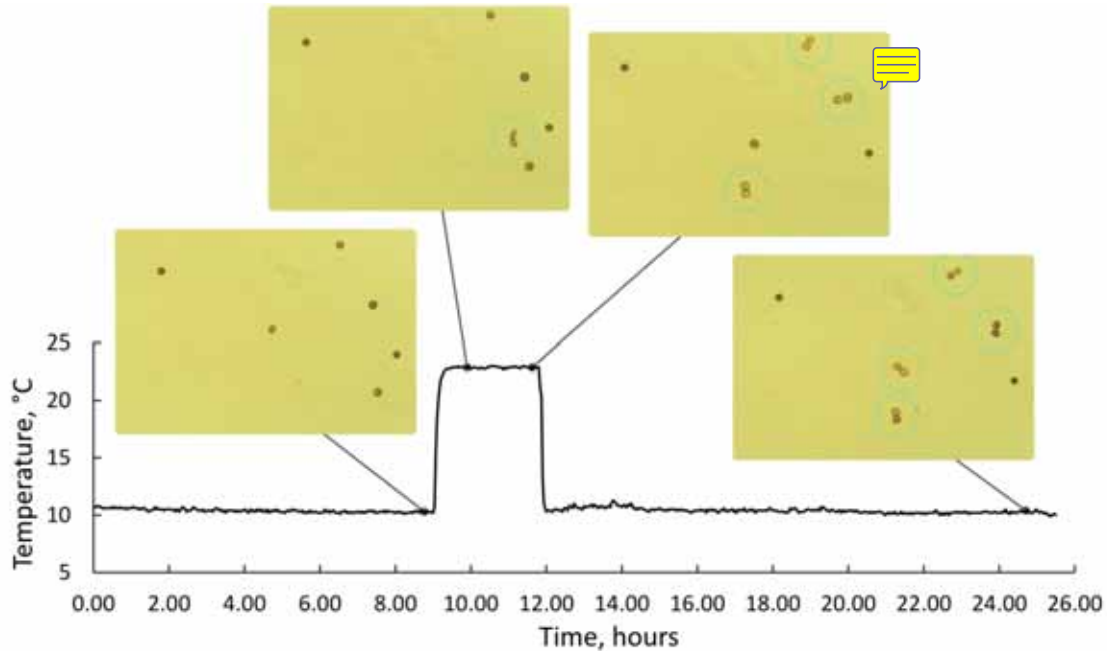
Figure 47. Monitoring of the division of *C. oculus-iridis* in the microfluidic cell during temperature changes.

4.6 Summary

In summary, freshwater pennate and marine centric diatom cultures were cultivated in the specially designed bioreactor and windowsill under specific conditions optimized for their growth. The growth of diatom colonies was monitored through the application of novel optical techniques, including fluorescence and photoacoustic visualization, which allowed for rapid evaluation of diatom growth without the need for extensive sample preparation. Consequently, the spectroscopic characterization confirmed the findings obtained through the IVIS and RSOM imaging systems, validating their efficacy in

assessing diatom growth. Diatoms exhibited pronounced photoacoustic signals attributed to the absorption properties of chlorophylls and carotenoids at the 532 nm wavelength.

Moreover, capabilities of transmission measurements using fabricated optical setup at the wavelength of 505 nm for seven diatom strains were demonstrated and compared to the spectrophotometric approach. As a result, the linear dependence of measured transmission on the diatom concentration was observed with high accuracy for all strains. The described approach is promising for continuous monitoring of diatoms in bioreactors, and can be improved with addition of transmission measurements at the wavelength of 680 nm and fluorescence measurements with the same emission wavelength, as well as fine tuning of a photodetector sensitivity based on the obtained dependencies of the linear fits on the diatom volume.

A specially designed microfluidic cell allowed for several days to carry out *in situ* monitoring of the process of division of individual cells with the possibility of varying the concentration of CO_2, temperature and flow rate of the nutrient medium.

Chapter 5. Visualization of living and cleaned individual diatoms

This chapter initiates the investigation of individual diatoms through the application of various methodologies employed to visualize both intact living cells and purified frustules devoid of organic constituents.

5.1 Background

Diatoms are classified based on their morphology and nanopatterned structures of their silica cell walls, allowing for accurate identification and classification. The study of diatom morphology and structure enables the characterization and classification of different diatom species, helping to understand their ecological roles and interactions. The changes in the diatom community structure and morphology are considered early warning signals of environmental impacts, such as pollution, eutrophication, and climate change. The study of diatom morphology and structure can, therefore, facilitate the detection of environmental changes and help develop management strategies for maintaining sustainable ecosystems. Understanding the diatom morphology and structure can also enable the design of custom-shaped silica structures with specific chemical and physical properties for targeted applications. The conservation and application of diatoms rely on the in-depth knowledge of their morphology and structure, making this an important research area with a broad spectrum of scientific and technological implications.

5.2 Scanning electron microscopy

The morphology of diatom frustules after purification from organic material was studied using SEM (Figure 48).
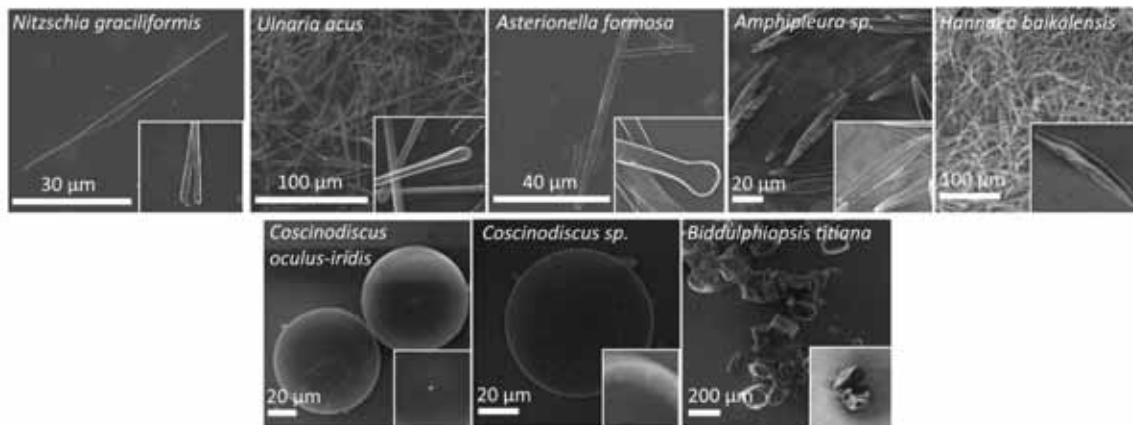
Figure 48. SEM images of different pennate and centric diatom frustules. Insets: enlarged view of individual frustules

Nitzschia graciliformis Lange-Bertalot & Simonsen

The cells are solitary needle-shaped, with two chloroplasts, one at each end of the cell. Valves are straight lanceolate, sharply narrowed to very thin ends. The keel runs along the edge of the cell; it contains a canal-suture with central pores. Fibulae, supports on which the tube of the canal-like suture is held, are located along the entire length of the leaf. The two median brooches are widely spaced and form a central knot. Terminal nodules are visible at the ends of the valves. Rows of areolas are distinguishable only in an electron microscope. The species is widely distributed in the pelagic zone of the lake Baikal, as well as in the river Selenga and in the Selenga shallow water.

Ulnaria acus (Kützing) Aboal

Cells are solitary, needle-shaped, two large chloroplasts are elongated along the valves. The valves are narrow towards the ends gradually narrowing; the axial field in the center of the valve is narrowly linear. Two-lipped outgrowths are located at each end of

the valve. At each end is a pore field - the ocellulimbus. It is one of the mass dominant species of phytoplankton in the pelagial of Lake Baikal.

Asterionella formosa Hassall

Cells are rod-shaped, connected in stellate colonies. Chloroplasts are small. The frustule is narrowly linear with widened ends, of which the basal end is wider than the head. Axial field narrowly linear, transverse rows of areoles consist of single areoles. At the ends of the valve there are two-lipped outgrowths, the slit of which opens on the outer surface with a hole much larger than the pores. Small irregular spines are located on the border of the front part of the valve and the bend. At the apical ends of both valves, there are fields of small pores arranged in short rows in the direction of the central axis of the valve. The species is widespread in the lake Baikal from spring to autumn.

Amphipleura Kutzing sp.

Valves linear-lanceolate and very narrow, gradually tapering to rounded ends. The suture branches are greatly shortened and only slightly increase in length as the valve length increases. On the branches of the seam, the seam is surrounded by two longitudinal ribs. The rows of areolas are very small and visible only under optimal lenses and illumination in a light microscope. The outer distal and proximal ends of the suture are straight. The strain was isolated from the river Yenisei.

Hannaea baicalensis Genkal, Popovskaya & Kulikovskiy

Cells are rod-shaped, slightly crescent-shaped, solitary. The single chloroplast is pressed against the girdle rims. The valves are crescent-curved with capitate ends, the suture is absent. Rows of areoles are parallel, interrupted in the middle on the ventral side

of the valve, where a unilaterally convex field is located. The axial field is narrow-linear. There are two-lipped outgrowths at the ends of the valve. The species is widespread in the littoral zone of the lake Baikal.

Coscinodiscus oculus-iridis (Ehrenberg) Ehrenberg

The frustule is low-cylindrical, the valves are flat, there are no hyaline fields on the valves. Areoles on valve are rounded, with external velum, unequal in size, densely spaced. There are no macroprotrusions on the valve fold on the inner side of the ring of bilabial outgrowths (rimoportula), which open from the outer side of the valve with simple holes. Plastids are small, granular, multiple, more or less evenly distributed throughout the entire thickness of the cytoplasm. The species is free-living, marine and often abundant in phytoplankton.

Coscinodiscus sp.

A species with a taxonomic position that has not yet been clarified by us. Cells are solitary, while frustule is cylindrical. The valves are flat. Chloroplasts are multiple, granular, in a healthy cell evenly distributed throughout the volume of the cytoplasm. At the time of measurements, the cell diameter of the strain *Coscinodiscus* sp. (Black Sea) 21.0407-OA varied from 28 to 35 μm.

The genus *Coscinodiscus* includes 221 species[10]. Representatives of the genus, apparently, are exclusively marine, with the exception of species with an unclear taxonomic position. This large genus requires taxonomic revision as there is a lot of variation at the ultrastructural level. Several species formerly in this genus have been

159

moved to the genus *Thalassiosira*, others to *Actinocyclus* - many of the changes concern species living in tropical lakes.

Biddulphiopsis titiana (Grunow) Stosch & Simonsen

Cells are rectangular with rounded corners, forming short chains that can attach to a substrate (usually other algae). The contour of the valve is oval to semicircular with deep vertical mantles. When viewed from the girdle, the surfaces of the valves look slightly convex. Areoles occluded by mouths (variant of velum) scattered over elongated central area, arranged radially in single row outside it. On the apexes there are areas with smaller pores, forming rather indistinct false eyes (pseudocellus). The edge of the mantle is slightly extended inward, forming a pseudo-septum. Next to the pseudocellus there is a row of rimoportulae, sometimes forming an irregular ring around them. The waistband consists of four closed rings. The marginal edges of the rims have short thin protrusions with a few inclusions of pores, inside which there is a smooth platform. The areoles run in rows down the rims and have single or multiple elongated mouths. Small, lamellar, multiple plastids occur in the peripheral cytoplasm and in strands extending from a prominent central nucleus. This widespread marine genus consists of two species, *B. titiana* and *B. membranacea*.

The cell ultrastructure examined using a transmission electron microscope is described in Appendix A.

160

5.3 Confocal laser scanning microscropy

Laser scanning microscopy (LSM) was used to observe the DNA material of diatom cells and newly formed valves during division, as described in the Materials and methods. Confocal images of pennate species (*U. acus*, *N. graciliformis*, *Amphipleura* sp., *A. formosa*) after staining are shown in Figure 49. Newly formed valves are visible on all images (Figure 49a-j). In the case of *Amphipleura* sp. Chloroplasts are clearly visible and occupy the central part of the cell (Figure 49e-h).
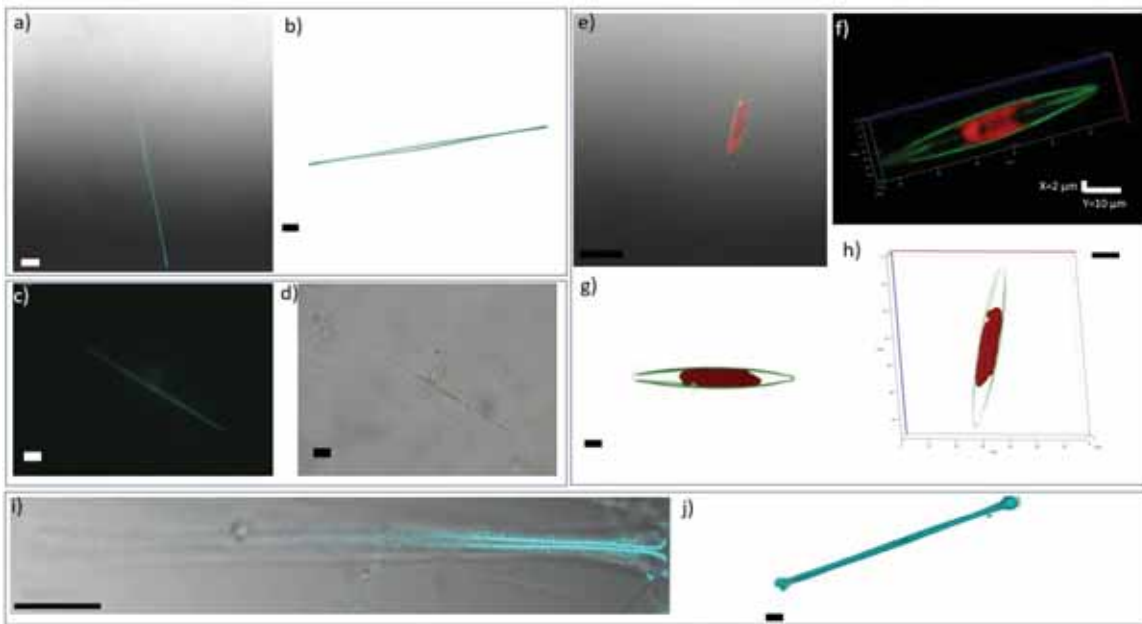
Figure 49. Visualization of pennate diatoms using laser scanning microscopy. a) Confocal image of *U. acus* (15k 595) after PDMPO staining, b) 3D confocal image of U. acus, c) Fluorescent image of *N. graciliformis*, d) Bright field image of *N. graciliformis*, e) Confocal image of *Amphipleura* sp. (Ov 466) after PDMPO staining, f) 3D confocal image of a dividing cell of *Amphipleura* sp., g)-h) 3D images of *Amphipleura* sp., i) Confocal image

of *A. formosa* (BZ 33) after PDMPO staining, j) 3D -confocal image of *A. Formosa*. Scale bar: a, b, c, d, i, h - 10 μm; e, g, j – 5 μm.

Confocal images of a marine culture of *C. oculus-iridis* after staining are shown in Figure 50.
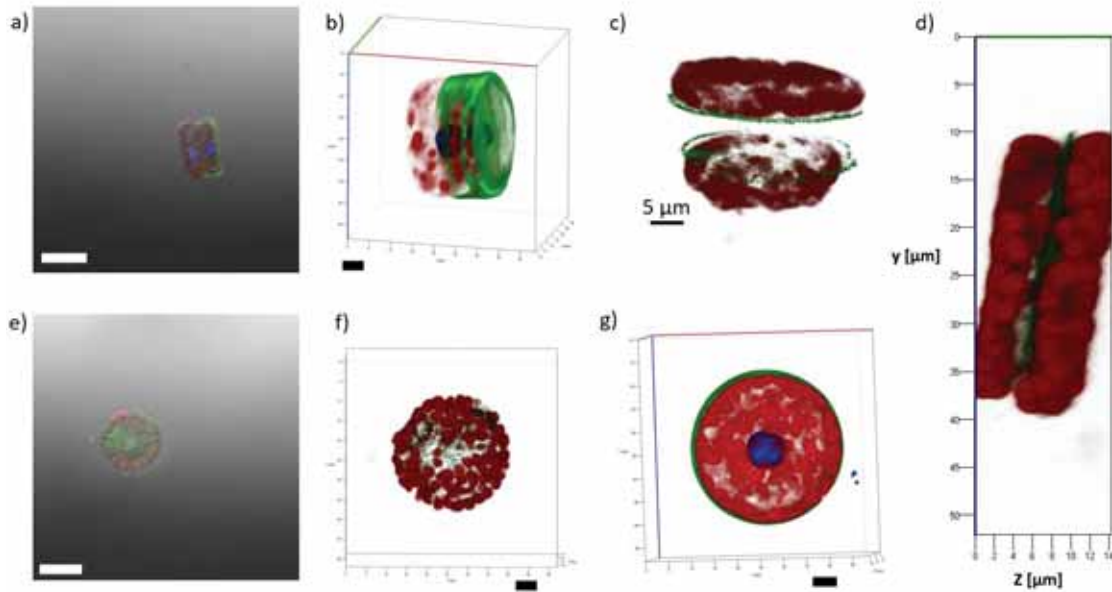
Figure 50. Visualization of *C. oculus-iridis* (strain 0.1211-OD) using laser scanning microscopy. a) Confocal image of a fixed *C. oculus-iridis* cell stained with LysoTracker Yellow and DAPI (lateral view), b) 3D image of a dividing cell with nuclei (lateral view), c) 3D image of a divided cell without a nucleus, d) 3D image image of a dividing cell, e) Confocal image of a fixed *C. oculus-iridis* cell (top view), f) 3D image of a cell without a nucleus (top view), g) 3D image of a cell with a nucleus (top view). Red: chlorophyll autofluorescence, green: newly formed valves, blue: nucleus. Scale bar: a, e – 20 μm; b, c, f, g – 5 μm.

According to Figure 50a, b, g, the nuclei located in the center of the cells are round. Oval-shaped chloroplasts are rather densely distributed inside the cells (Figure 50a, c, d, f, g). The formation of new valves (represented in green) is shown in Figure 50a-g. The state of chloroplasts and cell division indicate the viability of the culture.

5.4 FLIM visualization

Fluorescence lifetime imaging microscopy is a powerful tool for studying biological structures by measuring the fluorescence decay rate of molecules[15,178–180]. This technique has recently found use in many applications, because it can provide both information on the location of specific fluorophores and on their local environment[178,180,181]. As an intrinsic property of a fluorophore, the fluorescence lifetime depends on temperature, pH, concentration, polarity, the presence of fluorescence quenchers, and internal factors that are connected with fluorophore structure[181,182]. Therefore, it is important to understand the state of the fluorophore in diatoms. According to the literature, the fluorescence lifetimes of chlorophyll a range from 3.0 to 5.1 ns for an isolated molecule, depending on the polarity of the solvent[183]. In living cells, the lifetime ranges from 0.3 to about 1.5 ns, because a great amount of absorbed energy is used in photochemical reactions[183]. It is well known that diatoms use the mechanism of nonphotochemical quenching of chlorophyll a fluorescence to dissipate excess energy and prevent overexcitation of the photosynthetic apparatus[184].

The bright-field transmission and FLIM images of different pennate diatom species (*K. amoena*, *Haslea karadagensis*, *A. sibiricum*, *E. silesiacum*) are shown in Figure 51.
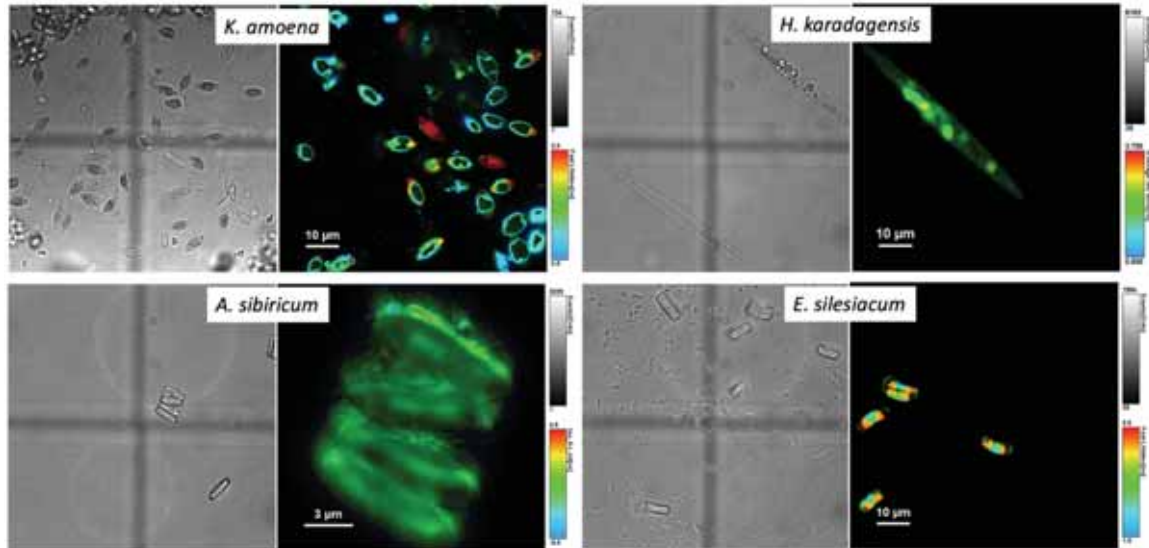
Figure 51. Transmission bright field (left) and FLIM images (right) of different pennate diatoms.

FLIM results demonstrate that diatoms generally have a very short yet changeable average lifetime—from 0.5 ns up to 2 ns. The fluorescence signal originated from chlorophyll a, because the detection system that was used includes a 402-nm and 638-nm lasers as the excitation source and a 690-nm bandpass filter, and it does not record signals other than those from chlorophyll *a*. The system records a variety of chlorophyll lifetimes, probably owing to the complex physiology of diatoms and the state of the cell. Another reason could be that in diatoms, pigments have different concentrations, and in some diatoms, they only partly fill the volume of the frustule. The longest fluorescence lifetime

was observed in the case of the old bacteria-contaminated culture of *E. silesiacum*, which confirms the assumption that these values may also depend on the life cycle of diatoms.

The bright-field transmission and FLIM images of different centric diatom species (*C. oculus-iridis*, *Coscinodiscus* sp., *B. titiana*) are shown in Figure 52.
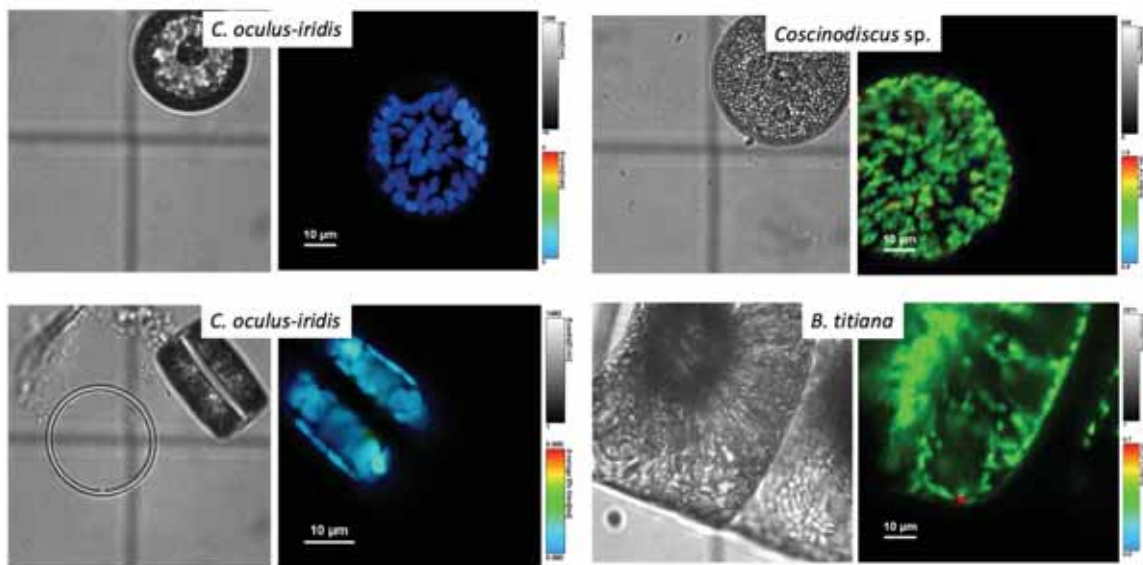
Figure 52. Transmission bright field (left) and FLIM images (right) of different centric diatoms.

While transmission bright field images demonstrate the highly ornamented silica frustule, FLIM images show the distribution of chloroplast inside the diatoms. In the case of *C. oculus-iridis*, chloroplast distribution is shown from the top and from the side. Also, Figure 52 on the left bottom demonstrates that there is no signal from the empty frustule without organic content. Fluorescence lifetime ranges from 0.4 to 0.8 ns.

The distribution of chloroplasts in the frustules is also demonstrated using Operetta High Content Imaging System in Figure 41.

5.5 Summary

In order to design silica structures with specific physical and chemical properties, it is necessary to understand the diatoms' morphology and structure, which were investigated after purification using SEM and TEM, respectively.

Living diatom cells were studied using different fluorescence-based techniques, such as confocal laser scanning microscopy, FLIM, and Operetta High Content Imaging system, owing to the presence of the main fluorophore – chlorophyll. Fluorescence images demonstrated the size, shape, and distribution of chloroplasts inside the frustules.

Chapter 6. Mechanical properties of diatoms

Interrogating the structure and properties of diatoms down to nanometer scale leads to breakthrough advances reported in this chapter in the nanomechanical characterization of *Coscinodiscus oculus-iridis* diatom silica frustules, as well as of air-dried and wet cells with organic content. The results on mechanical properties of diatom algae presented here are published in **Cvjetinovic J** et al.[1] *Scientific Reports*, 2023, 13(1), 5518, while results on resonant eigenmodes of diatoms are ready to be submitted to the journal *Applied Physics Letters*.

6.1 The biomimetic approach and research methodology

For the present study the centric diatom *Coscinodiscus oculus-iridis* was chosen as a representative sample with some of the most interesting variations in structural elements that can affect their mechanical and photonic properties. We investigated cleaned frustules consisting of two halves with different outer and inner surfaces, as well as wet and dried diatom cells containing organic components (Figure 53a). The state of the sample interrogated is indicated by the small cartoons shown in the upper right corner to aid understanding. The striking similarity between diatom valves and the membranes used in modern MEMS microphones[131] (Figure 53b) is shown in Figure 53c. Two different AFM modes used in this study are schematically illustrated in Figure 53d, whilst *in situ* nanoindentation in the SEM column is shown in Figure 53e. The details of these experimental approaches are explained in the Materials and Methods section. The mechanical contact between a sharp indenter and diatom frustule is a frequent occurrence in nature in the course of interaction with marine zooplankton. For example, several species

of copepods use the force of their mandibles to crush diatoms using silica-tipped parts called opal teeth[185], as illustrated in Figure 53f.
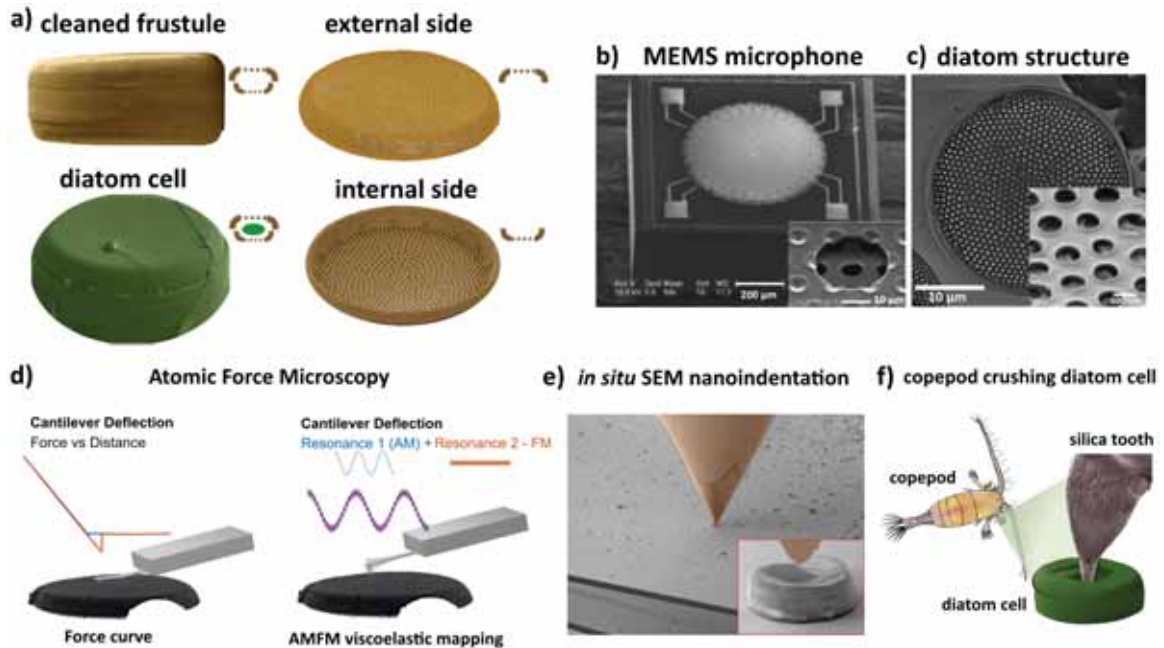
Figure 53. Study objects, biomimetic approach and research methodology. a) Samples used in this study: cleaned frustule (organic matter removed), external and internal sides of cleaned frustules, diatom cell containing organic components, b) SEM images of the MEMS microphone and the membrane perforation (inset). Adapted with a permission from[131]. c) SEM image of diatom frustule showing the porous structure (inset), d) Schematic diagrams of two modes of AFM measurement: force vs distance and amplitude modulation-frequency modulation (AMFM), e) In situ nanoindentation inside SEM column, f) Schematic illustration of a copepod crushing diatom cell with the help of a silica tooth as an example of indentation in nature. [1]

6.2 Morphology and topography study: from micro to nanoscale

Figure 54 shows morphology and topography of *Coscinodiscus oculus-iridis* first identified by Ehrenberg in 1839.
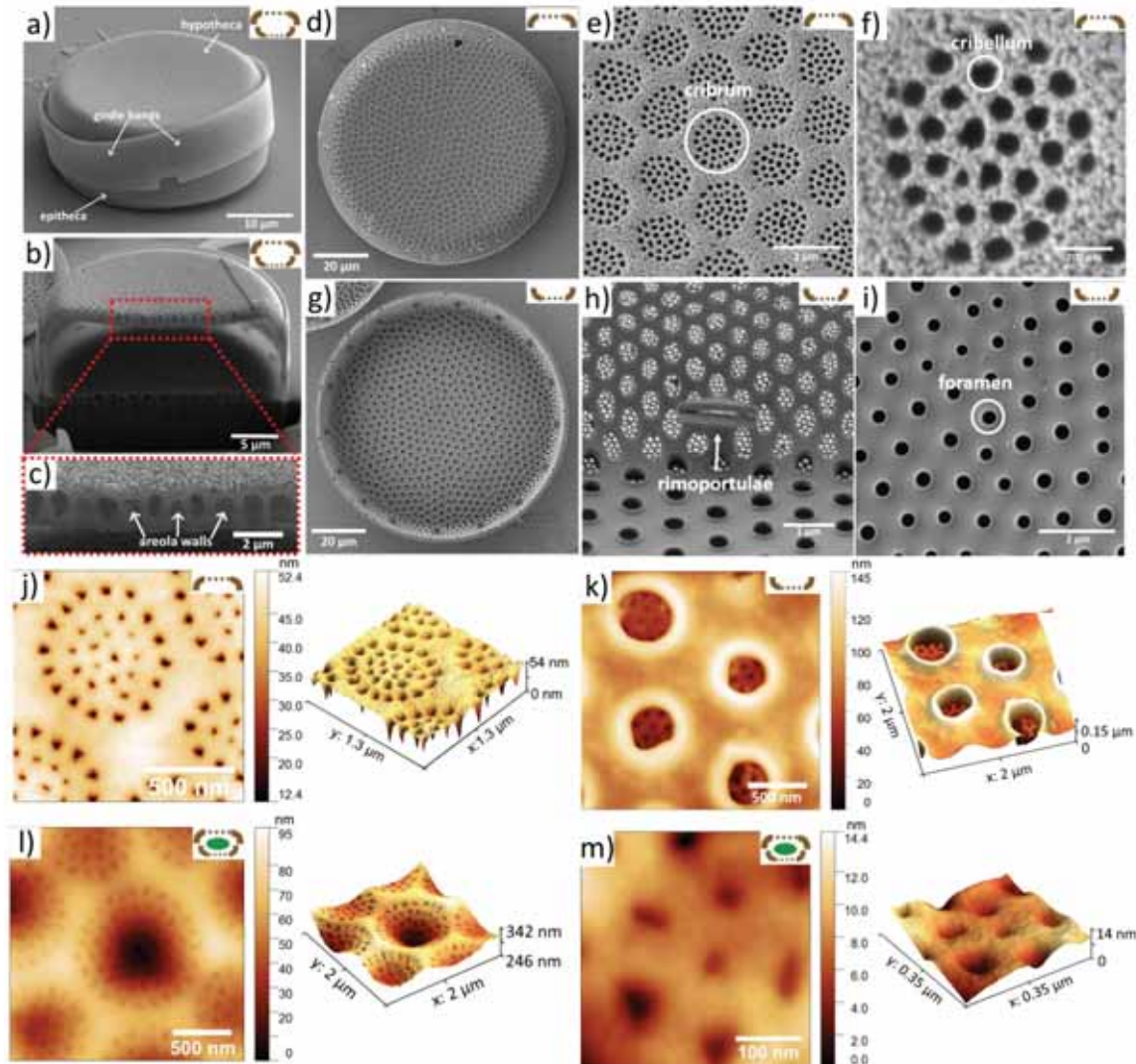
Figure 54. SEM images of: a) the cleaned diatom frustule consisting of a hypotheca and an epitheca joined together by girdle bands, b) the frustule FIB cross-section showing areola walls c, d) outer surface of the valve, e details of the external side of the valve: cribrum, f) cribellum, g) inner surface of the valve, h) details of the internal side of the valve:

rimoportulae, i) foramen. AFM topography of: j) an outer surface of the cleaned frustule decorated with porous domes (cribrum), k) foramen holes on the inner surface of a cleaned frustule, l) a surface of a wet diatom cell forming a hilly terrain, m) close view of regularly spaced pores on the outer surface (cribellum) of a wet diatom cell. [1]

The frustule shown in Figure 54a consists of two valves: the upper epitheca and the lower hypotheca, connected by a series of siliceous rings called girdle bands. The diameter of valves ranges from 30 to 70 μm, while their height varies from 10 to 15 μm, although much larger size ranges can be found in literature. The cross-sectional view of a diatom frustule after FIB (Figure 54b, c) demonstrates the multi-layered hierarchical structure of the cell wall, formed by orthosilicic acid in silica deposition vesicle[13,127]. The wall thickness is in the 0.3-1.5 μm range. The disk-shaped valve faces are slightly depressed in the central area, which is frequently less silicified than the peripheral region[186]. The outer thin perforated silica layer called cribrum (Figure 54d, e, j) consists of a regularly spaced array of 40-70 nm pores (cribellum)[187] (Figure 54f, m). The pore-to-pore distance in one array is around 100 nm. The honeycomb-like chambers called areolae are open to the cell interior via rimmed circular openings (Figure 54g) – foramen with a diameter of around 0.2-0.5 μm (Figure 54h, i). The porous pattern of the cribrum layer is located exactly above the foramen. The rimoportula openings having the shape of a pair of lips are distributed along the perimeter of the internal valve (Figure 54h). On the external valve face, the rimoportula opening is a simple, round aperture, through which they extrude polysaccharides and other carbon compounds. AFM topography images (Figure 54j-m)

show that the surface of the air-dried live diatom cell containing organic material is not flat and monotonously "smoothed", but form a hilly terrain (Figure 54l, m). Organic components of diatoms can be classified in the following way: 1) an organic casing represented by a thin layer surrounding silica wall, 2) the diatotepum or diatotepic layer located between the plasmalemma and the silica, 3) molecules or organic complexes trapped within the silica, 4) mucilage associated with the cell surface or secreted by diatoms which can be used for motility, adhesion or protection[188]. On the cleaned frustule the perforations on the outermost surface are simple openings (Figure 54j), while on the inner surface they have thickened rims (Figure 54k).

The analogy between the natural appearance of silica diatom frustule lase structure and artificial MEMS (especially microphone membrane) served as a motivation to carefully study diatoms as a mechanical system. Mechanical sensitivity of the MEMS capacitive microphones increases when the thickness of the diaphragm increases[189]. However, it is important to find an optimal size correlation between thickness and mechanical response. On the one hand, a thin membrane with a large radius has more flexibility, but at the same time can be brittle. On the other hand, a thick membrane with a small radius has a poor flexibility. According to the review article[190], the average membrane diameter is 600 μm, while the thickness makes up 1 μm, which corresponds well to the silica frustule thickness.

6.3 AFM and AMFM studies of mechanical properties of diatoms

Figure 55 shows AFM topography and corresponding maps of Young's modulus measured on the inner (Figure 55a, d) and the outer (Figure 55b, e) surfaces of cleaned diatom frustules and on the wet cell containing organic material (Figure 55c, f). The Young's modulus data were obtained by collecting force-distance curves in the elastic regime.
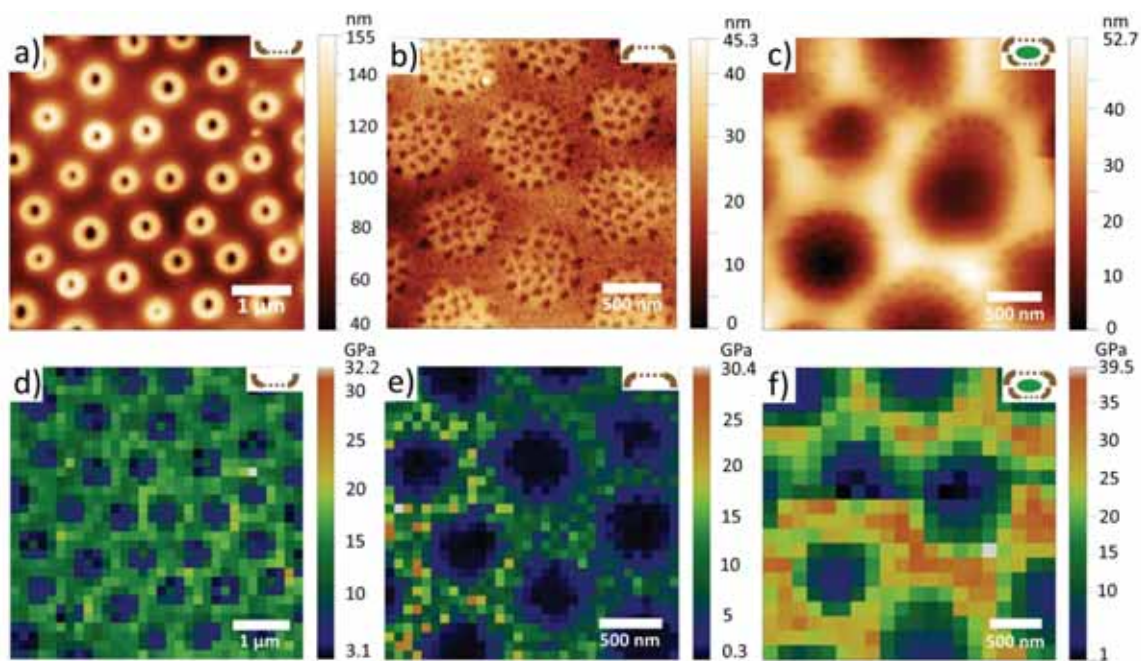
Figure 55. AFM study of cleaned frustules and wet diatom cells. Topography of a measured: a) inner side and b) outer side of cleaned frustule, c) wet diatom cell. Young's modulus of: d) inner and e) outer surface of cleaned frustule, f) wet diatom cell. [1]

The results show that Young's modulus of the thick space between pores is E=15±2 GPa and E=10±4 GPa for the inner and the outer surfaces of cleaned frustules, respectively, while for the wet diatom cell E=25±5 GPa, which was expected considering the support

from the organic material trapped inside the frustule. According to study [191], the introduction of molecular water into the silica network leads to an increase of Young's modulus of silica glass at low water content. On the other hand, due to excessive boiling in concentrated nitric acid, the frustule material can become friable and fine structures in some cases may be lost which leads to the lower mechanical performance. Conversely, if the oxidation was weak and the samples were poorly washed, the organic matter lays down on the surface of the frustule in a thin layer, covering and masking fine structures. The stronger mechanical structure of the internal plate is expected as this layer is the basic framework for building the other porous layers – cribrum and cribellum. However, that the values fall within the error margins (Figure 56).

173
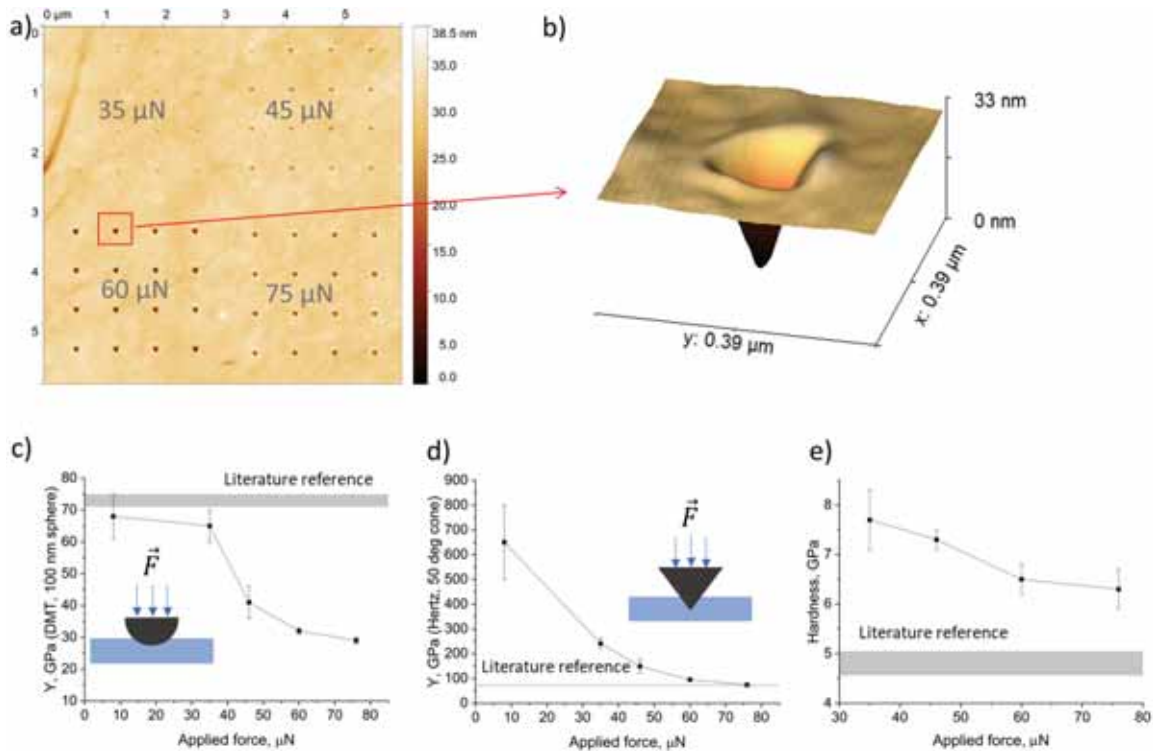
Figure 56. Calibration of a stiff diamond probe (k=400 N/m) on a fused silica reference sample. a) Topography, b) The stiff diamond cantilever, c) The DMT model, d The Hertz model), e) Hardness depending on the applied force. [1]

The stiff diamond cantilever has a spherical tip apex with R ≈ 100 nm and a pyramid body with half angle ≈ 45 deg (Figure 56b). During indentation the contact geometry changes from spherical at low force to pyramidal at high force. Different models were used to fit force-distance curves and calculate Young's modulus. Using the reference fused silica sample (Figure 56a) we established that at the low indentation force (≤20 µN) where the tip-sample contact geometry is mainly determined by the tip apex (assuming flat surface) the DMT (Derjaguin-Muller-Toropov) model gives results in agreement with literature reference, which can be found elsewhere (Figure 56c). Here the DMT model assumes a spherical indent with R=100 nm made of synthetic diamond, and the sample's Poisson ratio 0.15. At the high indentation force (>70 µN) where the tip-sample contact geometry is mainly determined by the tip body, the Hertz model gives adequate results (Figure 56d). The Hertz model assumes a conical indent with 50° half angle made of synthetic diamond, and the sample's Poisson ratio 0.15. For the diatom samples we applied low loading force and implemented the DMT model except for the hardness measurements.

Hardness was calculated as a ratio of indentation force to the indent area (Figure 56e). The measured hardness is higher than the literature reference, but of the same order of magnitude. The difference might be due to the size effect, since the AFM indents are much smaller than the Vickers indents.

Finite element simulation of an isolated pleura of *T. punctigera*[42] showed that the Young's modulus of diatom silica is 22.4 GPa, which is comparable to cortical bone (20 GPa) and in good agreement with our study. Young's modulus of the rims around pores is lower probably because the material of the rims is not clamped in in-plane direction, as shown in Figure 57.
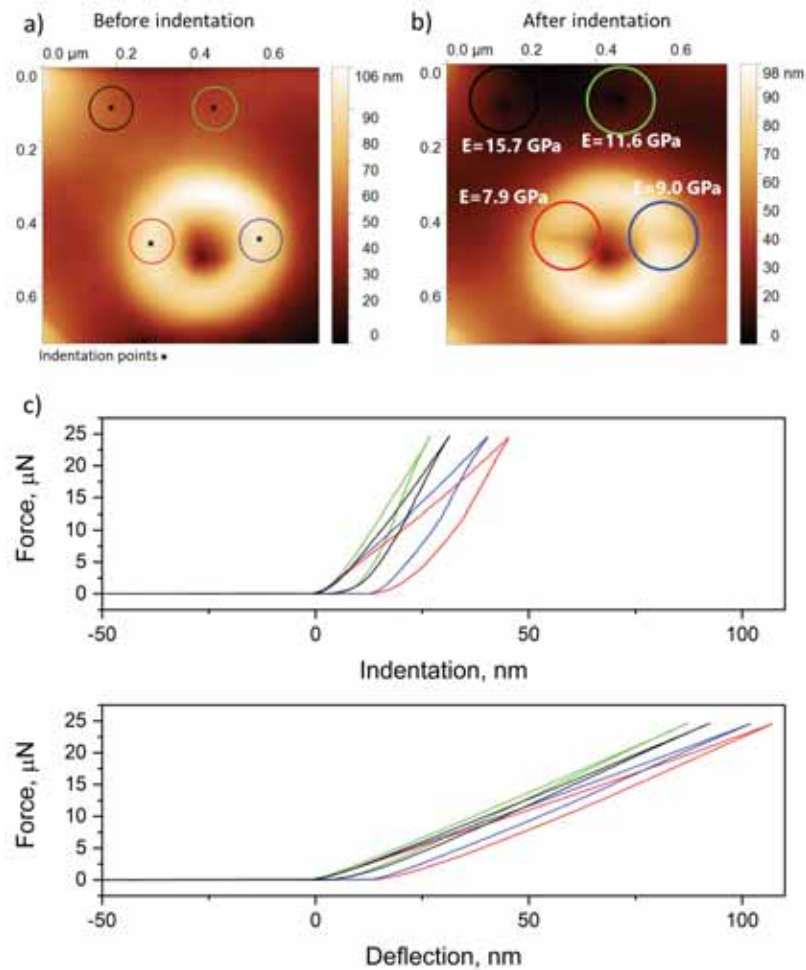
Figure 57. Inner surface of a frustule measured by the stiff diamond probe (k=400 N/m). a) Topography before nanoindentation, b) topography after nanoindentation with

indicated Young's modulus values calculated using DMT model, c) force-indentation and force-deflection curves collected at specific indentation points. [1]

We also performed indentation at specific points on the inner surface of the cleaned frustule by applying different indentation force, as indicated in Figure 58a.
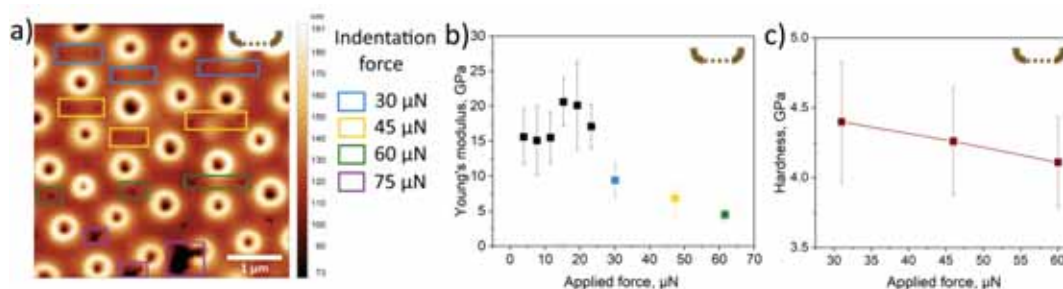
Figure 58. AFM indentation at specific points of a cleaned inner valve. a Inner surface of a frustule measured by the stiff probe after indentation at specific points by applying different indentation force, b Young's modulus calculated using the Derjaguin-Muller-Toropov (DMT) model at different applied forces after averaging over 10 points, c the dependence of hardness on the applied force. [1]

Young's modulus calculated from these data using the DMT model (Figure 58b) show the same trend as for the reference fused silica sample (Figure 57), i.e., correct values are at the applied force below 20 μN where the tip-surface contact geometry may be approximated by a sphere and interaction is mainly elastic. At higher forces the model does not fit well because the contact geometry deviates from the spherical one, while at 75 μN the valve breaks. Hardness calculated as a ratio of the maximum indentation force to the indent area is between 4.0 and 4.5 GPa and slightly decreases with increasing loading force,

which is typical for nanohardness measurements (Figure 58c).[192] Similar behaviour was observed on the reference fused silica sample (Figure 57). The hardness of the measured cleaned inner valve was significantly higher as compared to the previously reported[39] values obtained on the outer porous layers ((0.033 - 0.116 GPa) – at the center, (0.076 - 0.120 GPa) – at the edge). The Young's modulus values obtained in our study were higher than in the study by Losic et al.[39], where they varied from 0.591 to 2.768 GPa at the center of the frustule and from 0.347 to 2.446 GPa closer to the edge.

Young's modulus on the cribrum in Figure 55 appears smaller than on the thicker parts of the sample. It can be explained by the fact that the cribrum is so thin that during force-distance curve acquisition it bends as a membrane even at low applied force (100 nN). In this case the obtained values of Young's modulus do not correctly reflect properties of the material. In order to obtain more accurate results for the cribrum, we used a gentler AMFM viscoelastic mapping method[193], in which the AFM cantilever scans the sample's surface in the tapping mode in the repulsive regime[194] being excited simultaneously at two resonance frequencies. The results are shown in Figure 59.
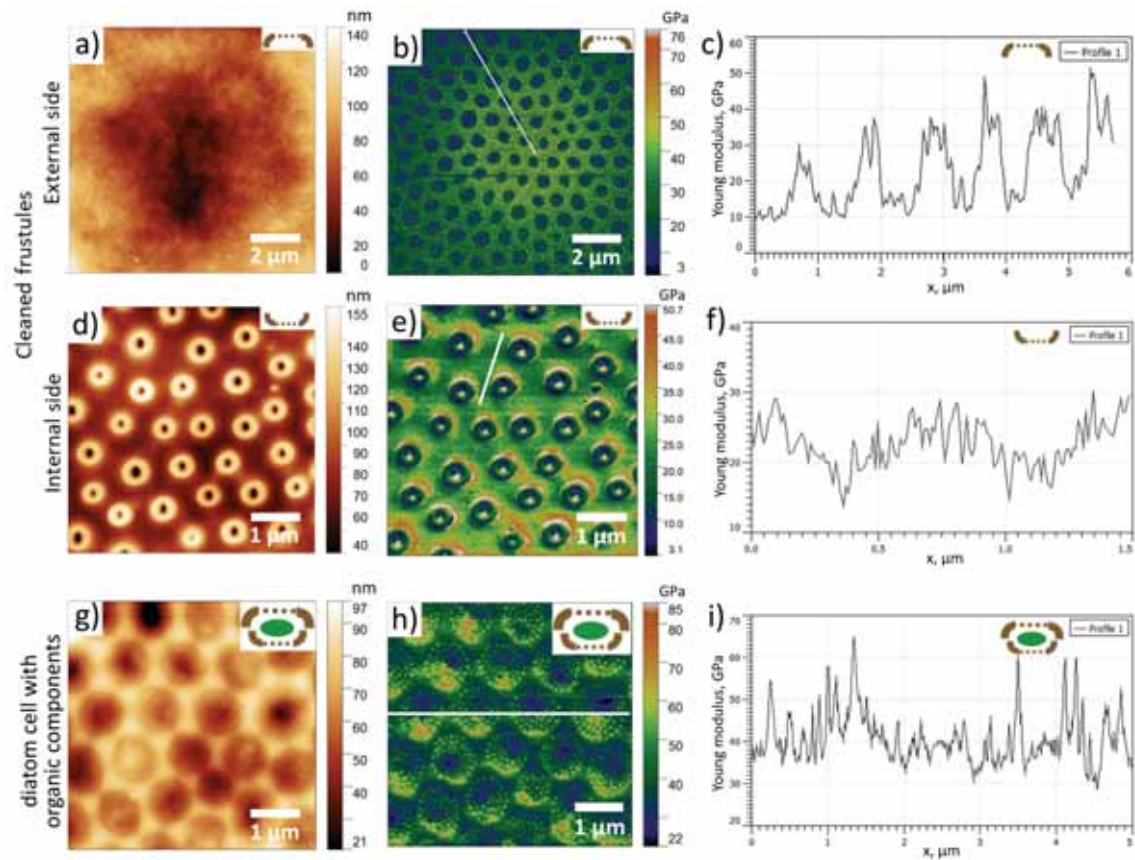
Figure 59. The AMFM study of cleaned frustules and wet diatom cells. External side of the cleaned valve: a) Topography, b) The AMFM Young modulus, c) The AMFM Young modulus profile along the white line shown in Figure 60b. Internal side of the cleaned valve: d) Topography, e) The AMFM Young modulus, f) The AMFM Young modulus profile along the white line shown in Figure 60e. External side of the wet diatom cell: g) Topography, h) The AMFM Young modulus, i) The AMFM Young modulus profile along the white line shown in Figure 60h.

The AMFM Young's modulus is up to two times higher than the modulus calculated from the force-distance curves. On the outer surface of the cleaned frustule

Young's modulus of the cribrum is about 3 times lower than of the thicker space in between, while on the wet diatom cell, where the inorganic frustule is supported by the organic interior, the difference almost vanishes. This result implies that Young's modulus calculated on the cribrum from the force-distance curves is indeed affected by the membrane effect and is lower than the real one.

To get deeper insight into mechanical properties of the cleaned valve we acquired force-distance curves from the edge towards the center of the outer surface along green lines shown in Figure 60a using the stiff diamond probe. The maximum loading force of 7.7 µN falls into the elastic regime (without indentation) and the frustule's outer surface bends as a membrane under the load. The results showed that the bending increases from the side towards the center of the valve. Young's modulus calculated using the Hertz fitting model decreases as the distance from the edge towards the center of the valve increases. There is a strong correlation between MEMS' performance and the mechanical properties of the materials they are constructed from. By selecting, designing, fabricating, and packaging materials in accordance with mechanical properties, some of the mechanical failure modes may be eliminated[195]. Polysilicon, the most frequently used MEMS material, has Young's modulus mostly in the range between 160 and 180 GPa, similar to single-crystal silicon (160 – 190 GPa)[195]. Silicon-carbide and silicon-nitride are also promising MEMS materials having Young's modulus values determined by indentation method 395 GPa and 101 – 251 GPa, respectively[195]. Silicon oxide is often included in MEMS devices (e. g. as a sacrificial material in polysilicon surface micromachining), but has low stiffness and strength (64 GPa)[195].

6.4 Compliance of cleaned frustules: Static vs. dynamic approach

The data obtained was used in combination with the analytical model for circular membrane deformation given by Melnikov[196]. The Green's function of a point force G(z,ζ) for Kirchhoff plates satisfies the equation:

$$\nabla^4 G(z,\zeta) = \delta(z - \zeta) \tag{3}$$

where $D = Eh^3/12(1 - v^2)$ is the flexural rigidity of the diatom valve given in terms of Young's modulus E, thickness h and v is Poisson's ratio, while $z = r(cos\varphi + i\ sin\varphi)$ and $\zeta = \rho(cos\ \psi + i\ sin\ \psi)$ represent the observation point and the force application point, respectively. The solution is given by:

$$G(z,\zeta) = \frac{1}{8\pi D}\left[\frac{1}{2a^2}(a^2 - |z|^2)(a^2 - |\zeta|^2) - |z - \zeta|^2 ln\ \frac{|a^2 - z\bar{\zeta}|}{a|z - \zeta|}\right] \tag{4}$$

where a is the radius of the diatom. By fitting the model to experimental observations, the membrane flexural rigidity can be used to determine the overall apparent Young's modulus of the diatom valve as a circular membrane. The compliance defined as the measure of the structure deformation under the action of external forces was calculated as the reciprocal of rigidity. The dependence of compliance on the relative radial position calculated using influence function of a point force is shown in Figure 60b. Maximum similarity with the experimental values was achieved at h=477 nm and E=9.35 GPa. In the study by Shubham et al.[132], the mechanical compliance of a semiconstrained polysilicon diaphragm with peripheral and center protrusions on the backplate is calculated to be 7.154 ×10⁻³ m/N, which is in good correspondence with our results, as demonstrated in Figure 60b.
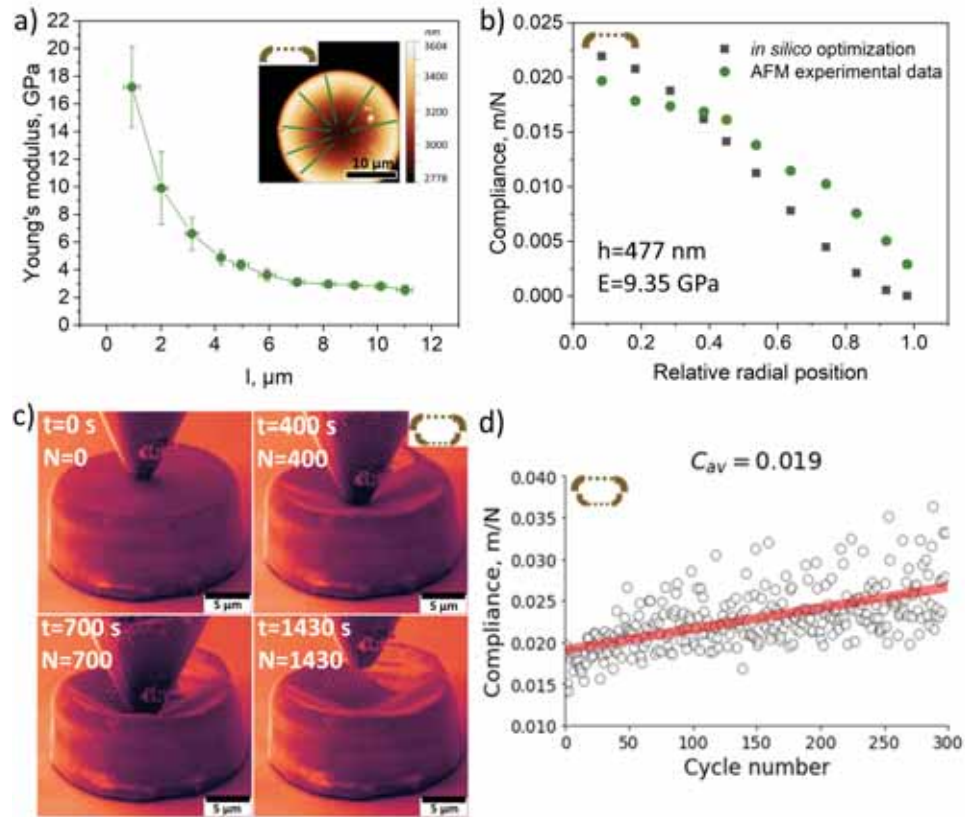
Figure 60. Compliance of cleaned frustules: static vs. dynamic approach. A) Young's modulus depending on the distance from the edge towards the center of the outer surface of the valve. Inset: topography of outer surface of a cleaned frustule. The measurements were carried out using AFM by pressing the diamond probe on the sample with a force of 7.7 µN along each green line. b) Compliance vs. relative radial position calculated using the Green's function of a point force, c) SEM images of whole diatom frustule acquired during different stages of nanoindentation in the SEM column, d) Calculated compliance vs. cycle number. [1]

The results of cyclic loading (amplitude 1 µm, period 1 s) performed on cleaned diatom frustule in the SEM column are shown in Figure 60c and Figure 61. Based on the

dependence of the displacement on time, considering sinusoidal motion represented as A·sin(ωt), we found the stiffness and subsequently compliance as a function of cycle number, as presented in Figure 60d. Compliance increases with increasing number of cycles. The average compliance was found to be 0.019. The frustule begins to break along one edge after ca. 300 s, but continues to oscillate during cyclic loading without complete rupture. Figures 61a-d show the analysis of vibration behaviour of upper diatom valve, while Figure 61e-h represent the analysis of the whole frustule.
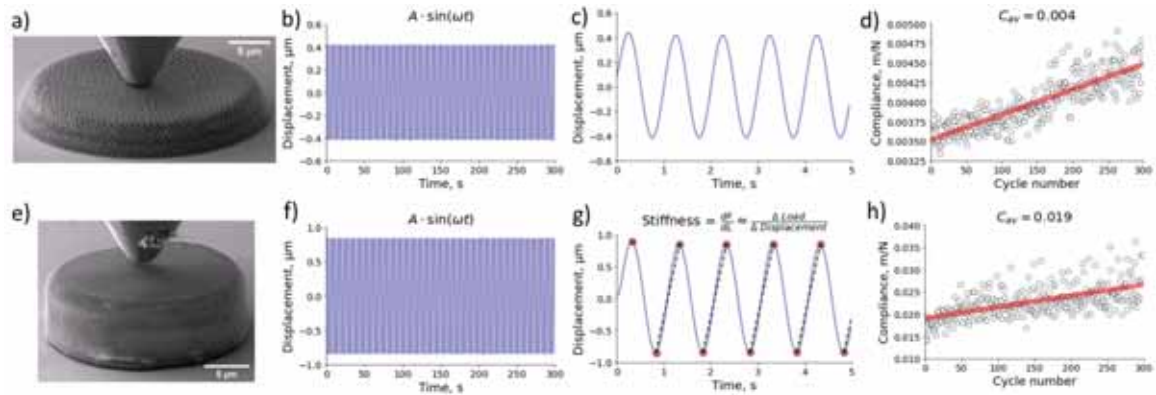
Figure 61. a) SEM image of a measured cleaned diatom upper valve, b) Displacement vs. time, the whole region – 300 seconds, c) Displacement vs. time, a short time interval – 5 seconds, d) Compliance vs. cycle number, e) SEM image of a measured cleaned diatom frustule, f) Displacement vs. time, the whole region – 300 seconds, g) Displacement vs. time, a short time interval – 5 seconds, h) Compliance vs. cycle number. Amplitude 1 µm, period 1s. [1]

Considering the deformation response of the frustule valve to local indentation illustrated in Figure 62, the total compliance of the system can be written as the sum of the local material compliance under the indenter, C_L, and the global structural compliance C_G:

$$C = \frac{\delta+u}{F} = \frac{\delta}{F} + \frac{u}{F} = C_L + C_G \tag{5}$$
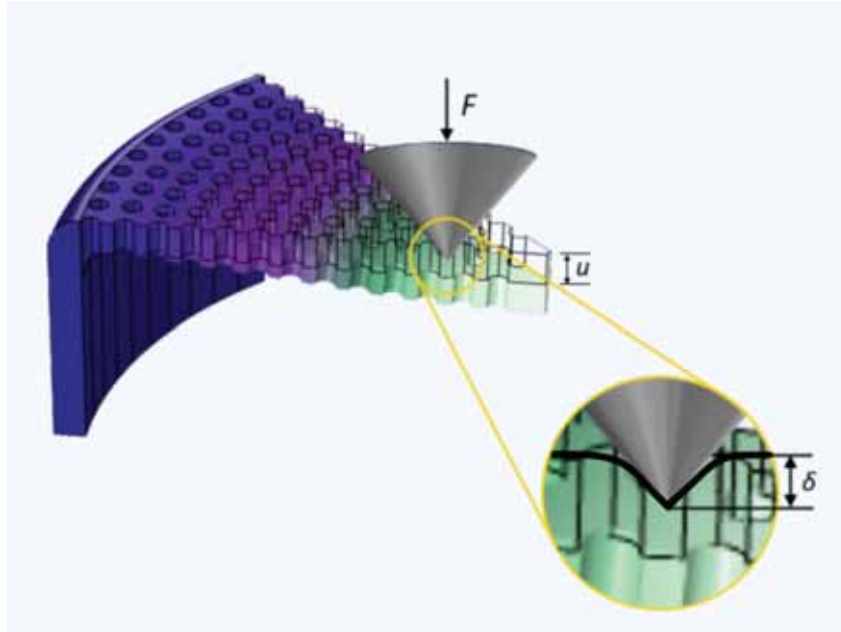
Figure 62. The deformation response of the frustule valve to local indentation [1]

It is well known from the literature for elastic[197,198] as well as plastic indentation[199] that the force-displacement relation is described by a power law function of the type $F \cong \delta^{(1+m)}$, where m>0. Therefore, the local compliance decays with increasing applied force as $C_L \cong F^{-m}$, whilst the global compliance C_G remains appreciably constant within the range of forces for which the structural deflection remains elastic. By the same argument, the local compliance C_L dominates over global compliance C_G for small applied forces. This transition between the two regimes takes place over a range of loads that depend on

the material properties and the indenter shape. It can therefore be concluded that both the local material and global structural responses can be interrogated via the suitable choice of loading conditions and indenter tips under the small and large applied forces, respectively. Both local and global effects can be considered together only once the global compliance has been calibrated.

6.5 In situ SEM nanoindentation

We also performed static in situ nanoindentation inside SEM on dried cells with cellular material (Figure 63a) as well as cleaned diatom frustules (Figure 63b) and based on the force- displacement curves we analyzed their mechanical performance. Static studies lead us to a more precise definition of the module of a material as a whole. Figure 63c shows the force-displacement curves of dried cells, which vary depending on the orientation and size. As can be seen, dried cells 1-4 (diameter, 37-40 µm; height, 11-13 µm) have a similar size and mechanical behaviour, which is different from the dried cell 5, whose diameter/height ratio is smaller (diameter, 41 µm; height, 18 µm). On the other hand, we observed a difference in mechanical performance when indenting a dried cell 6 from the girdle band point.
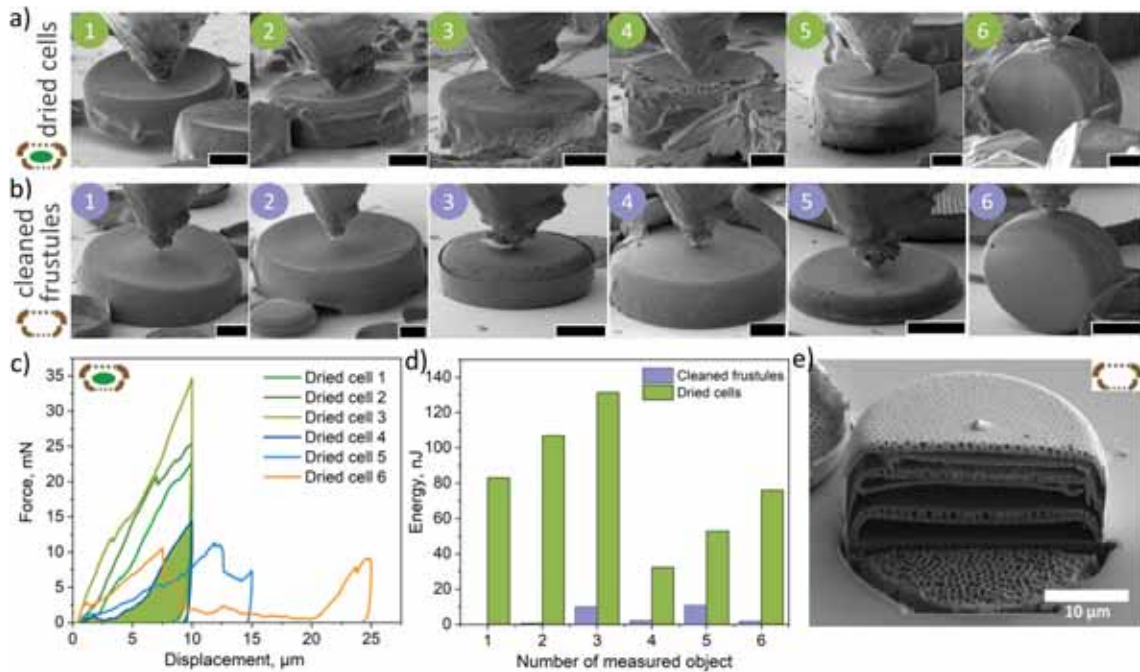
Figure 63. In situ SEM nanoindentation of cleaned frustules and dried diatom cells. a) SEM images of air-dried diatom cells measured by nanoindentation in the SEM column, b) SEM images of cleaned frustules. Scale bar, 10 µm. c) Force-displacement curves obtained during indentation of dried cells, d) Calculated area under the force-displacement curves of dried and cleaned diatoms equal to work done, e) The case of a layered structure of the frustules of some diatoms, potentially responsible for difference in the obtained force-distance curves. [1]

The nature of the curves of cleaned frustules and dried cell with organic material is different (Figure 64). Also, the forces are significantly lower in the case of cleaned frustules, as well as the area under the curves, which is equal to work done on the object (Figure 63d). With the help of AFM, we made local indentations which gives us more information about material, however we did not completely deform the structure, as in the

185

case of nanoindentation in SEM column performed with the blunt tip indenter. The differences between the values can also be attributed to the layered "burger" structure within the frustule of some diatoms, as demonstrated in Figure 63e. This situation can occur in old cultures when the process of cell division is corrupted and formation of the valves is not accompanied by cytokinesis. The combination of organic and inorganic components in diatom cells, leading to their superior mechanical characteristics, can serve as an inspiration for layer-by-layer assembly, which can be used to modify the inorganic substrate for the manufacture of multilayer composites.[200]
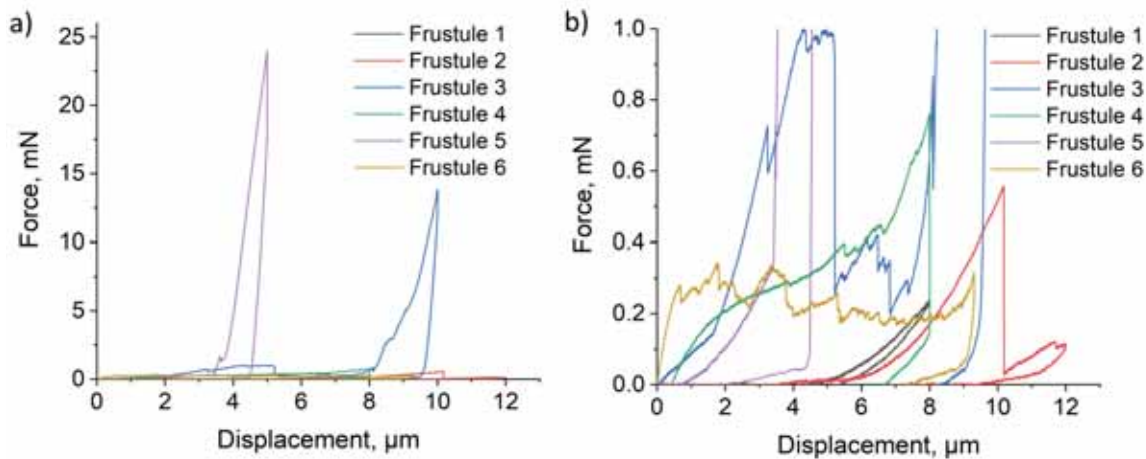
Figure 64. Force-displacement curves of cleaned frustules obtained by in situ SEM nanoindentation. a) force-displacement curves for forces up to 25 mN, b) magnified view of force-displacement curves for forces up to 1 mN. [1]

6.6 Vibrational eigenmodes of diatom frustules

In recent times, there has been a surge of interest in leveraging natural structures as a source of inspiration for innovative engineering solutions, showing the potential of biomimicry. One particularly intriguing avenue of research involves the utilization of diatom algae frustules ~~as an inspiration~~ for fabricating an array of micro- and nanoelectronic devices[126,135,201–203]. As already mentioned in this chapter, the high mechanical strength, small size, low density, optical properties and tailored nanostructures, have inspired researchers to explore their potential in the development of MEMS and NEMS devices with improved performance, efficiency, and longevity[1,137,204]. The dimensional and structural congruence observed between diatom exoskeletons and advanced devices, including PICs and MEMS microphones, represents a promising foundation for exploring additional avenues in the realm of nanotechnology component development through the application of biomimetics and biotechnology[1,129,131].

The resonant frequencies of MEMS devices play a crucial role in their design and performance optimization as they determine the dynamic behavior of the devices and significantly impact their functionality, efficiency, and reliability. Hence, understanding the resonant frequency characteristics of MEMS devices inspired by diatom algae frustules is of paramount importance. Resonant frequencies play also an important role in the characterization of other biological objects, including red blood cells[205], bacteria[206,207], virus[208], algae[209], etc. Zinin et al.[206] found that the natural vibrations of specific bacteria are in MHz range by solving the dispersion equation using a shell model that accounts for

the elastic properties of the membrane and the associated viscosities of the cytoplasm and the surrounding fluid.

Vibrational modes of diatom silica frustules have been an object of research, but primarily through the utilization of FEM as reported by Abdusatorov et al.[137] who explored the potential of using diatom silica frustules for vibrational MEMS applications. The results showed that diatom frustules have natural frequencies in the range between several ~~MHz~~ and tens of MHz and are determined by the stiffness and density of the material, the valve diameter, and the wall thickness of the frustules. Gutierrez et al.[210] investigated the mechanics of centric diatom frustules using the FEM in combination with morphology and material properties obtained from SEM and mechanical tests respectively. The study reveals that the first ten deformation modes correlate noticeably well with deformation patterns observed through SEM. A quadratic correlation was observed between the pore size and the critical buckling load, alongside a cubic relationship between the thickness of the frustule and the critical buckling load. The findings in this research provide insights into the mechanical response of diatom frustules that can aid the realization of tailored properties in new bio-inspired materials, in particular for nanotechnology applications, but also for advanced metamaterials and optomechanical devices.

Despite these notable advancements, further exploration and experimental validation of the resonant frequency characteristics of MEMS devices inspired by diatom algae frustules are warranted. We conducted the first experimental study of vibrational modes of a diatom silica frustule and compared the obtained results with computational data. The numerical simulations utilize FEA to model the dynamic response of the

frustules. This numerical approach allows for the evaluation of resonant frequencies based on the frustules' geometric and material properties, providing insights into their inherent mechanical behavior.

To experimentally validate the numerical findings and provide precise measurements of resonant frequencies of individual diatoms, two different methods to register vibrations were employed using an AFM optical detection system: (1) thermal spectra collection and (2) an external mechanical excitation followed by detection via a lock-in amplifier, which are described in the supplementary material. These experimental techniques allow for the direct observation of the frustules' dynamic behavior, providing valuable data for comparison with the numerical simulations.

As a model we used the same diatom frustules as for the study of mechanical properties – *Coscinodiscus oculus-iridis*. Firstly, we performed numerical calculations of eigenfrequencies of diatom frustule, taking into account its geometry, silica density, Young's modulus, and Poisson's ratio (Table 6) and applying Comsol Multiphysics Structural Mechanics module to obtain the simulation results, as illustrated in Figure 65a.

Table 6. Diatom model parameters

Frustule diameter	D=60/70/72 μm
Frustule thickness	t=1 μm
Frustule height	15 μm
Pore diameter	0.6 μm
Silica density	ρ=2300 kg/m^3
Poisson's ratio	ν=0.17

Young's modulus	E=15 GPa

For experimental validation samples were prepared by welding a frustule to an AFM Si cantilever chip by FIB, followed by sputtering a ~ 30 nm thick layer of gold on top of the frustule on order to increase laser reflectance (Figure 65b). The AFM measurements were performed by collecting thermal spectra from a still sample (Figure 65c), and by measuring the amplitude-frequency response from the sample which was externally excited by a piezodriver (Figure 65d).
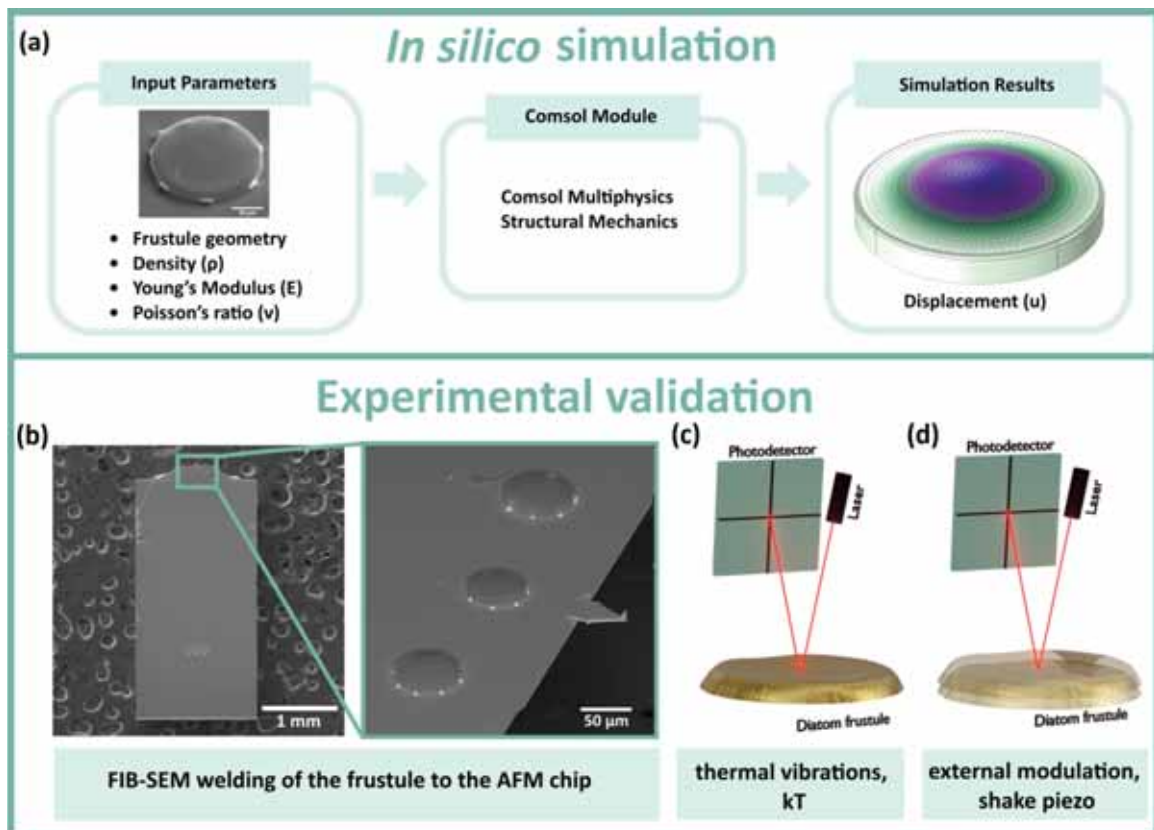
Figure 65. a) Flowchart of modelling steps using COMSOL Multiphysics. b) SEM image of AFM chip after FIB-assisted welding of diatom frustules, right: enlarged view of the samples. Schematic illustrations of two AFM approaches: c) thermal vibrations, d) external modulation. (Cvjetinovic J. et al. Probing vibrational eigenmodes in diatom frustules: a combined *in silico* study and atomic force microscopy-assisted measurements. Ready for submission to Applied Physics Letters)

The thermal frequency spectra obtained from different parts of the diatom frustule are shown in Figure 66a. They show that the vibration amplitude is position sensitive which corroborate the computational results, shown in Figure 66b. The experimental eigenfrequency values closely match those obtained by COMSOL calculations (1.93, 3.20, 3.65, 4.68, 5.43, 7.68 MHz) and highlighted by the color bars. The majority of the resonance peaks were ascertained through measurements conducted on the elevated region of the valve.
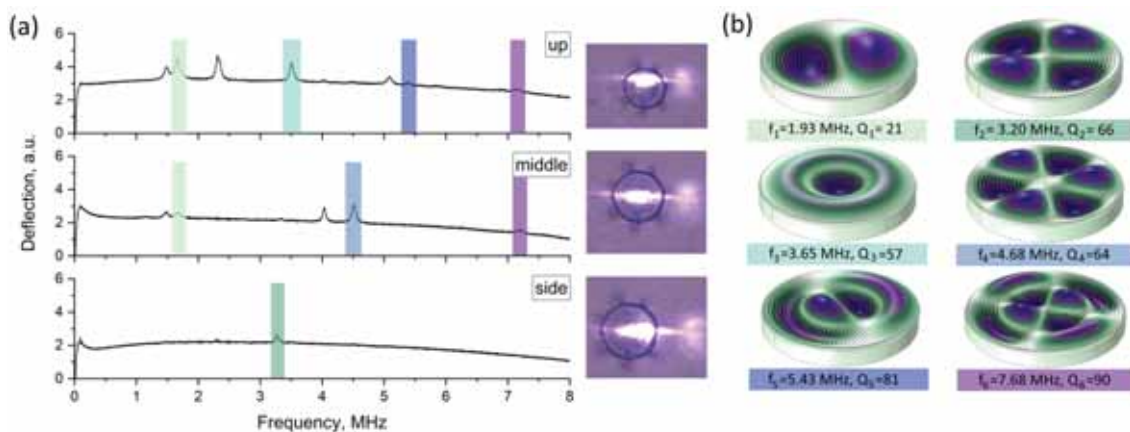
Figure 66. a) Experimental thermal spectra collected from different parts of the diatom frustule, as shown in the optical microscopy insets on the right side. The spectra were

smoothed to avoid spurious spectral lines. The raw spectra are shown in Appendix B. b) Calculated vibrational eigenmodes of diatom frustules with indicated frequencies and quality factors. (Cvjetinovic J. et al. Probing vibrational eigenmodes in diatom frustules: a combined *in silico* study and atomic force microscopy-assisted measurements. Ready for submission to Applied Physics Letters)

Using the peaks in Figure 66 we calculated quality factors ranging from 21 to 90 (Table 7). The quality factor (Q) was calculated based on the obtained thermal frequency spectra using the equation: $Q = f / \Delta f$, where f is the resonant frequency, and Δf represents the full-width at half-maximum (FWHM) of the resonance peak. The rigid nature of the diatom's silica cell wall contributes to the preservation of oscillation energy, resulting in high-quality oscillations characteristic of these microorganisms. As demonstrated in the work by Zinin, qualities of the quadrupole vibrations for different types of cells range from 0.8 (E. coli) to 23.2 (Carota).[206] It appears feasible for various types of bacteria characterized by a rigid cell wall to exhibit natural oscillations possessing a sufficiently high quality factor. While higher quality factors are generally desired in MEMS microphones to improve their sensitivity and performance, quality factors below 100 can still be suitable for certain applications with specific requirements, for example where a wider bandwidth is required rather than high sensitivity[211,212].

Inomata et al.[213] proposed a novel method for controlling the quality factor of mechanical resonators using a variable phononic bandgap on periodic microstructures. They showed how the vibration spectra of the resonator with 5.79 MHz resonant frequency

and Q-factor of 42,960 and 82,690 appeared at a displacement of 150 μm and 200 μm, respectively. The quality factors exhibited a hierarchical ranking, with the highest values observed in the following order: periodic microstructure, periodic microstructure with waveguide, non-periodic microstructure, and finally, the plain sample. As the resonant frequency exhibited an increment, a corresponding decrease in the quality factor was noted. Mechanical resonators characterized by shorter dimensions demonstrated higher resonant frequencies. Furthermore, a larger surface-to-volume ratio was found to be associated with a decrease in the quality factor due to increased energy loss from the surface. Similarly, a smaller length-to-width ratio resulted in higher energy loss via the supporting component, leading to a decline in the quality factor.

Experimentally obtained and calculated resonant frequencies as well as calculated quality factors are shown in Table 7.

Table 7. Experimentally obtained and calculated resonant frequencies and quality factors

Calculated frequency, MHz	Position	Peak №	Resonant frequency, MHz	FWHM, MHz	Q
0.93		1	1.48	0.09	16
1.93		2	1.67	0.08	21
3.20	Side up	3	2.32	0.08	28
3.65		4	3.50	0.06	57

4.68		5	5.09	0.08	64
5.43		6	5.40	0.07	81
6.38		7	7.16	0.13	56
7.68	middle	1	1.48	0.07	21
		2	1.68	0.07	24
		3	4.03	0.06	67
		4	4.51	0.07	64
		5	7.19	0.08	90
	middle-side	1	3.28	0.05	66

The observed peaks were successfully replicated in subsequent measurements conducted on the identical sample which was not welded to the chip by FIB (Figure 67).
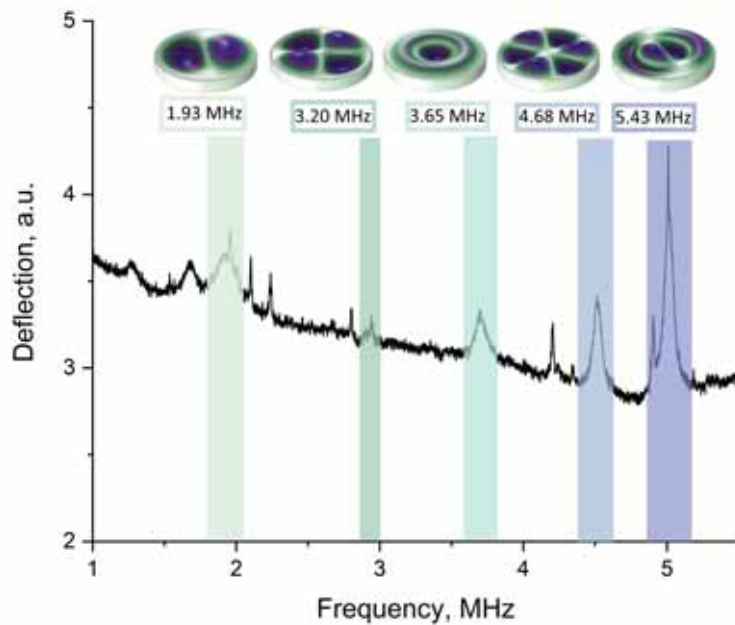
Figure 67. Thermal spectra of the diatom frustule with calculated eigenmodes.

Amplitude-frequency spectra of different parts of the diatom frustule obtained by external mechanical excitation are shown in Figure 68. Besides the pronounced background signal from the substrate in the frequency range below 1.5 MHz, two peaks can be distinguished at about 2 MHz, which is in agreement with the thermal spectra data. Intensity of these peaks is position sensitive. Higher order resonances were below the detection sensitivity.
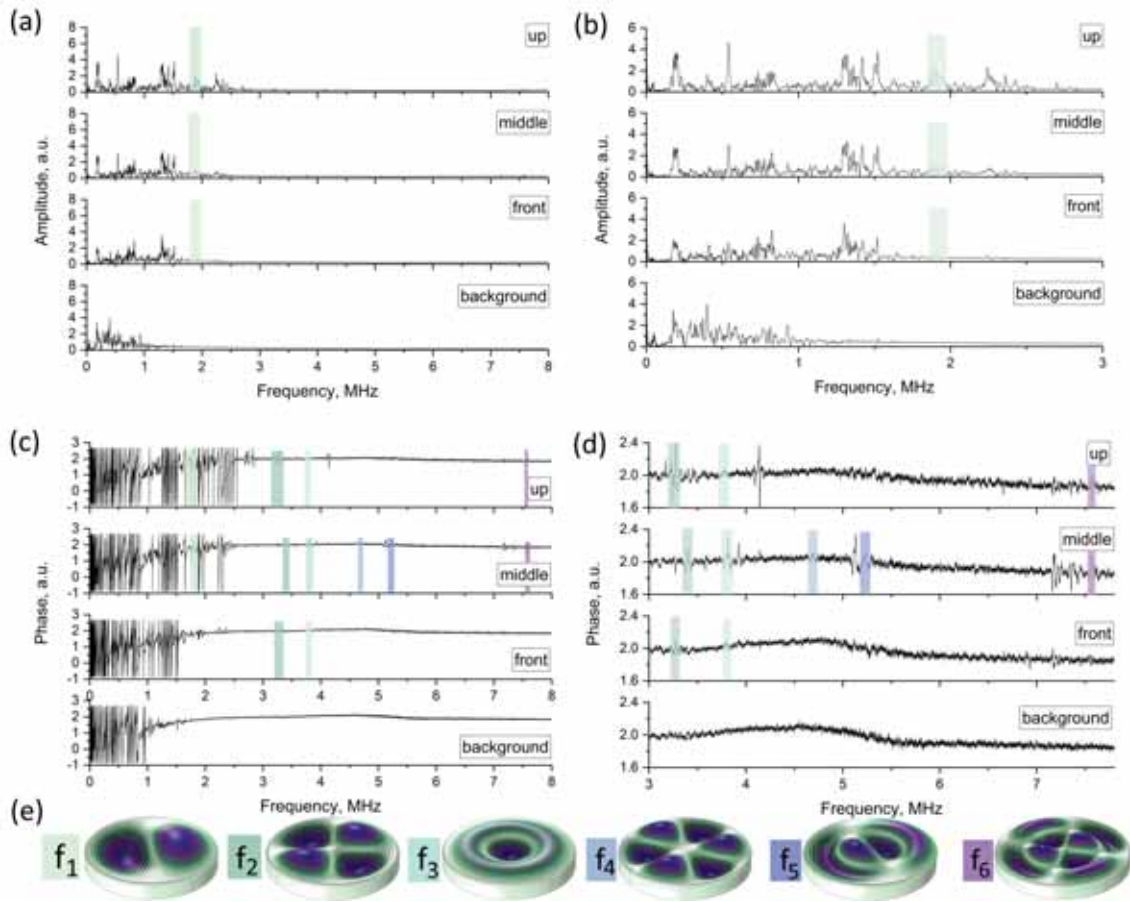
Figure 68. Amplitude-frequency spectra of different parts of diatom frustules obtained by mechanical excitation in the region: a) 0-8 MHz, b) 0-3 MHz. Phase frequency spectra collected at different positions in the region: c) 0-8 MHz, d) 3-7.8 MHz. (Cvjetinovic J. et al. Probing vibrational eigenmodes in diatom frustules: a combined *in silico* study and atomic force microscopy-assisted measurements. Ready for submission to Applied Physics Letters)

We also applied both techniques to measure three diatom frustules with diameters 60, 70 and 72 μm, as shown in Figure 69. Table 8 shows calculated resonant frequencies for all three diatom frustules.

Table 8. Calculated resonant frequencies for diatom frustules with diameters 60, 70 and 72 μm

Mode №	Calculated frequency for D=60 μm, MHz	Calculated frequency for D=70 μm, MHz	Calculated frequency for D=72 μm, MHz
1	1.29	0.93	0.89
2	2.62	1.93	1.82
3	4.35	3.20	3.03
4	4.96	3.65	3.45
5	6.36	4.68	4.43
6	7.30	5.43	5.14
7	8.67	6.38	6.04
8	9.66	7.68	7.28

The measured thermal spectra vibrations possess position sensitivity, but had much lower amplitude. The mechanical excitation vibrations showed resonance peaks at about 2 MHz as in the case discussed above.
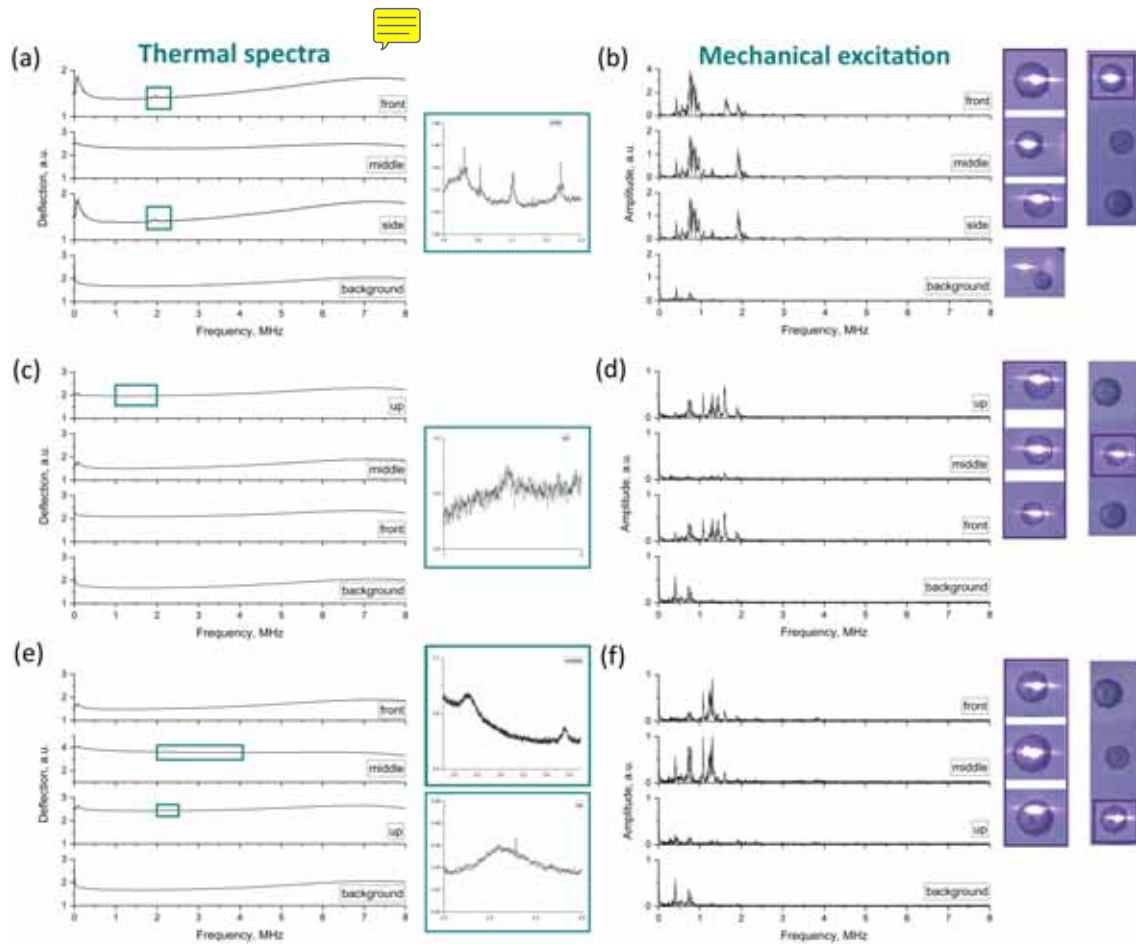
Figure 69. Thermal vibration spectra of diatoms with diameter: (a) 72 μm, (c) 60 μm, (e) 70 μm, with enlarged view of peaks on the right. Externally modulated vibration spectra of the same diatoms. Optical microscopy images of the samples and positions of the laser spot are shown on the right. (Cvjetinovic J. et al. Probing vibrational eigenmodes in

diatom frustules: a combined *in silico* study and atomic force microscopy-assisted measurements. Ready for submission to Applied Physics Letters)

Different sensitivity for different samples might be explained either by different properties of the samples or by specifics of the optical detection system of AFM. The optical detection system is optimized to measure an AFM cantilever deflection angle rather than direct displacement [214]. The incident laser beam is reflected from a cantilever into a photodetector. The cantilever deflection $\Delta\theta = \frac{3}{2}\frac{\Delta z}{l}$, where Δz is the cantilever displacement and l is the cantilever length, leads to change in the laser reflection by $2\Delta\theta$ and shift of the laser spot on the photodetector, which is measured. This means that the measured vibration amplitude depends not only on the actual surface displacement, but more on how this displacement is transferred into the reflection angle, which depends on the laser position on the surface and the surface geometry. The sample which demonstrated the highest vibration amplitudes possess a 1.5 μm dome-shaped valve in the middle (Figure 70), and the valve slope may facilitate transfer of the surface displacement into the laser reflection angle change. Surface with lower curvature may transfer surface displacement into the laser reflection angle change to a lower degree, which may explain the observed variation in vibration amplitudes obtained from different samples.

The cantilever deflection leads to change in the laser reflection angle, which is detected by the photodetector. This means that the measured vibration amplitude depends not only on the actual surface displacement, but more on how this displacement is

199

translated into the reflection angle, which depends on the laser position on the surface and the surface geometry.
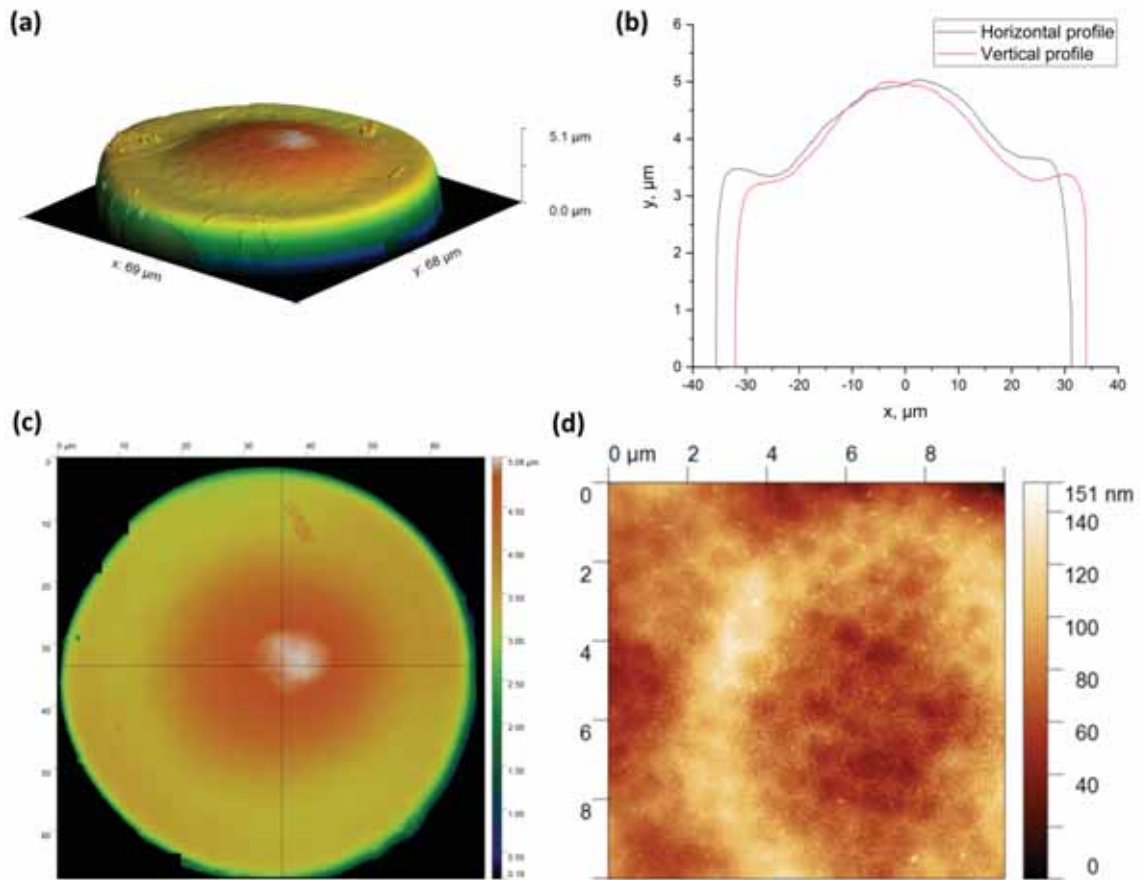
Figure 70. a) 3D AFM image of the diatom frustule. b) Horizontal and vertical profiles of diatom frustule as shown in the image c). d) Topography of the surface layer. (Cvjetinovic J. et al. Probing vibrational eigenmodes in diatom frustules: a combined *in silico* study and atomic force microscopy-assisted measurements. Ready for submission to Applied Physics Letters)

The deformation modes of the diatom frustule are similar to those of circular membranes, which are described by Bessel functions[215]. Gutierrez et al.[210] highlighted the importance of considering the curvature of the dome-shaped valve in the creation of a computer-aided design (CAD) model approximating a centric diatom frustule. However, they pointed out that a different curvature could be used instead of that chosen for the CAD model, or the frustule could be considered flat, suggesting that such changes are unlikely to significantly change the deformation modes of the structure. Here, we considered flat diatom frustule based on the SEM images. However, AFM scanning showed the 3D image of the frustule having the dome in the middle (Figure 70 a-c).

The simplified model utilized in this study disregards the intricate and multi-layered structure of diatom frustules, comprising three distinct layers possessing varying thickness, pore sizes, and pore distributions. Such structural complexity is known to impact the mechanical properties of diatom frustules, thereby potentially influencing their vibrational characteristics.

Two main factors that compete to determine the resonance frequency are mass changes and stiffness changes due to the porosity of the membrane. As the number of pores increases, the mass of the membrane decreases, which can lead to an increase in the resonance frequency. On the other hand, as the number of pores increases, the stiffness of the membrane decreases, which leads to a decrease in the resonance frequency.

In addition to these two factors, the study by Yoon et al.[216] found that the geometric structure of the pores can also have a significant impact on the resonance frequency of porous graphene membrane which can be useful for designing and optimizing graphene-

based devices for various applications such as sensors, actuators, and resonators. By changing the shape or orientation of the pores, the resonance frequency can fluctuate meaningfully, starting from 7.86 MHz (porosity, 10 %; number of pores, 6) to 16.1 MHz (porosity, 20 %, number of pores 3). Even though the frequency values are in the same range as we obtained in this study, the porosity of diatom frustules varies a lot depending on the layer. For example, the porosity of the cribrum layer of *Coscinodiscus* sp. (25.2 ± 2.5%) is significantly higher than that of the cribellum (7.5 ± 1.2%)[124]. Another study showed that when the diameter scale, pore size, and density of diatom frustules decrease, their natural frequencies increase[137]. Besides, frustules with lower stiffness and thickness vibrate at lower frequencies than frustules with higher stiffness and thickness.

Han Je et al. designed a surface-micromachined capacitive microphone consisting of a membrane center hole and back-plate supports with improved sensitivity and frequency response, which looks similar to diatom frustule[131]. In the proposed microphone, the resonant frequency of the back-plate is increased from 86 to 853 kHz by the back-plate supporting beams. Westerveld et al.[129] fabricated a ultrasound sensor based on silicon photonics technology that achieves remarkable sensitivity through the implementation of an innovative optomechanical waveguide. The waveguide employs two movable components with a highly confined 15 nm air gap, consisting of a silicon dioxide lower cladding and an upper cladding (membrane) structure. The performance of the resulting 20 μm sensor operating within the range 3-30 MHz, surpasses that of piezoelectric elements of equivalent dimensions by two orders of magnitude.

Understanding the eigenfrequencies exhibited by diatom frustules holds significance in comprehending their mechanical attributes, including stiffness, elasticity, and bending strength, thereby facilitating the design and fabrication of nanoscale devices like sensors, filters, and photonic devices. Furthermore, it can potentially serve to establish an avenue for taxonomic classification and species identification of diatoms, as they are vital indicators of environmental changes owing to their remarkable sensitivity to various environmental parameters[217]. Therefore, the measurement of frustule eigenfrequencies in sediment or fossil archives holds promise in revealing structural transformations and mechanical traits over geological time scales, thereby providing valuable inferences concerning past environmental conditions.

6.7 Summary

Static and dynamic mode AFM and in-SEM nanoindentation revealed the peculiarities of mechanical performance. Significant differences in the nanomechanical properties of the different frustule layers were observed. Furthermore, the deformation response depends strongly on silica hydration and on the support from the internal organic content. The AMFM viscoelastic mapping method gave up to two times higher Young's modulus values of the measured samples compared to the values calculated from the force-distance curves. Besides static *in situ* nanoindentation measurements, the behavior of the frustule was reported for the first time under the cyclic loading, which is vital for the application of diatom-like structures in MEMS devices. The nanoindentation measurements in the dynamic mode showed that the average compliance of a cleaned frustule is 0.019 m/N.

The intricate architecture of diatom frustules, combined with their unique properties, offer tremendous potential for the development of advanced MEMS devices. We aimed to investigate the resonant frequency characteristics of diatom algae frustules by employing combination of numerical simulations and experimental characterization using AFM technique. Numerically predicted eigenfrequencies of centric diatom frustule in the range 1-8 MHz were in good agreement with experimental data provided by AFM. We believe that our findings will contribute to a deeper understanding of the relationship between the structural attributes of diatom frustules and the resonant frequencies of MEMS devices, enabling the development of more efficient and optimized devices for a wide range of applications.

Chapter 7. Optical properties of diatoms

In this chapter the mechanisms behind diatom optics ~~using approaches like the Fourier modal method~~ have been presented and analyzed. By investigating how changes in cell wall geometry influence the interaction of light with periodic microscale structures, the optical effects of diatoms can be understood in more detail.

7.1 Background

The Fourier modal method provides an efficient approach for modeling the optical phenomena exhibited by periodic microscale structures in diatom frustules, such as light diffraction and interference. Diatoms provide a model system for understanding how to engineer microscale and nanoscale structures with precise control over their optical properties. Analyzing the diffraction of light by diatoms under different conditions also enables their properties to be applied for biosensing, such as detecting shifts in factors like pH, salinity, temperature, and the presence of chemicals.

When studying diatom frustule, two important factors need to be considered from an optical point of view. The first factor is the physical dimension of the periodic structure, which includes the number of porous silica layers, the thickness of each layer, and the size of the holes within the material. These parameters can affect how the material interacts with light, including how it scatters, diffracts, or guides light. The second factor is the refractive index contrast, which is created by the complementarity of silica (with a refractive index of approximately 1.45) and air pores (with a refractive index of 1) in the visible range. The refractive index contrast refers to the difference in refractive index between the silica-based material and the air pores within it. Silica has a higher refractive

index than air, which means that light will bend differently when passing through the material compared to when passing through air. This contrast is important for enabling and quantifying certain optical properties, such as light diffraction through silica/air patterns.

Overall, understanding these two factors is important for studying the optical properties of silica-based materials, particularly in relation to how they interact with light. Diatom valves with periodic patterns of holes can resemble a slab waveguide photonic crystal, enabling light-frustule interaction and particle (photon)-particle (matter) interaction.

7.2 The diatom model

The model of diatom *C. oculus-iridis* has been made based on the SEM and AFM images shown in Figure 54. *C. oculus-iridis* was chosen as a model due to the multilevel hierarchical 3D porous structure, which has been thoroughly described in the section 6.2. SEM and the corresponding pattern of the dielectric permittivity in each elementary layer (horizontal and vertical cross-sections) are shown in Figure 71.
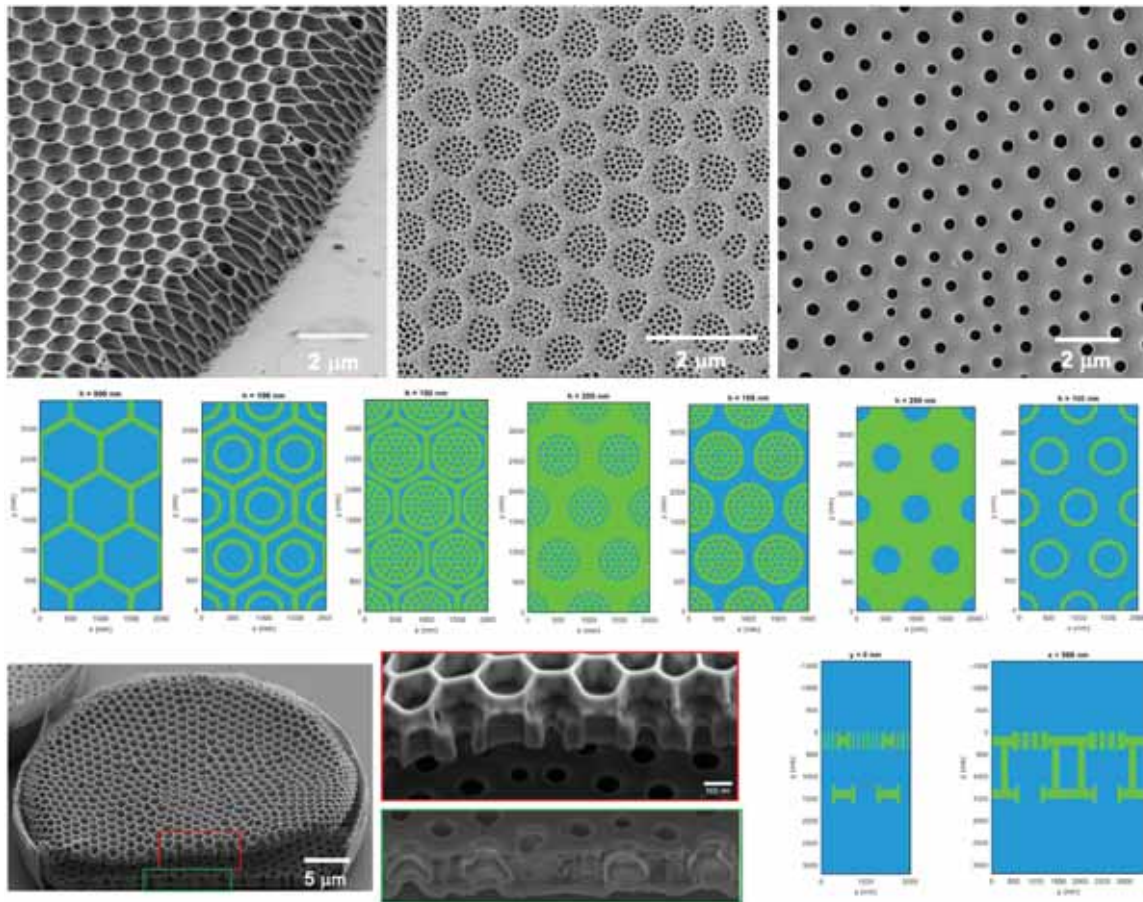
Figure 71. SEM images and the model of Coscinodiscus oculus-iridis. Blue: water (n=1.33), green: silica (n=1.45±0.03i)

All results are obtained based on the model presented in Figure 71.

7.3 Reflection and transmission

The results of numerical calculations of reflection and transmission of diatoms in the main, diffraction and all channels are shown in Figure 72 (incidence from top) and Figure 73 (incidence from bottom). The following diatom structure parameters were used for calculations: a_1=120 nm, h_1=200 nm, r_1=35 nm, a_2=1000.1 nm, h_2=200 nm, r_2=250 nm, h_g=800 nm, r_g=520 nm, h_d=100 nm, r_d=80 nm.
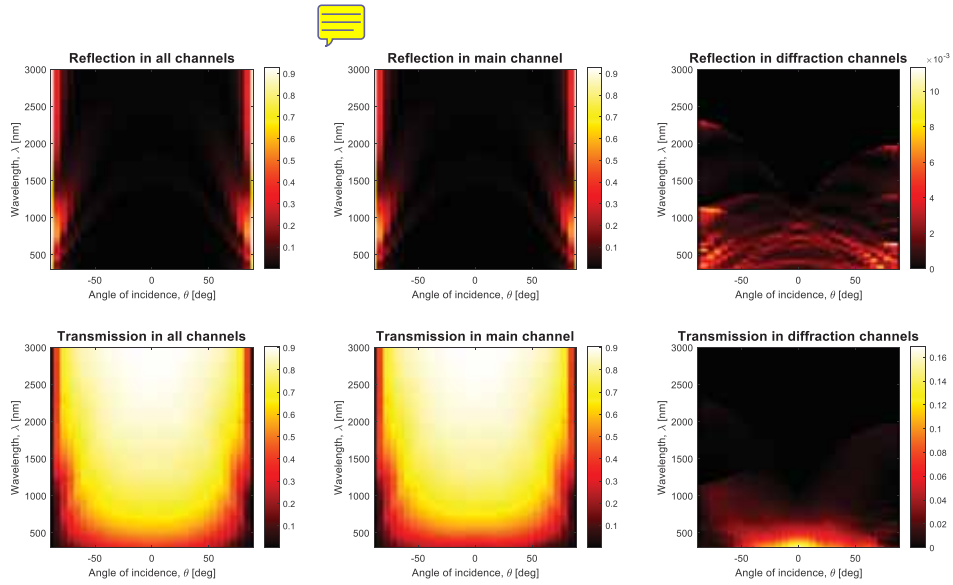
Figure 72. Reflection and transmission of diatoms – incidence from the top.

The reflection is observed mainly in the diffraction channel, in the region of wavelengths 400-1000 nm. The situation is similar in the case when the incidence is from the top (Figure 73).
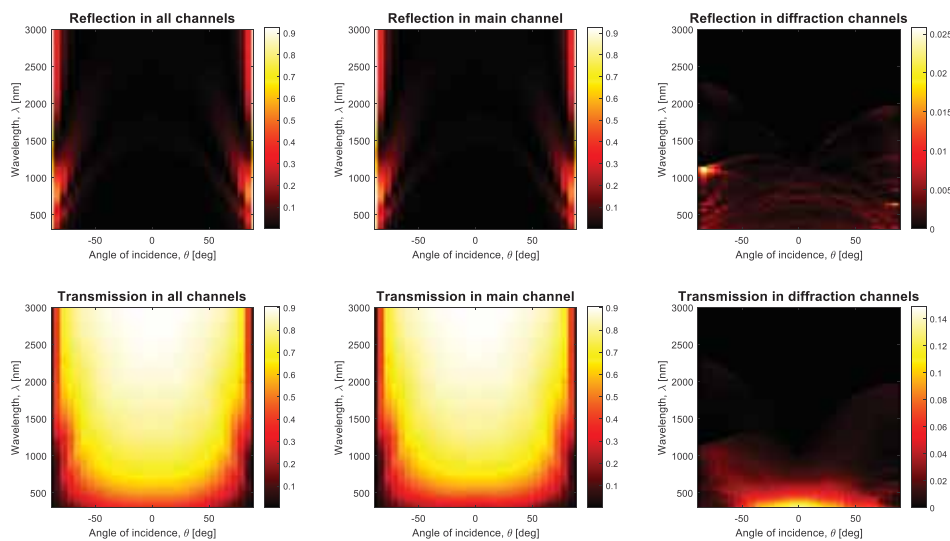
Figure 73. Reflection and transmission of diatoms – incidence from the bottom.

Transmission was calculated using the formalism of the Fourier modal method by calculating the z-components of the Poynting vector. The small absorption of the silica shell is taken into account. Water absorption is not taken into account, since it is very small for these wavelengths. More importantly, there is scattering by imperfections and non-periodicity, but we cannot account for scattering as long as we use the modal Fourier method. The transmission spectra of a non-periodic structure of the same thickness and the diatom frustule in the main, diffraction and all channels in the case of a normal incidence is shown in Figure 74.
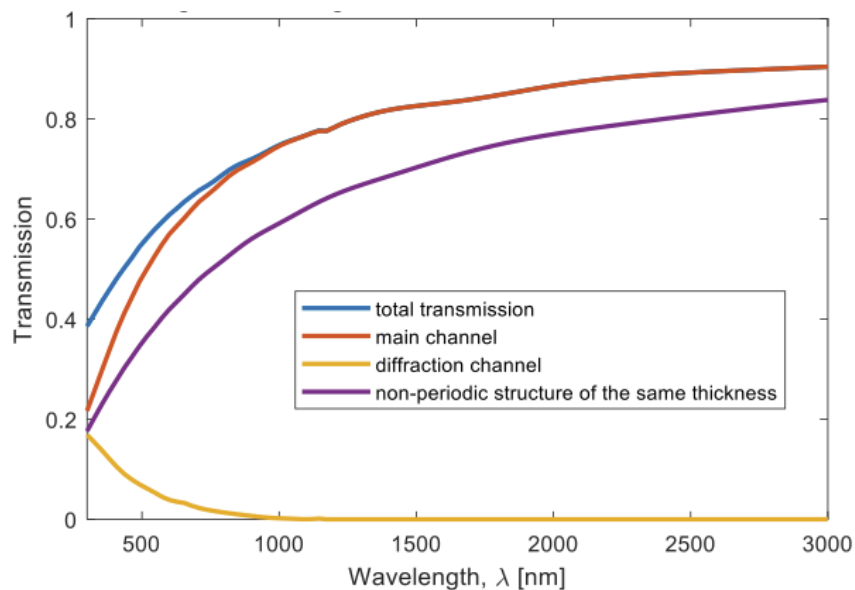
Figure 74. The transmission spectra of diatoms and non-periodic structure of the same thickness.

A dual-periodic photonic lattice due to diffraction increases the transmittance of light in the region $\lambda = 400$–500 nm by 1.5–2 times compared to a homogenous layer of the

same material with the same thickness. The none-periodic structure has the thickness: $h_1+h_2+h_g=1200$ nm. For calculations, it was assumed that the dielectric permittivity of silica has a small imaginary part.

The absorption of water is minimal just in the region of wavelengths 400-500 nm, in which chlorophyll a has an absorption maximum, as demonstrated in Figure 75. For this purpose, we collected the absorbance spectra from individual living diatom cells (Figure 75a) and cleaned frustules without organic material (Figure 75b).
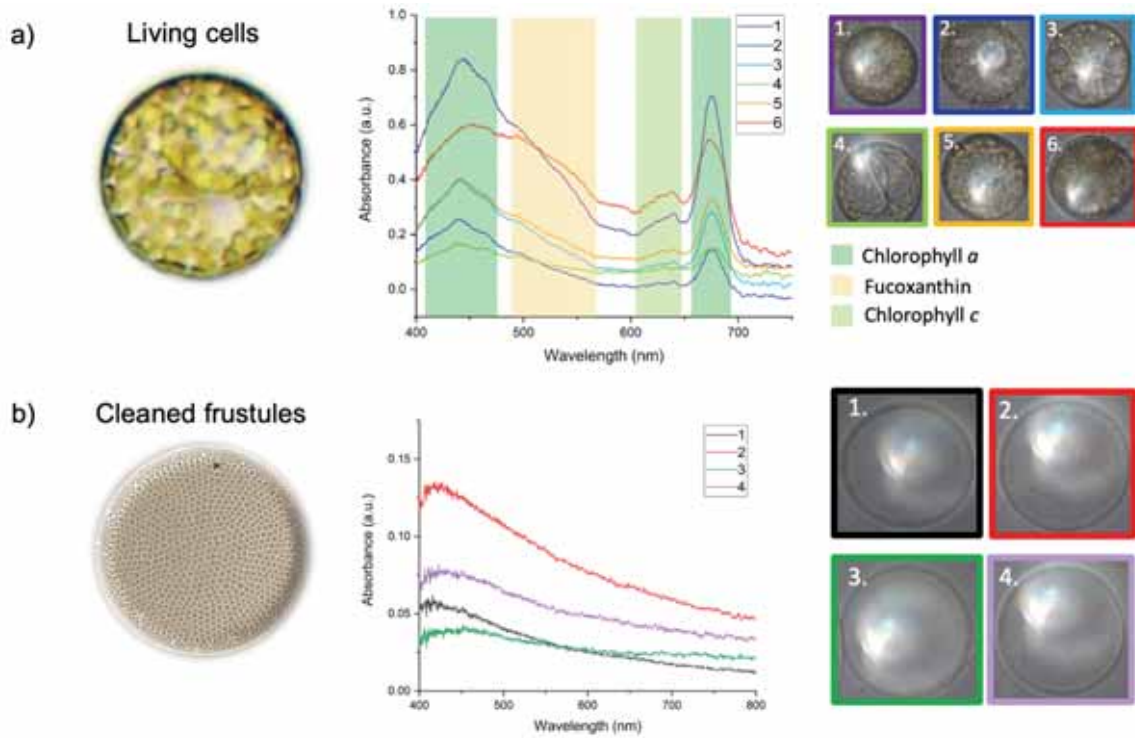
Figure 75. Absorption spectra of: a) individual living diatoms, b) individual cleaned frustules with corresponding images showing where the spectra were collected.

Besides chlorophyll *a*, the absorption spectra of living diatoms demonstrate peaks attributable to chlorophyll *c* and carotenoid fucoxanthin. On the other hand, the spectra of cleaned frustules show no peaks, as expected, since the organic content was removed during acid treatment.

7.4 Electric field intensity distribution

7.4.1. *The solar spectra at different depths in water*

The solar spectra at different depths in water (D65 illuminant) as well as modelled color of water as a function of depth are shown in Figure 76 (Color matching functions: CIE 1931; normalization: overlap integral of solar spectrum at sea level with Y-function equals to 1.)
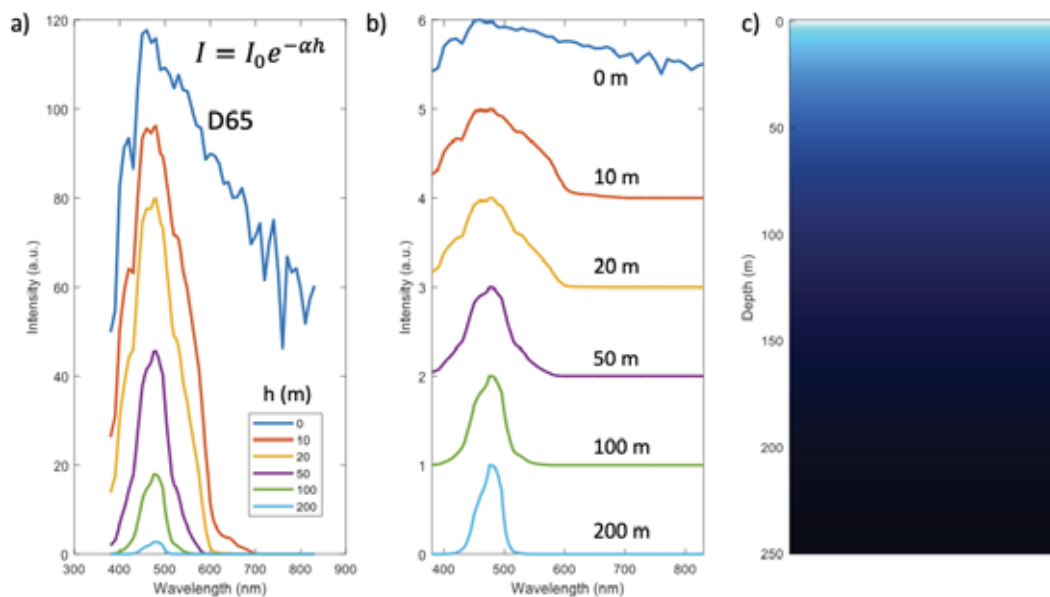
Figure 76. a) Solar spectra and b) normalized solar spectra at different depths in water, c) modelled color of water as a function of depth.

As sunlight penetrates into water, its spectral composition changes due to absorption and scattering properties of water (Figure 76a-c). The primary factors that influence the spectral composition of light in water are water depth, the angle of the sun, and water clarity. The rate of absorption of different wavelengths of light in water varies with depth, leading to distinct changes in the solar spectrum at different depths. In some cases, like algae blooms, the surface water can appear green due to chlorophyll, while in other cases, it can have a brownish or yellowish hue due to the presence of dissolved organic matter. At shallow depths up to 1 meter, the visible spectrum of sunlight dominates, with red and yellow wavelengths being absorbed more rapidly than green and blue. This effect is known as Rayleigh scattering, which occurs when sunlight interacts with small particles in the water. At depths greater than 3 meters, there is a significant drop in the amount of visible light, and the spectrum contains mostly blue and ultraviolet light. The water appears very dark blue or black in the deepest parts of the ocean, where sunlight is absent (Figure 76c). The availability of different wavelengths of light affects the photosynthesis rates of primary producers, the visual perception and behavior of predators and prey, and the distribution and abundance of different species in the water column.

Diatoms, since they are predominantly autotrophs, need enough light, so they inhabit the so-called euphotic zone in water bodies, which extends from the surface to the depth of the compensation point (where photosynthesis exceeds respiration). Usually, this depth corresponds to about 1% of the solar radiation coming to the surface of the water. In practice, the euphotic zone extends for several tens of meters, up to 150–200 m.

Coscinodiscus oculus-iridis used here as a model, represents a marine species obtained from samples from the Tsushima Strait (Sea of Japan). Since this is a planktonic species, it soars in the water column and lives at depths of up to several tens of meters.

7.4.2 Electric field intensity at specific incident angles

The first results of electric field simulation at λ=420 nm (θ=0°, φ=0°) are shown in Figure 77.
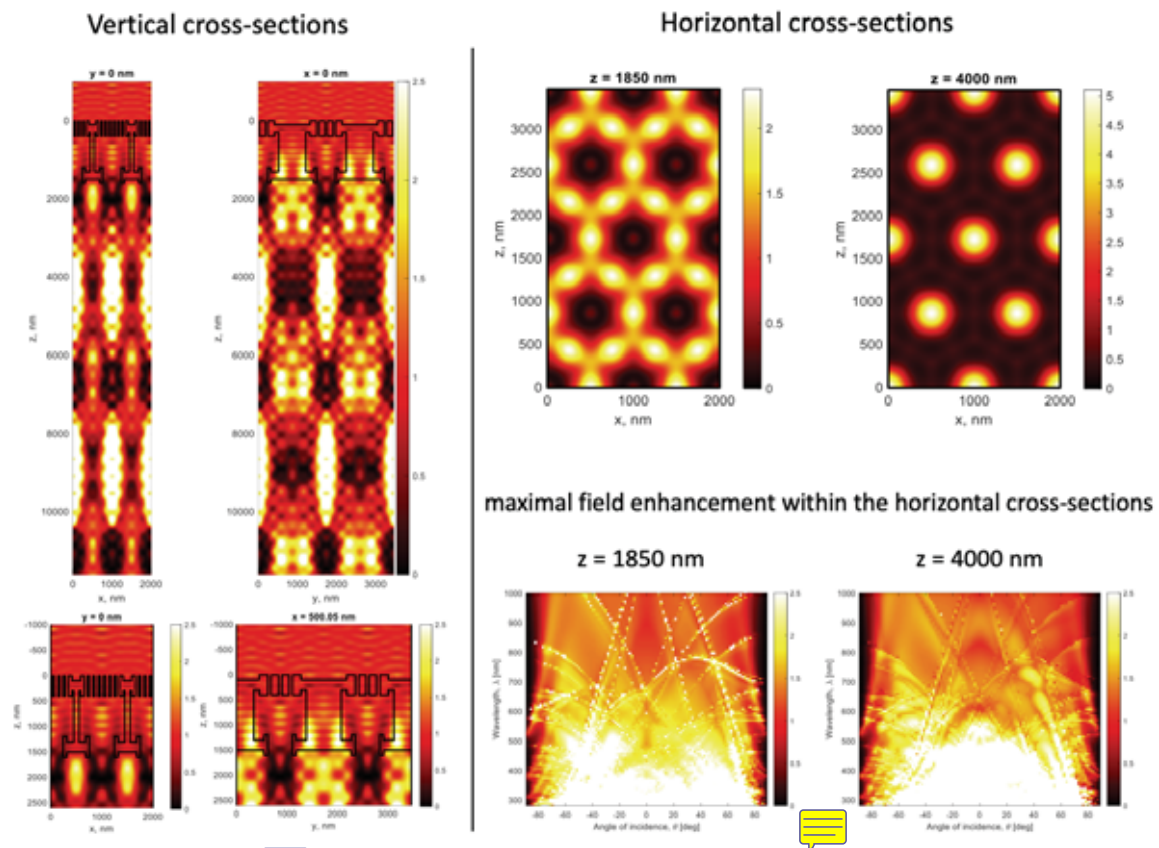
Figure 77. Electric field simulation at λ=420 nm, θ=0°, φ=0° on the surface of the frustule.

Figure 77 shows the intensity of the electric field and interference pattern within vertical and horizontal cross-sections of the diatom. Maximal field enhancement within the horizontal cross-section at z=1850 nm and z=4000 nm is also shown. The obtained interference pattern looks very similar to Talbot interference pattern[218]. The intensity of the electric field at bright points can be increased several times compared to the case of a flat homogenous frustule.

Electric field intensity at λ=420 nm, θ=45°, φ=0° is shown in Figure 78.
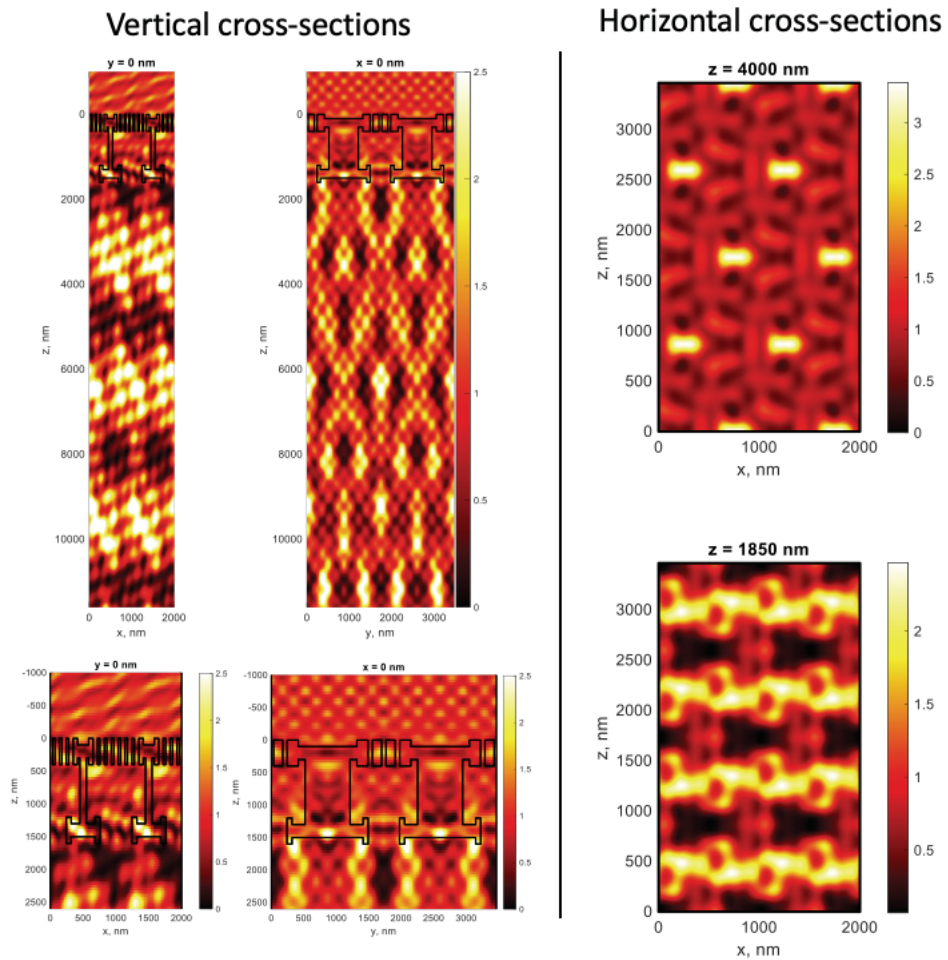
Figure 78. <mark>Electric field simulation</mark> at λ=420 nm, θ=45°, φ=0° on the surface of the frustule.

7.4.3. *<mark>Electric field intensity</mark> integrated over all incident angles and polarizations*

Since, due to the angle of incidence θ=45°, the interference pattern in Figure 78 has changed compared to Figure 77, the <mark>electric field intensity should be integrated over all incident angles and polarizations</mark>. Here we considered two different model structures: structure 1 "with cavity" – the whole frustule, and structure 2 "without cavity" – only one valve (Figure 79).
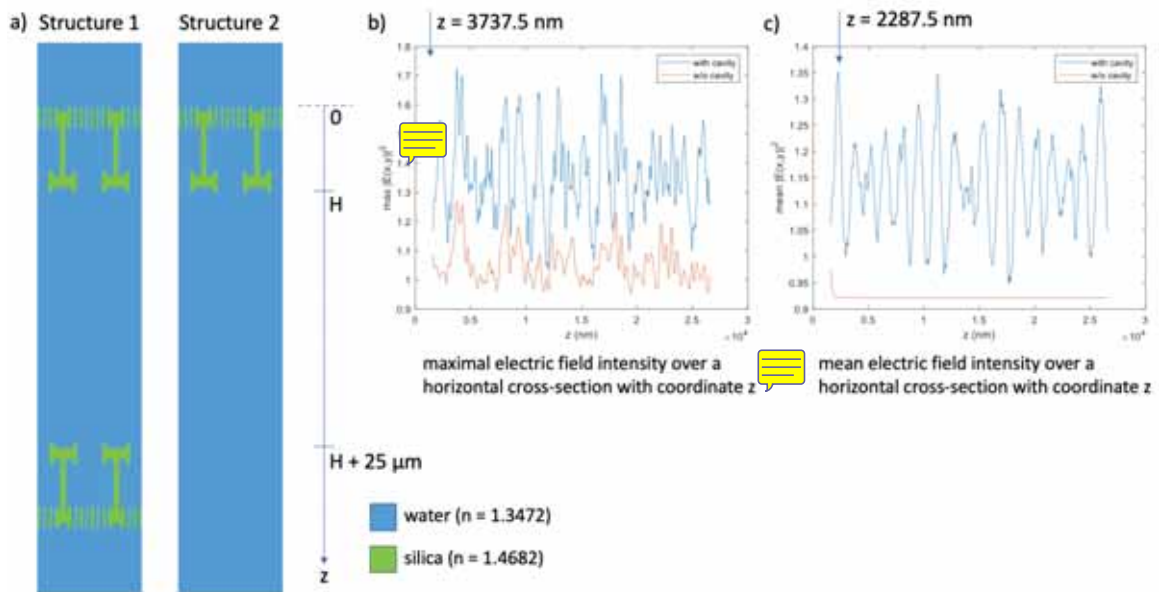
Figure 79. a) Vertical cross-sections of two model structures: 1 (with cavity) and 2 (without cavity). b) Maximal and c) mean electric field intensity over a horizontal cross-section with coordinate z.

The graph in Figure 79b represents the maximum intensity of the electric field depending on the z coordinate. Field distribution in xy plane is shown by fixing z-coordinate. Both maximal and mean fields have higher intensities in the case of a structure with cavity, due to the reflection of light and occurrence of Fabry Perot resonances. At bright points, for a structure with two halves, the maximum field is 1.7, and for a structure with one half, the maximum is 1.25 (Figure 79). For a structure without cavity, the mean field is slightly less than 1 because there is reflection and the tail indicates that the structure is a weak waveguide. This wave mode has a slightly stronger field compared to the surrounding field. The integral field for the structure with cavity along the plane reaches 1.33.
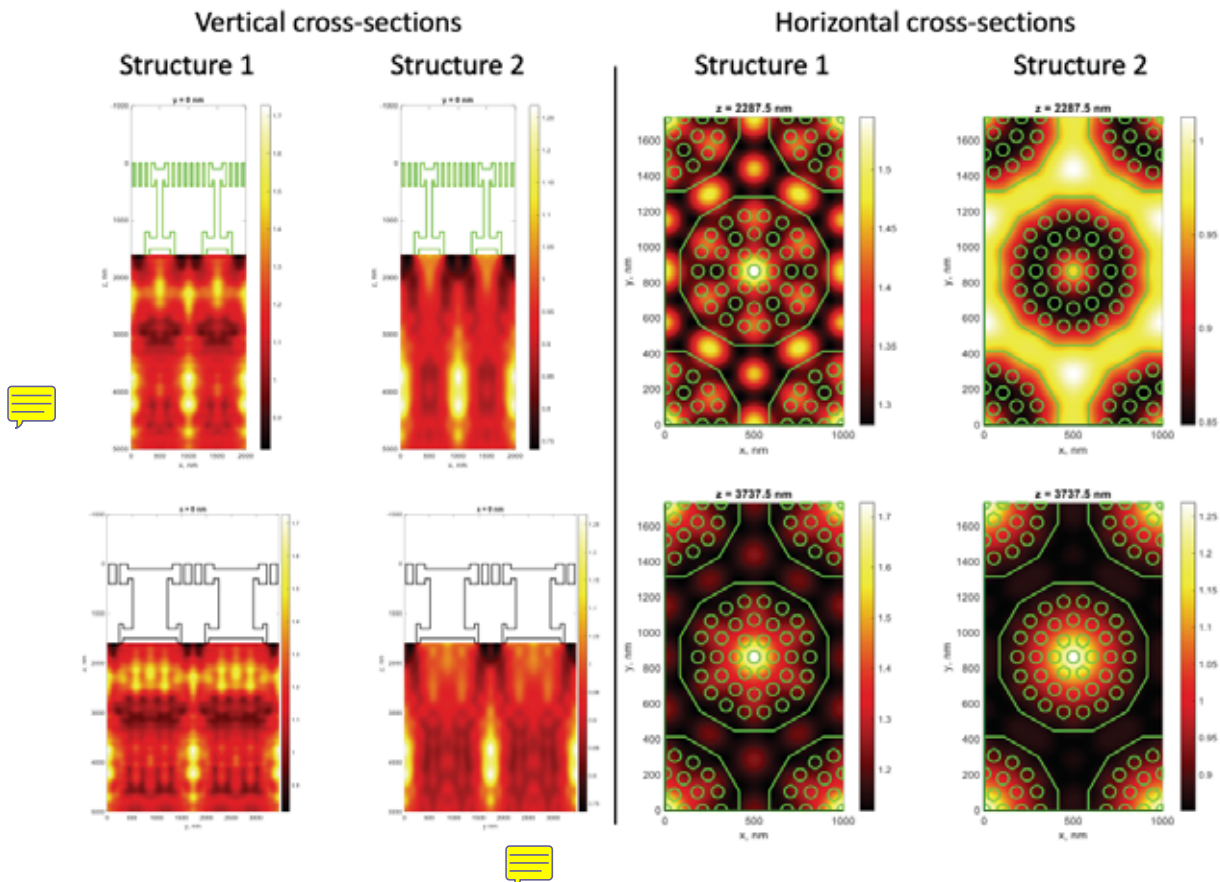
Figure 80. Electric field distribution with structure 1 and 2 at different coordinates.

Figure 80 shows the electric field intensity in the coordinates z=2287.5 nm z=3737.5 nm, which correspond to the point when the mean and maximal field intensities are large for the structure with cavity, respectively. The field in the case of a structure with a cavity integrated over the plane is 1.35 times larger than that of the incident field, and in the case of a structure without a cavity it is slightly less than 1.

The green lines represent the border of the materials and are superimposed here for visual evaluation. In essence, the periodic porous silica structure makes a diffraction image such that the intensity of the field increases under the holes where the chloroplasts are located, as demonstrated in Figure 81. FLIM data displayed here as color-coded intensity images, where the color or brightness of each pixel corresponds to the fluorescence decay rate, reveal details about the distribution of chloroplasts inside diatom frustules, such as their overall density and spatial variability.
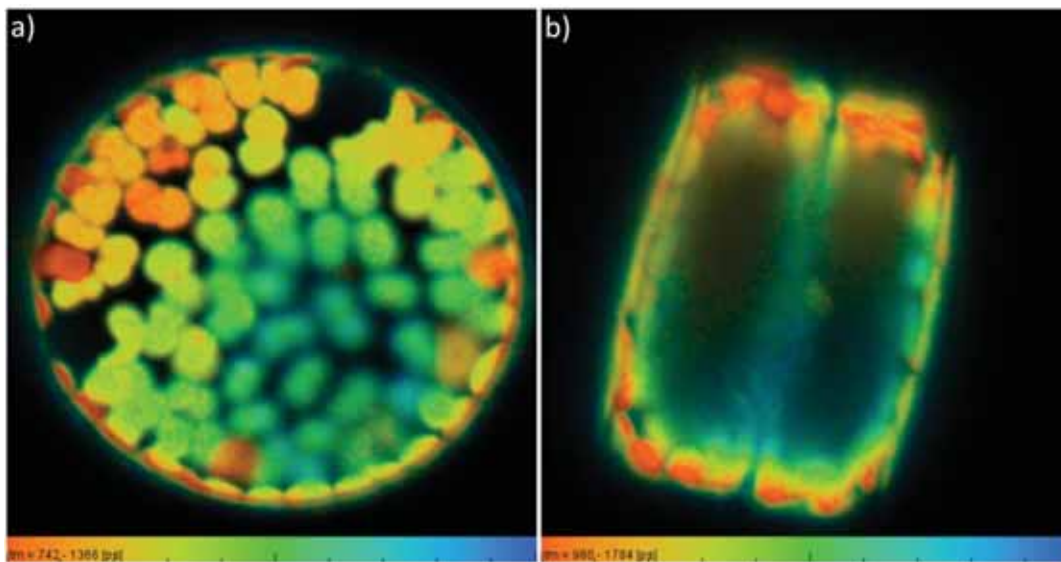
Figure 81. FLIM images of C. oculus-iridis showing distribution of chloroplasts in the frustule: a) top view, b) side view.

However, another question that also deserves attention is chloroplast migration in response to changes in light intensity and quality. When exposed to low light or directional light, diatom chloroplasts move to the cell periphery to capture incoming light, while under high light they move towards the cell center to reduce the amount of light absorbed and maintain photosynthesis efficiency[219,220]. The chloroplast migration in diatom algae is mediated by actin filaments, which form a cytoskeletal network inside the cells[221]. Actin filaments extend from the cell periphery towards the chloroplasts, binding to them and pulling them towards their desired location in the cell. During this process, the actin filaments and other associated proteins form a dynamic and flexible structure that allows for the movement and positioning of the chloroplasts.

The process of chloroplast migration in diatom algae occurs relatively rapidly[221], with chloroplasts changing their location within a few minutes of changes in light condition. Chloroplasts are also able to orient themselves within the cytoskeleton in a way that maximizes their exposure to light and minimizes the amount of shading from other chloroplasts. By optimizing their chloroplast positioning, diatoms can regulate their photosynthetic efficiency and minimize photodamage from excess light exposure. This can be especially important in environments with variable light conditions, where diatom algae must be able to quickly adapt to changing levels of irradiance.

7.4.4. *Electric field intensity depending on the distance between two valves and polarization*

In the previous section 7.4.3, we calculated the electric field intensity for a fixed distance between two plates or valves, equal to 25 μm, and integrated over all incidence angles and polarizations. However, we also analyzed separately S- and P-polarizations and take into account different distance between valves starting from g=5 μm to g=25 μm with the step of 5 μm (Figure 82). In a structure with two shells (valves), not only diffraction occurs, but also interference of two modes that propagate up and down, and therefore, as in any resonator structure of this kind, there are points at which the incident field is amplified both locally and on average over z-coordinate. The permeability contrast in this particular structure is small, and therefore the field enhancement is small, but it is still present. In a structure with one valve, only diffraction occurs, so although the field can be amplified locally, it is constant on average along the z-coordinate, with the exception of the region near the shell, where near evanescent fields associated with the shell itself make a contribution. The dependence of the maximal electric field intensities on z-coordinate exhibits similarities between S- and P-polarization for a specific height. This concordance suggests that certain underlying factors or mechanisms influence the electric field distributions similarly for these two polarization states. In contrast, when comparing different heights of the frustule, significant deviations arise in the dependency of the maximal electric field intensities on the z-coordinate between S- and P-polarizations. These variations imply that the electric field distributions and their corresponding intensities are influenced differently at varying heights within the frustule structure. The observed

discrepancies, thus, highlight the importance of sample height as one of determining factors in shaping the electric field characteristics and intensities for different polarization states.
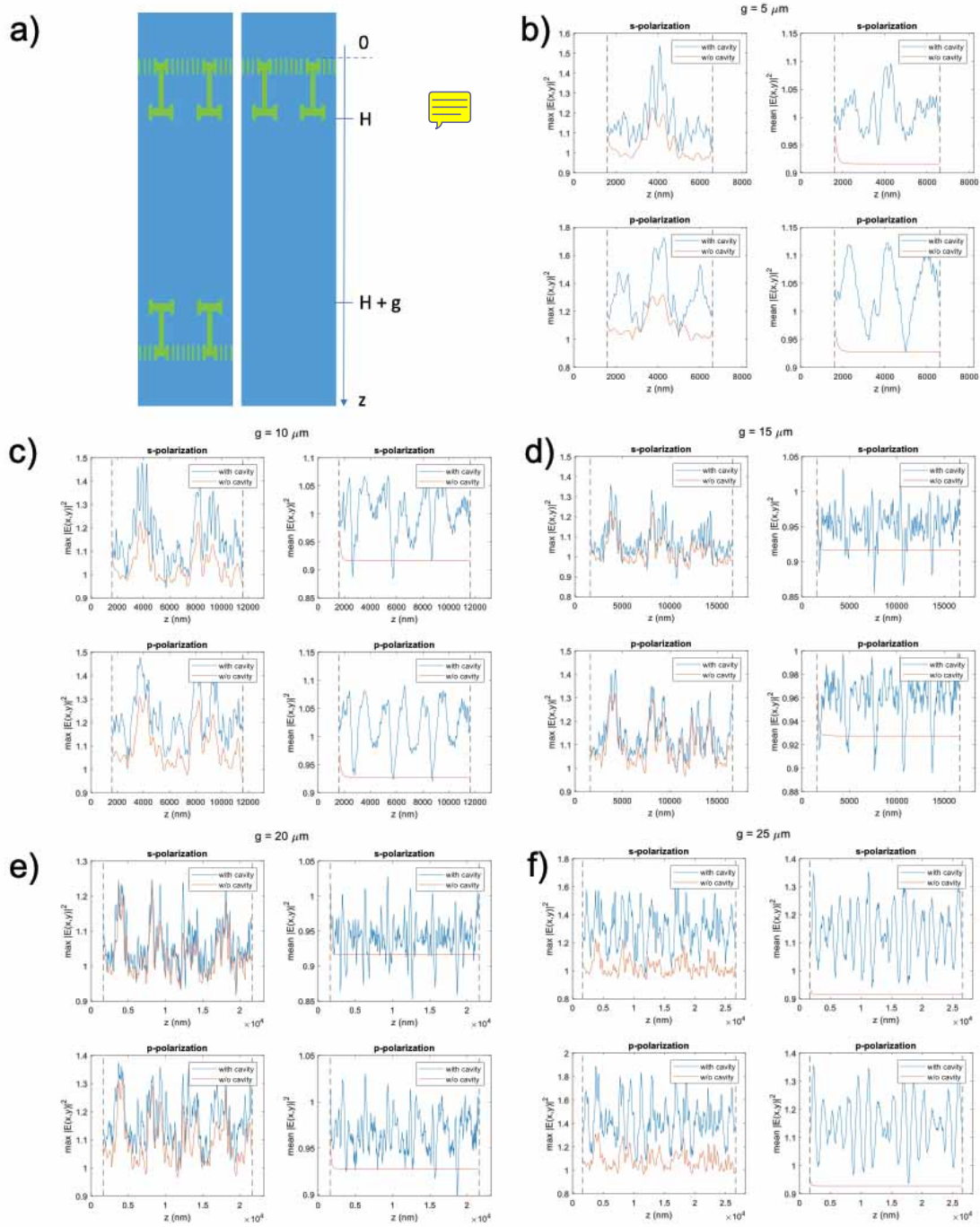
Figure 82. a) Two model structures: with cavity and without cavity. Mean and maximal electric field intensity calculated for S- and P- polarizations taking into account distance between valves g equal to: b) 5 μm, c) 10 μm, d) 15 μm, e) 20 μm, f) 25 μm.

As an example, here is shown electric field intensity calculated for S- and P-polarizations in the case of a sample with height g=5 μm (Figure 83). Results of calculations of electric field intensity for sample with height g=10 μm, 15 μm, 20 μm and 25 μm are shown in Appendix C.
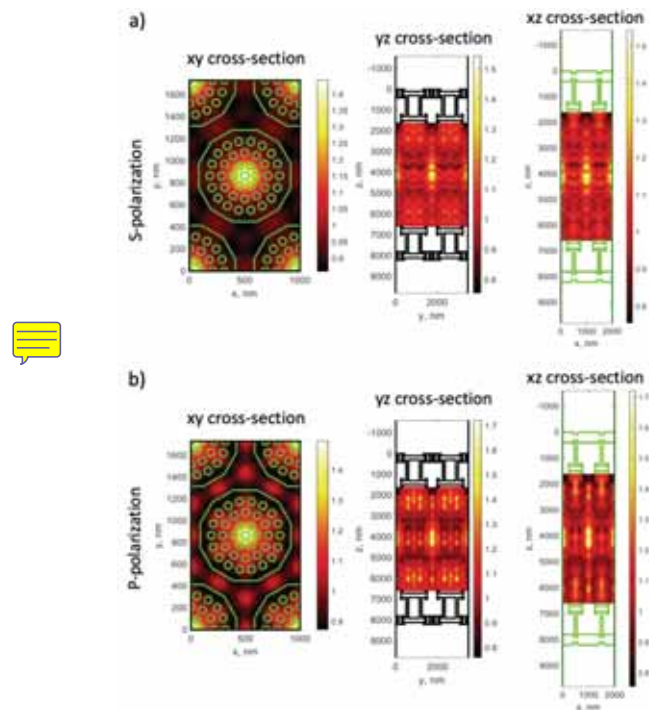
Figure 83. Electric field intensity calculated for: a) S- and b) P-polarization, within horizontal and vertical cross-sections of a sample with height g=5 μm.

Our numerical study demonstrates that across varying polarization states and sample heights, a distinct interference pattern emerged characterized by bright spots at specific positions. The repetitive occurrence of the interference pattern for all polarization states and sample heights underscores the ubiquity and generalizability of interference phenomena in optical systems. This finding emphasizes the fundamental nature of interference as a powerful tool for investigating and manipulating light.

7.5 Summary

This chapter is related to the theoretical study of optical properties by using Fourier modal method. A dual-periodic photonic crystal structure due to diffraction increases the transmittance of light in the region $\lambda = 400–500$ nm as well as intensity of electric field compared to a homogenous layer of the same material with the same thickness. Regardless of the polarization, the resulting interference pattern exhibited a consistent spatial arrangement of bright spots for specific diatom frustule height, characterized by enhanced intensity regions. The presence of these bright areas signifies the constructive interference of light waves and provides a foundation for further analysis of the underlying physical mechanisms governing interference. Further exploration of the mechanisms responsible for the observed differences among heights and polarization states will shed light on the intricate interplay between the frustule structure and the resultant electric field distributions. Such insights hold promising potential for advancing our understanding of the optical properties and functionalities of diatom frustules, ultimately fostering the development of novel optical devices and technologies inspired by these micro-scale structures.

Chapter 8. Modification of diatomite

In this chapter a modification of diatomite – a soft, loose, and fine-grained siliceous sedimentary rock composed of the remains of fossilized diatoms – by gold nanoparticles using layer-by-layer technology in combination with a freezing-induced loading approach is demonstrated. The obtained composite structures are characterized by dynamic light scattering, extinction spectroscopy, SEM and TEM, photoacoustic imaging technique, and tested as a platform for surface-enhanced Raman scattering (SERS) using Rhodamine 6G. The results presented here are published in article **Cvjetinovic J** et al.[83] *Physical Chemistry Chemical Physics*, 2022, 24: 8901-8912.

8.1 Gold nanoparticle characterization

Gold nanoparticles can be synthesized using different approaches depending on the desired size, shape, and surface functionality.[222] Here, we used a standard method developed by Turkevich et al.[223] According to bright-field TEM (BF-TEM) image in Figure 84a, the spherical gold nanoparticle sizes follow a normal distribution with an average diameter of 19 ± 5 nm (Figure 84b). The obtained gold nanoparticles have an absorption peak at 524 nm, as shown in Figure 84c. The absorption band results from the collective oscillation of the conduction electrons due to the resonant excitation by the incident photons.[224] Zeta potential measurements showed that the nanoparticles have an average surface charge of -29.3 ± 0.9 mV, indicating that their stability is on the borderline between incipient instability and moderate stability [225]. Owing to the unique features of gold nanospheres[226], such as size- and shape-related optoelectronic properties, good biocompatibility, low toxicity, large surface-to-volume ratio, they have been exploited for
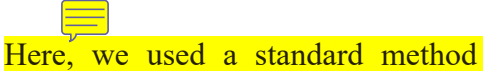
a wide range of applications in bionanotechnology, diagnostics, imaging, delivery, and therapy.[222,227] However, some of the most important physical properties are surface plasmon resonance, which occurs when free charges on the surface of AuNPs oscillate with the electromagnetic field, and the ability to quench fluorescence.[228] Moreover, AuNPs have been widely used as photoacoustic contrast agents in recent years.[229] Considering the abovementioned facts, in this study, we used AuNPs to modify the diatomite surface, expecting excellent photoacoustic and enhanced SERS signals.
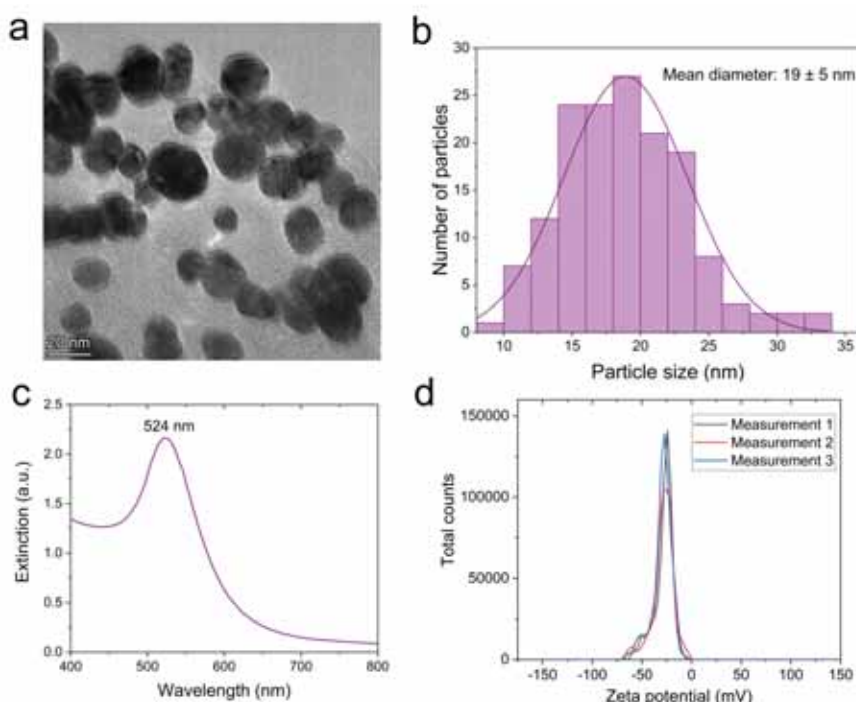
Figure 84. a) Typical BF-TEM image of gold nanoparticles (scale bar, 20 nm), b) Size distribution histogram of synthesized gold nanoparticles, c) Extinction spectrum of AuNPs, d) Zeta potential distribution of AuNPs. [83]

8.2 Fabrication of gold-coated diatomite

For the deposition of gold nanoparticles onto the surface of diatomite, we applied for the first time the LbL technique in combination with freezing-induced loading. LbL is based on electrostatic interactions between a positively charged polyelectrolyte and, in this case, negatively charged nanoparticles. Therefore, the desired composite material can be obtained by depositing alternating layers of oppositely charged materials with washing steps in between. PAH, as one of the most popular positively charged polyelectrolytes, according to the scheme shown in Figure 85a covers the negatively charged surface of the diatomite and subsequently attracts the negatively charged gold nanoparticles. The LbL+FIL process can be repeated several times, which makes it possible to obtain a high efficiency of nanoparticle deposition. Here, we applied it up to five times, which resulted in hybrid materials based on diatomite with different coverage by gold nanoparticles.

The freezing-induced loading approach is based on the controlled directional freezing, in which the ice crystals grow parallel to the a-direction of the hexagonal base and form the so-called cold-finger interfaces.[230] During crystallization, AuNPs and diatomite fragments were pushed by the crystallization front, so the nanoparticles concentrated around the diatomite surface. In the final stage of the process, the nanoparticles were pressed into the surface of the diatomite shards by the growing pressure of the forming ice. German et al. showed that the FIL method leads to a higher amount of magnetite adsorbed into vaterite particles, as compared to the conventional encapsulation methods, such as adsorption and coprecipitation. [230]

8.3 Extinction spectroscopy

Figure 85b shows the extinction spectra of bare AuNPs and gold-coated diatomite hybrid materials consisting of different number of layers. The absorption peak values, which correspond to the gold increase with the increasing number of deposition cycles up to three, but after that, we observed the decrease, which may be due to two processes. First, upon each layer deposition, we had to remove the weakly adsorbed polyelectrolytes and nanoparticles by rinsing with deionized water at least three times, which leads to the loss of the certain amount of particles. Therefore, even though the AuNPs can settle on the surface more, due to the smaller number of particles, the absorbance values decrease. Second, according to spectrum of gold-coated diatomite composites consisting of five PAH/AuNPs bilayers, the band at ca. 525 nm practically disappears. On the other hand, we can observe the long tail in the region 560-700 nm, which indicates the presence of aggregates. Thus, the number of small nanoparticles which absorb well at ca. 525 nm decreases, while the number of larger aggregates of various shapes increases.
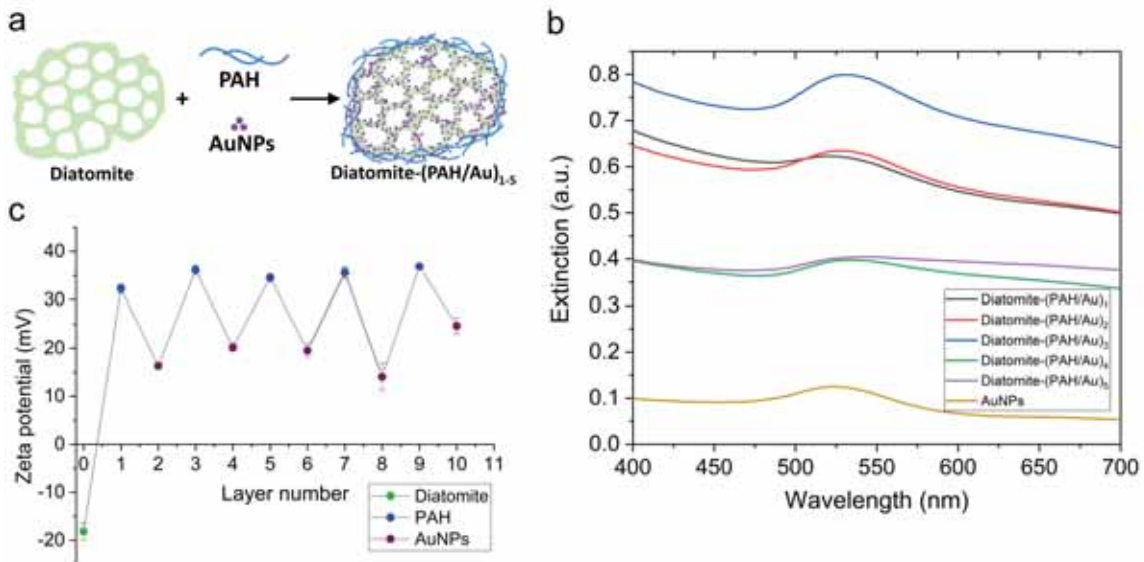
Figure 85. a) A schematic representation of layer-by-layer approach, b) Extinction spectra of AuNPs and diatomite decorated with different number of PAH/AuNPs bilayers, c) Zeta potential depending on the layer number. [83]

8.4 Zeta potential measurements

Figure 85c shows the change of zeta potential after each adsorption step depending on the layer number. Even though the AuNPs are negatively charged, upon deposition on PAH-coated diatomite, we did not observe the surface charge change. Usually, repeated adsorption of polyanions and polycations onto the charged particles leads to the change of zeta potential between positive and negative values. However, the absence of negative zeta potential values after depositing AuNPs indicates that they didn't completely cover the surface of diatomite as polyelectrolyte.

8.5 SEM study of degree of coverage of diatomite surface by gold

SEM images of diatomite decorated with one, three, and five PAH/AuNPs bilayers are shown in Figure 86. We can clearly see the difference in the level of coverage of the diatomite surface by AuNPs. One PAH/AuNPs bilayer leads to insufficient coverage, which significantly increases as the number of bilayers increases. The AuNPs are relatively uniformly distributed onto diatomite templates following their surface morphologies via electrostatic interactions. Nanoparticles are located more at the edges, along the rim, but we can also observe them around the pores. SEM images illustrate that the diatomite surface is not entirely covered with AuNPs, explaining the obtained zeta potential

227

distribution. Usually, nanoparticles at low concentrations are homogenously adsorbed on the substrates, but at higher concentrations, they tend to form clusters. Some nanoparticles get deposited in the proximity of other particles because, at high concentrations, all the favored sites at the polyelectrolyte surface become immediately occupied.[231,232] Generally, the deposition of a polycation on a surface previously treated and partially covered with negatively charged nanoparticles will occur predominantly on the nanoparticles' surface.[231,233] Subsequently, in the case of multilayer gold deposition, further anionic AuNPs also bind to locations of previously deposited AuNPs, and therefore, clusters are formed.
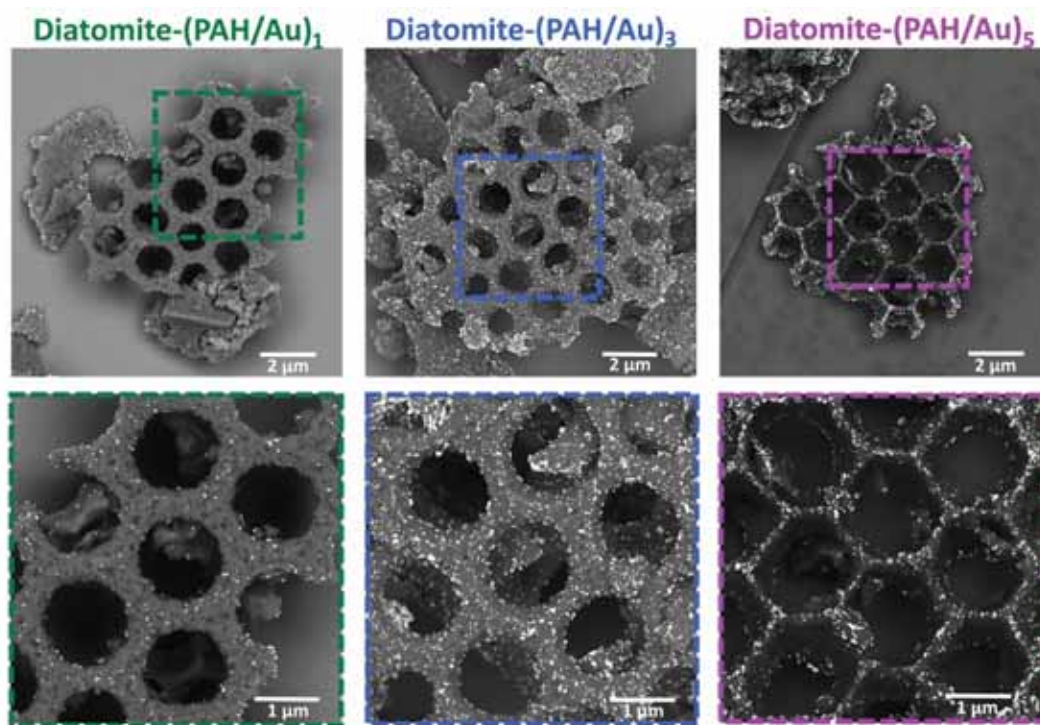
Figure 86. SEM images of gold-coated diatomite consisting of one (left), three (middle), and five (right) PAH/AuNPs bilayers. [83]

8.6 TEM and STEM-EDX study

Overview HAADF-STEM and BF-TEM images of a sample consisting of three PAH/AuNPs bilayers (Diatomite-(PAH/Au)$_3$) are shown in Figure 87a-d.
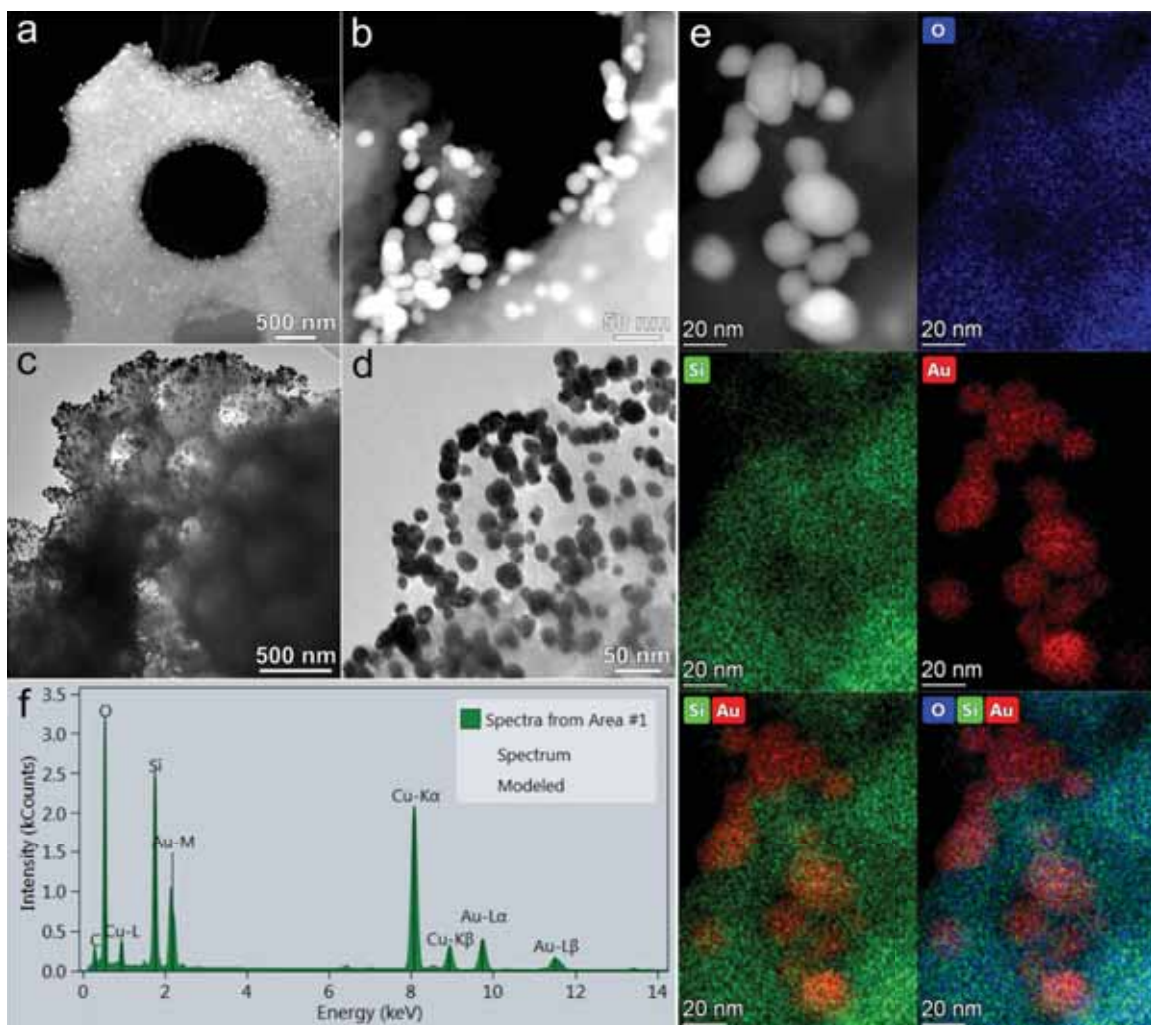
Figure 87. Diatomite-(PAH/Au)$_3$: a, b) HAADF-STEM image, c, d) TEM images, e) HAADF-STEM image, corresponding elemental EDX maps and f) EDX spectrum. [83]

In the HAADF-STEM images, the contrast is proportional to squared atomic number, and heavy gold nanoparticles appear as bright spots, while in the BF-TEM the

color scheme is different and AuNPs look dark. The diatomite is covered with a dense layer of AuNPs which tend to form clusters, especially along the edges. STEM-EDX maps and spectra confirmed the presence of AuNPs on the surface of diatomite, composed of silica (Figure 87e,f). The dominant peaks in the EDX spectrum arise from oxygen, silicon and gold, as expected. The C and Cu signals are attributed to the supporting TEM grid, though the carbon can be present also due to residual organics in the diatomite powder. The presence of Fe can be explained by the nature of diatomite which is composed of 2.5 wt. % iron oxide; as well, Fe-K can be interpreted as an escape peak of intensive Cu-Kα line.

8.7 Photoacoustic imaging

Given the fact that the generated photoacoustic pressure waves are linearly dependent on the absorption coefficient,[234] and thus, proportional to the concentration of gold nanoparticles which absorb well the 532 nm light, it can be used as an *in situ* method for characterizing the degree of modification of diatom biosilica surface with AuNPs. The photoacoustic signals from the gold-coated diatomite composites were collected using RSOM technique. RSOM images of all the fabricated samples are shown in Figure 88. Here we performed a 2-fold dilution to show the dependence of the signal intensity on the concentration of such hybrid materials. The number of applied PAH/AuNPS bilayers increases from the left to the right side. The images show the signal over the entire frequency range from 11 to 99 MHz. A low-frequency signal in the 11-33 MHz range, emitted by larger particles is shown with red color, while the green-colored high-frequency signal (33-99 MHz) corresponds to smaller objects. The signal decreases with the decrease

in concentration, as expected. The red-colored signal is usually higher indicating the aggregation of gold nanoparticles, especially at higher concentrations. On the other hand, the high frequency signal is higher in the case of low number of layers and lower concentrations.
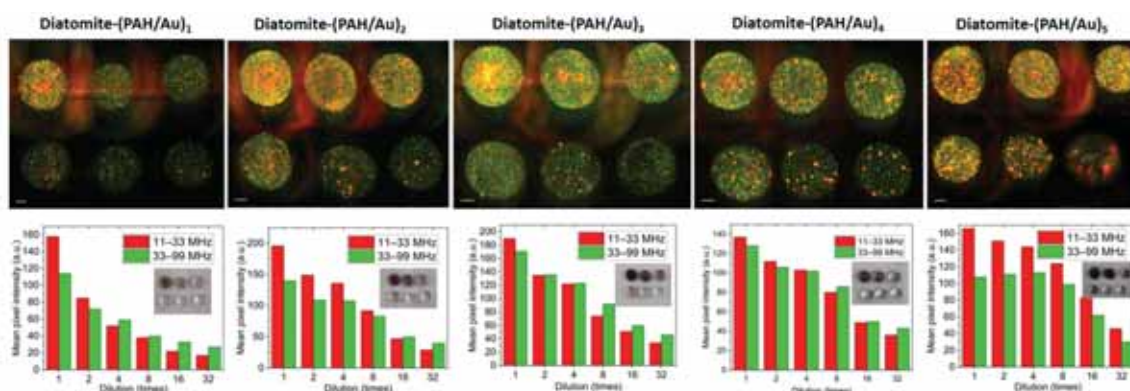
Figure 88. RSOM images of 2-fold diluted diatomite coated with different number of PAH/AuNPs bilayers (up) and the corresponding mean pixel intensity depending on the dilution (down). [83]

Figures 89a-c illustrate the RSOM signal from the bare AuNPs and stock suspensions of diatomite covered with different number of PAH/AuNPS bilayers in the frequency range 11-99 MHz, 11-33 MHz and 33-99 MHz, respectively. By comparing the collected signals from all samples, we can conclude that the highest value was obtained from the sample with three bilayers (Figure 89d). Here we also compared the extinction at 532 nm and mean pixel intensities in both frequency channels (Figure 89e) and observed the good agreement between extinction and signal in the frequency range from 33 to 99

MHz. Low frequency signal deviations can be explained by the tendency of particles to accumulate in the center of the droplet and probably insufficient mixing before measurements.
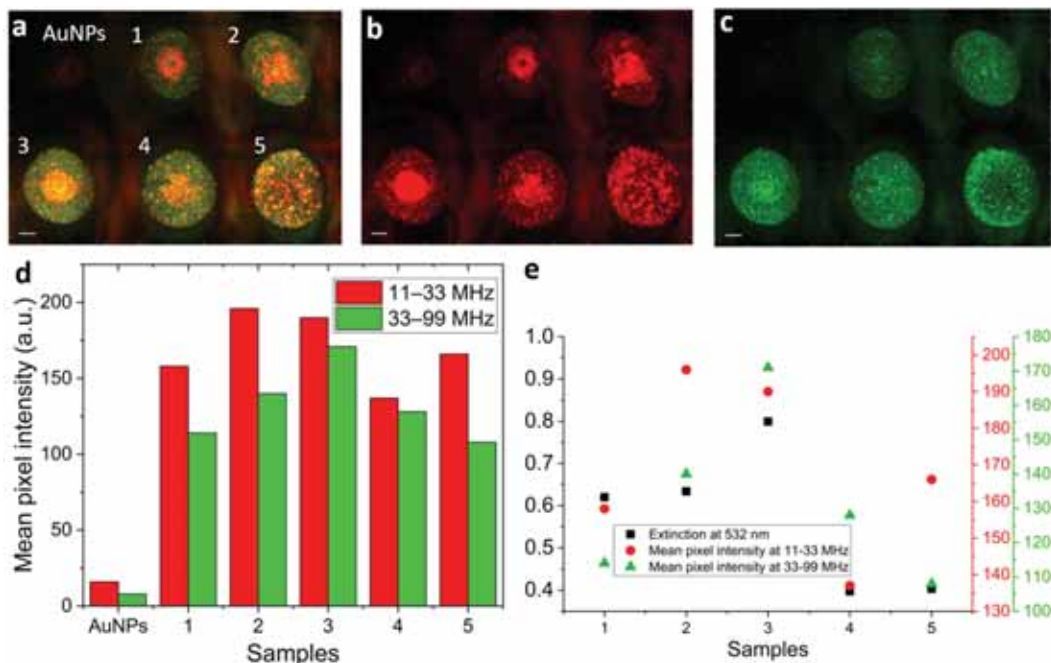
Figure 89. RSOM images of gold nanoparticles and stock suspensions of diatomite coated with different number of PAH/AuNPs bilayers at: a) 11-99 MHz, b) 11-33 MHz, c) 33-99 MHz frequency range, d) Mean pixel intensity depending on the sample, e) comparison of the extinction at 532 nm and mean pixel intensities at 11-33 and 33-99 MHz. 1-Diatomite-$(PAH/Au)_1$, 2-Diatomite-$(PAH/Au)_2$, 3-Diatomite-$(PAH/Au)3$, 4-Diatomite-$(PAH/Au)_4$, 5-Diatomite-$(PAH/Au)_5$. Scale bar, 200 μm. [83]

The signal from the bare AuNPs is very low when compared to that of AuNPs deposited on the diatomite surface. As already mentioned, the gold-based nanoparticles

232

have been widely used as photoacoustic contrast agents owing to their strong and tunable optical absorption that results from surface plasmon resonance (SPR) effect. When illuminated with a pulsed laser, AuNPs absorb light and generate substantial heat that can sometimes result in their melting. This problem can be solved by silica coating as it lowers the interfacial thermal resistance between gold and the surrounding medium. Moreover, some studies have shown the amplification of photoacoustic signals and the stability generated by silica-coated gold compared to pure gold caused by a decrease in the thermal resistance of gold to the solvent.[235–237]

8.8 SERS measurements

The potential of diatomite embedded with AuNPs to serve as a SERS platform was tested using Rhodamine 6G as a model analyte. The resulting Raman and SERS spectra of droplets on a glass slide containing bulk Rhodamine 6G, as well as bare diatomite and diatomite coated with one, three and five PAH/AuNPs bilayers incubated with Rhodamine 6G are shown in Figure 90.
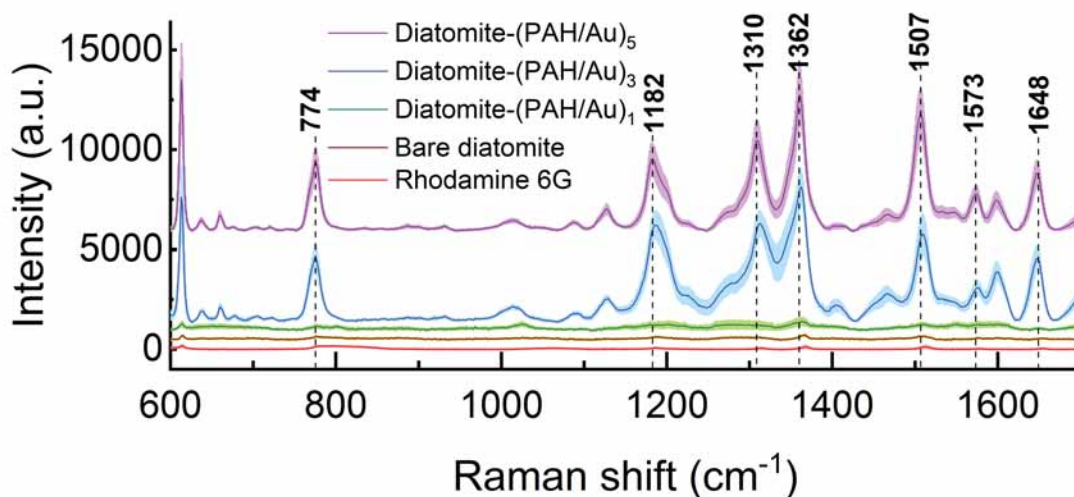
Figure 90. Surface-enhanced Raman spectra of Rhodamine 6G obtained using gold-coated diatomite hybrid materials with a different number of PAH/AuNPs bilayers. [83]

A variety of strong bands corresponding to Rhodamine 6G on the gold-coated diatomite can be identified. Rhodamine 6G provides an intense peak at 613 cm^{-1}, which is assigned to C–C–C ring in-plane bending.[238] The vibrational mode of 660 cm^{-1} band is due to a symmetric deformation localized in the phenyl ring.[239] 774 cm^{-1} corresponds to the C–H out-of-plane bending vibration, while 1127 and 1182 cm^{-1} are C–H in-plane bending. [238] Peaks at 1310, 1362, 1507, 1573, 1648 cm^{-1} are assigned to the aromatic C–C stretching vibrations. [238]

Figure 90 illustrates strong enhancement of SERS signal from Rhodamine 6G using diatomite coated with three and five PAH/AuNPs bilayers compared with bare analyte. Droplets of Rhodamine 6G with Diatomite-(PAH/Au)$_3$ or Diatomite-(PAH/Au)$_5$ substrates provided approximately 50 times stronger signal of an analyte, calculated at peaks ca. 1362 and 1507 cm^{-1} (Table 9).

Table 9. Raman and SERS intensities [83]

R6G			Diatomite-(PAH/Au)$_3$				Diatomite-(PAH/Au)$_5$			
Peak position, cm^{-1}	Mean intensity I_{RS}, a.u.	RSD	Peak position, cm^{-1}	Mean intensity I_{SERS}, a.u.	RSD	$\frac{I_{SERS}}{I_{RS}}$	Peak position, cm^{-1}	Mean intensity I_{SERS}, a.u.	RSD	$\frac{I_{SERS}}{I_{RS}}$
1368	122	41%	1363	7081	11%	58	1362	6426	26%	53
1512	120	44%	1509	4723	22%	39	1507	5523	27%	46

On the other hand, the Rhodamine 6G signal when using the substrate containing only one PAH/Au bilayer was not significantly improved. Spectra were collected at a set

234

of points on the surface of the samples, showing a consistent and reproducible scattering pattern without large variability in the intensity in the case of samples coated with three and five bilayers. A quantitative evaluation of the reproducibility of the spectra in terms of average relative standard deviation (RSD) over the intensities of the prominent Rhodamine 6G Raman peaks are provided in Appendix D. The enhancement factor (EF) was calculated as follows[240]:

$$EF = \frac{I_{SERS}/N_{surf}}{I_{RS}/N_{vol}} \tag{6}$$

where I_{RS}, I_{SERS} are Raman and SERS intensities of Rhodamine 6G, N_{surf} is the average number of Rhodamine 6G molecules adsorbed onto the gold-coated diatomite composite in the scattering area for the SERS measurements, and N_{vol} is the number of Rhodamine 6G molecules present in the bulk scattering volume for spontaneous Raman scattering measurements. For the EF estimation, Raman modes at ca. 1362 and 1507 cm^{-1} were used, as they correspond to benzene ring stretching and are the most prominent ones. The detailed calculation steps are provided in Appendix D. The SERS EF for diatomite coated with three PAH/AuNPs bilayers was calculated to be 6×10^3. Therefore, hybrid materials based on diatomite decorated with gold nanoparticles can be utilized as a low-cost and easy to fabricate SERS platform.

The signal enhancement introduced by diatomite embedded with gold nanoparticles can be explained from several aspects. Given that a diatomite has a high specific surface area, AuNPs can be adsorbed not only on the surface but also around the pores using LbL technique in combination with FIL.[241] Dense gold coating in an ordered manner creates

numerous ''hot spots'' and ensures high SERS enhancement and reproducibility. During multilayer deposition, AuNP clusters are formed, which is indicated by long tail in the extinction spectra of diatomite coated with three and five PAH/AuNPs bilayers (Figure 85b) and confirmed by photoacoustic imaging (Figure 88, 89). Strong SERS enhancement in the case of multilayer deposition, which is absent in the case of one bilayer, is probably resulting from the increase in the number and efficiency of SERS ''hot spots'' caused by the aggregation of AuNPs with the deposition procedures.

8.9 Summary

Here we demonstrated the capabilities of gold-coated diatomite as SERS platform. LBL+FIL hybrid material fabrication techniques resulted in a strong SERS signal due to the optimization of the spatial distribution of AuNPs over the surface of nanostructured silica substrate. Photoacoustic imaging offers a simple, fast and meaningful technique for the visualization and characterization of obtained materials and many other materials with SERS-active nanoparticles.

Chapter 9. Conclusions

This thesis focuses on the investigation of diatom algae and related materials at three distinct levels, namely diatom colonies in suspension, individual living diatoms cells and cleaned frustules, and diatomite powder. After each chapter, a concise summary was provided.

Based on the findings presented in this thesis, the following main conclusions can be drawn:

- The fluorescence and photoacoustic signal collected from diatoms depend on their growth phase and can be used for monitoring of their growth during long term cultivation.

- Diatoms exhibit strong photoacoustic signals owing to the presence of chlorophylls and carotenoids that absorb very well the 532 nm wavelength upon illumination.

- Using a fabricated optical device consisting of LED illumination with a central wavelength of 505 nm, a linear dependence of the measured transmission on the concentration of diatoms was obtained with high accuracy for 7 strains of diatoms of various shapes and volumes.

- Significant differences in the nanomechanical properties of the different frustule layers were observed (E=15±2 GPa (inner surface) and E=10±4 GPa (outer surface)). The deformation response depends strongly on the support from the organic content (E=25±5 GPa).

- The structure–mechanical properties relationship has a direct impact on the vibrational properties of the frustule as a complex micrometer-sized mechanical system. The diatom resonant frequencies in the range 1-8 MHz obtained from COMSOL calculations have been for the first time experimentally validated through AFM laser-induced resonance excitation.

- A dual-periodic photonic crystal structure due to diffraction increases the transmittance of light in the region $\lambda = 400$–500 nm as well as intensity of electric field compared to a homogenous layer of the same material with the same thickness.

- A novel approach to modifying the surface of diatomite with gold nanoparticles, based on a combination of layer-by-layer assembly and freeze-induced loading methods, resulted in 6×10^3 enhanced Raman signal from Rhodamine 6G owing to the optimization of the spatial distribution of AuNPs over the surface of nanostructured silica substrate.

Lessons from Nature's nanostructuring of diatoms open up pathways to new generations of nano- and microdevices for electronic, electromechanical, photonic, liquid, energy storage, and other applications.

Appendix A

Cell ultrastructure

To study the ultrastructure, the prepared sections of diatoms were examined using a transmission electron microscope.

Ulnaria acus (Kützing) Aboal

The internal structure of the cells of *Ulnaria acus* (Kützing) Aboal (=Synedra acus Kützing 1844) corresponds to previously obtained data [242] (Figure 91). Cross sections show a nucleus with a large nucleolus through the center of the cell, between two chloroplasts (Figure 91a-c). Chloroplasts are pressed against the valves and have an indistinct pyrenoid (Figure 91a, b). A few plastoglobuli are located between the thylakoids (Figure 91b). On sections of many cells, there are emerging girdle rims (Figure 91c). The Golgi apparatuses are adjacent to the nucleus (Figure 91a, c). Mitochondria on transverse sections are small rounded (Figure 91b), and on longitudinal sections they are elongated and can reach a length of more than 4 μm (Figure 91d).
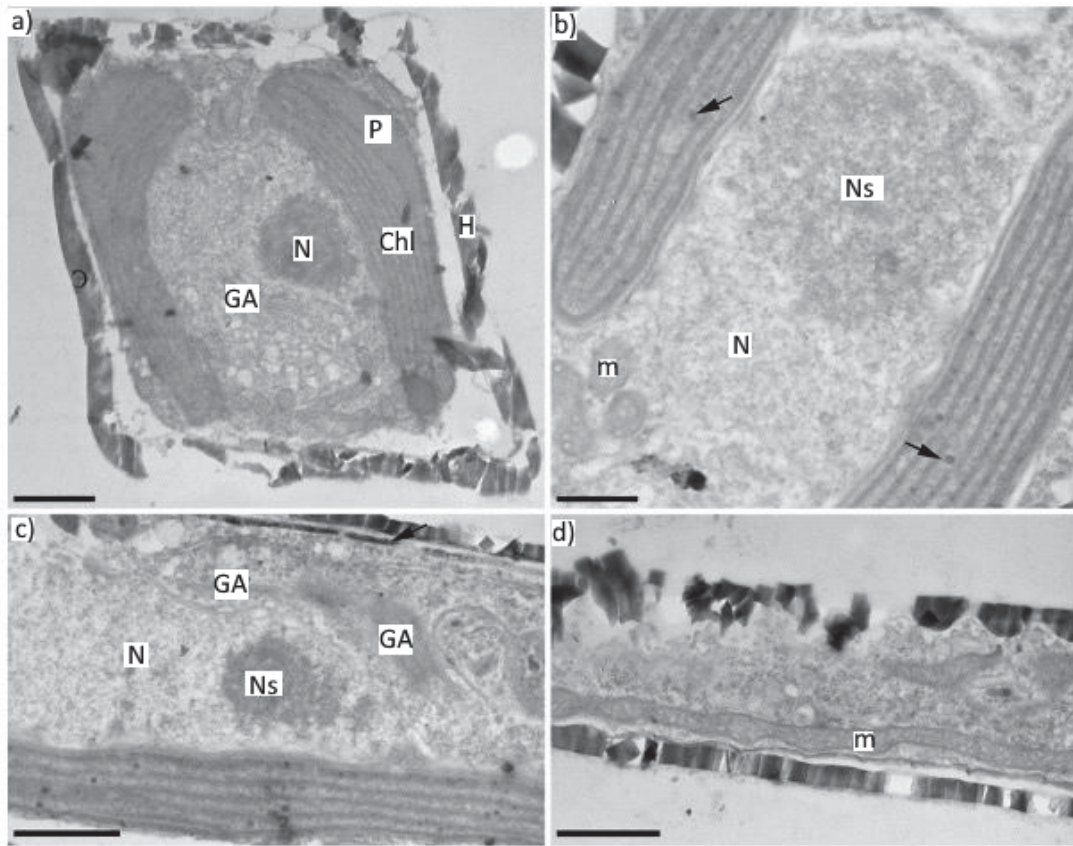
Figure 91. Structural details of *Ulnaria acus* 15K595 cells (TEM). Cross sections - a, b; longitudinal sections, c, d. The arrows in Figure 1b show plastoglobules, and in Figure 1c, a fragment of the forming girdle rim. Symbols: GA - Golgi apparatus; H - hypotheca; m - mitochondrion; P - pyrenoid; E - epitheca; N – nucleus, NS - nucleolus. Scale: a, c, d – 1 µm; b – 500 nm.

Coscinodiscus oculus-iridis (Ehrenberg) Ehrenberg

The cell ultrastructure of *Coscinodiscus oculus-iridis* (Ehrenberg) Ehrenberg has not been previously described. On sections, the nucleus with a large nucleolus is located in the center of the cell, surrounded by chloroplasts and lipid droplets, or can be shifted to the

girdle rims (Figure 92a). The bulk of the cell is occupied by the vacuole (Figure 92a). Numerous chloroplasts are pressed to the cell periphery, have a rounded pyrenoid (Figure 92b), thylakoids are packed in stacks of three and can form anastomoses (Figure 92d), plastoglobuli are located between the thylakoid stacks (Figure 92e). In all sections, the polysaccharide layer adjacent to the valve is clearly visible (Figure 92c). Mitochondria are oblong, most often pressed against the cell periphery (Figure 92c). On the periphery of the cytoplasm, there are vesicles transporting mucus to the plasmalemma (Figure 92e).
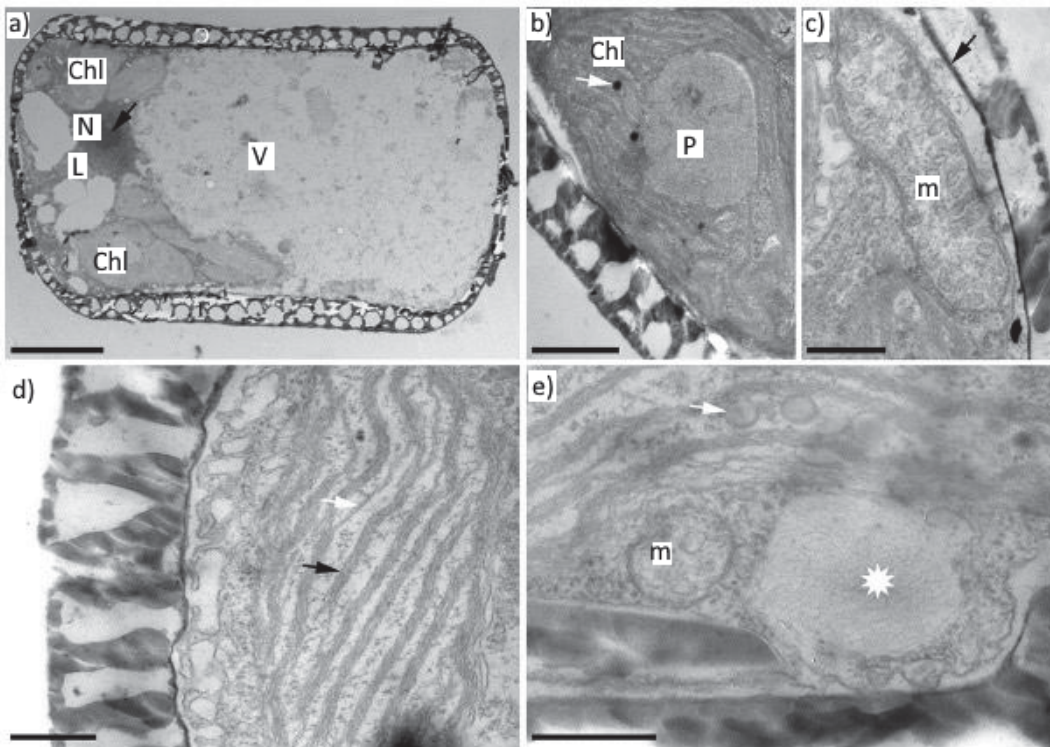
Figure 92. Details of the cell structure of *Coscinodiscus oculus-iridis*. a) general view of the cell, cross section, the arrow shows the nucleolus; b) section through the chloroplast (arrow – plastoglobules); c) section through the mitochondrion (arrow—polysaccharide layer); d) fragment of a chloroplast section (black arrow, thylakoid; white

arrow, anastomosis between stacks of thylakoids); e) Section fragment through the chloroplast (arrow – plastoglobule) and transport vesicle (asterisk). Scale: a – 5 μm; b – 1 μm; c-e - 500 nm. Designations as in the previous Figure 91.

Hannaea baicalensis Genkal, Popovskaya & Kulikovskiy

The ultrastructure of *Hannaea baicalensis* Genkal, Popovskaya & Kulikovskiy is described for the first time. The only chloroplast is pressed against the shell from the side of the girdle rims and is distinguished by a large pyrenoid located in the center of the chloroplast (Figure 93a, b). Stacks of thylakoids are not numerous - from 4 to 7 on a chloroplast section (Figure 93a-c), plastoglobuli are located between the thylakoids (Figure 93b). The nucleus is adjacent to the pyrenoid; it can be shifted to one of the lobes of the chloroplast (Figure 93a, b). Mitochondria are small and irregular in shape (Figure 93d). There are several Golgi apparatuses in the cell, but on the cut, as a rule, it is one and is adjacent to the nucleus (Figure 93b) or to the chloroplast (Figure 93e).
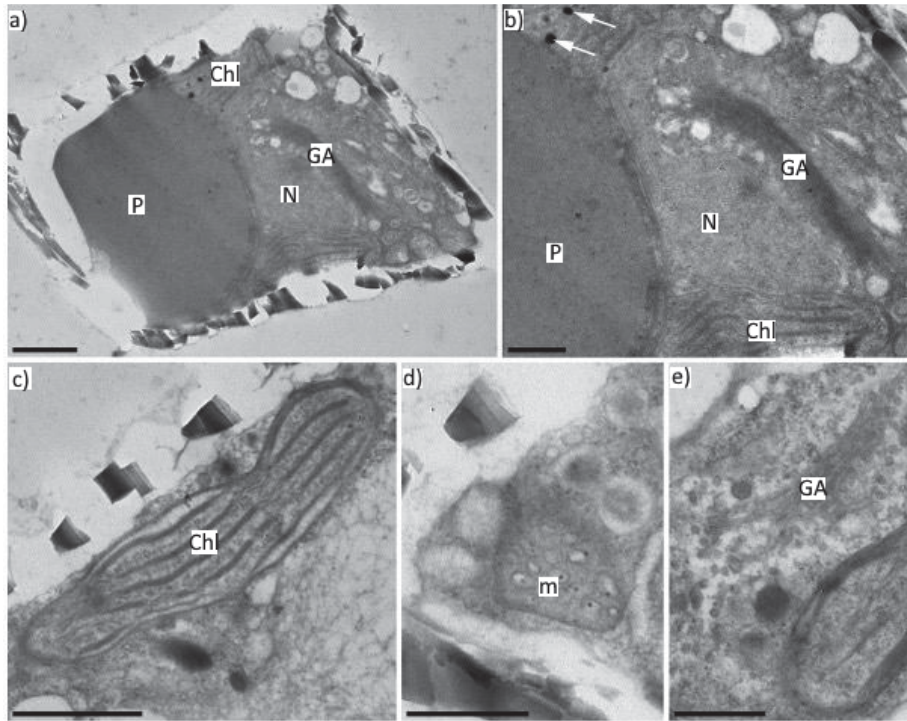
Figure 93. Details of the cell structure of *Hannaea baicalensis*. A) general view of the cell, cross section; b) enlarged fragment of figure 48a; c) section through a part of the chloroplast without a pyrenoid; d) cross section of mitochondria; e) section of the Golgi apparatus adjacent to the chloroplast. Scale: a, c – 1 µm; b, d, e – 500 nm. Designations as in Figure 91.

Appendix B

Thermal frequency spectra of diatom frustule at different positions are shown in Figure 94.
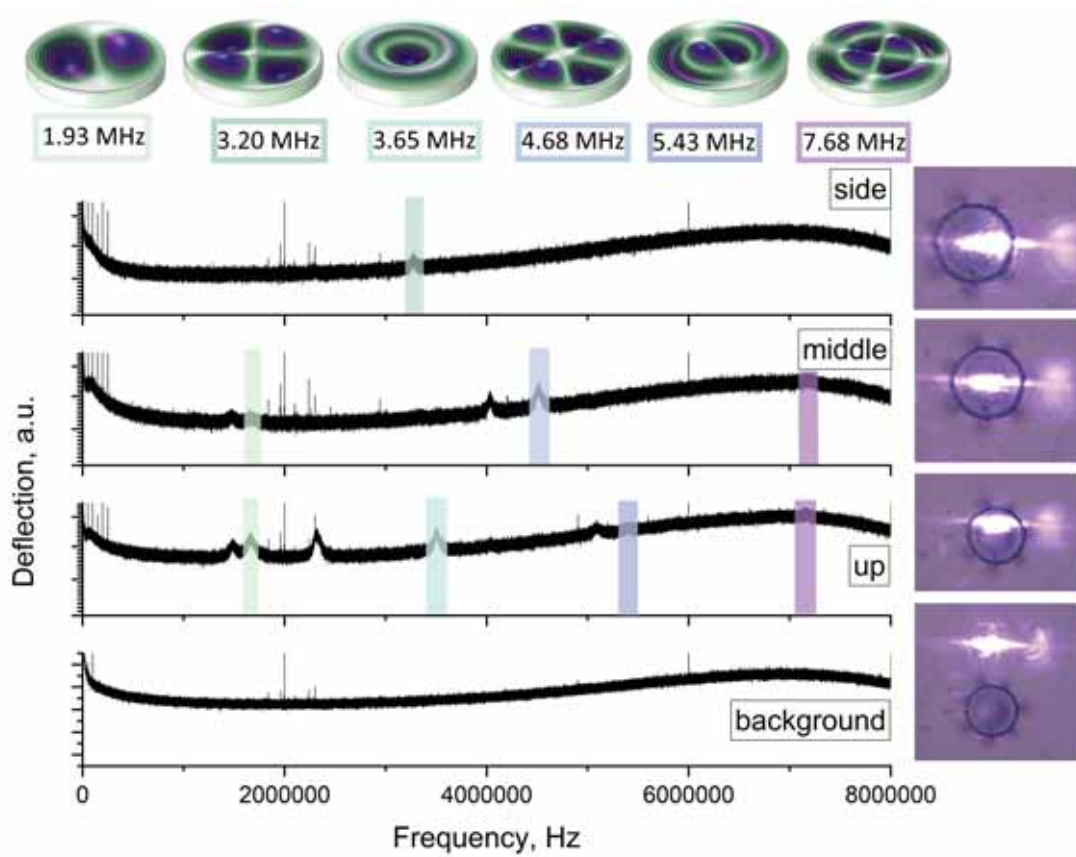
Figure 94. Raw thermal spectra of the diatom frustule collected at different spots.

Appendix C
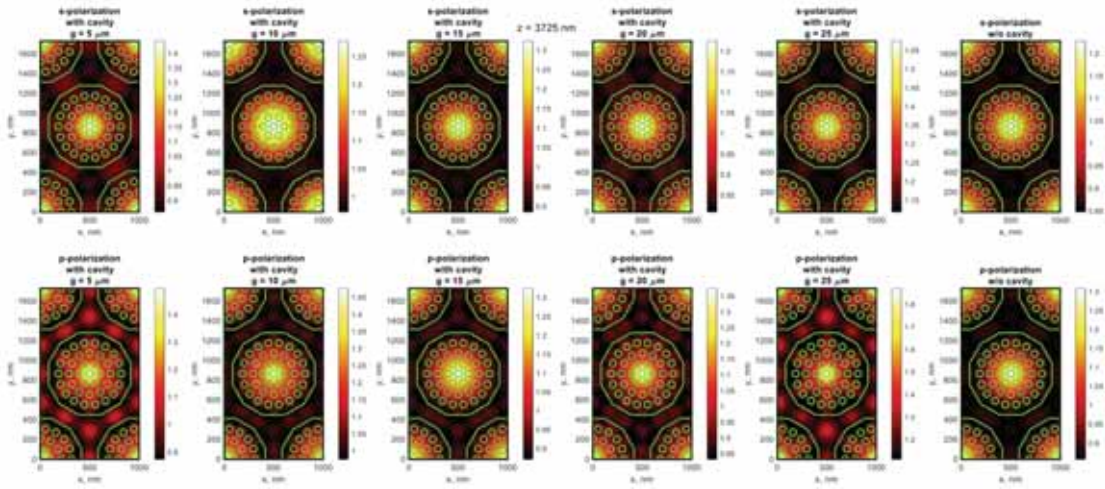
Figure 95. Electric field intensity calculated for: S- (upper row) and P-polarization (bottom row), within horizontal cross-sections of samples with height g=5, 10, 15, 20, 25 μm.
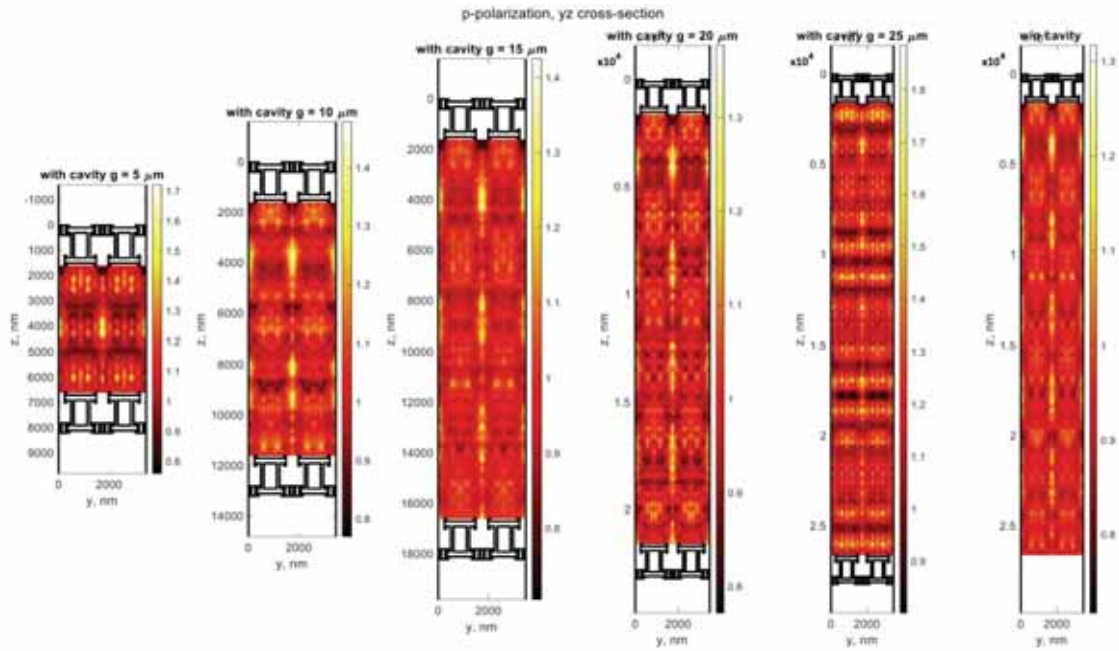
Figure 96. Electric field intensity calculated for P-polarization within vertical cross-sections of samples with height g=5, 10, 15, 20, 25 μm in yz plane.
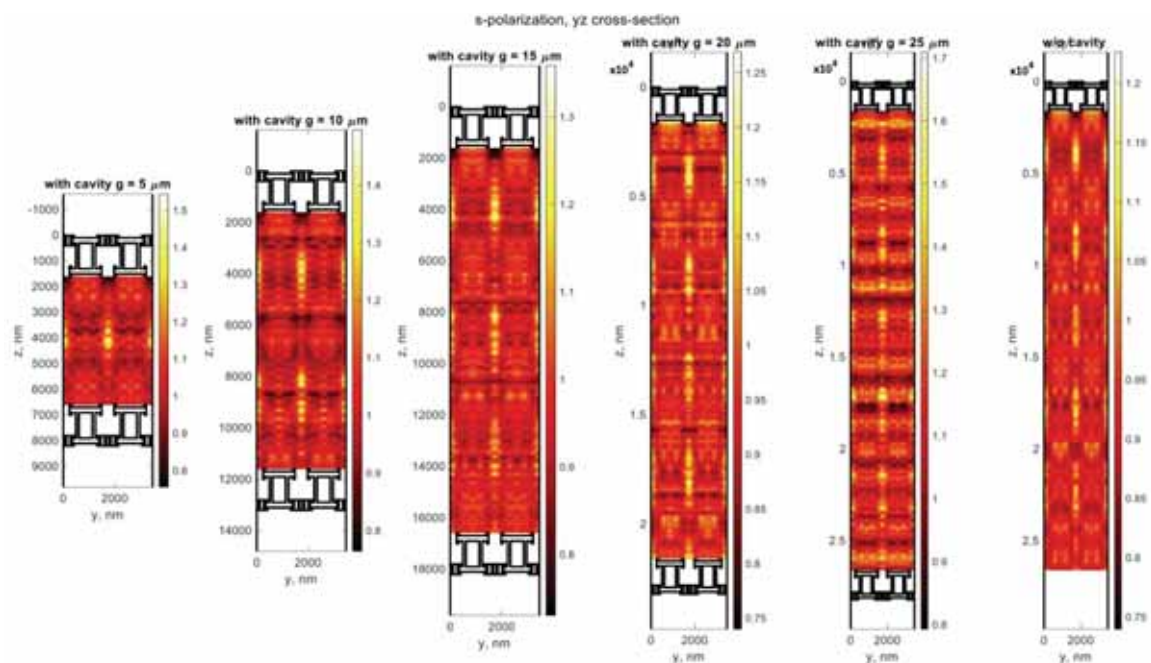
Figure 97. Electric field intensity calculated for S-polarization within vertical cross-sections of samples with height g=5, 10, 15, 20, 25 μm in yz plane.
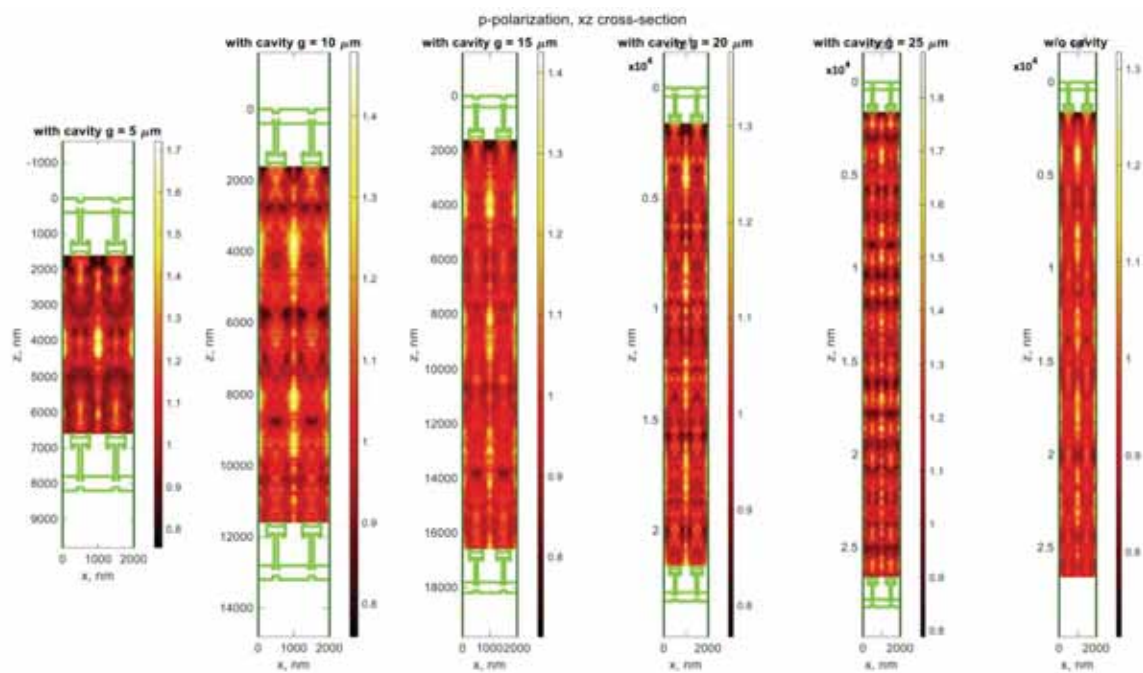
Figure 98. Electric field intensity calculated for P-polarization within vertical cross-sections of samples with height g=5, 10, 15, 20, 25 μm in xz plane.
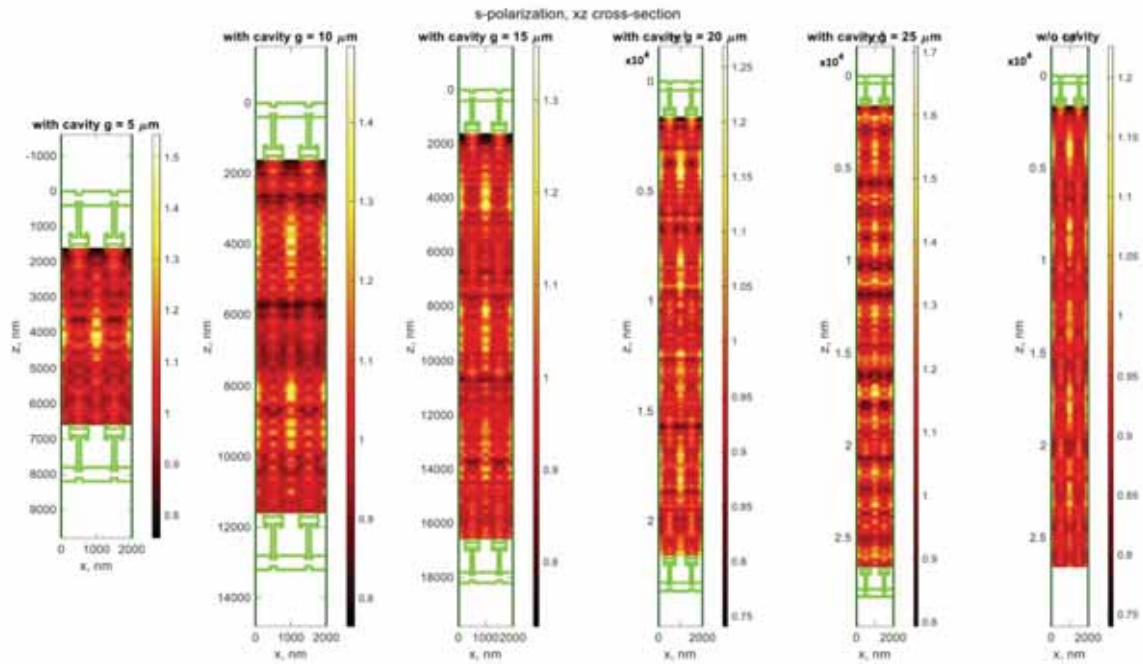
Figure 99. Electric field intensity calculated for S-polarization within vertical cross-sections of samples with height g=5, 10, 15, 20, 25 μm in xz plane.

Appendix D

SERS measurements justification

1. Choosing traces of Raman scattering

For each diatomite-based sample type, 9-10 measurements were taken. Then for each sample type intensity distribution of the modes around 1362 and 1509 cm^{-1} was analyzed, and measurements with amplitudes in the lower quartile (1-2 measurements per sample type) were excluded. Therefore, each sample type had 7-9 measurements that were used for further calculation of mean trace and its standard deviation, as shown in Figure 100.
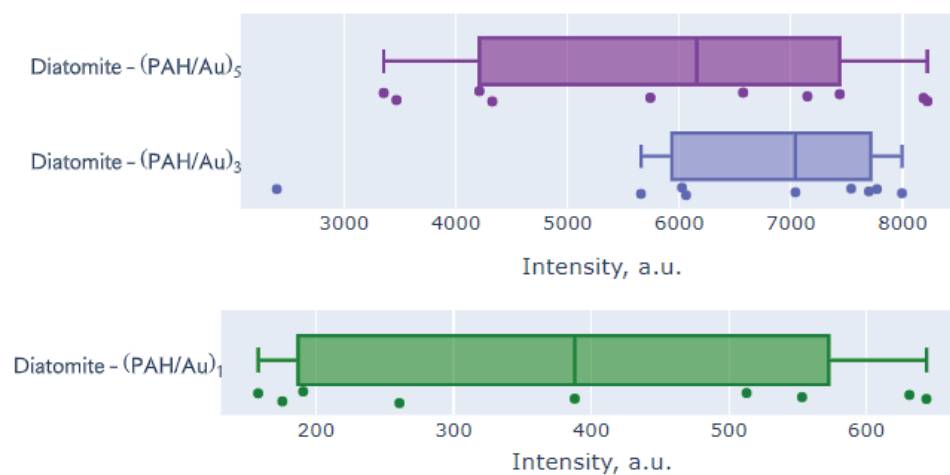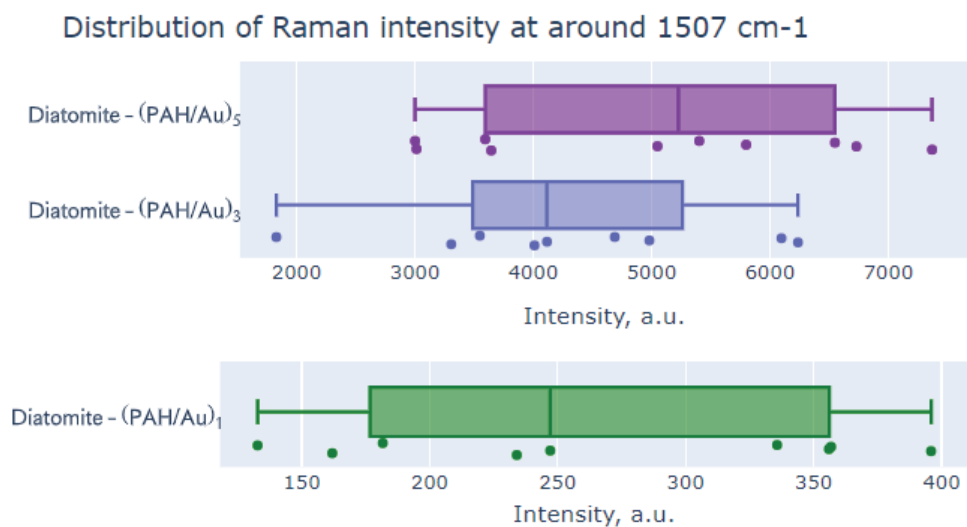
Figure 100. Distributions of peak intensities of two prominent peaks of Rhodamine 6G (1362 cm^{-1} – up, 1509 cm^{-1} – down).

In Table 9, mean intensity values and their relative standard deviations (RSD) are calculated for each pair of prominent Rhodamine 6G (R6G) Raman peaks detected. For a general enhancement factor (EF) estimation for the substrates, Raman modes at 1362 and 1509 cm^{-1} were used, as they correspond to benzene ring stretching and are the most prominent ones.

2. Enhancement Factor Calculation

The enhancement factor was calculated using equation (6), as shown in the section 8.8.

2.1. Determination of N_{surf}

To determine the average number of R6G molecules adsorbed onto the gold-coated diatomite composite in the scattering area, concentrations of bulk R6G before and after

incubation with Diatomite-(PAH/AuNPs)₃ were estimated by means of the calibration curve built for R6G absorption at 500 nm.

To absorb R6G on diatomite coated with PAH/AuNPs layers, 120 µL of 200 µM R6G, that equals to 24 nmoles, were mixed with 120 µL of Diatomite-(PAH/AuNPs)₃ with concentration $c_{Dt} = 1.3 \cdot 10^8$ particles/mL, that equals to $N_{Dt} = 1.56 \cdot 10^7$ particles in solution.

According to spectroscopic data obtained, the concentration of non-absorbed R6G after incubation with gold-coated diatomite was 72 µM, that equals to 17.3 nmoles. We presume that the rest of R6G molecules, $n_{R6G}^{abs} = 6.7$ nmol, were absorbed on gold-coated diatomite composites, therefore on average 1 diatomite absorbed $2.8 \cdot 10^8$ particles:

$$\frac{N_{R6G}}{N_{Dt}} = \frac{n_{R6G}^{abs} \cdot N_A}{c_{Dt} \cdot V_{Dt}} = 2.6 \cdot 10^8 \text{ molecules/particle}$$
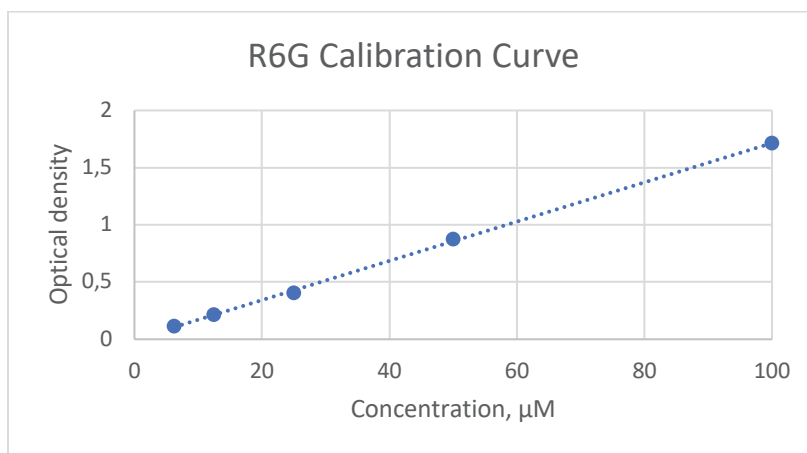
Figure 101. Calibration curve for R6G

Raman spectrometer was equipped with an objective having magnification M = 10 and the pinhole size Φ was set to 100 μm. Therefore, the laser spot size radius way be estimated as[243]:

$$r \approx \frac{\Phi}{2 \cdot 1.4 \cdot M} = 3.57$$

Then the laser spot area

$$S = \pi r^2 = 40 \ \mu m^2$$

That is obviously greater than the diatomite size, therefore we assume that we get a SERS signal from a single diatomite particle. We also assume that we collect only a half of intensity that could be obtained from one diatomite, as irradiation and detection is provided from just one side, in a backscattering mode. Furthermore, only molecules in vicinity of AuNPs are enhanced, and according to SEM images (Figure 86) 15.5% of diatomite surface is covered with AuNPs, therefore

$$N_{surf} = \frac{1}{2} \cdot \frac{N_{R6G}}{N_{Dt}} * 15.5\% = 2 \cdot 10^7 \text{ molecules}$$

2.2. Determination of N_{vol}

Liquid drop height h is around 0.5 mm. Assuming that for a given objective the whole height participates in Raman scattering, the volume participating may be found as

$$V_{RS} = S \cdot h = 2 \cdot 10^4 \ \mu m^3$$

Therefore, the number of R6G molecules participating in Raman scattering is

$$N_{vol} = V_{RS} \cdot c_{R6G} \cdot N_A = 2 \cdot 10^4 \mu m^3 \cdot 200 \cdot 10^{-21} \frac{mol}{\mu m^3} \cdot 6.02 \cdot 10^{23} \frac{1}{mol} = 2.4 \cdot 10^9 \text{ molecules}$$

2.3. Determination of the Enhancement Factor

Thus, according to equation (6) and data from Table 9, the EF may be estimated as:

$$EF = \frac{I_{SERS}}{I_{RS}} \cdot \frac{N_{vol}}{N_{surf}} \approx 6 \cdot 10^3$$

Bibliography

1.   Cvjetinovic, J. *et al.* Revealing the static and dynamic nanomechanical properties of diatom frustules-Nature's glass lace. *Sci Rep* **13**, 5518 (2023).

2.   Nelson, D. M., Tréguer, P., Brzezinski, M. A., Leynaert, A. & Quéguiner, B. Production and dissolution of biogenic silica in the ocean: Revised global estimates, comparison with regional data and relationship to biogenic sedimentation. *Global Biogeochem Cycles* **9**, 359–372 (1995).

3.   Field, C. B., Behrenfeld, M. J., Randerson, J. T. & Falkowski, P. Primary production of the biosphere: Integrating terrestrial and oceanic components. *Science (1979)* **281**, 237–240 (1998).

4.   Sethi, D., Butler, T. O., Shuhaili, F. & Vaidyanathan, S. Diatoms for Carbon Sequestration and Bio-Based Manufacturing. *Biology 2020, Vol. 9, Page 217* **9**, 217 (2020).

5.   Cheng, W. *et al.* Global monthly gridded atmospheric carbon dioxide concentrations under the historical and future scenarios. *Sci Data* **9**, (2022).

6.   Collins, S., Rost, B. & Rynearson, T. A. Evolutionary potential of marine phytoplankton under ocean acidification. *Evol Appl* **7**, 140–155 (2014).

7.   Salimon, A. I., Cvjetinovic, J. *et al. On the Mathematical Description of Diatom Algae: From Siliceous Exoskeleton Structure and Properties to Colony Growth Kinetics, and Prospective Nanoengineering Applications* in The *Mathematical Biology of Diatoms,* ed. Janice L. Pappas, Scrivener Publishing LLC, 63-102 (2023).

8.   Medlin, L. K., Kooistra, W. H. C. F., Sims, P. & Wellbrock, U. Is the origin of the diatoms related to the end-Permian mass extinction? *Nova Hedwigia* **65**, 1–11 (1997).

9.   Harwood, D. M. & Nikolaev, V. A. Cretaceous Diatoms: Morphology, Taxonomy, Biostratigraphy. *Short Courses in Paleontology* **8**, 81–106 (1995).

10.   AlgaeBase: Listing the World's Algae. https://www.algaebase.org/.

11.   Aitken, Z. H., Luo, S., Reynolds, S. N., Thaulow, C. & Greer, J. R. Microstructure provides insights into evolutionary design and resilience of Coscinodiscus sp. frustule. *Proc Natl Acad Sci* **113** (8), 2017-2022 (2016).

12.   Mishra, M., Arukha, A. P., Bashir, T., Yadav, D. & Prasad, G. B. K. S. All new faces of diatoms: Potential source of nanomaterials and beyond. *Frontiers in Microbiology* **8** (2017).

13.   Bedoshvili, Y., Gneusheva, K., Popova, M., Morozov, A. & Likhoshway, Y. Anomalies in the valve morphogenesis of the centric diatom alga Aulacoseira islandica caused by microtubule inhibitors. *Biol Open* **7**, (2018).

14.   Jain, S. *Marine Diatoms* in *Fundamentals of Invertebrate Palaeontology,* Springer Geology, Springer Science and Business Media Deutschland GmbH, 131–142 (2020).

15.   Cvjetinovic, J. *et al.* Photoacoustic and fluorescence lifetime imaging of diatoms. *Photoacoustics* **18**, 100171 (2020).

16.   Haeckel, E. Kunstformen der Natur, Bibliographisches Institut, Leipzig-Vienna, 1904.

17.   Salimon, A. I. *et al.* A Mini-Atlas of diatom frustule electron microscopy images at different magnifications. in *Materials Today: Proceedings* **33**, 1924–1933 (2020).

18.   Darwin, C. On the origin of species by means of natural selection, or the preservation of favoured races in the struggle for life, John Murray, p.502 (1859).

19.   Nemoto, T., Best, P. B., Ishimaru, K., & Takano, H. Diatom films on whales in South African waters. *Sci. Rep. Whales Res. Inst*. **32**, 97-103 (1980).

20.   Malviya, S. *et al.* Insights into global diatom distribution and diversity in the world's ocean. *Proc Natl Acad Sci* **113**, E1516–E1525 (2016).

21.   Falciatore, A., Jaubert, M., Bouly, J. P., Bailleul, B. & Mock, T. Diatom molecular research comes of age: Model species for studying phytoplankton biology and diversity. *Plant Cell* **32**, 547-572 (2020).

22.   Zgłobicka, I. *et al.* Insight into diatom frustule structures using various imaging techniques. *Scientific Reports 2021 11:1* **11**, 1–10 (2021).

23.   Zhang, D. Y. *et al.* Bio-manufacturing technology based on diatom micro- and nanostructure. *Chinese Science Bulletin* **57**, 3836–3849 (2012).

24.   Bruder, K. & Medlin, L. K. Morphological and molecular investigations of naviculoid diatoms. II. Selected genera and families. *Diatom Research* **23**, 283–329 (2008).

25.   Urbani, R., Magaletti, E., Sist, P. & Cicero, A. M. Extracellular carbohydrates released by the marine diatoms Cylindrotheca closterium, Thalassiosira pseudonana and Skeletonema costatum: Effect of P-depletion and growth status. *Science of The Total Environment* **353**, 300–306 (2005).

26.   Hoppenrath, M. *et al.* Thalassiosira species (Bacillariophyceae, Thalassiosirales) in the North Sea at Helgoland (German Bight) and Sylt (North Frisian Wadden Sea) - A first approach to assessing diversity. *Eur J Phycol* **42**, 271–288 (2007).

27.   De Tommasi, E., Gielis, J. & Rogato, A. Diatom Frustule Morphogenesis and Function: a Multidisciplinary Survey. *Mar Genomics* **35**, 1–18 (2017).

28.   Aguirre, L. E. *et al.* Diatom frustules protect DNA from ultraviolet light. *Sci Rep* **8**, 1–6 (2018).

29.   Romann, J. *et al.* Wavelength and orientation dependent capture of light by diatom frustule nanostructures. *Sci Rep* **5**, (2015).

30.   Sprynskyy, M. *et al.* Naturally organic functionalized 3D biosilica from diatom microalgae. *Mater Des* **132**, 22-29 (2017).

31.   Fabritius, H. O., Sachs, C., Triguero, P. R. & Raabe, D. Influence of structural principles on the mechanics of a biological fiber-based composite material with hierarchical organization: The exoskeleton of the lobster homarus americanus. *Advanced Materials* **21**, 391–400 (2009).

32.   Korsunsky, A. M., Sapozhnikov, P. V., Everaerts, J. & Salimon, A. I. Nature's neat nanostructuration: The fascinating frustules of diatom algae. *Materials Today* **22**, 159–160 (2019).

33.   Sumper, M. A Phase Separation Model for the Nanopatterning of Diatom Biosilica. *Science (1979)* **295**, 2430–2433 (2002).

34.   Mazumder, N., Gordon, R. *Diatom Microscopy*. Wiley Scrivener Publishing, p.368 (2022).

35.   Zgłobicka, I. *et al.* Visualization of the internal structure of Didymosphenia geminata frustules using nano X-ray tomography. *Sci Rep* **7**, (2017).

36.   Taveri, G., Grasso, S., Gucci, F., Toušek, J. & Dlouhy, I. Bio-Inspired Hydro-Pressure Consolidation of Silica. *Adv Funct Mater* **28**, (2018).

37.   Sumper, M. & Kröger, N. Silica formation in diatoms: the function of long-chain polyamines and silaffins. *J. Mater. Chem.* **14**, 2059–2065 (2004).

38.   Subhash, G., Yao, S., Bellinger, B. & Gretz, M. R. Investigation of mechanical properties of diatom frustules using nanoindentation. *J Nanosci Nanotechnol* **5**, 50–56 (2005).

39.   Losic, D., Short, K., Mitchell, J. G., Lal, R. & Voelcker, N. H. AFM nanoindentations of diatom biosilica surfaces. *Langmuir* **23**, 5014–5021 (2007).

40.   Losic, D., Pillar, R. J., Dilger, T., Mitchell, J. G. & Voelcker, N. H. Atomic force microscopy (AFM) characterisation of the porous silica nanostructure of two centric diatoms. *Journal of Porous Materials 2006 14:1* **14**, 61–69 (2006).

41.   Almqvist, N. *et al.* Micromechanical and structural properties of a pennate diatom investigated by atomic force microscopy. *J Microsc* **202**, 518–532 (2001).

42.   Hamm, C. E. *et al.* Architecture and material properties of diatom shells provide effective mechanical protection. *Nature 2003 421:6925* **421**, 841–843 (2003).

43.   Wegst, U. G. K. & Ashby, M. F. The mechanical efficiency of natural materials. *Philosophical Magazine* **84**, 2167–2186 (2004).

44.   Xing, Y. *et al.* Characterization and analysis of Coscinodiscus genus frustule based on FIB-SEM. *Progress in Natural Science: Materials International* **27**, 391–395 (2017).

45.   Aggrey, P. *et al.* In Situ Formation of Nanoporous Silicon on a Silicon Wafer via the Magnesiothermic Reduction Reaction (MRR) of Diatomaceous Earth. *Nanomaterials* **10**, 601 (2020).

46.   Moreno, M. D., Ma, K., Schoenung, J. & Dávila, L. P. An integrated approach for probing the structure and mechanical properties of diatoms: Toward engineered nanotemplates. *Acta Biomater* **25**, 313–324 (2015).

47.   Luo, S. & Greer, J. R. Bio-Mimicked Silica Architectures Capture Geometry, Microstructure, and Mechanical Properties of Marine Diatoms. *Adv Eng Mater* **20**(9), (2018).

48.   Topal, E. *et al.* Numerical and experimental study of the mechanical response of diatom frustules. *Nanomaterials* **10**, 1–14 (2020).

49.   Yao, S., Subhash, G. & Maiti, S. Analysis of nanoindentation response of diatom frustules. *J Nanosci Nanotechnol* **7**, 4465–4472 (2007).

50.   Parker, A. R. *Natural photonic structures: an overview* in *Optical Biomimetics* Woodhead Publishing Limited, p.1-19 (2012).

51.   Vukusic, P. & Sambles, J. R. Photonic structures in biology. *Nature* **424**, 852–855 (2003).

52.   Parker, A. R. & Townley, H. E. Biomimetics of photonic nanostructures. *Nat Nanotechnol* **2**, 347–353 (2007).

53.   Mcheik, A. *et al.* Optical properties of nanostructured silica structures from marine organisms. *Frontiers in Marine Science* **5**, (2018).

54.   Kuczynska, P., Jemiola-Rzeminska, M. & Strzalka, K. Photosynthetic pigments in diatoms. *Mar Drugs* **13**, 5847–5881 (2015).

55.   De Tommasi, E. *et al.* UV-shielding and wavelength conversion by centric diatom nanopatterned frustules. *Sci Rep* **8**, 1–14 (2018).

56.   Ellegaard, M. *et al.* The fascinating diatom frustule—can it play a role for attenuation of UV radiation? *J Appl Phycol* **28**, 3295–3306 (2016).

57.   Richard, B. & Hoover, M. J. Optical phenomena in diatoms. *Journal of the Arkansas Academy of Science* **24**, (1970).

58.   Stefano, L. De, Rendina, I., Stefano, M. De, Rea, I. & Moretti, L. Lensless light focusing with the centric marine diatom Coscinodiscus walesii. *Optics Express, Vol. 15, Issue 26, pp. 18082-18088* **15**, 18082–18088 (2007).

59.   De Tommasi, E. *et al.* Multi-wavelength study of light transmitted through a single marine centric diatom. *Optics Express* **18**, 12203–12212 (2010).

60.   Ferrara, M. A. *et al.* Optical properties of diatom nanostructured biosilica in Arachnoidiscus sp: Micro-optics from mother nature. *PLoS One* **9**, (2014).

61.   Knight, J. C. Photonic crystal fibres. *Nature* **424**, 847–851 (2003).

62.   Chen, X., Wang, C., Baker, E. & Sun, C. Numerical and experimental investigation of light trapping effect of nanostructured diatom frustules. *Sci Rep* **5**, 1–9 (2015).

63.   Kieu, K. *et al.* Structure-based optical filtering by the silica microshell of the centric marine diatom Coscinodiscus wailesii. *Opt Express* **22**, 15992 (2014).

64.   Yoneda, S., Ito, F., Yamanaka, S. & Usami, H. Optical properties of nanoporous silica frustules of a diatom determined using a 10 μm microfiber probe. *Jpn J Appl Phys* **55**, (2016).

65.   Yamanaka, S. *et al.* Optical properties of diatom silica frustule with special reference to blue light. *J Appl Phys* **103**, 074701 (2008).

66.   Yoon, H. & Goorsky, M. S. A systematic study of the structural and luminescence properties of P-type porous silicon. *MRS Online Proceedings Library* **378**, 893–898 (1995)

67.   Cullis, A. G., Canham, L. T. & Calcott, P. D. J. The structural and luminescence properties of porous silicon. *Journal of Applied Physics* **82**, 909–965 (1997).

68.   De Tommasi, E. *et al.* Intrinsic photoluminescence of diatom shells in sensing applications. in *Optical Sensors* **7356**, 735615 (2009).

69.   De Stefano, L., Rendina, I., De Stefano, M., Bismuto, A. & Maddalena, P. Marine diatoms as optical chemical sensors. *Appl Phys Lett* **87**, 1–3 (2005).

70.   Bismuto, A., Setaro, A., Maddalena, P., De Stefano, L. & De Stefano, M. Marine diatoms as optical chemical sensors: A time-resolved study. *Sens Actuators B Chem* **130**, 396–399 (2008).

71.   Townley, H. E., Woon, K. L., Payne, F. P., White-Cooper, H. & Parker, A. R. Modification of the physical and optical properties of the frustule of the diatom Coscinodiscus wailesii by nickel sulfate. *Nanotechnology* **18**, (2007).

72.   De Stefano, L. *et al.* Marine diatoms as optical biosensors. *Biosens Bioelectron* **24**, 1580–1584 (2009).

73. Camargo, E. *et al.* Chemical and optical characterization of Psammodictyon panduriforme (Gregory) Mann. comb. nov. (Bacillariophyta) frustules. *Opt Mater Express* **6**, 1436 (2016).

74. Arteaga-Larios, N. V., Nahmad, Y., Navarro-Contreras, H. R., Encinas, A. & García-Meza, J. V. Photoluminescence shift in frustules of two pennate diatoms and nanostructural changes to their pores. *Luminescence* **29**, 969–976 (2014).

75. Rea, I. & De Stefano, L. Recent advances on diatom-based biosensors. *Sensors (Switzerland)* **19**, (2019).

76. Leonardo, S., Prieto-Simón, B. & Campàs, M. Past, present and future of diatoms in biosensing. *TrAC Trends in Analytical Chemistry* **79**, 276–285 (2016).

77. Jeffryes, C., Campbell, J., Li, H., Jiao, J. & Rorrer, G. The potential of diatom nanobiotechnology for applications in solar cells, batteries, and electroluminescent devices. *Energy Environ Sci* **4**, 3930–3941 (2011).

78. Viji, S. *et al.* Diatom-Based Label-Free Optical Biosensor for Biomolecules. *Appl Biochem Biotechnol* **174**, 1166–1173 (2014).

79. Selvaraj, V., Muthukumar, A., Nagamony, P. & Chinnuswamy, V. Detection of typhoid fever by diatom-based optical biosensor. *Environmental Science and Pollution Research* **25**, 20385–20390 (2018).

80. Kong, X. *et al.* Chemical and biological sensing using diatom photonic crystal biosilica with in-situ growth plasmonic nanoparticles. *IEEE Trans Nanobioscience* **15**, 828–834 (2016).

81.   Vona, D. *et al.* Light emitting silica nanostructures by surface functionalization of diatom algae shells with a triethoxysilane-functionalized π-conjugated fluorophore. *MRS Adv* **1**, 3817–3823 (2016).

82.   Rogato, A. & De Tommasi, E. Physical, chemical, and genetic techniques for diatom frustule modification: Applications in nanotechnology. *Applied Sciences (Switzerland)* **10**, 1–23 (2020).

83.   Cvjetinovic, J. *et al.* A SERS platform based on diatomite modified by gold nanoparticles using a combination of layer-by-layer assembly and a freezing-induced loading method. *Physical Chemistry Chemical Physics* **24**, 8901–8912 (2022).

84.   Kim, J., Seidler, P., Wan, L. S. & Fill, C. Formation, structure, and reactivity of amino-terminated organic films on silicon substrates. *J Colloid Interface Sci* **329**, 114–119 (2009).

85.   Ruggiero, I. *et al.* Diatomite silica nanoparticles for drug delivery. *Nanoscale Res Lett* **9**, 1–7 (2014).

86.   Bariana, M., Aw, M. S., Kurkuri, M. & Losic, D. Tuning drug loading and release properties of diatom silica microparticles by surface modifications. *Int J Pharm* **443**, 230–241 (2013).

87.   Losic, D. *et al.* Surface functionalisation of diatoms with dopamine modified iron-oxide nanoparticles: toward magnetically guided drug microcarriers with biologically derived morphologies. *Chemical Communications* **46**, 6323 (2010).

88.   Terracciano, M. *et al. Silica-Based Nanovectors: From Mother Nature to Biomedical Applications* in *Algae - Organisms for Imminent Biotechnology*, INTECHopen (2016).

89.   Terracciano, M. *et al.* Surface bioengineering of diatomite based nanovectors for efficient intracellular uptake and drug delivery. *Nanoscale* **7**, 20063–20074 (2015).

90.   Delasoie, J. & Zobi, F. Natural diatom biosilica as microshuttles in drug delivery systems. *Pharmaceutics* **11**, 1–21 (2019).

91.   George, J. *et al.* Metabolic Engineering Strategies in Diatoms Reveal Unique Phenotypes and Genetic Configurations With Implications for Algal Genetics and Synthetic Biology. *Front Bioeng Biotechnol* **8**, (2020).

92.   Stukenberg, D., Zauner, S., Dell'Aquila, G. & Maier, U. G. Optimizing CRISPR/cas9 for the diatom Phaeodactylum tricornutum. *Front Plant Sci* **9**, (2018).

93.   Huang, W. & Daboussi, F. Genetic and metabolic engineering in diatoms. *Philosophical Transactions of the Royal Society B: Biological Sciences* **372**, (2017).

94.   Jeffryes, C., Gutu, T., Jiao, J. & Rorrer, G. L. Two-stage photobioreactor process for the metabolic insertion of nanostructured germanium into the silica microstructure of the diatom Pinnularia sp. *Materials Science and Engineering: C* **28**, 107–118 (2008).

95.   Jeffryes, C., Gutu, T., Jiao, J. & Rorrer, G. L. Metabolic Insertion of Nanostructured TiO 2 into the Patterned Biosilica of the Bioreactor Cultivation Process. *ACS Nano* **2**, 2103–2112 (2008).

96.   Jeffryes, C., Gutu, T., Jiao, J. & Rorrer, G. L. Peptide-mediated deposition of nanostructured TiO2 into the periodic structure of diatom biosilica. *J Mater Res* **23**, 3255–3262 (2008).

97.   Bandara, T. M. W. J., Furlani, M., Albinsson, I., Wulff, A. & Mellander, B. E. Diatom frustules enhancing the efficiency of gel polymer electrolyte based dye-sensitized solar cells with multilayer photoelectrodes. *Nanoscale Adv* **2**, 199–209 (2020).

98.   Xiao, X. *et al.* A Visible-NIR Responsive Dye-Sensitized Solar Cell Based on Diatom Frustules and Cosensitization of Photopigments from Diatom and Purple Bacteria. *J Chem* **2020**, (2020).

99.   Machill, S. *et al.* Analytical studies on the incorporation of aluminium in the cell walls of the marine diatom Stephanopyxis turris. *BioMetals* **26**, 141–150 (2013).

100.   Zhang, G. *et al.* Preparation of silicate-based red phosphors with a patterned nanostructure via metabolic insertion of europium in marine diatoms. *Mater Lett* **110**, 253–255 (2013).

101.   Basharina, T. N. *et al.* The Effect of Titanium, Zirconium and Tin on the Growth of Diatom Synedra Acus and Morphology of Its Silica Valves. *Silicon* **4**, 239–249 (2012).

102.   Gannavarapu, K. P., Ganesh, V., Thakkar, M., Mitra, S. & Dandamudi, R. B. Nanostructured Diatom-ZrO2 composite as a selective and highly sensitive enzyme free electrochemical sensor for detection of methyl parathion. *Sens Actuators B Chem* **288**, 611–617 (2019).

103.   Brzozowska, W. *et al.* "Outsourcing" Diatoms in Fabrication of Metal-Doped 3D Biosilica. *Materials* **13**, 2576 (2020).

104. Truong, H. T., Nguyen, T. D. & Nguyen, H. Q. Nanocomposite of silver nanoparticles/diatomite against pathogenous bacteria for catfish. *Aquac Rep* **16**, 100286 (2020).

105. Sun, H. *et al.* Biocompatible silver nanoparticle-modified natural diatomite with anti-infective property. *J Nanomater* **2018**, (2018).

106. Jantschke, A., Herrmann, A. K., Lesnyak, V., Eychmüller, A. & Brunner, E. Decoration of diatom biosilica with noble metal and semiconductor nanoparticles (<10 nm): Assembly, characterization, and applications. *Chem Asian J* **7**, 85–90 (2012).

107. Fischer, C. *et al.* Gold nanoparticle-decorated diatom biosilica: A favorable catalyst for the oxidation of d-glucose. *ACS Omega* **1**, 1253–1261 (2016).

108. Pannico, M. *et al.* Electroless Gold-Modified Diatoms as Surface-Enhanced Raman Scattering Supports. *Nanoscale Res Lett* **11**, (2016).

109. Kong, X. *et al.* Plasmonic nanoparticles-decorated diatomite biosilica: extending the horizon of on-chip chromatography and label-free biosensing. *J Biophotonics* **10**, 1473–1484 (2017).

110. Kamińska, A., Sprynskyy, M., Winkler, K. & Szymborski, T. Ultrasensitive SERS immunoassay based on diatom biosilica for detection of interleukins in blood plasma. *Anal Bioanal Chem* **409**, 6337–6347 (2017).

111. Onesto, V. *et al.* Silica diatom shells tailored with Au nanoparticles enable sensitive analysis of molecules for biological, safety and environment applications. *Nanoscale Res Lett* **13**, 1–9 (2018).

112. Villani, M. *et al.* Transforming diatomaceous earth into sensing devices by surface modification with gold nanoparticles. *Micro and Nano Engineering* **2**, 29–34 (2019).

113. Terracciano, M., Napolitano, M., De Stefano, L., De Luca, A. C. & Rea, I. Gold decorated porous biosilica nanodevices for advanced medicine. *Nanotechnology* **29**, (2018).

114. Briceño, S., Chavez-Chico, E. A. & González, G. Diatoms decorated with gold nanoparticles by In-situ and Ex-situ methods for in vitro gentamicin release. *Materials Science and Engineering C* **123**, (2021).

115. Zahajská, P., Opfergelt, S., Fritz, S. C., Stadmark, J. & Conley, D. J. What is diatomite? *Quaternary Research (United States)* **96**, 48–52 (2020).

116. Delalat, B. *et al.* Targeted drug delivery using genetically engineered diatom biosilica. *Nature Communications 2015 6:1* **6**, 1–11 (2015).

117. Zobi, F. Diatom Biosilica in Targeted Drug Delivery and Biosensing Applications: Recent Studies. *Micro* **2**, 342–360 (2022).

118. Aggrey, P. *et al.* On the diatomite-based nanostructure-preserving material synthesis for energy applications. *RSC Adv* **11**, 31884–31922 (2021).

119. Sun, X. W., Zhang, Y. X. & Losic, D. Diatom silica, an emerging biomaterial for energy conversion and storage. *J Mater Chem A Mater* **5**, 8847–8859 (2017).

120. Cassaignon, S., de Maleprade, R., Nassif, N. & Livage, J. From Living Light to Living Materials. *Mater Today Proc* **1**, 209–215 (2014).

121.   Li, A., Zhao, X., Duan, G., Anderson, S. & Zhang, X. Diatom Frustule-Inspired Metamaterial Absorbers: The Effect of Hierarchical Pattern Arrays. *Adv Funct Mater* **29**, 1809029 (2019).

122.   Kumari, S., Min, K. H., Kanth, B. K., Jang, E. K. & Pack, S. P. Production of TiO2-deposited Diatoms and Their Applications for Photo-catalytic Degradation of Aqueous Pollutants. *Biotechnology and Bioprocess Engineering* **25**, 758–765 (2020).

123.   Köhler, L. *et al.* Are Diatoms "Green" Aluminosilicate Synthesis Microreactors for Future Catalyst Production? *Molecules* **22**, 2232 (2017).

124.   Losic, D., Rosengarten, G., Mitchell, J. G. & Voelcker, N. H. Pore architecture of diatom frustules: potential nanostructured membranes for molecular and particle separations. *J Nanosci Nanotechnol* **6**, 982–989 (2006).

125.   Roychoudhury, P., Bose, R., Dąbek, P. & Witkowski, A. Photonic Nano-/Microstructured Diatom Based Biosilica in Metal Modification and Removal—A Review. *Materials 2022, Vol. 15, Page 6597* **15**, 6597 (2022).

126.   Korsunsky, A. M. *et al.* Siliceous diatom frustules - A smart nanotechnology platform. *Mater Today Proc* **33**, 2032–2040 (2020).

127.   Gordon, R., Losic, D., Tiffany, M. A., Nagy, S. S. & Sterrenburg, F. A. S. The Glass Menagerie: diatoms for novel applications in nanotechnology. *Trends Biotechnol* **27**, 116–127 (2009).

128.   Rabiee, N. *et al.* Diatoms with invaluable applications in nanotechnology, biotechnology, and biomedicine: Recent advances. *ACS Biomater Sci Eng* **7**, 3053–3068 (2021).

129. Westerveld, W. J. *et al.* Sensitive, small, broadband and scalable optomechanical ultrasound sensor in silicon photonics. *Nat Photonics* **15**, 341–345 (2021).

130. Bogaerts, W. *et al.* Basic structures for photonic integrated circuits in Silicon-on-insulator. *Optics Express* **12**, 1583–1591 (2004).

131. Je, C. H., Lee, J., Yang, W. S., Kim, J. & Cho, Y. H. A surface-micromachined capacitive microphone with improved sensitivity. *Journal of Micromechanics and Microengineering* **23**, 055018 (2013).

132. Shubham, S. *et al.* A Novel MEMS Capacitive Microphone with Semiconstrained Diaphragm Supported with Center and Peripheral Backplate Protrusions. *Micromachines* **13**, 22 (2021).

133. Tommasi, E. De, Tommasi, E. De, Luca, A. C. De & Luca, A. C. De. Diatom biosilica in plasmonics: applications in sensing, diagnostics and therapeutics. *Biomedical Optics Express* **13**, 3080–3101 (2022).

134. Jeffryes, C. *et al.* Electroluminescence and Photoluminescence from Nanostructured Diatom Frustules Containing Metabolically Inserted Germanium. *Advanced Materials* **20**, 2633–2637 (2008).

135. Tommasi, E. De *et al.* Optics with diatoms: towards efficient, bioinspired photonic devices at the micro-scale. *SPIE Proceedings* **8792**, 99–104 (2013).

136. Kong, X. *et al.* Plasmonic nanoparticles-decorated diatomite biosilica: extending the horizon of on-chip chromatography and label-free biosensing. *J Biophotonics* **10**, 1473–1484 (2017).

137.   Abdusatorov, B., Salimon, A. I., Bedoshvili, Y. D., Likhoshway, Y. V. & Korsunsky, A. M. FEM exploration of the potential of silica diatom frustules for vibrational MEMS applications. *Sens Actuators A Phys* **315**, 112270 (2020).

138.   Gebeshuber, I. C. *et al.* Exploring the innovational potential of biomimetics for novel 3D MEMS. *Adv Mat Res* **74**, 265–268 (2009).

139.   Kim, K., Liang, Z., Liu, M. & Fan, D. E. Biobased High-Performance Rotary Micromotors for Individually Reconfigurable Micromachine Arrays and Microfluidic Applications. *ACS Appl Mater Interfaces* **9**, 6144–6152 (2017).

140.   Kawahara, T. *et al.* On-chip microrobot for investigating the response of aquatic microorganisms to mechanical stimulation. *Lab Chip* **13**, 1070–1078 (2013).

141.   Cvjetinovic, J. *et al.* Photonic tools for evaluating the growth of diatom colonies during long-term batch cultivation. *J Phys Conf Ser* **2172**, 012011 (2022).

142.   Cvjetinovic, J. *et al.* In situ fluorescence/photoacoustic monitoring of diatom algae. SPIE Proceedings **8** (2021).

143.   Davidovich, N. A., Davidovich, O. I. & Podunay, Y. The diatom culture collection at Karadag Scientific Station (Crimea). *Marine Biological Journal* **2**, 18–28 (2017).

144.   Andersen, R. A. *Algal Culturing Techniques*. Academic Press, p. 596 (2004).

145.   Medlin, L. K. & Kaczmarska, I. Evolution of the diatoms: V. Morphological and cytological support for the major clades and a taxonomic revision. *Phycologia* **43**, 245–270 (2004).

146.	Polyakova, S. L., Davidovich, O. I., Podunay, Y. A. & Davidovich, N. A. Modification of the ESAW culture medium used for cultivation of marine diatoms. *Marine Biological Journal* **3**, 73–80 (2018).

147.	Shishlyannikov, S. M. *et al.* A procedure for establishing an axenic culture of the diatom Synedra acus subsp. Radians (Kütz.) Skabibitsch. From Lake Baikal. *Limnol Oceanogr Methods* **9**, 478–484 (2011).

148.	Thompson, A. S., Rhodes, J. C. & Pettman, I. Culture collection of algae and protozoa : catalogue of strains (1988).

149.	Cvjetinovic, J. *et al.* Assessment of diatom growth using fluorescence imaging. *J Phys Conf Ser* **1984**, 012017 (2021).

150.	Cvjetinovic, J. *et al.* Concentration Dependence of Optical Transmission and Extinction of Different Diatom Cultures. *J Biomed Photonics Eng* **9**(1), 010303 (2023).

151.	Cvjetinovic, J. *et al.* Photoacoustic visualization of diatom algae. *Limnol Freshw Biol* **4**, (2020).

152.	Croce, R. & Van Amerongen, H. Natural strategies for photosynthetic light harvesting. *Nature Chemical Biology* **10**, 492–501 (2014).

153.	Bedoshvili, Y. D., Kaluzhnaya, O. V. & Likhoshway, Y. V. The frustules morphogenesis of aulacoseira baicalensis in the natural population. *Journal of Advanced Microscopy Research* **7**, 219–223 (2012).

154.	Salakhova, N. S., Fradkin, I. M., Dyakov, S. A. & Gippius, N. A. Fourier modal method for moiré lattices. *Phys Rev B* **104**, (2021).

155.   Griffiths, M. J., Garcin, C., van Hille, R. P. & Harrison, S. T. L. Interference by pigment in the estimation of microalgal biomass concentration by optical density. *J Microbiol Methods* **85**, 119–123 (2011).

156.   Touliabah, H. E., Abdel-Hamid, M. I. & Almutairi, A. W. Long-term monitoring of the biomass and production of lipids by Nitzschia palea for biodiesel production. *Saudi J Biol Sci* **27**, 2038–2046 (2020).

157.   Knefelkamp, B., Carstens, K. & Wiltshire, K. H. Comparison of different filter types on chlorophyll-a retention and nutrient measurements. *J Exp Mar Biol Ecol* **345**, 61–70 (2007).

158.   Schagerl, M., Siedler, R., Konopáčová, E. & Ali, S. S. Estimating Biomass and Vitality of Microalgae for Monitoring Cultures: A Roadmap for Reliable Measurements. *Cells* **11**, (2022).

159.   Esra Erçetin Bursa Teknik Üniversitesi, V., Esra Dökümcüoğlu, V. & Yılmaz, M. *Assessment of Cell Counting Method Based on Image Processing for a Microalga Culture. MedFAR* **3** (2020).

160.   Manohar, S. & Razansky, D. Photoacoustics: a historical review. *Adv Opt Photonics* **8**, 586 (2016).

161.   Li, C. & Wang, L. V. Photoacoustic tomography and sensing in biomedicine. *Phys Med Biol* **54**, (2009).

162.   Wang, L. V. & Hu, S. Photoacoustic tomography: In vivo imaging from organelles to organs. *Science* **335**, 1458–1462 (2012).

163.   Korsunsky, A. M. & Salimon, A. I. On the paradigm of Hierarchically Structured Materials, in conjunction with the Virtual Special Issue on Functional Materials. *Mater Des* **158**, 1–4 (2018).

164.   Abdusatorov, B., Everaerts, J., Salimon, A. I. & Korsunsky, A. M. On the prospects of using Biogenic Silica for MEMS (Micro-Electro-Mechanical Systems). *Proceedings of the World Congress on Engineering*, (2019).

165.   Lamastra, F. R. *et al.* Photoacoustic Spectroscopy Investigation of Zinc Oxide/Diatom Frustules Hybrid Powders. *Int J Thermophys* **39**, 1–10 (2018).

166.   Pinchasov, Y., Porat, R., Zur, B. & Dubinsky, Z. Photoacoustics: A novel tool for the determination of photosynthetic energy storage efficiency in phytoplankton. *Hydrobiologia* **579**, 251–256 (2007).

167.   Akimoto, S. *et al.* Excitation relaxation dynamics and energy transfer in fucoxanthin–chlorophyll a/c-protein complexes, probed by time-resolved fluorescence. *Biochimica et Biophysica Acta (BBA) - Bioenergetics* **1837**, 1514–1521 (2014).

168.   Millie, D. F., Schofield, O. M. E., Kirkpatrick, G. J., Johnsen, G. & Evens, T. J. Using absorbance and fluorescence spectra to discriminate microalgae. *Eur J Phycol* **37**, 313–322 (2002).

169.   Burson, A., Stomp, M., Greenwell, E., Grosse, J. & Huisman, J. Competition for nutrients and light: testing advances in resource competition with a natural phytoplankton community. *Ecology* **99**, 1108–1118 (2018).

170.   Sullivan, C. W. Diatom mineralization of silicic acid. II. Regulation of $Si(OH)_4$ transport rates during the cell cycle of Navicula pelliculosa. *J Phycol* **13**(1), 86-91(1977).

171.	Kulikovskiy, M., Lange-Bertalot, H., Witkowski, A. & Khursevich, G. Achnanthidium sibiricum (Bacillariophyceae), a new species from bottom sediments in Lake Baikal. *Arch Hydrobiol Suppl Algol Stud* **136-137**, 77-87 (2011).

172.	Bedoshvili, Y. D. *et al.* Frustule morphogenesis of raphid pennate diatom Encyonema ventricosum (Agardh) Grunow. *Protoplasma* **255**, 911–921 (2018).

173.	Rothemund, P. Hemin and Chlorophyll: the Two Most Important Pigments for Life on Earth. *The Ohio Journal of Science* **56**, 193–202 (1956).

174.	Wang, J. K. & Seibert, M. Prospects for commercial production of diatoms. *Biotechnology for Biofuels* **10**(1), (2017).

175.	Li, X. L. *et al.* A novel growth method for diatom algae in aquaculture waste water for natural food development and nutrient removal. *Water Science and Technology* **75**, 2777–2783 (2017).

176.	Salimon, A. I., Everaerts, J., Sapozhnikov, P. V, Statnik, E. S. & Alexander, M. On Diatom Colonization of Porous UHMWPE Scaffolds. Proceedings of the World Congress on Engineering **II**, 4–8 (2018).

177.	Holdsworth, E. S. Effect of growth factors and light quality on the growth, pigmentation and photosynthesis of two diatoms, Thalassiosira gravida and Phaeodactylum tricornutum. *Marine Biology* **86**, 253–262 (1985).

178.	Chang, C. W., Sud, D. & Mycek, M. A. Fluorescence Lifetime Imaging Microscopy. *Methods Cell Biol* **81**, 495–524 (2007).

179.	Elson, D. *et al.* Biomedical Applications of Fluorescence Lifetime Imaging. *Opt Photonics News* **13**, 26 (2002).

180.   Becker, W. Fluorescence lifetime imaging - techniques and applications. *J Microsc* **247**, 119–136 (2012).

181.   Chen, L. C., Lloyd, W. R., Chang, C. W., Sud, D. & Mycek, M. A. Fluorescence lifetime imaging microscopy for quantitative biological imaging. *Methods in Cell Biology* **114**, 457-488 (2013).

182.   Korczyński, J. & Włodarczyk, J. Fluorescence lifetime imaging microscopy (FLIM) in biological and medical research. *Postepy Biochem* **55**, 434–40 (2009).

183.   Falkowski, P. G., Lin, H. & Gorbunov, M. Y. What limits photosynthetic energy conversion efficiency in nature? Lessons from the oceans. *Philosophical Transactions of the Royal Society B: Biological Sciences* **372**, 2–8 (2017).

184.   Lavaud, J. & Lepetit, B. An explanation for the inter-species variability of the photoprotective non-photochemical chlorophyll fluorescence quenching in diatoms. *Biochim Biophys Acta Bioenerg* **1827**, 294–302 (2013).

185.   Michels, J., Vogt, J. & Gorb, S. N. Tools for crushing diatoms – opal teeth in copepods feature a rubber-like bearing composed of resilin. *Scientific Reports* **2**, 1–6 (2012).

186.   Sancetta, C. Three species of Coscinodiscus Ehrenberg from North Pacific sediments examined in the light and scanning electron microscopes. *Micropaleontology* **33**, 230–241 (1987).

187.   Gogorev, R. M., Chudaev, D. A., Stepanova, V. A. & Kulikovskiy, M. S. Russian and English terminological glossary on morphology of diatoms. *Nov Sist Nizs Rast* **52**, 265–309 (2018).

188.   Tesson, B. & Hildebrand, M. Characterization and Localization of Insoluble Organic Matrices Associated with Diatom Cell Walls: Insight into Their Roles during Cell Wall Formation. *PLoS One* **8**, e61675 (2013).

189.   Loboda, V. V & Salamatova, U. V. Capacitive MEMS microphones for medical applications. *Computing, Telecommunications and Control* **14**, 65–78 (2021).

190.   Zawawi, S. A., Hamzah, A. A., Majlis, B. Y. & Mohd-Yasin, F. A review of MEMS capacitive microphones. *Micromachines* **11**, (2020).

191.   Mei, H. *et al.* Effects of water on the mechanical properties of silica glass using molecular dynamics. *Acta Mater* **178**, 36–44 (2019).

192.   Bhushan, B. & Koinkar, V. N. Nanoindentation hardness measurements using atomic force microscopy. *Appl Phys Lett* **64**, 1653 (1998).

193.   Garcia, R. & Proksch, R. Nanomechanical mapping of soft matter by bimodal force microscopy. *Eur Polym J* **49**, 1897–1906 (2013).

194.   García, R. & Pérez, R. Dynamic atomic force microscopy methods. *Surf Sci Rep* **47**, 197–301 (2002).

195.   Stanimirović, Z. & Stanimirović, I. *Mechanical Properties of MEMS Materials* in *Micro Electronic and Mechanical Systems*, ed. Takahata, K., IntechOpen, (2009).

196.   Melnikov, Y. A. Influence Functions of a Point Force for Kirchhoff Plates with Rigid Inclusions. *Journal of Mechanics* **20**, 249–256 (2004).

197.   Korsunsky, A. M. The influence of punch blunting on the elastic indentation response. *J Strain Anal Eng Des* **36**, 391–400 (2001).

198.   Korsunsky, A. M. & Constantinescu, A. The influence of indenter bluntness on the apparent contact stiffness of thin coatings. *Thin Solid Films* **517**, 4835–4844 (2009).

199.   Korsunsky, A. M. & Constantinescu, A. Work of indentation approach to the analysis of hardness and modulus of thin coatings. *Materials Science and Engineering: A* **423**, 28–35 (2006).

200.   Podsiadlo, P. *et al.* Ultrastrong and stiff layered polymer nanocomposites. *Science* **318**, 80–83 (2007).

201.   Pan, J., Cai, J., Zhang, D., Wang, Y. & Jiang, Y. Micro-arraying of nanostructured diatom microshells on glass substrate using ethylene-vinyl acetate copolymer and photolithography technology for fluorescence spectroscopy application. *Physica E Low Dimens Syst Nanostruct* **44**, 1585–1591 (2012).

202.   Jeffryes, C., Campbell, J., Li, H., Jiao, J. & Rorrer, G. The potential of diatom nanobiotechnology for applications in solar cells, batteries, and electroluminescent devices. *Energy and Environmental Science* **4**, 3930–3941 (2011).

203.   Parkinson, J. & Gordon, R. Beyond micromachining: the potential of diatoms. *Trends Biotechnol* **17**, 190–196 (1999).

204.   Simovic-Pavlovic, M., Bokic, B., Vasiljevic, D. & Kolaric, B. Bioinspired NEMS—Prospective of Collaboration with Nature. *Applied Sciences (Switzerland)* **12**, (2022).

205.   Ackerman, E. Resonances of biological cells at audible frequencies. *The bulletin of mathematical biophysics* 13, 93-106 (1951).

206.   Zinin, P. V., Allen, J. S. & Levin, V. M. Mechanical resonances of bacteria cells. *Phys Rev E Stat Nonlin Soft Matter Phys* **72**, (2005).

207.   Zinin, P. V. & Allen, J. S. Deformation of biological cells in the acoustic field of an oscillating bubble. *Phys Rev E Stat Nonlin Soft Matter Phys* **79**, (2009).

208.   Ford, L. H. Estimate of the vibrational frequencies of spherical virus particles. *Phys Rev E Stat Phys Plasmas Fluids Relat Interdiscip Topics* **67**, 3 (2003).

209.   Miller, D. K. Effects of a High-Amplitude l-MHz Standing Ultrasonic Field on the Algae Hydrodictyon. *IEEE Trans Ultrason Ferroelectr Freq Control.* **33**, 165-170, (1986).

210.   Gutiérrez, A., Gordon, R. & Dávila, L. P. Deformation Modes and Structural Response of Diatom Frustules. *Journal of Materials Science and Engineering with Advanced Technology* **15**, 105–134 (2017).

211.   Shah, M. A., Shah, I. A., Lee, D. G. & Hur, S. Design approaches of MEMS microphones for enhanced performance. *Journal of Sensors* **2019**, (2019).

212.   Williams, M. D., Griffin, B. A., Reagan, T. N., Underbrink, J. R. & Sheplak, M. An AlN MEMS piezoelectric microphone for aeroacoustic applications. *Journal of Microelectromechanical Systems* **21**, 270–283 (2012).

213.   Inomata, N., Tonsho, Y. & Ono, T. Quality factor control of mechanical resonators using variable phononic bandgap on periodic microstructures. *Sci Rep* **12**, (2022).

214.   Putman, C. A. J., De Grooth, B. G., Van Hulst, N. F. & Greve, J. A detailed analysis of the optical beam deflection technique for use in atomic force microscopy. *J Appl Phys* **72**, 6–12 (1992).

215. Gordon, R. & Tiffany, M. A. *Possible Buckling Phenomena in Diatom Morphogenesis* in *The Diatom World*, eds. Seckbach, J. & Kociolek, P., Springer Netherlands, 245–271 (2011).

216. Yoon, J., Kwon, M. H., Shin, D. H. & Lee, S. W. Mechanical resonance properties of porous graphene membrane; simulation study and proof of concept experiment. *Current Applied Physics* **23**, 30–35 (2021).

217. Dixit, S. S., Smol, J. P., Kingston, J. C. & Charles, D. F. Diatoms: powerful indicators of environmental change. *Environ Sci Technol* **26**, 22–33 (1992).

218. Kim, M.-S. *et al.* Fractional Talbot imaging of phase gratings with hard x rays. *J. Lightwave Technol* **25**, (2008).

219. Hermanowicz, P., Banaś, A. K., Sztatelman, O., Gabryś, H. & Łabuz, J. UV-B Induces Chloroplast Movements in a Phototropin-Dependent Manner. *Front Plant Sci* **10**, (2019).

220. Furukawa, T., Watanabe, M. & Shihira-Ishikawa, I. Green- and blue-light-mediated chloroplast migration in the centric diatomPleurosira laevis. *Protoplasma* **203**, 214–220 (1998).

221. Sakai, Y. & Takagi, S. Roles of actin cytoskeleton for regulation of chloroplast anchoring. *Plant Signal Behav* **12**, (2017).

222. Yeh, Y. C., Creran, B. & Rotello, V. M. Gold nanoparticles: Preparation, properties, and applications in bionanotechnology. *Nanoscale* **4**, 1871–1880 (2012).

223. Turkevich, J., Stevenson, P. C. & Hillier, J. A study of the nucleation and growth processes in the synthesis of colloidal gold. *Discuss Faraday Soc* **11**, 55–75 (1951).

224.	Miller, M. M. & Lazarides, A. A. Sensitivity of metal nanoparticle plasmon resonance band position to the dielectric environment as observed in scattering. *Journal of Optics A: Pure and Applied Optics* **8**, 21556–21565 (2006).

225.	Salopek, B., Krasic, D. & Filipovic, S. Measurement and application of zeta-potential. *Rudarsko-geolosko-naftni zbornik* **4**, 147–151 (1992).

226.	Sau, T. K., Rogach, A. L., Jäckel, F., Klar, T. A. & Feldmann, J. Properties and applications of colloidal nonspherical noble metal nanoparticles. *Advanced Materials* **22**, 1805–1825 (2010).

227.	Xu, R. X. Multifunctional microbubbles and nanobubbles for photoacoustic imaging. *Contrast Media Mol Imaging* **6**, 401–411 (2011).

228.	Amendola, V., Pilot, R., Frasconi, M., Maragò, O. M. & Iatì, M. A. Surface plasmon resonance in gold nanoparticles: A review. *Journal of Physics Condensed Matter* **29**, (2017).

229.	Cheheltani, R. *et al.* Tunable, biodegradable gold nanoparticles as contrast agents for computed tomography and photoacoustic imaging. *Biomaterials* **102**, 87–97 (2016).

230.	German, S. V. *et al.* High-efficiency freezing-induced loading of inorganic nanoparticles and proteins into micron- and submicron-sized porous particles. *Sci Rep* **8**, 17763 (2018).

231.	Yashchenok, A. M. *et al.* Impact of magnetite nanoparticle incorporation on optical and electrical properties of nanocomposite LbL assemblies. *Physical Chemistry Chemical Physics* **12**, 10469–10475 (2010).

232. Bédard, M. F. *et al.* On the mechanical stability of polymeric microcontainers functionalized with nanoparticles. *Soft Matter* **5**, 148–155 (2009).

233. Yashchenok, A. M., Inozemtseva, O. A., Gorin, D. A. & Khlebtsov, B. N. Effect of the size of colloidal gold nanoparticles on the physical parameters of nanocomposite microcapsule shells. *Colloid Journal* **71**, 422–429 (2009).

234. Esenaliev, R. O. Optoacoustic monitoring of physiologic variables. *Front Physiol* **8**, 1–6 (2017).

235. Jokerst, J. V., Thangaraj, M. & Gambhir, S. S. *Photoacoustic imaging of mesenchymal stem cells in living mice via silica-coated gold nanorods* in *Photons Plus Ultrasound: Imaging and Sensing 2014*, eds. Oraevsky, A. A. & Wang, L. V., SPIE **8943**, 89431O (2014).

236. Chen, Y., Xu, C., Cheng, Y. & Cheng, Q. Photostability enhancement of silica-coated gold nanostars for photoacoustic imaging guided photothermal therapy. *Photoacoustics* **23**, 100284 (2021).

237. Chen, Y. S. *et al.* Silica-coated gold nanorods as photoacoustic signal nanoamplifiers. *Nano Lett* **11**, 348–354 (2011).

238. He, X. N. *et al.* Surface-enhanced Raman spectroscopy using gold-coated horizontally aligned carbon nanotubes. *Nanotechnology* **23**, (2012).

239. Watanabe, H., Hayazawa, N., Inouye, Y. & Kawata, S. DFT vibrational calculations of Rhodamine 6G adsorbed on silver: Analysis of tip-enhanced Raman spectroscopy. *Journal of Physical Chemistry B* **109**, 5012–5020 (2005).

240.   Le Ru, E. C., Blackie, E., Meyer, M. & Etchegoint, P. G. Surface enhanced raman scattering enhancement factors: A comprehensive study. *Journal of Physical Chemistry C* **111**, 13794–13803 (2007).

241.   Chen, J. *et al.* A synergistic combination of diatomaceous earth with Au nanoparticles as a periodically ordered, button-like substrate for SERS analysis of the chemical composition of eccrine sweat in latent fingerprints. *J Mater Chem C Mater* **3**, 4933–4944 (2015).

242.   Bedoshvili, Y. D. & Likhoshway, Y. V. *Changing of silica valves of diatom Synedra acus subsp. radians influenced by paclitaxel Bacillariophyta*. Tsitologiya **59**(1), 53-61 (2017).

243.   Tomba, J. P., Arzondo, L. M. & Pastor, J. M. *Depth Profiling by Confocal Raman Microspectroscopy: Semi-empirical Modeling of the Raman Response*. Applied Spectroscopy, **61**(2), (2007).